A MULTIWAVELENGTH STUDY OF GALACTIC STAR-FORMING REGIONS

Thesis Submitted for the Degree of

DOCTOR OF PHILOSOPHY (SCIENCE)
in
PHYSICS (EXPERIMENTAL)

by

ALIK PANJA

Department of Physics
University of Calcutta

2022

To the Nature

The more we evolve, the closer we move toward the episodes of mass extinction. All our evolution will be undone in a catastrophic scale. No single species can dominate over an indefinite time. The nature will rebuild itself with or without us.

Contents

List of Figures

List of Tables

Abstract

The thesis comprises a comprehensive investigation of multiple young protostellar clusters located in the Galactic disk. These protocluster systems are the hub to inhold many complex and diverse physical phenomena concerned with the formation and early evolution of the stellar sources. Such aspects are explored based on the combination of ground to space facility telescopes, from observed to archival catalogs covering optical to radio wavelengths. Most stars form in groups or clusters embedded within giant regions of molecular clouds. Likewise, the Galactic H II regions Sh2-242 and Sh2-112 depict star formation activity in an extended scale. Employing the dust mapping methods, multiple complexes with excessive extinction are revealed, with all of them interconnected via filamentary clouds. Both the regions harbour a rich population of young stars and Hα emitters, characterized with excess emission. The young stars spatially correlate with the filament patterns, whereas their groupings preferentially coincide with the high extinction complexes together with the densest parts of the molecular clouds, signifying active ongoing star formation. Moreover, the filament associated with Sh2-112 is dynamic with the radial velocity, showing evidence of cloud fragmentation and formation of several cores. Illuminated by massive ionizing stars, these H II regions manifest likelihood of triggered star formation activity. The star formation and evolution is hardly in isolation, however, in the Galactic open cluster M 36, multiple stellar population coexist along the same line of sight, stipulating a tantalizing evidence of sustained star formation activity. The young star cluster exhibits distinct peaks for the proper motion and the parallax distribution. A massive cloud core with uniform velocity continuity correlates with a highly obscured and compact extinction complex, where young stars in their infancy reside. If physical association between M 36 and the young stellar population can be unambiguously established, this manifests a convincing example of prolonged star formation activity spanning up to tens of Myrs in molecular clouds.

Publications

Thesis Related Publications in Refereed Journals

1. **Alik Panja**, Soumen Mondal, Somnath Dutta, Santosh Joshi, Sneh Lata, & Ramkrishna Das, 2020, *"Census of the Young Stellar Population in the Galactic H II Region Sh2-242"*, AJ, 159, 153, doi: 10.3847/1538-3881/ab737a
2. **Alik Panja**, Wen Ping Chen, Somnath Dutta, Yan Sun, Yu Gao, & Soumen Mondal, 2021, *"Sustaining Star Formation in the Galactic Star Cluster M 36?"*, ApJ, 910, 80, doi: 10.3847/1538-4357/abded4
3. **Alik Panja**, Yan Sun, Wen Ping Chen, & Soumen Mondal, 2022, *"Star and Cluster Formation in the Sh2-112 Filamentary Cloud Complex"*, ApJ, 939, 46, doi: 10.3847/1538-4357/ac940f

Thesis Related Publications in Conference Proceedings

1. **Alik Panja**, Soumen Mondal, Somnath Dutta, Santosh Joshi, Sneh Lata, Ramkrishna Das, & Siddhartha Biswas, 2019, *"Characterization of pre-main sequence population in H II region Sh2-242"*, Bulletin de la Société Royale des Sciences de Liège, 88, 270, doi: 10.25518/0037-9565.8959

Other Publications in Refereed Journals

1. Samrat Ghosh, Soumen Mondal, Somnath Dutta, Ramkrishna Das, Santosh Joshi, Sneh Lata, Dhrimadri Khata, & **Alik Panja**, 2021, *"Fast Photometric Variability of Very Low Mass Stars in IC 348: Detection of Superflare in an M-dwarf"*, MNRAS, 500, 5106, doi: 10.1093/mnras/staa3574

Acknowledgements

Throughout the course of this journey many people have left their mark in my work as well as in livelihood in a unique and undeniable way.

Prof. Wen-Ping Chen is the most significant figure in my academic activities during this tenure. He has liberally and consistently rendered enough time and efforts to improve both the scientific content and the manuscript presentation. I never had that much of academic discussions with anyone else other than him. It has been a privilege for me working in his lab for a certain period. Since then I continued to collaborate with him.

Thanks to my supervisor Prof. Soumen Mondal for giving me the freedom to choose my own fields and encouraging me to develop myself as an independent researcher. This offered me ample scope to thrive my knowledge, skills, and patience. It is my pleasure that he introduced me with Prof. Chen. Dr. Yan Sun has provided a great deal of radio data, results from which are extensively incorporated in my works. Dr. Santosh Joshi and Dr. Sneh Lata have dealt with allocation of observing nights in DFOT. Prof. Yu Gao has managed time to check my manuscripts earnestly. Thanks to Dr. Ramkrishna Das for his assistance during observations in some of the cycles in DFOT. We have spent quality times in numerous occasions.

The observatory (HCT & DFOT) staff members have provided hospitality in a homely and humour manner and done their job with sincere professionalism. A special mention goes to Mr. Sanjoy Choudhury and Mr. Bijoy Pramanik (Computer Services Cell) for their kind and friendly appearances to everyone and making sure that the computers and networks were working properly. Mr. Gurudas Ghosh and Mr. Amit Roy (Library Section) have done their part always with extra care and sweetness. The SNB Mess has been an integral part and resource to an enjoyable life for a considerable time.

Much of the thesis work (for about two years) has been done from my home during the Covid-19 pandemic. In this prolonged phase, my family members have been continually supportive without even causing a single distraction to my attention while keeping their faith. Friends have been an inseparable part of my daily life all along the way. They have always been there regardless of any cause or need and I still can feel their affection every now and then. My feelings for them and memories with them are the most valuable treasures forever. Friends and family (specifically) are beyond any formal obligations to my extent and I dare not attempt so.

I acknowledge the support provided by the S. N. Bose National Centre for Basic Sciences particularly for a year of extension to complete this study.

Chapter 1

Introduction

Stars are the cosmic furnaces that eventually produce all the heavier elements necessary for the existence of life. They are the only sources that may hold and support the planetary systems, and supply essential resources for a sustainable life. So the origins of life and in turn to planets are inextricably related to the formation of stars. On the macroscopic sense, the star formation processes have major implications in the reprocessing of interstellar matter that modulates the chemical evolution of the host galaxy.

1.1 The Formation of Stars

Stars are formed out of the condensed gas in the molecular clouds (Evans & Lada 1991, Elmegreen 1993). A significant fraction, if not the vast majority, of all the stars are born within embedded clusters (Lada & Lada 2003). The richness of such embedded clusters in the galactic disk population makes them suitable testbeds for studies of the stellar dynamics. As the stars are formed more or less simultaneously from the same progenitor molecular cloud, they share the common heritage of similar space motion, distance, age, and composition. At the initial stages stars are heavily obscured by circumstellar gas and dust, making them barely visible other than in the infrared wavelengths. However, over the recent decades, the development of observational technology has drastically improved the situation. From the initial collapse of the cloud cores to the onset of hydrogen fusion involves a multitude of complex processes. In the subsequent sections, a brief overview of our current understanding on the formation of stars and on their early stage evolution is presented.

1.1.1 Molecular Cloud Structures

Molecular clouds are the densest components of the interstellar medium in the galaxies and are the prime sites of star formation. Molecular clouds comprise hierarchical structures that are often irregular and widely distributed (Dickman et al. 1990). The size and mass of the observable molecular clouds vary from a few parsecs and $\sim 10\ M_\odot$ to ~ 100 pc and $\sim 5 \times 10^5\ M_\odot$ for the giant molecular clouds (GMCs) (Stark & Blitz 1978;

Blitz & Shu 1980). The cloud densities vary in the order of $\sim 10^{-22}$ to 10^{-18} g cm^{-3} with a typical temperature of ~ 10 K (Sanders et al. 1985). In general, the molecular cloud boundaries represent the transition state from molecular gas to atomic gas distributed in extended envelopes (Falgarone et al. 1991). This layer of atomic gas shields the molecules inside from the interstellar ultraviolet radiation field. Therefore, the molecular composition of the cloud is dependent on the local gas density and predominantly on the column density of the atomic gas. In the solar vicinity, the typical column density of the atomic gas is $\sim 2 \times 10^{20}$ cm^{-2} (Bohlin et al. 1978). The molecular clouds are mostly composed of H_2, and depending on the shielding, other molecules – such as CO, H_2O, NH_3, OH, and HCN may form. To form CO, the required column density is of the order of $\sim 1.4 \times 10^{21}$ cm^{-2} (van Dishoeck & Black 1988). The CO molecules can be easily excited and thus are suitable to probe the masses and properties of the molecular clouds.

Molecular clouds are transient entities with a typical survival period of $\sim 10^7$ years (Blitz & Shu 1980; Larson 1981). Within this relatively short time period, the molecular clouds undergo frequent structural transformation due to turbulent reprocessing of the gas at the boundary or formation and destruction of clumps, leading to its dynamical evolution. Usually the stars or clusters that are formed from them, disperse away most of their natal clouds within a timescale of 10 to 20 Myr, and no longer contain significant amounts of gas or dust surrounding them. Since the formation, evolution, and destruction of the molecular clouds all happen in a rather short and similar timescale, and those can occur simultaneously in different parts of the same star-forming complex, therefore the processes are inherently difficult to disentangle in time.

1.1.2 Star Formation Paradigm

The onset of star formation begins soon after the cloud has formed. Although not all of the molecular clouds contribute in forming stars. However, the time duration between the cloud formation and the onset of star formation cannot exceed the dynamical or free-fall time of the cloud. In elongated molecular clouds, the star formation may already proceed in some parts while the cloud itself is still assembling material.

Cloud Collapse and Fragmentation

The collapse can happen in the densest part of a large-scale cloud, even if the cloud as a whole is not collapsing. The gravitational instability is the prime factor responsible for the onset of collapse, wherein the surface density of gas exceeds certain threshold (Kennicutt 1989). Following the collapse, the cloud fragments into smaller bound clumps. Those gravitationally bound fragments, that have a minimum mass of Jeans mass, eventually develop into stars or groups of stars.

Filaments, Clumps, and Cores

Not necessarily the collapsing clouds take a spherical shape, but tend to produce flattened or filamentary structures, due to the effects of initial asymmetries, magnetic fields, and turbulence (Larson 1985). Tentatively the flattened structures are the first to be formed, then they break into filaments before finally fragmenting into clumps (Miyama et al. 1987a; 1987b). Filaments may also originate from cylindrical clouds, as the clouds tend to collapse toward the axis (Larson 1972). Observationally there are abundant evidence of molecular clouds showing elongated or filamentary shapes (Schneider & Elmegreen 1979; Myers et al. 1991; Dobashi et al. 2005; André et al. 2014). The over-dense regions of the GMCs are termed as clumps (mass $\sim 100\ M_\odot$, size $\sim$ few parsecs) out of which the stellar clusters form. The GMCs can contain $\sim$ 10–100 density enhanced clumps or sub-structures. Cores (mass $\sim$ 1–10 $M_\odot$, size $\sim$ 0.5 pc) are the dense regions of molecular clouds out of which individual stars (or multiple systems like binaries) form, and are necessarily gravitationally bound (McKee & Ostriker 2007). However, most of the total cloud mass is found to be concentrated within the most massive clumps. The distribution of the compact and point sources in the Monoceros OB 1 filamentary cloud in a submillimeter map is shown in Figure 1.1.

H ii Regions and Feedback

A newly formed massive (OB) star or a group of massive stars influences their ambient interstellar medium by means of ionization through the combined effects of stellar wind and energetic (ultraviolet) radiation. Surrounding the star a spherical shell of hot ionized gas is created, known as an H ii region (Strömgren 1939; Kahn 1954; Spitzer 1978; Tremblin et al. 2014). The radiation with excessive energy heats up the gas from ~ 10 K to $\sim 10^4$ K (Bisbas et al. 2009). This abrupt rise in temperature creates a huge contrast in pressure between the ionized gas and the surrounding medium. Driven by the thermal pressure of the ionized gas, rapidly expanding ionized bubbles form. Depending on the nature of the surrounding medium two processes might come into play. In the *"radiation driven implosion"* mechanism, the expanding H ii regions overrun and compress nearby pre-existing clouds, rendering them unstable and causing them to collapse (Sandford et al. 1982; Bertoldi 1989; Lefloch & Lazareff 1994). In the *"collect and collapse"* scenario, the surrounding neutral gas is swept up by the expanding H ii region into a dense shell, which is likely to become gravitationally unstable (Elmegreen & Lada 1977; Whitworth et al. 1994; Deharveng et al. 2005). These instabilities trigger the fragmentation and consequently lead to star formation. In both the cases, the H ii regions invoke to drive the self-propagating star formation, thus result in positive feedback. Conversely, the H ii regions might also result in negative feedback by disrupting the adjacent residual dense gas.

Cloud Destruction and Recycling

Star formation in one way plays a critical role in the destruction and recycling of molecular clouds. Ionization by hot massive stars is the most effective way to do that. Since

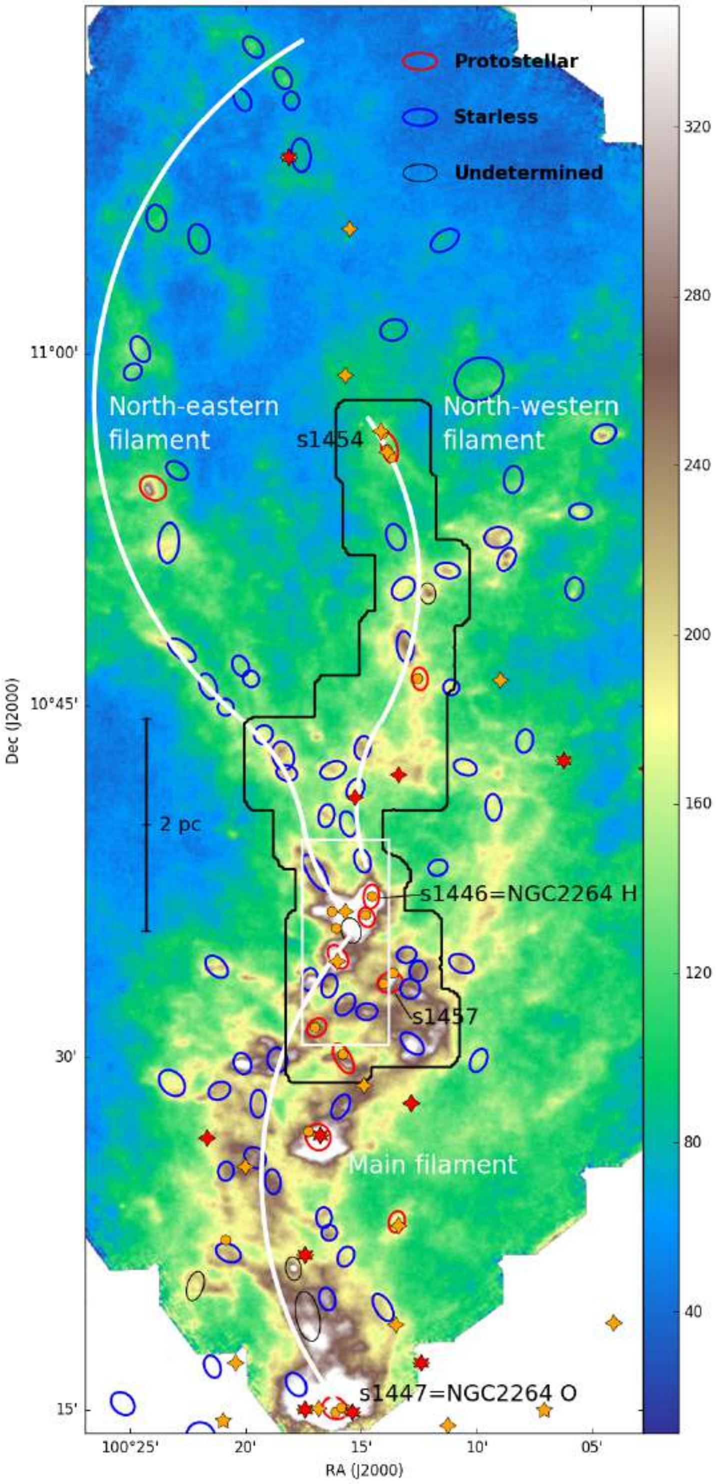

Figure 1.1: Star formation activity in a sub-region (∼ 10 pc × 3 pc) of the Monoceros OB 1 cloud, showing interconnected filamentary structures, adopted from Montillaud et al. (2019). This complex site harbors sources of all evolutionary stages from starless cores to Class III protostars. A chain of massive cores (10–50 $M_\odot$) is evident on the PACS 160 μm surface brightness (MJy sr^{-1}) map.

the newly formed stars, if massive enough, are capable of destroying their surrounding birth clouds and dispersing the matter back into the interstellar medium in more diffuse forms. It is only $\sim 4\%$ of the total cloud mass that is necessary to convert into stars, to produce enough hot stars and sufficient ionizing radiation to completely ionize and evaporate the rest of the cloud (Whitworth 1979). However the observed star formation efficiency is somewhat smaller (2% or less), which is explainable by considering the significant contribution in the dispersion process by the stellar wind (Leisawitz et al. 1989), in addition to the ionization. Eventually the restructured cloud is continually used as the raw material for building new molecular clouds, thus completing the recycling process.

1.1.3 Low-mass Star Formation

The star formation is conventionally divided into two categories: the low-mass stars form within the Kelvin-Helmholz time, whereas formation of the high-mass stars takes longer than that (Kahn 1974). A mass of 8 $M_\odot$ is considered to confine between the low- and high-mass stars. In case of low-mass star formation, the protostellar cores have a mass of the order of the thermal Jeans mass and their luminosities are dominated by accretion. In contrast, the high-mass stars form when the cores masses are significantly above the thermal Jeans mass and their luminosities are mostly dominated by nuclear burning. The low-mass stars are formed from the gravitationally bound cores through the core collapse and protostellar infall or the star-disk accretion system (Larson 2003). The timescale for accretion determines the accretion luminosity and therefore the core mass. Naturally, the rate of accretion is initially high but declines with time as the surrounding envelope is depleted. Eventually when the opacity (density $\sim 10^{-13}$ g cm^{-3}) of the collapsing core becomes large enough, the gas within switches from approximately isothermal to adiabatic nature. At this phase the gas becomes hot enough to stop the collapse, and the first core forms, initiating the formation of an accretion shock. Once the gas becomes sufficiently hotter (temperature ~ 2000 K) to dissociate the hydrogen molecules, a second collapse ensues and the protostar is formed (McKee & Ostriker 2007). The results presented in this thesis mainly deal with the low-mass star formation.

1.1.4 Protostellar Evolution

Disks, Jets, and Outflows

The protostar grows as matter continues to accrete onto the central core. Because the protostellar cores are rotating, at some point, the centrifugal force of the gas halts the gravitational collapse perpendicular to the axis of rotation. But the collapse can continue parallel to this axis. Thus the conservation of angular momentum leads to the formation of a centrifugally supported disk (Terebey et al. 1984; Andrews & Williams 2007). The average disk sizes around T Tauri stars (TTSs; Calvet et al. 2004) are ≈ 200 AU that can be extended upto 1000 AU (Muzerolle et al. 2003). The disk masses for the T Tauri systems vary in the range $\sim 10^{-3}$–10^{-1} $M_\odot$ with a median of ~ 0.005 $M_\odot$ (Andrews & Williams 2005). The overall disk lifetimes are ≈ 6 Myr, although the lifetimes appear to be correlated better with the core mass (Haisch et al. 2001; Bally 2007; Hernández et al. 2007). However, within a timescale of 2–3 Myr, for $\sim 70\%$ of the young stars, the disks become optically thin in the infrared (Lada 2006). As a consequence of the rotating accretion disks and open magnetic field lines, small amounts of material are ejected from the disk centrifugally, carrying away angular momentum. This results in the formation of highly collimated bipolar jets with rapid velocities ($\gtrsim 100$ km s^{-1}) (Reipurth & Bally 2001; Bally 2007). The launch of jets induces momentum to the surrounding molecular clouds, forming large-scale (size $\sim$ several parsecs, mass $\sim 10^{-2}$–$200\ M_\odot$) outflows with typical velocities of tens of km s^{-1} (Bachiller 1996).

Spectral Energy Distributions

Once the protostars have acquired most of their core masses, the envelopes gradually start to dissipate. As the stars evolve, the envelopes become optically thinner. The contributions from envelopes, disks to cores become increasingly evident, traceable mostly in the near- to mid-infrared. This evolutionary progression is reflected in the spectral energy distributions (SEDs) of the continuum. Conventionally the protostellar SEDs are divided into four classes, from Class 0–III (Adams et al. 1987; Myers et al. 1987; Andre et al. 1993), based on the relative significance of the radiation emitted by a dust disk with respect to the stellar black-body. Their evolutionary nature can be interpreted in terms of the spectral index (α) measured in the range $\sim$ 2.0–25 μm (Lada 1987). A schematic diagram for the evolutionary progression from Class 0–III phase is portrayed in Figure 1.2.

Class 0: Sources are extremely young and they have significant infalling envelopes. At this phase the objects assemble bulk of their final stellar mass. Although significant disks might not have formed yet but they are already driving jet-like outflows. They display a greybody spectrum at submillimeter wavelengths ($\sim$ 10–30 K) and are barely detectable at $\lambda < 10\ \mu$m, extremely faint at optical and near-infrared. The typical lifetime in this phase is 1–3 $\times 10^4$ years.

Class I: Sources ($\alpha > 0$) are relatively evolved protostellar cores surrounded by compact circumstellar disks (radius $\sim$ 10–100 AU), which are self-embedded in more extended infalling envelopes ($\sim 10^4$ AU). Class I sources drive outflows that are broader and slower than those of Class 0 sources. They have rising mid-infrared SEDs supposed to be produced by the warm circumstellar dust envelopes, and are predominant over the stellar photospheric emission. They have a typical lifetime of 1–2 $\times 10^5$ years.

Class II: Sources ($-1.5 < \alpha < 0$) have optically thick disks ($\sim$ 100 AU) and possibly a tenuous envelope (classical TTSs). Their SEDs peak at near-infrared and show substantial infrared excess due to the disk emission, but are dominated by the stellar photospheric radiation.

Class III: Sources ($\alpha < -1.5$) with optically thin disks or mostly cleared away (weak-line TTSs). The SEDs decrease in luminosity toward the longer wavelengths showing negligible infrared excesses and are well-fitted by a black-body spectrum owing to the central star.

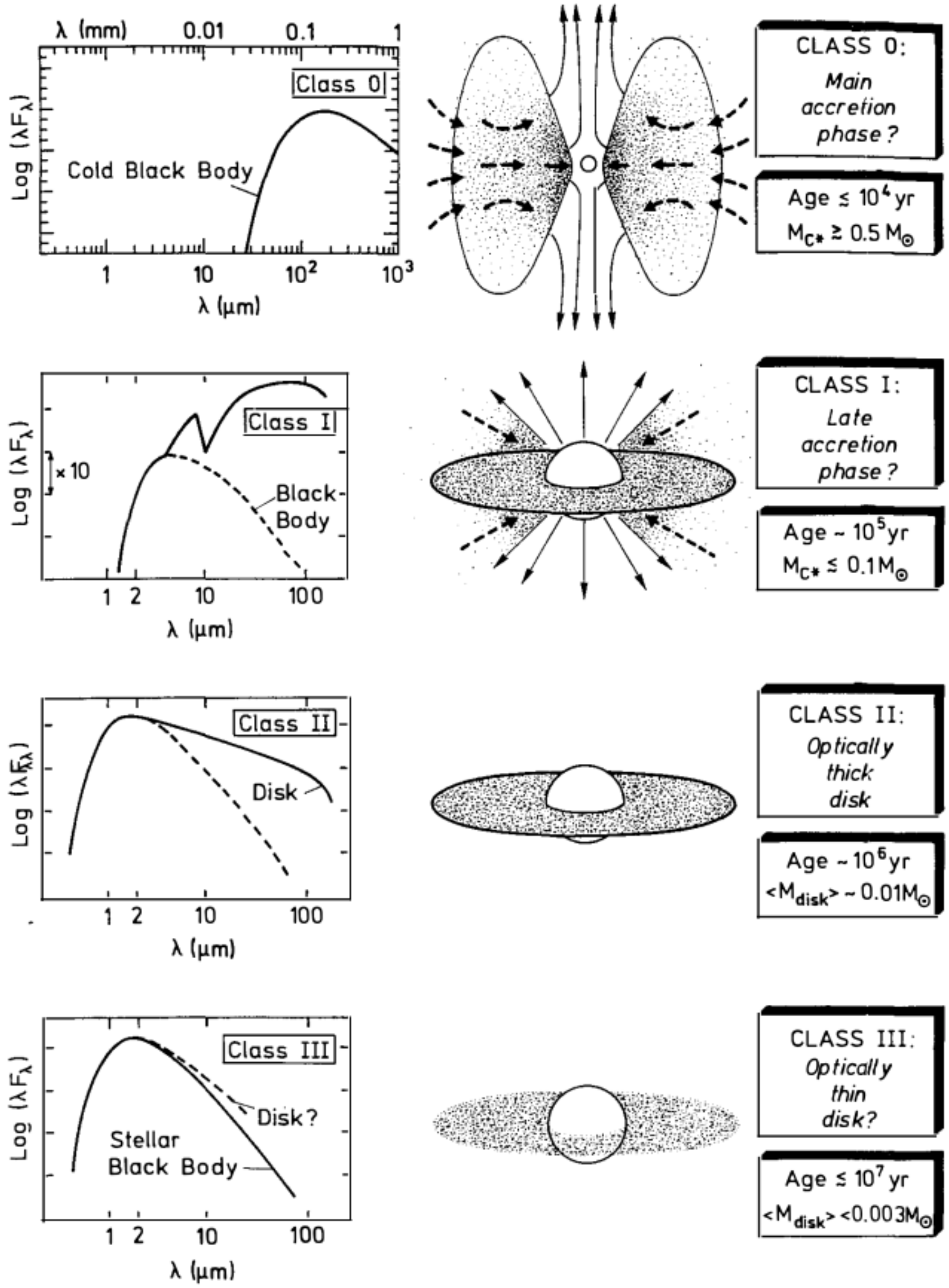

Figure 1.2: Evolutionary sequence of the spectral energy distributions from Class 0–III for low-mass ($< 8\ M_\odot$) young objects, adopted from André (1994).

1.2 Interstellar Dust and Extinction

Dust is primarily localized in the galactic plane with an extreme irregular distribution. They make up $\sim 0.7\%$ mass of the interstellar material in the form of diffuse clouds (Mathis et al. 1977). Interstellar dust processes about one-half or more of the stellar energy in the ultraviolet-optical budget of the universe into the infrared (Calzetti 2001; Hauser & Dwek 2001). Therefore the infrared luminosity of a galaxy is a measure of its dust content. In fact, the dust content is related to both metallicity and gas content of galaxies. The primary composition of the dust grains is silicate, graphite or amorphous carbon (Draine 2003), which are injected into the interstellar medium by oxygen-rich M stars and carbon-rich objects (such as planetary nebulae and carbon stars) (Cohen et al. 1981; Mathis 1990). The most abundant element of the interstellar medium H_2 forms on dust grains (Spitzer 1978).

The background radiation field is undoubtedly influenced by interstellar dust by the processes of absorption and scattering, and is re-radiated at higher wavelengths or in a different direction. In both the processes, the brightness of the background starlight is diminished. The amount of magnitude by which the reprocessed radiation differs from the actual radiation field is referred as extinction (Trumpler 1930a). In the regions, where interstellar clouds collapse to form stars, the dust opacity becomes higher, thereby the extinction effects are considerable. Although infrared is the dominant window to study the dust properties, the extinction measurements in this regime are potentially subject to a few limitations. Factors such as, wavelength dependency of extinction is still controversial particularly in the infrared, and discriminating intrinsically reddened stars due to circumstellar dust emission from the background comparison stars in a reddened zone is difficult, can cause severe uncertainties (Savage & Mathis 1979). Therefore the infrared/optical/ultraviolet data are required to be corrected for the extinction effects according to an extinction curve, as shown in Figure 1.3. In the infrared, prominent absorption features are observed at 3.07 μm and 9.7 μm (Merrill et al. 1976). The 3.07 μm absorption is commonly attributed to solid H_2O and NH_3 found within molecular clouds. The 9.7 μm absorption is found mostly in the objects that are embedded in molecular clouds. This feature is also detected in emission in some stars and nebulae, that accompany heated circumstellar dust, and is produced by silicates. Another noticeable feature in the ultraviolet portion is the broad bump centered near 4.6 μm^{-1} (2175 Å), caused by small uncoated graphite grains (Koornneef & Code 1981; Mathis 1990).

1.3 Young Open Clusters

Clusters are groups of stars that are physically related and held together by inherently complex gravitational attraction of its individual members (Trumpler 1930b; Lada & Lada 2003). Necessarily, the gravity is accountable to render the group stable against tidal disruption by the galaxy or by passing interstellar clouds. Clusters are found in a broad range of age ($\sim$ 1 Myr to $\sim$ 10 Gyr), mass ($\sim 10^2$–10^6 $M_\odot$), and size or density

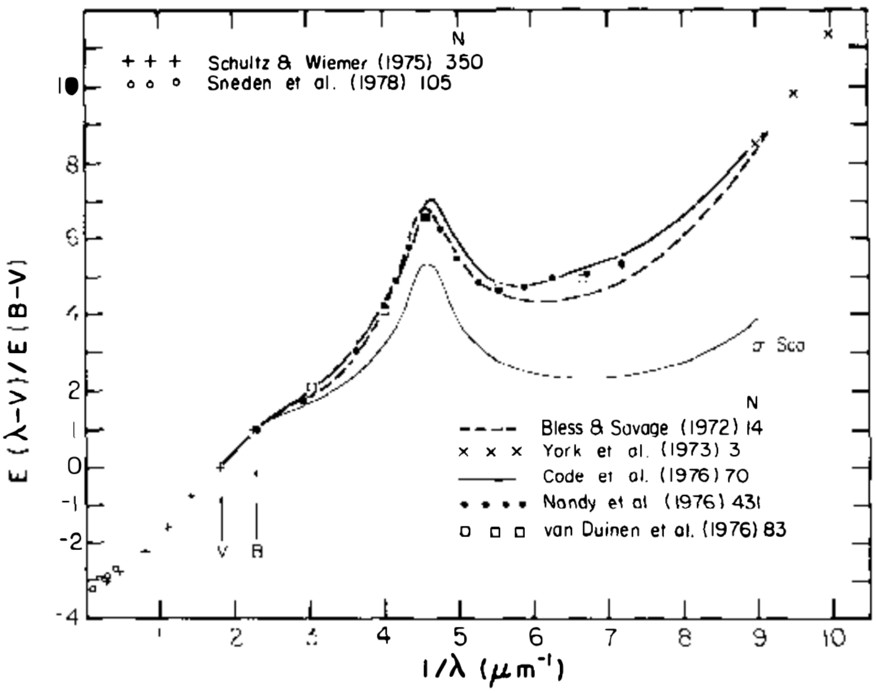

Figure 1.3: Average normalized interstellar extinction curves plotted in the range λ^{-1} = 0 to 10 μm^{-1}, adopted from Savage & Mathis (1979). The broad bump centered near 4.6 μm^{-1} is caused by small graphite particles present in interstellar grains. The references for various curves, along with the number of stars used to generate them, are mentioned in the diagram.

variations (Clark et al. 2005; Kenyon et al. 2008; Kharchenko et al. 2013; Krumholz et al. 2019). Some clusters take compact shape whereas others are sparse and extended. According to their evolutionary nature, clusters are divided into two categories. In embedded clusters the protostellar cores are still fully or partially associated with interstellar gas and dust, by the time upon surviving the internal stellar encounters, the systems emerge as exposed clusters, where little or no interstellar matter is associated. The star clusters that are located in the Galactic disk are generally referred as open clusters (mass $\lesssim 5 \times 10^3$ $M_\odot$, age $\lesssim$ 6 Gyr) (Lynga 1982; Piskunov et al. 2006; Motte et al. 2018), which are traditionally separated from the globular clusters (mass $\gtrsim 5 \times 10^4$ $M_\odot$, age $\gtrsim$ 6 Gyr) (Gratton et al. 2012; Bekki et al. 2017; Bastian & Lardo 2018) as those located in the bulge or halo. Although in the current paradigm there is a substantial overlap in this scenario. Often young open clusters with ages less than a few hundred million years are organized hierarchically and have the possibility to be embedded in gravitationally unbound associations. The evolutionary progression for a range of star clusters is illustrated in Figure 1.4.

1.3.1 Dynamical Evolution

The evolution of a cluster at the earliest phases is determined by a combination of processes, among them the prevalent are gas dynamics, stellar dynamics, stellar evolution, and radiative transfer (Kroupa et al. 1993; Elmegreen 2007; Price & Bate 2009). The star clusters that have survived the primordial gas removal phase would subsequently be driven by the relaxation. Likely the clusters tend to reach dynamical equilibrium through the mutual exchange of energy among the member stars. During this prolonged phase, the evolution of the cluster is dominated by the stellar mass loss, accounted mostly by evaporation and tidal stripping (Spitzer 1987; Baumgardt & Makino 2003; D'Ercole et al. 2008). As a consequence of the cluster expansion due to stellar mass loss, the low-mass members are occasionally disintegrated from the cluster either by achieving high-velocity enough to escape the cluster gravity or by approaching the cluster perimeter. Conversely, the massive stars lose energy at the fastest rate and sink deeper into the cluster potential. Therefore the most massive members are preferentially found to populate the cluster center, a phenomena commonly known as mass segregation (Fischer et al. 1998; de Grijs et al. 2002; McMillan et al. 2007; Vesperini et al. 2009). Eventually the clusters dissolve on timescales comparable to the median age ($\sim$ 250 Myr) of the open clusters in the Solar Neighborhood (Kharchenko et al. 2005). The cluster disruption can also be prompted in presence of any external perturbation, such as encounters between cluster and GMCs (Spitzer 1958).

1.3.2 Gas Expulsion

Once the condensation and conversion of the primordial cloud to stars has completed, the star formation process is supposed to end, and thereafter the gas expulsion phase begins (Verschueren & David 1989; Goodwin & Bastian 2006; Farias et al. 2018; Pang et al. 2020). The feedback from the evolving stars (stellar winds, ionization, radiation

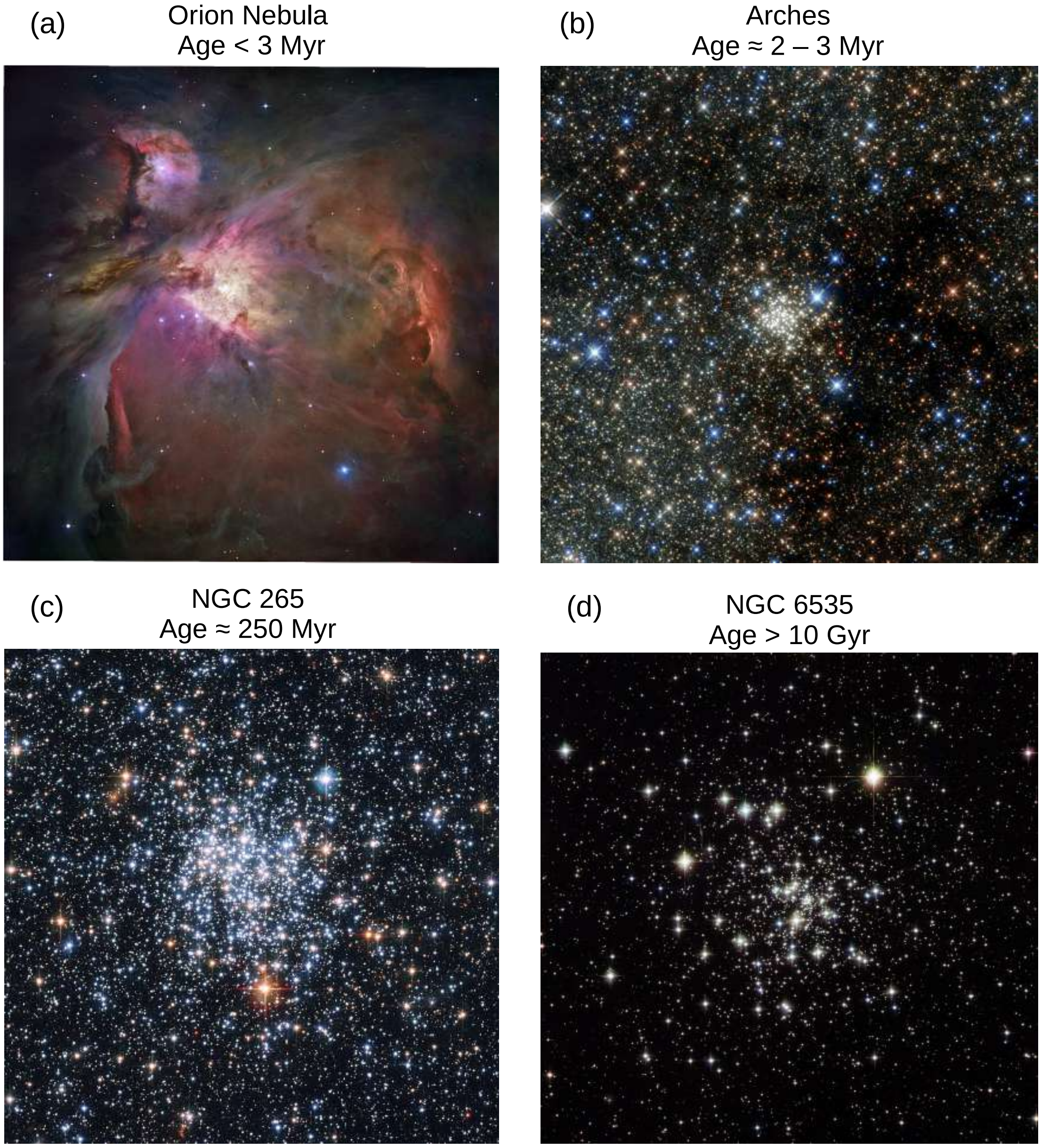

Figure 1.4: Images for a range of star clusters, adopted from Krumholz et al. (2019). The clusters span ages from ~ 1 Myr to > 10 Gyr and masses from $\sim 10^2$–10^6 $M_\odot$.

pressure, or the first supernovae) act together to clear away any residual gas from the protostellar cluster. Thus a fraction of the cluster mass is carried away, thereby reducing the cluster potential energy. The gas expulsion timescale is relatively short and is of the order of several dynamical times (Portegies Zwart et al. 2010; Dinnbier & Walch 2020).

1.4 Multiwavelength Aspects

A combination of the data that span not only in wavelength but also in resolution, pixel scale, and sky mapping area, is a powerful means to study the young stellar populations, particularly those embedded in the molecular clouds. The radiation emitted by various components in a star forming region is detected at separate wavelengths, depending on the temperature of the source. So the different wavelengths trace different emission features such as from the stars, dense cores, dust, and clouds along the same line-of-sight, as shown in Figure 1.5.

Identification of the cluster members is an elementary requirement in diagnosing an embedded or open star cluster. The young stellar objects (YSOs) are primarily identified and characterized based on their near- to mid-infrared properties (mostly color excess) (Adams et al. 1987; Wilking et al. 1989; Myers & Ladd 1993). Due to their star, disk, and envelope coupling, the emission contribute significantly in the infrared bands. Furthermore the near-infrared surveys are an eminent tool in studying the surface density, size, and structure of the embedded clusters in addition to the extinction mapping through the methods of star counts by employing statistical approach (Lada et al. 1991; Carpenter 2000; Gutermuth et al. 2005). Toward the longer wavelength (mid- to far-infrared) baseline, identification of the evolved disks becomes crucial, as they lack excess emission at shorter wavelengths. The youngest protostars (Class 0) are probed by strong far-infrared and sub-millimeter emission due to their enormous envelope material (Andre et al. 1993; Allen et al. 2007). The dust continuum observations at sub-millimeter and millimeter wavelengths reveal complex filaments and dense clouds in embedded clusters. The radio mapping surveys (GHz) offer advantages of studying both the distributed and clustered populations from the densest to the dust-enshrouded regions within a molecular cloud. These observations provide detailed information about the molecular cloud morphology, size, column density, and mass including the cloud dynamics. The radio continuum (centimeter) flux density is a measure of the ionizing photons emitted by massive stars (Churchwell 2004). For the relatively evolved populations, the optical spectroscopic and photometric surveys are very reliable techniques in studying the young cluster members.

1.5 Thesis Outline

The thesis presents systematic analysis concerned on young protocluster systems embedded in the galactic molecular clouds.

In this chapter (Chapter 1), the physical processes related with the formation of stars

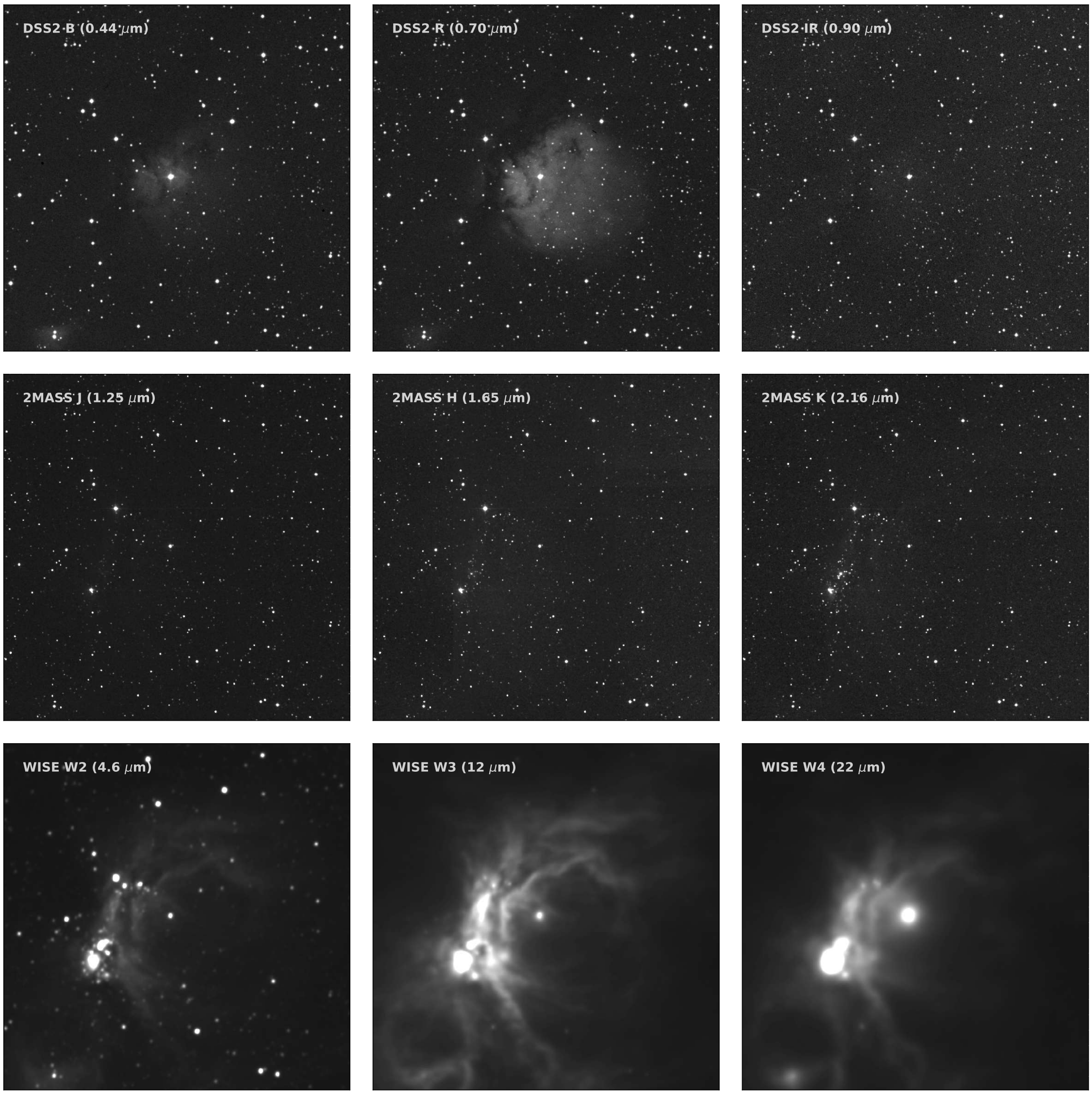

Figure 1.5: Multiwavelength view of a star-forming region Sh2-242 ($\ell = 182^{\circ}\!.3464$, $b = 0^{\circ}\!.2065$) for a field-of-view of $30' \times 30'$. The appearance of the same region is shown for different telescopes (DSS2, 2MASS, and *WISE*) in different bands (from 0.44 μm to 22 μm).

are outlined, with an emphasis on the characteristics of molecular clouds, low-mass star formation mechanisms, interstellar dust properties, and evolution to open clusters.

The data sources used in this study are introduced in Chapter 2. Multi-scale data products from a variety of telescopes and catalogs are incorporated. New data (both photometric and spectroscopic) through on-site observations as well as archival data covering a broad range of wavelengths are obtained. Their reduction processes and the necessary software/pipeline tools are described in this chapter.

Chapter 3 deals in detail characterization of the young stellar population in an active star-forming region Sh2-242. The dust distribution reveals nature of the clumpiness toward this region. Spectrophotometric study of the massive members in relevance with the stellar feedback effects is included here. From the spatial correspondence between young objects and extinction distribution, an overall census of the star formation activity is presented.

Chapter 4 presents analysis of the stellar contents associated with the Sh2-112 complex using multiwavelength data. Large-scale molecular clouds with multiple dense sub-structures are traced along a filamentary like distribution. The YSO groupings indicate cloud fragmentation and core formation along the filament. The formation of H II regions by massive stars and their influence on the nearly clouds on the star formation process is studied.

Chapter 5 presents characterization of the member candidates in a Galactic star cluster M 36 (age $\sim$ 15 Myr) using astrometric and kinematic properties. A highly obscured compact cloud core is detected along the same line-of-sight in both the extinction map and the molecular maps. YSOs in a very early stage (age $<$ 0.2 Myr) of their evolution are found to coexist with this complex. The dynamical properties of the molecular clouds are studied to infer the interaction among the multiple stellar populations.

Finally in Chapter 6, a summary of all our results and a scope for future endeavours is briefed.

Chapter 2

Data, Software, and Reduction

The works presented in this thesis are the outcomes obtained by merging the analytical results from a variety of telescopes and catalogs. Star formation is a multi-stage process, that requires observations covering a broad wavelength range. Using national facility telescopes ground based observations are carried out, as well as archival data from multiple space observatories are collected, wherever the science persisted. Each of the telescopes require a separate reduction tool and pipeline to process the raw data into science frames. In this chapter, a brief interpretation of the observations strategy, telescope parameters, software tools, and reduction techniques is outlined.

2.1 Telescopes and Catalogs

As the stars are formed from the giant molecular clouds, initially the young protostars are embedded within the cloud. Additionally, due to the presence of circumstellar disk and envelope, such pre-main sequence objects radiate most of their energy in the infrared. Here, utilizing the excess infrared emission properties, the YSOs are identified and characterised using a combination of near- to mid-infrared photometric data. The dust properties of the medium are traced using infrared datasets. Due to the accretion activity of the young stars, they show Hα emission, an attempt has been made to filter such Hα emission line young objects. Mid- to far-infrared imaging of the regions are suitable to analyse the molecular cloud morphology together with ionization distribution. The molecular cloud kinematics and dynamics are studied using the CO isotopologues and radio surveys. The presence of any massive star/stars (O to early-B type) can highly influence the star formation activity in their vicinity, therefore their spectroscopic observations are necessary to study the spectral type, ionizing radiation, and/or any feedback mechanisms. As the stars evolve over time and the opacity reduces, the clusters become visible in optical. Thus the study of proper motion and parallax measurements are performed using optical catalogs.

2.1.1 Optical Observations

For this thesis purpose, new observations are carried out using moderate size (up to 4 m class) telescopes hosted by national level observatories. Both photometric and spectroscopic data are acquired in optical bands.

DFOT

The Devasthal Fast Optical Telescope (DFOT[1]; Sagar et al. 2012) is located in the foothills of central Himalayas in Devasthal[2] (Longitude: 79°41′04″ E, Latitude: 29°21′40″ N, Altitude: 2450 m), which is an emerging astronomical site with a minimum ground level atmospheric seeing of $0\farcs6$ and a median of $1\farcs1$. Operated by Aryabhatta Research Institute of Observational Sciences (acronym ARIES[3]), the 1.3 m (aperture) fast beam (f/4, plate scale $\sim 40''$ mm^{-1}) telescope provides photometry in broad-band $UBVRI$ (Johnson-Cousins), SDSS *ugriz* and narrowband Hα, O[III], S[II] interference filters. The optical imager has a flat field-of-view (diameter $\sim 66'$), making it suitable for wide-area survey of a large number of point as well as extended sources. The telescope is currently equipped with two CCD (Charged Coupled Device) cameras. One is with 13.5 μm pixel, 2k×2k Andor iKon Camera covering a square area of about $18' \times 18'$ on the sky, another is of 16 μm pixel, 512×512 Andor iXon Camera covering a square area of $7' \times 7'$.

In this context, the 2k×2k Andor Camera is used for the target regions. Photometric imaging data in $UBVRI$ bands are acquired for a total of 8 nights during 2016 to 2018 in several seasons. In addition multiple bias and flat frames are collected to apply for instrumental and detector corrections. Suitable standard fields are observed at different airmasses for extinction correction and calibration into standard frames. Furthermore, the derivation of coefficients and the reduction processes will be discussed in an upcoming section (Section 2.3.1).

HCT

The Himalayan Chandra Telescope (HCT[4]; Prabhu 2014) is an Indian Astronomical Observatory (IAO[5]) project, located to the north of Western Himalayas in Hanle (Longitude: 78°57′51″ E, Latitude: 32°46′46″ N, Altitude: 4500 m). Because of its higher altitude, uninterrupted monsoon, and minimal light pollution; this cold desert site delivers a maximum number of clear and highly transparent skies, making it an promising site for next generation astronomical observations. The observatory is maintained by Indian Institute of Astrophysics (IIA[6]) and its operation is remotely controlled via a

---

[1] https://www.aries.res.in/facilities/astronomical-telescopes/130cm-telescope

[2] Meaning abode of God

[3] https://www.aries.res.in/aries-0

[4] https://www.iiap.res.in/centres_iao.htm?q=telescope_iao

[5] https://www.iiap.res.in/?q=iao.htm

[6] https://www.iiap.res.in/

dedicated satellite link. The HCT is supported with optical to infrared range observations with a 2 m diameter telescope covering a field-of-view of $7'$ on a side. The telescope optics is of Ritchey-Chretien design with a F-ratio of f/1.75 for primary and f/9 for Cassegrain providing an image scale of $11\farcs5$ mm^{-1}. The telescope is presently mounted with three science instruments: Himalaya Faint Object Spectrograph and Camera (HFOSC[7]), TIFR Near Infrared Spectrometer and Imager (TIRSPEC[8]), and Hanle Echelle Spectrograph (HESP[9]). HFOSC serves as an optical imager cum spectrograph covering wavelength range 350–900 nm by using a 2k×4k CCD detector with pixel size of 15×15 microns (pixel scale $0\farcs296$). HFOSC includes a broad list of slits (67, 100, 134, 167, 335, 1340 micron), filters (Bessell $UBVRI$ and few narrow bands), and grisms (Gr 5, 7–12, 14, 15, 17). TIRSPEC covers both spectroscopy and imaging with medium resolution in near-infrared (1–2.5 μm) using 1k×1k detector array. In imaging mode, the field-of-view is $307'' \times 307''$ with resolution of $0\farcs3$ pixel^{-1} (pixel size 18 micron), whereas in spectroscopy mode the resolution is $\sim$ 1200. For imaging, the available filters are broadband JHK and few narrowband filters are also implemented. Spectroscopy can be done in single order mode ($YJHK$) as well as in cross dispersed mode (YJ, HK), in combination with preferred slit width (S1–S5, L1–L5). HESP is a high resolution ($\sim$ 30,000 and 60,000) spectrograph covering wavelength range (350–1000 nm) by using 4k×4k CCD detector system, that will allow precise measurement of chemical abundance and radial velocity during stellar evolution.

For this study, the HFOSC facility is explicitly used for both photometry (R, I) and spectroscopy (Gr 5, Gr 7, Gr 8, Hα-Br) that covers more than 15 nights during 2016–2018. For imaging data multiple bias and flat frames are collected. Target regions are simultaneously monitored in R and I bands to detect the young variable stars. Slit spectroscopic observations for a few of the bright stars toward the regions covered in this thesis are conducted using several grisms. Immediately after the target stars are observed, the corresponding lamp spectra are taken for wavelength calibration. Multiple spectroscopic bias frames are collected to rectify the raw target spectra. Standard stars are observed in respective grisms to calibrate the flux. Additionally, slitless spectroscopy is employed to detect the Hα emitting stars by using a broadband Hα filter in combination with a grism (5/7/8) in slitless mode. The complete reduction technique will be discussed in Section 2.3.2. An overview of the observations performed using DFOT and HCT is given in Table 2.1.

---

[7] https://www.iiap.res.in/?q=iao_2m_hfosc

[8] https://web.tifr.res.in/~daa/tirspec/

[9] https://www.iiap.res.in/?q=hanle_echelle_spectrograph

Table 2.1: An overview of optical photometric and spectroscopic observations

Region Observed	Telescope	Photometry/ Spectroscopy	Filter/ Grism	Date of Observations	No. of Nights
Sh2-242	HCT	Spectroscopy	Grism 8	2016 Nov 03	0.5
Sh2-242	DFOT	Photometry	B, V, R, I	2016 Dec 18–20	3
Sh2-242	HCT	Spectroscopy, Slitless Spectroscopy	Grism 7, Grism 8/Hα-Br	2017 Jan 23–24	2
Sh2-112	DFOT	Photometry	B, V, R, I	2017 May 31	1
Sh2-112	HCT	Spectroscopy	Grism 7/8	2017 Jul 24–25	2
Sh2-242, Sh2-112	HCT	Photometry, Spectroscopy, Slitless Spectroscopy	R, I, Grism 7/8, Grism 5/Hα-Br	2017 Dec 15–16	2
Sh2-242	HCT	Photometry, Spectroscopy	R, I, Grism 7/8	2018 Jan 17–19	3
Sh2-242	DFOT	Photometry	U, B, V, R, I	2018 Feb 18–19	2
Sh2-112	HCT	Spectroscopy	Grism 7/8	2018 Jul 10–11	2
Sh2-112	HCT	Spectroscopy, Slitless Spectroscopy	Grism 7/8, Grism 5/8/Hα-Br	2018 Dec 01–03	3
Sh2-112	DFOT	Photometry	U, B, V, R, I	2018 Dec 08–09	2

2.1.2 Optical to Near-Infrared Database

Gaia

The *Gaia* (Gaia Collaboration et al. 2016a) is a unique mission in its type because of its micro-arcsecond astrometry (down to $G \simeq 20.7$ mag), an astronomical discipline concerned with the measurement of positions of celestial objects. The *Gaia* satellite, build by European Space Agency (ESA), was designed for a five-year nominal science operations started in the summer of 2014. The mission enables a combination of accuracy, sensitivity, dynamic range, and sky coverage, which is only achievable from space. The astrometric successor *Gaia* comprises absolute astrometry (positions, proper motions, and parallaxes), broad-band photometry in the unfiltered G band, low-resolution blue and red (spectro-)photometry (BP and RP), and integrated G_{BP} and G_{RP} photometry. The first release of *Gaia* data (*Gaia* DR1; Gaia Collaboration et al. 2016b), an outcome of the raw data collected during the first 14 months of the nominal lifetime and processed by the *Gaia* Data Processing and Analysis Consortium (DPAC), comprises astrometry, photometry, and variability for over 1 billion sources. The second *Gaia* data release, (*Gaia* DR2; Gaia Collaboration et al. 2018), that covers data spanned during the first 22 months, encompasses astrometry, photometry, radial velocities, astrophysical parameters (stellar effective temperature, extinction, reddening, radius, and luminosity), and variability information for more than 1.3 billion stellar sources with unprecedented accuracy. The *Gaia* DR2 is a major advancement over the previous release in terms of survey completeness, precision and accuracy, and the richness of the published data. For this purpose, the latest released (*Gaia* DR2) version is considered and in some cases the results are verified with the early instalment of the third *Gaia* data release, *Gaia* EDR3 (Gaia Collaboration et al. 2021).

IPHAS

The Isaac Newton Telescope (INT) Photometric Hα Survey of the Northern Galactic Plane (IPHAS; Drew et al. 2005) is a CCD survey that covers a sky area of 1800 deg^2 in the northern Milky Way spanning the Galactic latitudes $|b| < 5°$ and longitudes $\ell = 30°$–$215°$. Using a wide field camera mounted on the 2.5 m INT at the Roque de los Muchachos Observatory in La Palma, the imager scans the sky in broadband Sloan r and i, and narrowband Hα filters, with a sensitivity reaching down to $r \simeq 20$ (10σ). A combination of four 4k$\times$2k CCDs provides data with a pixel dimension of 13.5 μm (pixel scale $0\farcs33$ pixel^{-1}), and is configured to achieve sub-arcsecond seeing (median seeing $1\farcs1$). IPHAS is a major resource in studying the Hα emission line stars, prominent in pre- and post-main-sequence stars as well as binaries. The final catalogue of IPHAS point sources contains single-epoch photometry for 219 million objects. Photometric data for the target regions are obtained from the IPHAS DR2 (Barentsen et al. 2014), which is the first quality-controlled and globally calibrated source catalogue.

Pan-STARRS 1

The Panoramic Survey Telescope and Rapid Response System 1 (Pan-STARRS 1; Chambers et al. 2016) is an innovative wide-field astronomical imaging and data processing facility, collecting multi-epoch, multi-color observational data of the northern sky (declination $\sim -30^\circ$) with unprecedented depths. The distinct synoptic images are obtained by a 1.8 m aperture, f/4.4 primary mirror with a 0.9 m secondary, Richey-Chretien type telescopes located at Haleakala Observatories, where the site has a median image quality of $0''.83$ (Tonry et al. 2012). The field of view is approximately 7 square degrees with low distortion and minimal vignetting even at the edges of the illuminated region, producing pixel scale of $0''.258$ pixel^{-1}. The observations are carried out through a set of five broadband filters, designated as $g_{\rm P1}$, $r_{\rm P1}$, $i_{\rm P1}$, $z_{\rm P1}$, and $y_{\rm P1}$, covering about 400 nm to 1 μm (Stubbs et al. 2010).

LAMOST

The Large Sky Area Multi-Object Fiber Spectroscopic Telescope (LAMOST, also called the Guoshoujing Telescope) operated by National Astronomical Observatories, is a reflecting Schmidt telescope that adopts an active optics technique, achieved by continuously adjusting the mirror surface during observations (Cui et al. 2012). It has an effective aperture that varies from 3.6–4.9 m in diameter, a focal length of 20 m, and a field of view of 5° (Zhao et al. 2012). With this novel combination of large aperture and wide field-of-view, LAMOST has conducted spectroscopic survey over much of the northern sky between $-10^\circ \sim +90^\circ$ declination, during 2012 to 2017. The unique design of LAMOST enables it to take 4000 spectra in a single exposure to a limiting magnitude as faint as r = 19 at resolution R = 1800. LAMOST yields a spectral wavelength coverage of 370–900 nm with “native” resolution of the default grating setup as R $\approx$ 1000, which can be increased by using a slit of fixed width.

2.1.3 Near-Infrared to Mid-Infrared Catalog

WIRCam

The Wide-field InfraRed Camera (WIRCam; Puget et al. 2004), at the forefront of deeper imaging, is a near-infrared (0.9–2.4 μm) imager developed for the prime focus of the Canada France Hawaii Telescope (CFHT), a 3.6 m diameter telescope located at Mauna Kea, Hawaii. Using four 2k×2k detector arrays, the camera covers an almost contiguous field-of-view of $20'.5 \times 20'.5$ providing $0''.3$ pixel^{-1} sampling. The imaging data is publicly accessible via the CFHT archive[10]. The raw images are reduced using an Interactive Data Language (IDL) based package–SIMPLE Imaging and Mosaicking PipeLinE (SIMPLE[11]; Wang et al. 2010b). Briefly, as the near-infrared sky color varies rapidly, the dithered images which are taken within $\sim$0.5 hr, are grouped, then corrected for non-linearity. The images are then normalized, median-combined to form a sky flat field, and flattened

---

[10] http://www.cadc-ccda.hia-iha.nrc-cnrc.gc.ca/en/cfht/

[11] http://group.asiaa.sinica.edu.tw/whwang/idl/SIMPLE/

with that. The flattened, sky-subtracted, and crosstalk-removed images are used to detect the objects and to determine their pixel coordinates by using either the SExtractor (Bertin & Arnouts 1996) package or the point-spread function (PSF) fitting algorithm from the DAOFIND (Stetson 1987) package in the IRAF (Tody 1986; 1993) software. To convert the pixel frames into astrometric frames, a certain number of objects (bright and isolated) positions in the WIRCam are matched with that of the Two Micron All Sky Survey (2MASS; Skrutskie et al. 2006) frame, and generated an astrometric catalog. The WIRCam frames are then projected onto a common sky plane. The cosmic rays are removed by applying the sigma clipping and then the corrected images are mean-combined to form a deep mosaic. Photometric calibrations are done by measuring the object fluxes using the DAOPHOT package (Stetson 1987) and cross-correlating the results with the 2MASS Point Source Catalog (PSC; Skrutskie et al. 2006). The 2MASS K-band range of 14.44–16.34 mag are adopted to calibrate the absolute flux, as objects brighter than this range are affected by WIRCam nonlinearity (despite the correction for linearity) and objects fainter than this range show a significant selection effect in the 2MASS fluxes.

UKIDSS

The United Kingdom Infra-Red Telescope (UKIRT) Infrared Deep Sky Survey (UKIDSS; Lawrence et al. 2007) is a seven-year long survey began in 2005, carried out using the UKIRT wide field camera. UKIDSS is a portfolio of five survey components of complementary combinations of depth and area, covering various combinations of the broad-band filter set $ZYJHK$ (0.83–2.37 μm). The Galactic Plane Survey (GPS; Lucas et al. 2008) covers approximately 1868 deg^2 extended over the northern and equatorial Galactic plane ($-5^\circ < b < +5^\circ$), upto a depth of $K \sim 18$ mag. The camera (3.8 m aperture) has a considerably larger field-of-view (0.21 deg^2) with a pixel size of $0\farcs4$ along with a good image quality (median seeing $0\farcs6$). The computed values for each of the five UKIDSS elements are normalized according to the 2MASS values considering the 2MASS fainter limit of $K \simeq 15.50$ (Skrutskie et al. 2006). The UKIDSS data are released as sophisticated Structured Query Language (SQL[12]) databases at intervals of 6–12 months.

2MASS

The 2MASS (Skrutskie et al. 2006) collected imaging data covering 99.998% of the celestial sphere in the near-infrared J (1.25 μm), H (1.65 μm), and K_s (2.16 μm) bandpasses, by using two dedicated 1.3 m diameter equatorial telescopes. The northern telescope is located at Whipple Observatory, Mount Hopkins, Arizona, while the southern telescope site is at Cerro Tololo Inter-American Observatory, Cerro Tololo, Chile. The mirror optics provides a Cassegrain focal ratio of f/13.5 and a Cassegrain plate scale of $11\farcs97$ mm^{-1}. 2MASS produced a PSC containing 471 million sources reaching millijansky sensitivity and arcsecond resolution. The ground-based virtually full-sky survey

---

[12] http://wsa.roe.ac.uk/sqlcookbook.html

performs simultaneous imaging of an $8'.5 \times 8'.5$ field at a pixel scale of $2''$ pixel^{-1} in the three wave bands. The 10σ detection limit is achieved at or fainter than $J = 15.8$, $H = 15.1$, and $K_s = 14.3$ mag for point sources.

Spitzer

The *Spitzer Space Telescope* (Werner et al. 2004) is an infrared observatory equipped with an 85 cm diameter primary mirror and three scientific instruments providing imaging and spectroscopy over a wavelength range of 3.6 to 160 μm. The three focal plane instruments are Infrared Array Camera (IRAC; Fazio et al. 2004), the Infrared Spectrograph (IRS; Houck et al. 2004), and the Multiband Imaging Photometer for *Spitzer* (MIPS; Rieke et al. 2004). IRAC is a four-channel wide-field camera, covering $5'.2 \times 5'.2$ fields of view, that obtains simultaneous broadband images at 3.6, 4.5, 5.8, and 8.0 μm with a plate scale of $1''.2$ pixel^{-1}. The IRS comprises four separate spectrograph modules covering the wavelength ranges from 5.3–14, 10–19.5, 14–40, and 19–37 μm with spectral resolutions of R = 90 and 600. The MIPS provides long-wavelength imaging capability at 24, 70, and 160 μm bands with a plate scale of $2''.45$ pixel^{-1} and measurements of spectral energy distributions between 52 and 100 μm with low spectral resolution ($\sim 7\%$). After the end of the cryogenic mission, the *Spitzer* Warm Mission (Mahoney et al. 2010) began, and temperature increases to 27.5 K, keeping IRAC 3.6 and 4.5 μm channels operational. The imaging data are collected from the publicly available *Spitzer* Data Archive[13] site.

WISE

The *Wide-field Infrared Survey Explorer* (*WISE*; Wright et al. 2010) has mapped the entire sky in four mid-infrared wavebands at 3.4, 4.6, 12, and 22 μm with an angular resolution of $6''.1$, $6''.4$, $6''.5$, and $12''.0$, respectively. *WISE* adopted a basic strategy of scanning great circles with a center located at the Sun, which keeps the solar elongation at 90°, therefore a Sun-synchronous orbit was chosen to give a precession rate of 360° in one year. The cryostat based facility was launched in 2009, and had a time span of about eight-months. The medium-class explorer mission consists of a 40 cm space-based telescope covering $47' \times 47'$ field of view. *WISE* provides 5σ point source sensitivities of 0.08, 0.11, 1, and 6 mJy, respectively for the corresponding four bands.

2.1.4 Mid-Infrared to Far-Infrared Survey

IRAS

The *Infrared Astronomical Satellite* (*IRAS*; Neugebauer et al. 1984) is the first-ever space telescope, launched on 1983, to perform an extensive exploration of the entire sky at 12, 25, 60, and 100 μm (mid- to far-infrared). Ground-based observations at infrared lack depth and sensitivity due to obscuration caused by the Earth's atmosphere and the warm thermal radiation from the atmosphere. *IRAS* was designed to overcome these

---

[13] `https://irsa.ipac.caltech.edu/data/SPITZER/docs/spitzerdataarchives/`

issues by observing from space, orbiting above the Earth's atmosphere (near-polar) with a cryogenically cooled technology. The telescope is of f/9.6 Ritchey-Chrétien design with a 5.5 m focal length, and a 0.57 m aperture. Using the High Resolution Image Restoration technique, a spatial resolution ranging from $30''$ to $1\overset{\prime}{.}5$ is achieved for the *IRAS* images.

AKARI

The AKARI (Murakami et al. 2007) is the second Japanese infrared astronomical space mission launched on 2006 with an in-orbit cryogenic lifetime of one and a half years. The satellite is equipped with a 68.5 cm aperture telescope, combined with two focal-plane instruments, which survey more than 90% of the sky in multiple wavelength bands ranging from mid- to far-infrared (2–180 μm). The AKARI telescope optics is a Ritchey–Chretien type and a total $f/6$ system with pointing accuracy less than $3''$. The two scientific instruments are the Far-Infrared Surveyor (FIS; Kawada et al. 2007) and the Infrared Camera (IRC; Onaka et al. 2007), both performing imaging and spectroscopy. The field of view for the FIS is $8'$ and for the IRC $10'$. The FIS photometric bands are centred at 65, 90, 140, and 160 μm, with a pixel pitch of $29\overset{\prime\prime}{.}5$ for the first two bands and $49\overset{\prime\prime}{.}1$ for the last two bands. The imaging data obtained by FIS are used in this study.

2.1.5 Far-Infrared to Millimeter Survey

Herschel

The *Herschel* space observatory (Pilbratt et al. 2010) offers unprecedented observational capabilities in the far-infrared and submillimeter spectral range 55–671 μm. *Herschel* was launched on 2009 and the mission lifetime is limited by the cryostat hold time. The optical design is of a passively cooled Cassegrain telescope with a 3.5 m physical diameter (primary). The science payload comprises three instruments: the Photodetector Array Camera and Spectrometer (PACS; Poglitsch et al. 2010), the Spectral and Photometric Imaging REceiver (SPIRE; Griffin et al. 2010), and the Heterodyne Instrument for the Far Infrared (HIFI; de Graauw et al. 2010). The PACS and SPIRE are the direct detection cameras/medium resolution spectrometers, while the HIFI performs as a very high-resolution heterodyne spectrometer. The complements of the three instruments offer photometric imaging capability in six broad-band wavelengths centered at 70, 100, 160, 250, 350, and 500 μm.

Bolocam

The Bolocam Galactic Plane Survey (BGPS; Ginsburg et al. 2013) is the millimeter (1.1 mm/268 GHz) dust continuum emission survey from the northern Galactic plane. The survey covers the Galactic plane from $-10^\circ < \ell < 90\overset{\circ}{.}5$ and $-0\overset{\circ}{.}5 < b < 0\overset{\circ}{.}5$ by using the Bolocam instrument at the Caltech Submillimeter Observatory. BGPS has a typical 1σ rms sensitivity of 30–100 mJy in a $\sim 33''$ beam. This catalog contains more than 8000 sources extracted from the wide-field Bolocam mapping survey. The millimeter-wave thermal dust emission has the property of being optically thin and minimally affected by the temperature. The 1.1 mm band is the longest wavelength that is unaffected by the free–free emission, probing the least optically thin dust emission and therefore total dust mass. Thus the millimeter continuum observations are efficient to trace the densest molecular gas, ranging from star-forming cores to whole clouds across the Galaxy. The complete data has been made available over the BGPS archive[14].

2.1.6 Radio Continuum Maps

PMO

The Milky Way Imaging Scroll Painting (MWISP[15]) project is an unbiased CO survey covering the Galactic plane $-10° < \ell < +250°$ and $|b| \lesssim 5\overset{\circ}{.}2$ with the 13.7 m telescope of the Purple Mountain Observatory (PMO), Delingha (Latitude: 37°22′.4 N, Longitude: 97°33′.6 E, Altitude: 3200 m). The legacy survey observes ^{12}CO, ^{13}CO, and C^{18}O (J=1–0) lines simultaneously using the nine-beam Superconducting SpectroScopic Array Receiver system (Shan et al. 2012) with an instantaneous bandwidth of 1 GHz. The telescope has a tracking accuracy of $\sim 1''$–$3''$ in both azimuth and elevation, and a pointing accuracy of $\sim 5''$ for the whole sky. The typical rms noise levels are ~ 0.5 K for ^{12}CO at the channel width of 0.16 km s^{-1} and ~ 0.3 K for ^{13}CO and C^{18}O at 0.17 km s^{-1} (Su et al. 2019). The typical system temperatures are ~ 250 K for ^{12}CO at the upper sideband and ~ 140 K for ^{13}CO and C^{18}O at the lower sideband, respectively. The spatially dynamic coverage range, combined with uniform sensitivity and moderate resolution ($\sim 50''$) of this survey allows for a systematic investigation of the molecular cloud structures, traced by the triple CO isotopologues lines.

NVSS

The NRAO VLA Sky Survey (NVSS; Condon et al. 1998) covers 82% of the northern celestial sphere ($\delta = -40°$, J2000.0) at 1.4 GHz (21 cm). The continuum images have rms brightness fluctuations of $\sigma \approx 0.45$ mJy beam^{-1} (0.14 K) for Stokes I (total intensity) and $\sigma \approx 0.29$ mJy beam^{-1} (0.09 K) for Stokes Q and U (linear polarization). The catalog of sources extracted from these images contains $\sim 2 \times 10^6$ discrete sources ($S \approx 2.5$ mJy), including radio galaxies and quasars. The star-forming galaxies, containing H II regions ionized by massive ($M \gtrsim 8 M_\odot$), short-lived ($\tau \lesssim 3 \times 10^7$ yr) stars, are the distinct populations of radio sources. The scientific potential of this facility is to uncover such Galactic radio emission components. All of its data products are publicly released via the NVSS archive[16].

---

[14] https://irsa.ipac.caltech.edu/data/BOLOCAM_GPS/

[15] http://english.dlh.pmo.cas.cn/ic/in/

[16] https://www.cv.nrao.edu/nvss/

Planck

The *Planck* satellite surveyed the entire sky in nine frequency bands during 2009–2013 (Planck Collaboration et al. 2016) using the High Frequency Instrument (HFI: 857, 545, 353, 217, 143, and 100 GHz) and the Low Frequency Instrument (LFI: 70, 44, and 30 GHz), impacting the effective angular resolution ranging from $\sim 5'$ to $\sim 33'$ (FWHM), respectively. *Planck* is the third generation space-based telescope to conduct measurements of the intensity and polarization anisotropies of the cosmic microwave background. The *Planck*[17] mission has provided the first uniform submillimeter surveys that cover both the Galactic plane and the regions at intermediate and high latitudes, with high sensitivity and wide wavelength (350 μm–1 cm) coverage. The survey provides all-sky maps of the thermal dust emission and, in particular, of the emission arising from cold dust, which is primarily associated with dense regions of molecular clouds, within which the early phases of stellar formation emerge. The *Planck* channel maps from the six HFI frequencies are utilized.

FUGIN

The FUGIN (FOREST Unbiased Galactic plane Imaging survey with the Nobeyama 45 m telescope; Umemoto et al. 2017) project is dedicated to investigate the distribution, kinematics, and physical properties of both diffuse (density $\sim 10^2$ cm^{-3}) and dense (density $\sim 10^3$–10^4 cm^{-3}) molecular gases in the Galaxy by observing ^{12}CO, ^{13}CO, and C^{18}O (J=1–0) lines simultaneously. A wide area mapping of the first quadrant ($10° \leq \ell \leq 50°$, $|b| \leq 1°$; 80 deg^2) and the third quadrant ($198° \leq \ell \leq 236°$, $|b| \leq 1°$; 76 deg^2) of the Galaxy are conducted using the FOur-beam REceiver System on the 45 m Telescope (FOREST). The higher angular resolution ($20''$ for ^{12}CO and $21''$ for ^{13}CO and C^{18}O) of this legacy project makes it possible to detect and resolve the smallest scale structures (filaments/clumps/cores) with a deeper insight compared to its previous surveys. The telescope has a beam size of $14''$ for ^{12}CO and $15''$ for ^{13}CO and C^{18}O with a velocity resolution of 1.3 km s^{-1}. By tracing diffuse (using ^{12}CO) and dense (using ^{13}CO and C^{18}O) molecular gases over a wide spatially dynamic range (~ 1 pc to > 50 pc) with higher sensitivity, the FUGIN data will make a major contribution to constitute a link of the interplay between atomic and molecular gas, the evolution of molecular clouds and dense gas, the interaction between star-forming region and interstellar gas, and so on.

In addition to the above mentioned datasets, few more relevant catalogs are used in necessity or cross-checked for better results, such as DSS1 (Lasker et al. 1990), DSS2 (McLean et al. 2000), PPMXL (Roeser et al. 2010), USNO-B1.0 (Monet et al. 2003), URAT (Zacharias et al. 2015), and MSX (Price et al. 2001).

---

[17] `https://www.esa.int/Science_Exploration/Space_Science/Planck`

Altogether, archival data from at-least 15 separate telescopes (international) in multiple wavelength/frequency bands with varying levels of resolution are collected. The datasets cover a broad range in wavelength from optical (nm), infrared (μm), sub-millimeter (sub-mm), millimeter (mm) up-to centimeter (cm), including radio frequency (GHz) bands. Thus, using a combination of such data, multiwavelength perspective of star formation activity is presented here. A summary of the telescope parameters is presented in Table 2.2.

Table 2.2: Parameters of the telescopes and catalogs used in this study

Telescope/ Catalog	Filter/ Grism	Wavelength/ Frequency	Field-of-view	Plate Scale	Resolution/ Beam size
DFOT	U, B, V, R, I	360–900 nm	$18' \times 18'$	$0''.53$ pixel^{-1}	
HCT (HFOSC)	B, V, R, I, Grism 5, Grism 7, Grism 8	440, 550, 700, 900 nm, 380–1030 nm	$10' \times 10'$	$0''.296$ pixel^{-1}	870, 1330, 2190
Gaia DR2	G, G_{BP}, G_{RP}	330–1050 nm			
IPHAS	r, i, Hα	624, 774, 656 nm		$0''.33$ pixel^{-1}	
Pan-STARRS 1	g, r, i, z, y	400–1000 nm	$3^{\circ}.3$	$0''.258$ pixel^{-1}	
LAMOST		370–900 nm	5°		1000
WIRCam	J, H, K	0.9–2.4 μm	$20' \times 20'$	$0''.3$ pixel^{-1}	
UKIDSS	Z, Y, J, H, K	0.83–2.37 μm	0.21 deg^2	$0''.4$ pixel^{-1}	
2MASS	J, H, K_s	1.25, 1.65, 2.16 μm		$2''.0$ pixel^{-1}	
Spitzer (IRAC)	ch1, ch2, ch3, ch4	3.6, 4.5, 5.8, 8.0 μm		$1''.2$ pixel^{-1}	
WISE	W1, W2, W3, W4	3.4, 4.6, 12, 22 μm			$6''$–$12''$
IRAS	*I1, I2, I3, I4*	12, 25, 60, 100 μm			$30''$–$1'.5$
AKARI (FIS)	*N60, WIDE-S, WIDE-L, N160*	65, 90, 140, 160 μm			$1'.0$–$1'.5$
Herschel		70, 100, 160, 250, 350, 500 μm		$3''.2$–$14''$ pixel^{-1}	
PMO	^{12}CO, ^{13}CO				0.16 km s^{-1}, 0.17 km s^{-1}
NVSS		21 cm/1.4 GHz			$45''$
Planck		857–100 GHz			$5'.0$–$9'.6$
FUGIN	^{12}CO, ^{13}CO, C^{18}O				1.3 km s^{-1}

2.2 Software and Pipelines

A variety of software and pipeline facilities are used in this study. Among them a few of the major tools are briefly outlined.

IRAF

The Image Reduction and Analysis Facility (IRAF[18]; Tody 1986), designed and supported by the National Optical Astronomy Observatories (NOAO), is the most commonly and widely used software system coupled with a large selection of programs for the purpose of core astronomical data reduction. The IRAF software includes a core system of image processing tasks, several packages, a scripting facility, and a programming environment. An image refers to a representation of the primary data type, which is an arbitrarily complex data object stored in a Flexible Image Transport System (FITS; Wells et al. 1981) format. The tasks are executed by using a command line interface to perform various functions. Each task consists of a parameter file that is required to be modified accordingly. The software packages are capable of reducing both photometric and spectroscopic data over a broad range of wavelength coverage. Some of the prominent IRAF packages are mentioned hereafter.

CCDRED: The non-interactive header driven CCD reduction package includes tasks that make corrections to the raw data from any detector signatures and atmospheric noises. The bias and flat-field images are combined to beat down the noise in the calibrations.

CRUTIL: This package involves detection of cosmic rays and replacing those by an average of neighbouring pixels. A certain detection threshold limit is to be set depending on the noise characteristics of the image and how weak the cosmic rays may be for detection.

DAOPHOT: This package enables detection of objects, fitting point spread functions, subtracting stars, and performing photometry in a crowded field such as a globular cluster or open cluster. DAOPHOT contains pertinent information out of separate parameter files that are shared between tasks. Some of the parameters are in fact parameter files themselves, such as DATAPARS (data dependent parameters), FINDPARS (object detection parameters), CENTERPARS (centering algorithm parameters), FITSKYPARS (sky fitting algorithm parameters), PHOTPARS (photometry parameters), and DAOPARS (DAOPHOT fitting parameters).

IMCOORDS: Transforms the pixel frames to celestial frames by computing the plate solutions using matched pixel and celestial coordinate lists.

PHOTCAL: Performs the transformation of instrumental to standard magnitudes by computing and solving for color and extinction coefficients in the transformation equations.

APEXTRACT: Define, modify, trace, and extract apertures (one dimensional sums) from the two dimensional spectra. Derive size and location of the extraction apertures,

---

[18] https://iraf-community.github.io/

background windows, and the functions and coefficients of the trace fit, which are used to extract the object spectrum by comparing with the lamp spectrum.

ONEDSPEC: Identify features in spectrum for dispersion correction, wavelength calibrate, continuum fit, and perform arithmetic operations in spectra.

GILDAS

The Grenoble Image and Line Data Analysis Software (GILDAS[19]; Gildas Team 2013) is a collection of state-of-the-art image processing systems, jointly maintained by IRAM and CNRS. The GILDAS facility offers astronomical data reduction applications in the (sub-)millimeter (radio) regime, most of which are oriented towards spectral line mapping and many kinds of 3-dimensional data. GILDAS consists of five major dedicated utilities: GREG (for 1-D and 2-D graphic programs), CLASS (for single-dish data processing), ASTRO (an astronomical tool to prepare an observing session), CLIC (to calibrate interferometer data), and Mapping (an interactive imaging and deconvolution package) and numerous tasks to perform non interactive time consuming processing (smoothing, transpositions, fitting).

Montage

The Montage Image Mosaic Engine[20] (Berriman & Good 2017) is a scalable portable toolkit for assembling FITS images into custom mosaics, in response to the user's specifications of output coordinate system, image reprojection, pixel sampling, and image rotation angle. Montage models and rectifies the variable sky background to a common level and thus reveals faint, diffuse features by adapting an image stretching method that preserves the full dynamic range of a FITS image. The utility supports tools for creating cutout and downsampled versions of large images. The facility offers capabilities for web-based interactive visualization of multi-dimensional images including Python wrappers. The functionality of this facility is still under active development.

SED Fitter

The package provides a method to analyze the spectral energy distributions (SEDs) of young objects based on grid of models generated using the Monte Carlo radiation transfer code. The models incorporate a vast range of parameter space, including the contribution from stellar mass, radius, and temperature, evolutionary stage, star, disk, and envelope signatures, accretion rate, and inclination angle (Robitaille et al. 2006; 2007). The models are convolved with a large number of common filter bandpasses, ranging from optical to submillimeter wavelengths. In the fitting process, the luminosity, distance and extinction are considered as free parameters.

---

[19] https://www.iram.fr/IRAMFR/GILDAS/

[20] http://montage.ipac.caltech.edu/

Clumpfind

The objective routine (Williams et al. 1994) analyzes the clumpy structures in molecular clouds using radio observations (spectral line mapping). The algorithm searches for local peaks of emission which locate the clumps, then follows them down to lower intensity levels, by contouring the data at a multiple of the rms noise. The contour levels are set at least twice the rms noise of the map to depict the cloud structures properly. The output result is a decomposition of the data into a set of discrete structural units (clumps) in which the emission is concentrated.

Additionally, some of the facilities are most frequently used for this study, such as: SIMBAD[21] astronomical database (Wenger et al. 2000), VizieR[22] database of astronomical catalogues (Ochsenbein et al. 2000), SAO/NASA Astrophysics Data System[23], NASA/IPAC Infrared Science Archive[24], SAOImage DS9[25] (Smithsonian Astrophysical Observatory 2000; Joye & Mandel 2003), ALADIN[26] sky atlas (Bonnarel et al. 2000), AstroImageJ[27] (Collins et al. 2017), WCSTools[28] (Mink 1997), SExtractor (Bertin & Arnouts 1996), BeSSeL[29] Survey (Reid et al. 2016), Astropy Project (Astropy Collaboration et al. 2013; 2018), APLpy (Robitaille 2019), and HEALPix (Górski et al. 2005).

2.3 Methodology and Reduction

2.3.1 Photometric Reduction

The optical photometric data reduction steps for B (440 nm), V (550 nm), R (700 nm), and I (900 nm) bands for the data acquired from DFOT are briefly explained here. The reductions are performed using the IRAF software.

CCD Reduction

Before any photometric measurements are made, the detector signatures must be removed from the raw images in order to improve the signal-to-noise ratio and precision of the data. The process involves multiple stages, such as: DC offset subtraction, flat-fielding to remove pixel-to-pixel gain variations and large scale gradients, and cosmic ray removal.

---

[21] https://simbad.u-strasbg.fr/simbad/
[22] https://vizier.u-strasbg.fr/viz-bin/VizieR
[23] https://ui.adsabs.harvard.edu/
[24] https://irsa.ipac.caltech.edu/frontpage/
[25] https://sites.google.com/cfa.harvard.edu/saoimageds9
[26] https://aladin.u-strasbg.fr/
[27] https://www.astro.louisville.edu/software/astroimagej/
[28] http://tdc-www.harvard.edu/wcstools/
[29] http://bessel.vlbi-astrometry.org/

Bias Frames: Bias frames are used to remove the pre-flash illumination or any residual structure in the DC offset. For each day sequence of biases are taken with zero second integration exposures throughout the observing run. The bias frames are combined (average) using the ZEROCOMBINE task from the CCDRED package in the IRAF software. The gain and read-out-noise are set according to the instrument values.

Twilight Flats: The pixel-to-pixel variations and the sky gradients are removed by using the flat field exposures. The twilight flats are taken with short exposure times (normally 5–10 second) in each of the filters with at least three exposures, during the evening and morning twilight. The telescope is projected toward the bright (uniformly illuminated) twilight sky with minimal stars. For each filter, the flat frames are combined (median) separately to generate a master flat by using the FLATCOMBINE task.

Cosmic Ray Removal: Cosmic ray particles induce spurious signal. Cosmic rays are filtered out using the task COSMICRAYS from the CRUTIL package. A flux ratio threshold (a typical value of 5σ of the background) is set interactively for each of the target frames. Depending on which the cosmic ray events are detected and replaced with the average of four neighbouring pixels.

CCD Processing: CCD processing of the target frames are performed using the CCDPROC task. Using the zero length exposure calibration image the zero level subtraction is done, followed by division with the scaled flat filed calibration image. Before the flat-field division, a normalization of the flat-field is applied, in order to preserve the correct counts of the target objects, the process is automatically done in CCDPROC.

Photometry

The corrected science frames are now ready for computing the photometric magnitudes.

Source Detection: Sources in the target frames are detected using two common facilities: the DAOFIND task in the DAOPHOT (Stetson 1987) package or the SExtractor (Bertin & Arnouts 1996) software. The image statistics is studied using the IMEXAMINE or IMSTATISTICS tools to obtain the initial input parameters, such as FWHM of the PSF in scale units, standard deviation of background in counts, minimum good data value, maximum good data value (saturation limit), and threshold in sigma for feature detection. DAOFIND searches for local density maxima (convolving Gaussian profile) throughout the image depending on the specified FWHM and threshold values, and detects objects that are stellar or close to stellar. The non-stellar objects (cosmic rays, background galaxies, bad columns, fingerprints) are rejected based on certain roundness and sharpness criteria. Finally DAOFIND generates an output file containing pixel coordinates (positions) and shape parameters for all the detected objects.

Aperture Photometry: Mostly aperture photometry is performed in uncrowded or moderately crowded fields. Nonetheless, aperture photometry is required to provide the initial magnitude scale and sky estimates to the PSF fitting code. The task PHOT is used to derive the instrumental magnitudes for the list of objects. An important step is to select the proper aperture for the program stars from the growth-curve (Stetson 1990) analysis. For that a set of varying apertures (through a progression of increasing radii) is considered and photometric magnitudes are computed, from which growth-curve is

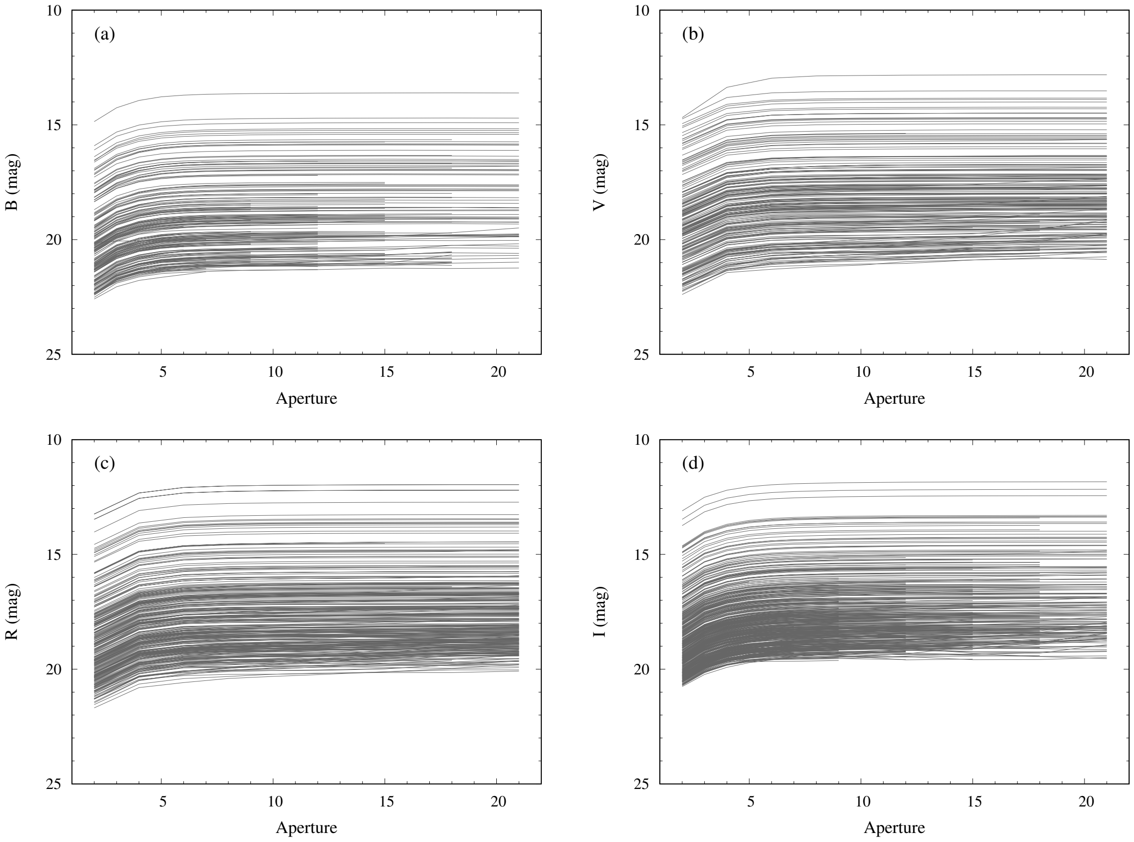

Figure 2.1: The growth-curve for the B, V, R, and I filters. The photometric data are obtained using the DFOT for the Sh2-242 ($\ell = 182\overset{\circ}{.}3464$, $b = 0\overset{\circ}{.}2065$) site. The field-of-view of the instrument is $18' \times 18'$.

generated for each of the filters. The typical growth-curves generated in this study is shown in Figure 2.1. The sky annulus (inner radius and width in scale units) is estimated by examining the images. Final photometry for all the detected objects is performed by choosing a suitable aperture radius.

PSF Photometry: PSF fitting technique is performed in crowded fields to overcome any effect from the wings of the neighboring stars. PSF photometry is employed to obtain the improved signal-to-noise at the faintest magnitudes and to reject the bad data. Computing the PSF model and generating the photometry involve a combination of tasks, such as PSF, NSTAR, SUBSTAR, and ALLSTAR, all from the DAOPHOT package. To compute the zeroth-order PSF convolution kernel, a set of comparatively bright (unsaturated) and isolated stars are selected that are well distributed over the image and have no close neighbors or underlying detector blemishes. For each of the candidate stars, the residuals are checked and the PSF list is updated. Magnitudes for all the program stars in the input list are computed by grouping the stars and fitting the PSF model to the stars in each group simultaneously. Each star in the PSF fitted photometry list are subtracted from the input image. At this phase, the subtracted star list should be checked carefully to avoid the appearance of any neighboring stars. Depending on the crowdedness of the objects in an image, the PSF fitting may be an iterative process of successively removing the neighbor stars and recomputing the PSF on the neighbor subtracted image. After a clean subtraction, when the residual size is comparable with the noise model, the improved (refitted) PSF model is constructed, with which the final photometry is achieved for the program stars.

Astrometry

Conversion of the target frames from pixel coordinates to celestial coordinates (usually equatorial) is performed in this step. Initially a catalog of sources is prepared, whose columns contain matched pixel (from any filter) and celestial coordinates (from any known catalog, say 2MASS PSC). About 20–30 moderately bright and isolated sources are chosen in the list. The CCMAP task from the IMCOORDS package is used to determine the plate solutions for the set of images. The tool uses sky projection geometry in combination with a polynomial fit to the residuals. With the computed plate solutions, the CCSETWCS task creates image world coordinate system (WCS) and modify the header information. The pixel list of the program stars obtained from the PSF photometry is converted to the WCS system using the WCS image and the WCSTools (Mink 1997) software.

Calibration

The instrumental magnitudes for the program stars, obtained from the PSF photometry, require standardization. Because the Earth's atmosphere inevitably absorbs all kind of radiation from every celestial objects as well as from the polluted light within the atmosphere (if any). The amount of energy absorbed is expressed in terms of atmospheric extinction, that can be derived from the observations of a set of standard stars at different airmasses. In addition, the instrumental magnitudes are still limited by the telescope and detector signatures, which can be taken care by the comparison of standard star colors. Thus, the measurement of extinction coefficients and color coefficients enables to correlate between instrumental and standard magnitudes via some transformation equations. In this part, using the standard star photometry, the calibration methods from instrumental to standard magnitudes are discussed.

Standard Star Photometry: Standard fields are observed at-least three times in each night at varying (low to high) airmasses with all of the filters. The standard fields are chosen mainly from the Landolt (1992) list, in such a way that there are at-least 10 standard stars in a field, whose colors vary in a wide range, and are observable throughout the night. Standard fields are suitable for a relatively uncrowded photometry. The photometric reduction steps are mostly similar as with the program stars. The bias and flat field corrections are made for all of the standard frames. Suitable aperture radius is chosen from the growth-curve analysis. Standard stars from the field are identified interactively either by cursor or by using the automatic star finding algorithm DAOFIND after setting up various parameter files. Finally aperture photometry is run on the list of standard stars for all the frames.

Extinction Coefficients: The atmospheric extinction, which is a measurement of opacity of the atmosphere, is expressed in terms of absorption coefficient (K). Since K is a function of wavelength, the filter name is denoted alongside to K, such as K_b if measured with the B filter. The amount of absorption in a filter varies depending upon the path length that the radiation travels through the Earth's atmosphere or more specifically on the telescope mounting angle. Therefore, a group of standard stars that fit in a single CCD frame are observed at different airmasses by observing at several times (at-least three) during a night with all the filters. The instrumental magnitudes for each of the standard star for each frame and in each filter are computed. The fact that the Earth's atmosphere is not plane-parallel, due to the curvature of the Earth, is taken into account by the instrument itself during the measurement of airmass. Thus from the instrumental magnitude vs airmass plot (Figure 2.2), the slopes are calculated by using a linear least-square fitting routine, which provides the extinction coefficients.

Color Coefficients: The instrumental magnitudes that are obtained for the standard stars are used to correlate with the standard system, by availing the routines from the PHOTCAL package. An image set file, containing the standard fields and their corresponding images organized according to the filter names, is created using the task MKIMSETS or using any editor. The MKNOBSFILE task is used to create the standard star observations file that consists of airmass, instrumental magnitudes and errors arranged according to filter names for each set of the standard star. A standard star catalog that contains the magnitudes and color indices on the standard system is required to relate with the instrumental values. A suitable catalog of the Landolt $UBVRI$ standards (Landolt 1992) is already inbuilt within the IRAF system. To create any other catalog, the MKCATALOG task can be implemented. The MKCONFIG task is run to create a configuration file that contains the algebraic form of the transformation equations and declare the file variables. The file is inspected and the unnecessary equations and variables are removed. A sample template of the transformation equations is given as follows (Equations 2.1, 2.2, 2.3, and 2.4).

$$b = B + c_b + m_b \times (B - V) + (K_b \times X_b) \tag{2.1}$$

$$v = V + c_v + m_v \times (B - V) + (K_v \times X_v) \tag{2.2}$$

$$r = R + c_r + m_r \times (V - R) + (K_r \times X_r) \tag{2.3}$$

and

$$i = I + c_i + m_i \times (V - I) + (K_i \times X_i) \tag{2.4}$$

where instrumental magnitudes (b, v, r, i) are on the left and standard magnitudes (B, V, R, I) and indices are on the right. The best values of the zero-point constants (c_b, c_v, c_r, c_i) and the color coefficients (m_b, m_v, m_r, m_i) are derived in a least-square fitting sense, after correcting the instrumental magnitudes for the airmasses (X_b, X_v,

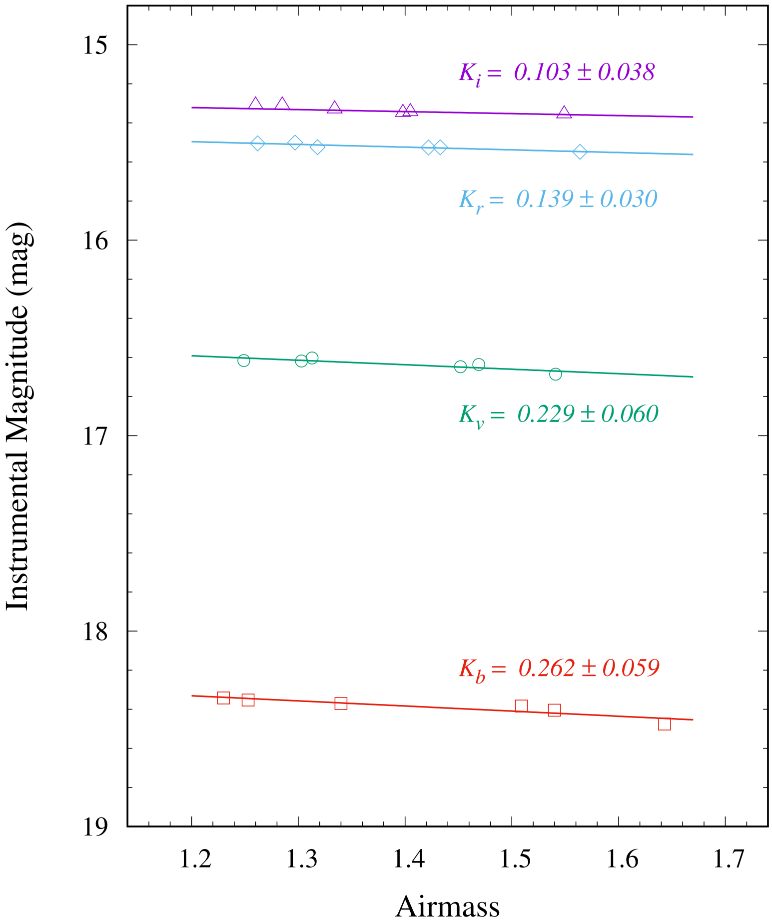

Figure 2.2: The atmospheric extinction coefficients (K) are derived for the B, V, R, and I filters using the least-square fitting routine. The instrumental magnitudes of the standard stars are plotted along the Y-axis. The photometric data are for the standard field SA 95 (Landolt 1992) obtained using the DFOT.

X_r, X_i) using the extinction coefficients (K_b, K_v, K_r, K_i). Also there are second-order color terms that are by default included in the equations, but are implicitly set to zero considering insignificant contribution. The variables are fitted interactively and solutions are obtained for the transformation equations using the FITPARAMS task. To be noted that all the solutions must converge, or if required the tolerance may be compromised in order to do so. By running the INVERTFIT task, that inverts the system of equations defined in the configuration file and evaluates the fit, the residuals are generated for the standards. A typical plot of the residuals is shown in Figure 2.3.

Transformation: The reduced photometric files of the program stars are now used to create a observations file that consists of instrumental magnitudes, airmasses, and relevant parameters for each set of filters using the task MKOBSFILE. Finally the standardization to the program stars are applied using the task INVERTFIT, by adopting the transformation equations and the fitting parameters. The calibrated photometric file is now ready for further scientific analysis.

Additional tasks that are useful and relevant in the photometric reduction process are IMHEADER (list header parameters), HEDIT (edit or view image header), IMALIGN (compute relative shifts and align images), IMCOPY (copy and trim images), DISPLAY (load and display image), TVMARK (mark objects on the image display), and TXDUMP (print fields from selected records).

2.3.2 Spectroscopic Reduction

Slit spectroscopic data for the selected bright stars toward the target regions are obtained with the HFOSC of the HCT using Grism 7 (380–684 nm) and Grism 8 (580–830 nm). The extraction and calibration of the spectra are performed using the IRAF software.

Initially the raw stellar spectra are corrected for any detector signature. The bias frames are average combined using the ZEROCOMBINE task, that takes care of the DC-offset. The zero level image is subtracted from the target frames and the CCD processed spectra are generated using CCDPROC, following which the cosmic rays are removed using COSMICRAYS. The CCD reduction processes follow more or less similar conception as with the photometric reduction steps.

Aperture Extraction

The apertures are extracted from the two dimensional spectra using the APALL task from the APEXTRACT package. This single task provides multiple functions for defining, modifying, tracing, and extracting apertures through interactive graphical interface. The extraction window and the background window parameters are set by specifying the number of pixels relative to the center profile. According to the aperture centering parameters, the task automatically traces the center of spatial profile as a function of the dispersion axis. The selected apertures are interactively recentered and resized based on

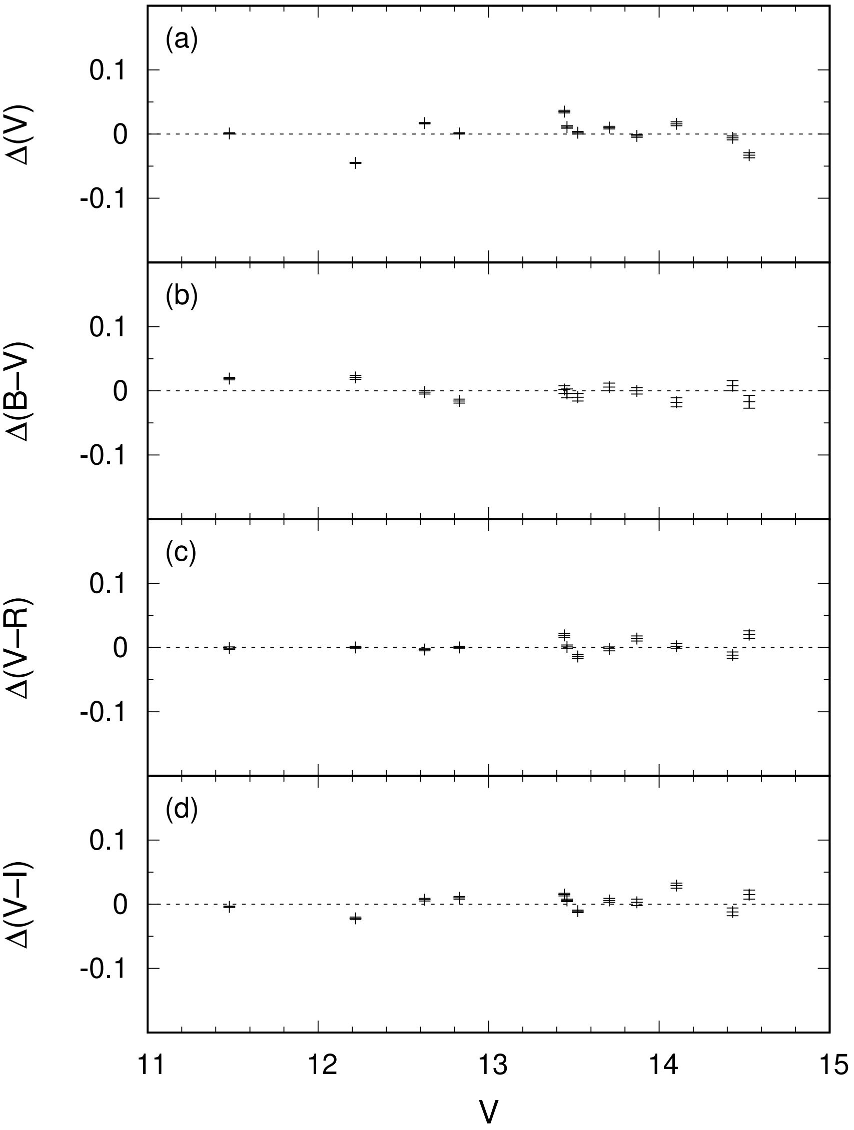

Figure 2.3: Plot of residuals between transformed magnitudes and colors with standard values as a function of standard V magnitudes, obtained during the calibration process.

the spectrum profile width. At each point along the dispersion axis, the counts within the extraction apertures is integrated and the one dimensional spectra is generated. The process includes the possible subtraction of sky background, variance weighting, and bad pixel rejection. Once the target star spectra is reduced, the corresponding lamp spectra is reduced in a similar approach.

Wavelength Calibration

The pixel coordinates of the object frames are scaled to wavelength coordinates by using a combination of tasks from the ONEDSPEC package. Using the IDENTIFY task, the spectral line features in the one dimensional lamp spectrum are interactively marked and assigned with user coordinates. A function is fitted to the provided coordinates as a function of pixel coordinates to find the dispersion functions for the spectra. The quality of the fit is checked, depending on the rms value the bad data points are rejected, and refitted again. The dispersion function is saved in a database directory as a series of coefficients, defining the function and the fitting parameters. The dispersion solution of the object spectra is calculated using the REFSPECTRA task, by assigning the reference spectra (lamp). Finally, using the DISPCOR task, the dispersion corrected and wavelength calibrated object spectra is obtained.

Normalization

The wavelength calibrated spectra still bears wavelength-dependent signature due to change in detector sensitivity over the observed wavelength range. For this, the object spectrum is normalized to unity using the CONTINUUM task. A one dimensional cubic spline (spline3) function of a given order is fitted through the continuum and the spectrum is divided by this fit. The normalized object spectra is then used for further scientific precessing.

Additional useful tasks in the spectroscopic reduction process are SPLOT (plot and analyse spectra), LISTPIXELS (print the pixel values for an image), SHIFTLINES (shift lines in an image), and SARITH (perform arithmetic operations on spectra).

Chapter 3

Census of the Young Stellar Population in the Galactic H II Region Sh2-242

3.1 Introduction

Stellar clusters are recognized as promising astrophysical sites as their formation and early evolution take place primarily in the Galactic spiral arms (Lada & Lada 2003). Systematic studies of young clusters probe several dominant astrophysical problems, such as formation of stars and planetary systems, evolution of open clusters, to galactic disk structures (Adams et al. 2006; Adams 2010; Santos-Silva & Gregorio-Hetem 2012). Most of the stars originate in populous groups within giant regions of molecular clouds (Carpenter 2000; Palla & Stahler 2002; Porras et al. 2003). Massive stars ($>8\ M_\odot$) play an immense role to create a birthplace for next generation stars by emitting huge amounts of energy in the ultraviolet range (Elmegreen & Lada 1977). The Lyman continuum radiation gradually ionizes the surrounding interstellar medium and creates H II regions. The newly formed H II regions are the zero-age objects compared with the age of the Milky Way and are thus efficient tracers of star formation at the present epoch (Anderson et al. 2014). Zones of H II regions are presumed to be the productive sites of next generation star formation (Elmegreen 1998). The early phases of stellar evolution occur within the dense regions of molecular clouds, where young stellar populations are invariably associated with significant amounts of interstellar dust and gas (Lada & Adams 1992). Young stars associated in a cluster are thought to have formed almost simultaneously from the same progenitor molecular cloud and share similar heritage of age, distance, and chemical composition (Fukuda & Hanawa 2000). The infrared and radio wavelength surveys provide comprehensive pictures on young star-forming regions and on their dynamical evolution. Additionally, the parameters of a young cluster can be estimated from the optical photometric study of the stellar sources and the spectroscopic data of massive exciting stars associated with the cluster. Despite recent advancements in observational and theoretical prospects, the complete star formation census is still poorly understood and requires further exploration.

In this context, we present a multiwavelength analysis of the Galactic H II region Sh2-242 (S242; $\alpha_{(2000)} = 05^{\rm h}51^{\rm m}54^{\rm s}$, $\delta_{(2000)} = +27°01'54''$), located in the Taurus constellation. Mayer & Macák (1973) first classified the principal ionizing source of the region, BD+26 980 as a spectral type of B0 V. Using the UBV photoelectric photometry, they somehow overestimated the distance of the star as 3.39 kpc. Using a different approach of spectroscopic observations and Hγ equivalent widths, Crampton & Fisher (1974) also obtained the spectral type of BD+26 980 as B0 V. Using absolute magnitude from the spectroscopic classification and assuming the ratio of total-to-selective absorption as 3.0, the authors derived the distance of the star to be 2.1 kpc. Using the $UBVRI$ photometric observations, Lahulla (1987) estimated the distance to the exciting star to be 2.5 kpc and the extinction as 2.4 mag [$E(B-V) = 0.76$ mag]. To calculate the distance, they used an absolute magnitude based on a B0 V spectral type and assuming $A_V/E(B-V)$ = 3.1. Hunter & Massey (1990) too found the spectral type of BD+26 980 to be similar (B0 V) using optical spectroscopy. For this same star they obtained a comparatively larger distance (2.7 kpc) using simulated B and V photometry.

Together, these studies indicate that the S242 region is an active site of star formation and also harbors a massive star of spectral type B0 V. In this chapter, we present a multiwavelength survey on the identification and characterization of the young stellar population toward this region. In Section 3.2, we describe the observational and archival data sets used, including their reduction processes. Section 3.3 comprises the results of spectroscopically observed bright sources and identification and classification of the YSOs using archival data sets. Characterization of YSOs, such as spectral nature, age, and mass spectrum, and the region properties are discussed in Section 3.4. Our final results are summarized and concluded in Section 3.5.

3.2 Data and Reduction

3.2.1 New Observations

Optical Photometry

Optical photometric data for B (360 nm), V (550 nm), and I (900 nm) bands are acquired with the 1.3 m Devasthal Fast Optical Telescope (DFOT; Sagar et al. 2012), Nainital, India, with different exposure times to cover bright to faint sources. The photometric observations are carried out using a 13.5 micron pixel, 2K×2K Andor CCD camera, which covers a square area of about $18'\times18'$ on the sky with a plate scale of $0''.53$ pixel^{-1}. The CCD has a readout noise and gain of 7 e^- and 2.2 e^- ADU^{-1} respectively. During the observations, the average seeing is measured to be $\sim 2''$. The photometric standard field SA 95 (Landolt 1992) is observed on the same night with different airmass, to apply atmospheric and instrumental corrections to the target frames. The log of optical photometric observations is given in Table 3.1. The color composite image (blue: B, green: V, and red: I) generated from optical observations toward the S242 region is shown in the Figure 3.1(a). The sources marked with yellow circles represent the stars observed with slit spectroscopy (see Section 3.2.1) and their corresponding ID numbers (Table 3.1) are given. The optical/infrared three color image generated from DSS2 R 0.70 μm (blue), 2MASS K 2.2 μm (green), and *WISE* $W2$ 4.6 μm (red) for the region is shown in the Figure 3.1(b). The main illuminating source BD+26 980 is depicted in both the panels.

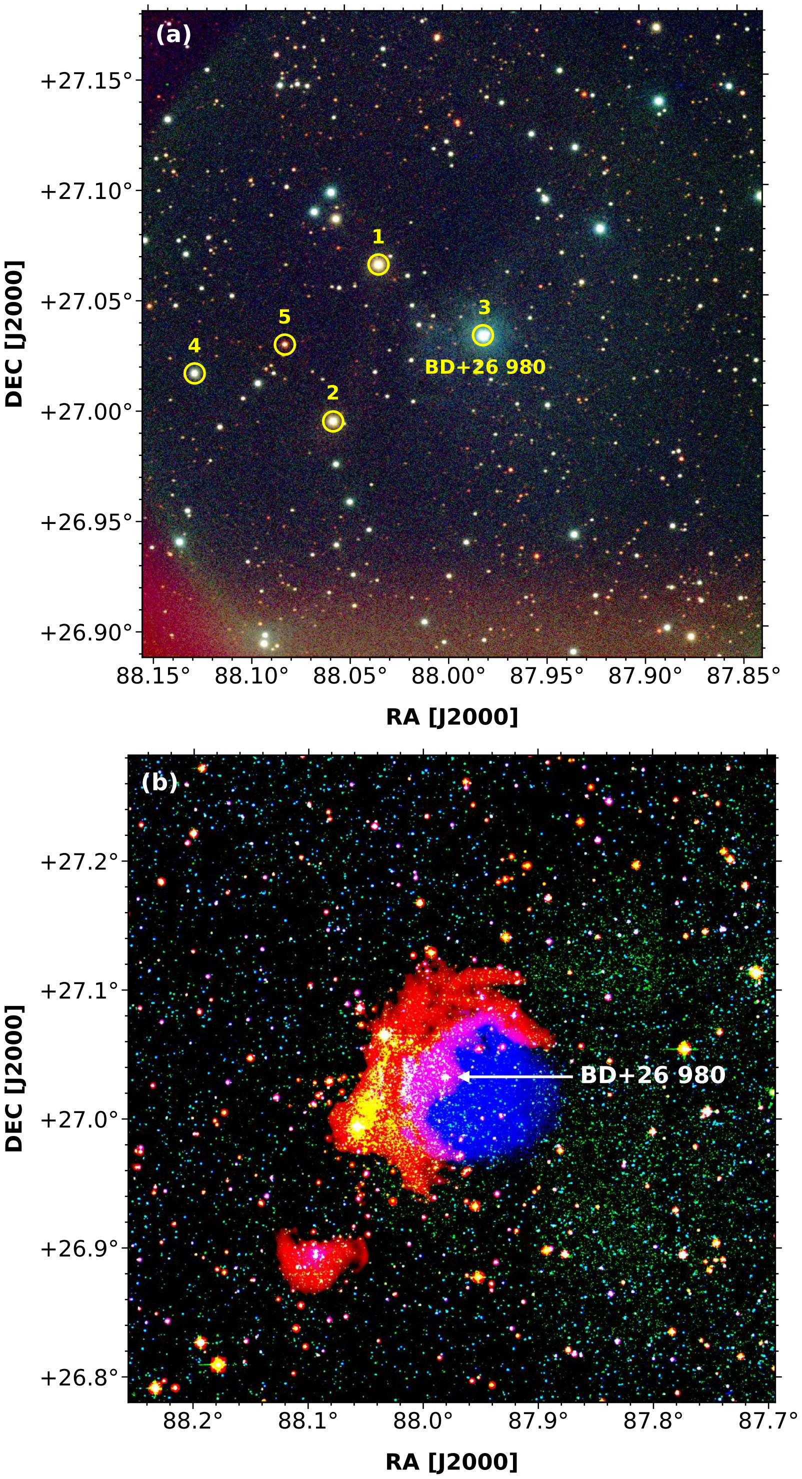

Figure 3.1: (a) Optical color composite image of the S242 region, created with B 360 nm (blue), V 550 nm (green), and I 900 nm (red) bands for a sky area of 18×18 arcmin^2, acquired with the 1.3 m DFOT. Spectroscopically observed sources from the 2 m HCT are numbered and marked with yellow circles and the main ionizing source BD+26 980 is depicted. (b) Color composite image of the S242 region with optical and infrared counterparts taken from DSS2 R 0.70 μm (blue), 2MASS K 2.2 μm (green), and *WISE* $W2$ 4.6 μm (red) bands.

Table 3.1: Log of optical photometric and spectroscopic observations toward S242

ID	R.A. (J2000) (h:m:s)	Decl. (J2000) (d:m:s)	Date of Observations	Filter/ Grism	Exp. time (s) × No. of frames	Airmass/ SNR	V (mag)	$B-V$ (mag)
				Photometry				
Sh2-242	05:52:20	+27:02:30	2016 Dec 19	B	500×3, 60×3	1.018		
Sh2-242	05:52:20	+27:02:30	2016 Dec 19	V	500×3, 60×3	1.679		
Sh2-242	05:52:20	+27:02:30	2016 Dec 19	I	300×3, 10×3	1.130		
				Slit Spectroscopy				
1	05:52:08.13	+27:03:55.64	2016 Nov 03	7, 8	900×1, 900×1	18, 27	10.864	1.608
2	05:52:13.83	+26:59:40.83	2016 Nov 03	7, 8	1200×1, 1200×1	20, 28	11.313	1.451
3	05:51:55.41	+27:01:58.03	2016 Nov 03	7, 8	1200×1, 900×1	29, 41	10.128	0.483
4	05:52:30.68	+27:01:01.15	2017 Jan 23	7, 8	1800×1, 1800×1	24, 26	11.978	0.914
5	05:52:19.65	+27:01:46.83	2017 Jan 23	7, 8	1800×1, 1800×1	14, 17	14.246	1.879
				Slitless Spectroscopy				
Sh2-242_1	05:52:24.03	+26:58:29.57	2017 Dec 15	Gr5/H_α-Br	1800×1	1.273		
Sh2-242_2	05:51:44.16	+26:58:38.72	2017 Dec 15	Gr5/H_α-Br	1800×1	1.361		
Sh2-242_3	05:51:44.34	+27:07:36.12	2017 Dec 15	Gr5/H_α-Br	1800×1	1.657		
Sh2-242_4	05:52:24.45	+27:07:31.31	2017 Dec 15	Gr5/H_α-Br	1800×1	1.882		

Table 3.2: Color coefficients, constant terms, and extinction coefficients used for optical photometric calibrations

Parameters	Constants
Color coefficients	
m_{bv}	1.326 ± 0.023
m_{vi}	0.897 ± 0.014
m_v	-0.125 ± 0.011
Zero-point constants	
c_{bv}	-1.019 ± 0.027
c_{vi}	0.384 ± 0.016
c_v	-2.024 ± 0.013
Extinction coefficients	
K_b	0.262 ± 0.010
K_v	0.229 ± 0.005
K_i	0.103 ± 0.005

Optical photometric data are reduced using sophisticated tasks from the IRAF[1] software. The raw CCD images are cleaned by subtracting the median combination of bias and flat frames, following cosmic ray removal. Point sources are extracted using the DAOFIND task from the DAOPHOT package with necessary sky background and detection threshold limits. A PSF fitting algorithm is performed on all the sources using the ALLSTAR routine (Stetson 1987). Atmospheric extinction and color coefficients are calculated from observations of the standard field for corresponding filters by fitting a linear least-squares fit regression method (Stetson 1992). A set of transformation equations (Equations 3.1, 3.2, and 3.3) are used to convert the instrumental magnitudes to the standard systems as follows.

$$(B-V) = m_{bv}(b-v) + c_{bv} \tag{3.1}$$

$$(V-I) = m_{vi}(v-i) + c_{vi} \tag{3.2}$$

and

$$V = v + m_v(V-I) + c_v \tag{3.3}$$

where B, V, and I are the magnitudes in standard systems and b, v, and i are instrumental magnitudes corrected for the atmospheric extinction due to airmass. The details of color coefficients (m_{bv}, m_{vi}, m_v), constant terms (c_{bv}, c_{vi}, c_v), and extinction coefficients (K_b, K_v, K_i) are tabulated in Table 3.2.

A total of 12 standard stars is used to calculate the color coefficients and zero-point constants in the standard field. Figure 3.2 shows the variation of residuals between transformed and standard colors and magnitudes as a function of V magnitude.

The world coordinate system on the physical frames is obtained by selecting 24 unsaturated, isolated, and moderately bright stars from the 2MASS catalog for the

---

[1] Image Reduction and Analysis Facility (IRAF) (`http://iraf.noao.edu/`)

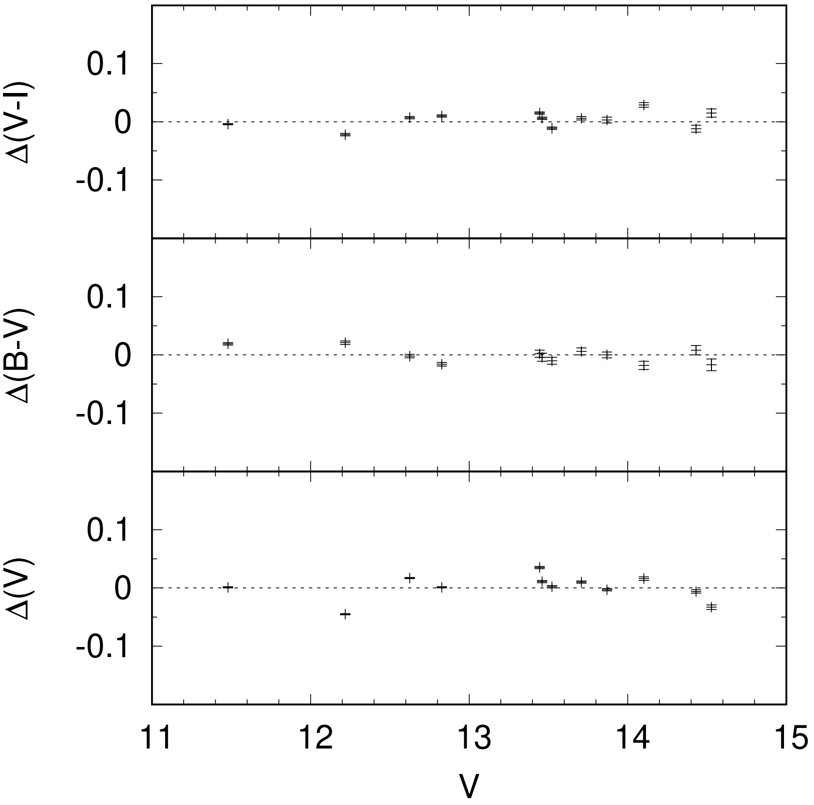

Figure 3.2: Plot of residuals between transformed colors and magnitudes with standard values as a function of standard V magnitudes.

same field. We used the IRAF tasks CCMAP, and CCSETWCS and the WCSTools package to obtain the astrometric solutions.

Optical Slit Spectroscopy

Optical slit spectroscopic observations for five bright sources within the region are carried out using the Himalaya Faint Object Spectrograph and Camera (HFOSC) on the 2 m Himalayan Chandra Telescope (HCT). Spectra are taken with Grism 7 (380 - 684 nm) and Grism 8 (580 - 830 nm) with resolutions of 1330 and 2190, respectively. The spectroscopic standard star Feige 34 (Oke 1990) is observed on the same night for flux calibration. The FeAr and FeNe arc lamp observations are conducted immediately after the target observations for wavelength calibration. The log of optical spectroscopic observations is shown in Table 3.1.

After being rectified by bias subtraction and cosmic ray correction, the monodimensional spectra are extracted using the APALL task in the IRAF software. The spectra are then wavelength calibrated from corresponding lamp observations. The data are corrected for atmospheric extinction and instrument sensitivity availing the standard star observations.

Table 3.3: Extinction vector, R, adopted in this work for the Pan-STARRS 1 catalog, are based on Schlafly et al. (2016)

g_{P1}	r_{P1}	i_{P1}	z_{P1}	y_{P1}
3.384	2.483	1.838	1.414	1.126

Optical Slitless Spectroscopy

Slitless spectroscopic data are obtained from the HCT to detect Hα emission line stars toward the region. The data are acquired using a broadband Hα filter (630 - 674 nm) in combination with Grism 5 (520 - 1030 nm) in slitless mode (Table 3.1). The 2K×2K CCD has a field of view (FOV) of 10×10 arcmin^2 with an image scale of $0\farcs296$ pixel^{-1}. The resolution of Grism 5 is 870. The data are taken for four overlapping frames covering a total sky area ($18' \times 18'$) similar to that of the optical photometric observations (Section 3.2.1). The Hα emitting sources show certain enhancements in their spectra over the continuum. We have visually identified three sources having prominent Hα emissions from these observations.

3.2.2 Pan-STARRS 1 Photometry

As a complementary data set to the observed optical photometry (Section 3.2.1), we used optical/near-infrared imaging from the Panoramic Survey Telescope and Rapid Response System 1 (Pan-STARRS 1; Chambers et al. 2016). The Pan-STARRS 1 camera consists of a mosaic of 60 edge-abutted 4846×4868 pixel detectors, with 10 μm pixels subtending $0\farcs258$. It provides homogeneous and deeper coverage photometry in five broad passbands g_{P1}, r_{P1}, i_{P1}, z_{P1}, and y_{P1}, ranging from 400 nm to 1000 nm (Stubbs et al. 2010). The effective wavelengths for the five filters are roughly 480, 620, 750, 870, and 960 nm, respectively, similar to those used by the SDSS (York et al. 2000), with most significant difference being the replacement of the Sloan u band with a near-infrared band y_{P1}. The Pan-STARRS 1 image processing, astrometry, and photometry are detailed in Magnier et al. (2020a; 2020b) and the relative and absolute calibration survey are reported in Schlafly et al. (2012) and Tonry et al. (2012). The typical single-epoch 5σ photometric depths in the corresponding five passbands are 22.0, 21.8, 21.5, 20.9, and 19.7 mag (AB), respectively (Chambers et al. 2016). The empirical components of the adopted extinction vector are taken from Schlafly et al. (2016) and given in Table 3.3.

3.2.3 *G*aia DR2 Astrometry

The *Gaia* Data Release 2 (*Gaia* DR2; Gaia Collaboration et al. 2018) provides five parameter (position, proper motion, and parallax) astrometric results for over 1.3 billion sources from the observations of the European Space Agency *Gaia* satellite (Gaia Collaboration et al. 2016a). The parallaxes of the sources toward the S242 region are collected from the *Gaia* DR2 archive[2]. The distance and membership status of the sources are estimated by restricting the data to only positive parallaxes. The positive parallaxes with relative uncertainties typically below 20% are primarily considered as reliable astrometry (Luri et al. 2018).

3.2.4 IPHAS DR2 Photometry

The INT Photometric Hα Survey of the Northern Galactic Plane (IPHAS; Drew et al. 2005) is an imaging survey covering an 1800 deg^2 sky in broadband Sloan r (624 nm) and i (774.3 nm), and narrowband Hα (656.8 nm) filters using a wide field camera on the 2.5 m Isaac Newton Telescope (INT) in La Palma. The camera generates a mosaic of four CCDs at a pixel scale of $0.''33$ pixel^{-1}. This survey offers an unique facility to detect Hα emission line objects by comprehensive CCD photometry of point sources at visible wavelengths. The photometric data for r, i, and Hα bands are obtained from the IPHAS DR2 catalog (Barentsen et al. 2014) for the S242 region.

3.2.5 Infrared Catalogs

Near-Infrared Data: WIRCam and 2MASS

The Wide-field InfraRed Camera (WIRCam; Puget et al. 2004) is the near-infrared mosaic imager mounted at the prime focus of the 3.6 m Canada-France-Hawaii Telescope (CFHT) on Maunakea, Hawaii. The WIRCam consists of four 2048×2048 HAWAII2-RG detectors covering a field of view of 20 arcmin^2 with a pixel scale of $0.''3$. The images in J (1.25 μm), H (1.63 μm), and K (2.14 μm) bands[3] for the S242 region are collected from the CFHT archive[4] for Proposal ID 06BF14 and 06BF96, respectively. The observations were carried out under principal investigator Lise Deharveng on December 28, 2006 and January 01, 2007 accordingly. The raw data are optimized using the Interactive Data Language (IDL) based interface the SIMPLE Imaging and Mosaicking Pipeline (SIMPLE; Wang et al. 2010b). The astrometric and photometric reductions are performed in a similar way, as are outlined in Dutta et al. (2018). Briefly the dithered images are mosaicked using median combination technique. The astrometric calibrations of the combined images are performed in comparison with the 2MASS reference frames. The point sources in the reduced astrometric frames are identified by using PSF fitting algorithm from the DAOFIND package (Stetson 1992) in the IRAF software. Photometric calibrations of the WIRCam frames are performed in comparison with the 2MASS catalog considering all the sources with magnitude uncertainty < 0.1 mag.

The 2MASS Point Source Catalog (PSC; Skrutskie et al. 2006) photometry in J, H, and K bands are taken as a complementary data set. In an attempt to avoid the inclusion of saturated sources in WIRCam photometry, we replaced all the sources in WIRCam with 2MASS magnitudes for $J < 13$ mag, $H < 12.5$ mag, and $K < 12$ mag

---

[2] `https://gea.esac.esa.int/archive/`

[3] `http://www.cfht.hawaii.edu/Instruments/Filters/wircam.html`

[4] `http://www.cadc-ccda.hia-iha.nrc-cnrc.gc.ca/en/cfht/`

(Lucas et al. 2008). A photometric uncertainty < 0.1 mag for all the bands is considered as quality criteria for reliable photometry, which provides S/N ≥ 10.

Mid-Infrared Data: *Spitzer*

We obtained mid-infrared photometry for point sources toward the S242 region from the *Spitzer* Warm Mission (Hora et al. 2012) survey. Magnitudes from the Infrared Array Camera (IRAC; Fazio et al. 2004) [3.6] and [4.5] μm bands with a pixel scale of $1\farcs2$ pixel^{-1} are downloaded from the highly reliable Glimpse360[5] catalog (Program Id: 61070, PI: Whitney, Barbara A). We restricted the sources with photometric uncertainty $\sigma < 0.2$ mag for all the IRAC bands to achieve good quality photometric catalog.

3.2.6 Multiwavelength Catalog

The final catalog is generated by matching different optical to infrared data sets in stages. The BVI catalog is built by cross-matching all the sources detected from optical photometry (Section 3.2.1) with a radial tolerance of $2''$. As the seeing ($\sim 2''$) is not sufficiently good, we used a matching radius of $2''$ to match the sources detected in optical photometry. We performed several test matches by increasing the radial distance from $1''$ to $3''$ in steps of $0\farcs1$ to pick up the suitable matching radius for each catalog data. In case of multiple sources matched within a given matching radius, we have taken the nearest one as the preferred match. To match the sources detected from WIRCam JHK bands, a matching radius of $1''$ is used. JHK, IRAC, and IPHAS catalogs are matched within a matching radius of $1''$. We have adopted the matching radius of $1''$ to match the sources selected from optical and infrared catalog data.

We have used histogram turn over method to estimate the completeness of our utilized data sets. In general, the completeness limits are calculated from histograms, where the logarithmic distribution of the sources deviates from the linear distribution. The completeness limits for different data sets for the S242 region are $V = 17.8$ mag, $J = 18.4$ mag, $H = 17.6$ mag, $K = 17.2$ mag, $[3.6] = 16.8$ mag, and $[4.5] = 16.4$ mag, respectively. However, there may be several additional factors, such as saturation caused by bright luminous sources, variable reddening, stellar crowding, telescope detection sensitivity, etc., that can constrain the completeness of different data sets (Jose et al. 2013).

3.3 Results

3.3.1 Spectral Classification of the Spectroscopically Observed Stars

The target stars for spectroscopic observations are selected based on their brightness ($J < 11$ mag) toward the region. The details of observations for each star are listed in

---

[5] `http://www.astro.wisc.edu/sirtf/glimpse360/`

Table 3.1. The flux-calibrated normalized spectra of the observed stars obtained with Grism 7 and 8 are presented in Figure 3.3.

Spectral classifications are done by comparison to the spectral indices of Danks & Dennefeld (1994), Kobulnicky et al. (2012), and Hernández et al. (2004), and comparison with the spectral atlas of Jacoby et al. (1984), Walborn & Fitzpatrick (1990), and Torres-Dodgen & Weaver (1993). The classification scheme relied on the marking and utilizing of strong conspicuous features for any spectral range. For early-type stars (B, A, and F), we compared the strength of atomic absorption lines, such as hydrogen Balmer series (Hδ λ4102 Å, Hγ λ4340 Å, Hβ λ4861 Å, Hα λ6563 Å), He I ($\lambda\lambda$5876, 6678, 7065 Å), and He II ($\lambda\lambda$4200, 4541, 4686, 5411, 5720 Å) lines. Whereas for cooler stars like G-type or later than that, different metallic line features such as Mg I triplet ($\lambda\lambda$5167, 5172, 5183 Å), Mg II ($\lambda\lambda$4481, 6347 Å), Ca I ($\lambda\lambda$6122, 6162 Å), and Fe I ($\lambda\lambda$6495, 7749, 7834 Å) are used. We also adopted certain constraints on the specific line features. The absence of He II λ5411 Å line in any spectra limits the spectral type to B0.5 or later (Kobulnicky et al. 2012), while the absence of He I λ5876 Å constrains the spectral type to later than A0 (Lundquist et al. 2014). Si III λ4552 Å and O II λ4650 Å show maximum strength at spectral type B0.5 V, and He II λ4686 Å is last seen up to types B0.5−B0.7 V (Walborn & Fitzpatrick 1990). The declining strength of C III λ4070 Å and O II λ4650 Å blends are used as an additional criteria to classify the stars in the spectral range B1−B2 V. He I line strength is maximum for B2 type stars, whereas for later than that Si II $\lambda\lambda$4128−4130 Å and Mg II λ4481 Å increase distinctly (Walborn & Fitzpatrick 1990). He I λ6678 Å appears strongest at O9 V, before disappearing at B8 V (Danks & Dennefeld 1994). The weak presence of O I λ7776 Å is notable at B2 V, strengthens to maximum at A5 V and disappears at G0 V. The appearance of Fe I λ6495 Å is evident at A2 V and grows in strength to K0 V (Danks & Dennefeld 1994). The presence of Fe I $\lambda\lambda$7749, 7937 Å in any spectrum is an indication of K dwarfs (Allen & Strom 1995). We also compared the equivalent widths of He II λ5411 Å, He I λ5876 Å and Hα λ6563 Å for B-type stars, and Na I ($\lambda\lambda$5890−5896 Å), Hα and Ca II triplet ($\lambda\lambda$8498, 8542, 8662 Å) for later-type stars with the spectral indices of Danks & Dennefeld (1994), Kobulnicky et al. (2012), and Lundquist et al. (2014).

The spectroscopic analysis of the observed sources produced only one massive and early-type star (B0.5 V). Other spectroscopically observed sources are found to be late-type (either G or K) stars. The star ID 1 shows weaker Hα λ6563 Å and Na I $\lambda\lambda$5893, 8195 Å absorption features, presence of Fe I $\lambda\lambda$6495, 7747, 7834 Å and Ca II triplet $\lambda\lambda$8498, 8542, 8662 Å indicative of an early-K type star (K1 V-III). The star ID 2 is classified as K0 V-III, from similar diagnostic as ID 1. The spectrum of star ID 3 shows strong He I λ5876 Å and Hα absorption feature along with the presence of He II λ4200 Å and He I $\lambda\lambda$6678, 7065 Å lines. As no signature of He II λ5411 Å is detected from the spectrum, we categorized the star as B0.5 V spectral type. The stars ID 4 and 5 are classified as G9 V and G0 V type, respectively, for showing weak and narrow Hα absorption features and presence of Mg I triplet at $\lambda\lambda$5167, 5172, 5183 Å. We designated the stars with luminosity class V/III, as their spectral resemblance with the main-sequence/giants are better than super-giants. Also in some cases it is difficult

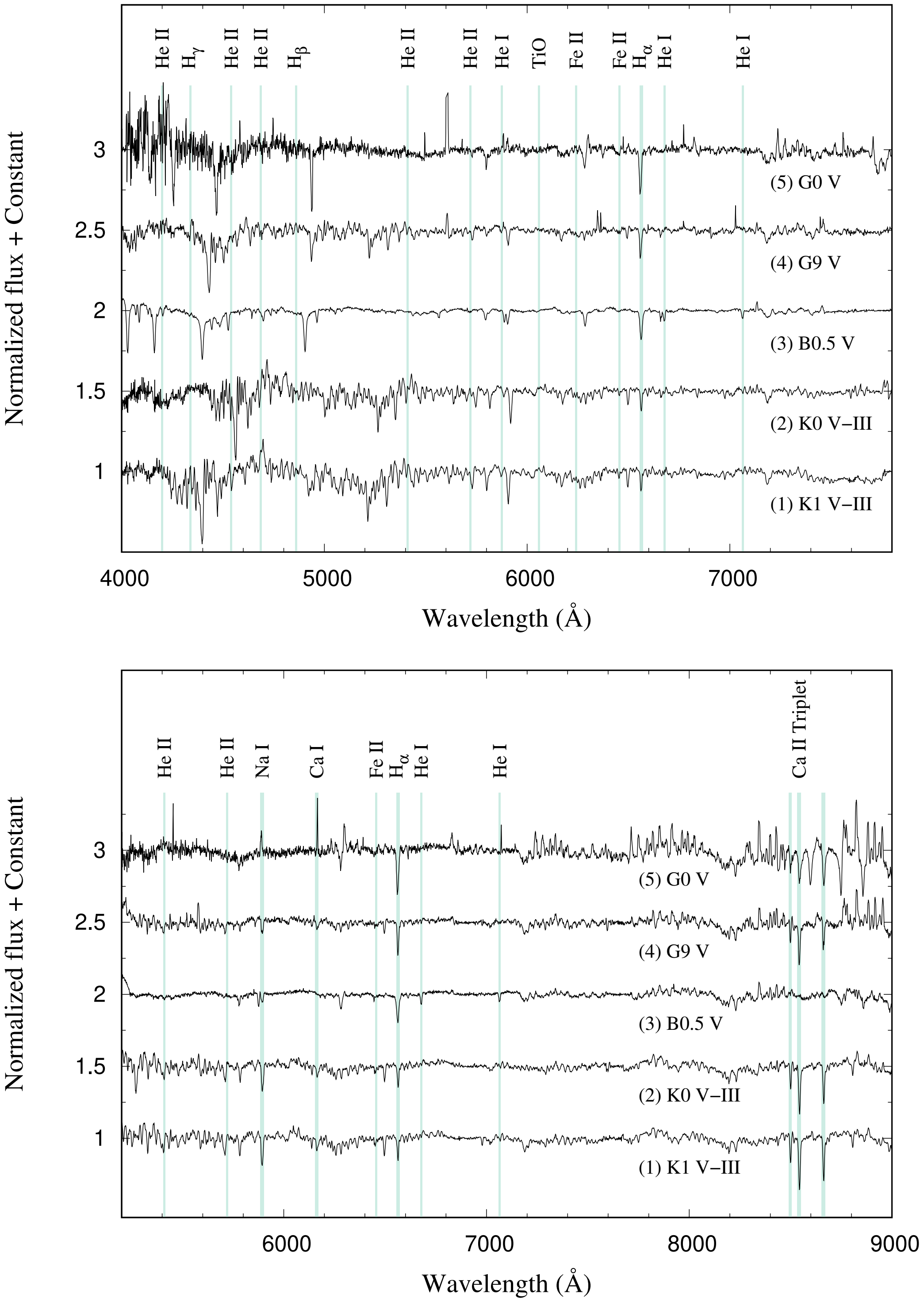

Figure 3.3: Flux-calibrated normalized spectra for the spectroscopically observed stars toward S242, obtained with the 2-m HCT using Grism 7 (top) and Grism 8 (bottom) respectively. The important emission and absorption line features are marked.

to properly distinguish between the main-sequence and the giant stars. Based on the low-resolution spectroscopy, an uncertainty of ±1 spectral subtype for early-type stars up to F- and ±3 subtype for G-type and later stars is expected. The photometric and spectroscopic details of the five observed stars are tabulated in Table 3.4.

Table 3.4: Details of the spectroscopically observed stars

Star ID (1)	R.A. (J2000) (h:m:s) (2)	Decl. (J2000) (d:m:s) (3)	Spectral Type (4)	*J* (mag) (5)	*H* (mag) (6)	*K* (mag) (7)	Spectroscopic A_V (mag) (8)	Distance Modulus (9)	Distance (pc) (10)	Distance from *Gaia* (pc) (11)	Remarks
1	05:52:08.13	+27:03:55.64	K1 V–III	7.977	7.309	7.065	2.38	...	...	1141	Foreground
				± 0.009	± 0.057	± 0.009	± 0.06			± 64	
2	05:52:13.83	+26:59:40.83	K0 V–III	8.709	8.088	7.884	2.12	...	...	1103	Foreground
				± 0.015	± 0.019	± 0.023	± 0.02			± 70	
3	05:51:55.41	+27:01:58.03	B0.5 V	9.155	9.110	8.982	1.80	11.58	2076	2079	Member
				± 0.021	± 0.025	± 0.020	± 0.04	± 0.05	± 239	± 192	
4	05:52:30.68	+27:01:01.15	G9 V	10.399	10.007	9.868	0.24	6.19	173	769	Foreground
				± 0.019	± 0.024	± 0.019	± 0.03	± 0.04	± 16	± 32	
5	05:52:19.65	+27:01:46.83	G0 V	10.006	9.383	9.004	3.28	...	...	2764	Background
				± 0.019	± 0.024	± 0.017	± 0.03			± 506	

Notes:
(1) ID Number of the spectroscopically observed stars.
(2-3) Equatorial coordinates of the stars in degrees.
(4) Spectral types estimated from the spectroscopic observations.
(5-7) Photometric parameters of the stars from 2MASS catalog (Skrutskie et al. 2006).
(8-9) Visual extinction (A_V) and distance modulus are calculated from spectral types and infrared photometry.
(10) Spectroscopic distances of the stars.
(11) Distance of the stars from *Gaia* DR2 catalog (Gaia Collaboration et al. 2018).

3.3.2 Reddening and Membership of the Spectroscopically Observed Stars

Membership estimation of the observed stars toward a cluster region is a crucial step to quantify the essential cluster parameters. The relevant parameters used to ascertain the spectrophotometric distances for each star are listed in Table 3.4. We used the spectral types and infrared photometry (J, H, and K) to determine the distances of the spectroscopically observed bright sources. We have estimated the spectroscopic A_V of individual sources, using the relation $E(J-H) = (J-H)-(J-H)_0$, and similar relations simultaneously for other two bands, where $(J-H)$ is the observed color and $(J-H)_0$ being the intrinsic color. The intrinsic distance modulus $(J_0 - M_J)$, $(H_0 - M_H)$, and $(K_0 - M_K)$ are calculated from reddening A_V, absolute (M_J, M_H, M_K) and observed (J, H, K) magnitudes. The intrinsic values of magnitudes and colors are taken from Pecaut & Mamajek (2013). The intrinsic distance modulus of star ID 3 is calculated as 11.58 ± 0.05 mag, which corresponds to a distance of 2.08 ± 0.24 kpc. Additionally from the *Gaia* DR2 catalog, the distance of the source is derived as 2.08 ± 0.19 kpc, which is in close agreement with our estimated spectrophotometric distance. Out of the five spectroscopically observed stars, we assigned BD+26 980 (star ID 3) of spectral type B0.5 V, a massive member of the cluster. Others are either foreground or background stars as mentioned in Table 3.4.

Figure 3.4 shows the distribution of sources detected from the observed optical photometry toward S242 in the $V/(B-V)$ and $V/(V-I)$ color-magnitude diagrams. The black filled circles represent the sources with photometric uncertainty < 0.1 mag and gray filled circles are those with photometric uncertainty higher than this. The spectroscopically observed stars are numbered and marked with red circles. The blue solid lines represent the locus of the zero-age main sequence (ZAMS) taken from Girardi et al. (2002) and corrected for the cluster distance of 2.08 kpc, and reddening $E(B-V) = 0.56$ and $E(V-I) = 0.70$ mag [$E(B-V)/E(V-I) = 0.794$; Cohen et al. 1981]. In order to shift the ZAMS, we used the extinction $A_V = 1.8$ mag (Table 3.4) of the main illuminating source BD+26 980 of the region. The photometric catalog of optically observed point sources toward the S242 region is tabulated in Table 3.5. A total of 503 sources is detected at least in B, V, or I band with a limiting magnitude of $V \sim 19.4$ mag. We obtained a total of 291 sources having counterparts in all the three B, V, and I bands, within a $18' \times 18'$ sky area. Although the spatial variation of extinction can be non-uniform throughout the region. There may be several causes for the broad distribution of sources in the color-magnitude diagrams, such as variable reddening, presence of field stars, binaries, and peculiar stars. However it is difficult to differentiate the cluster members and field stars from these diagrams.

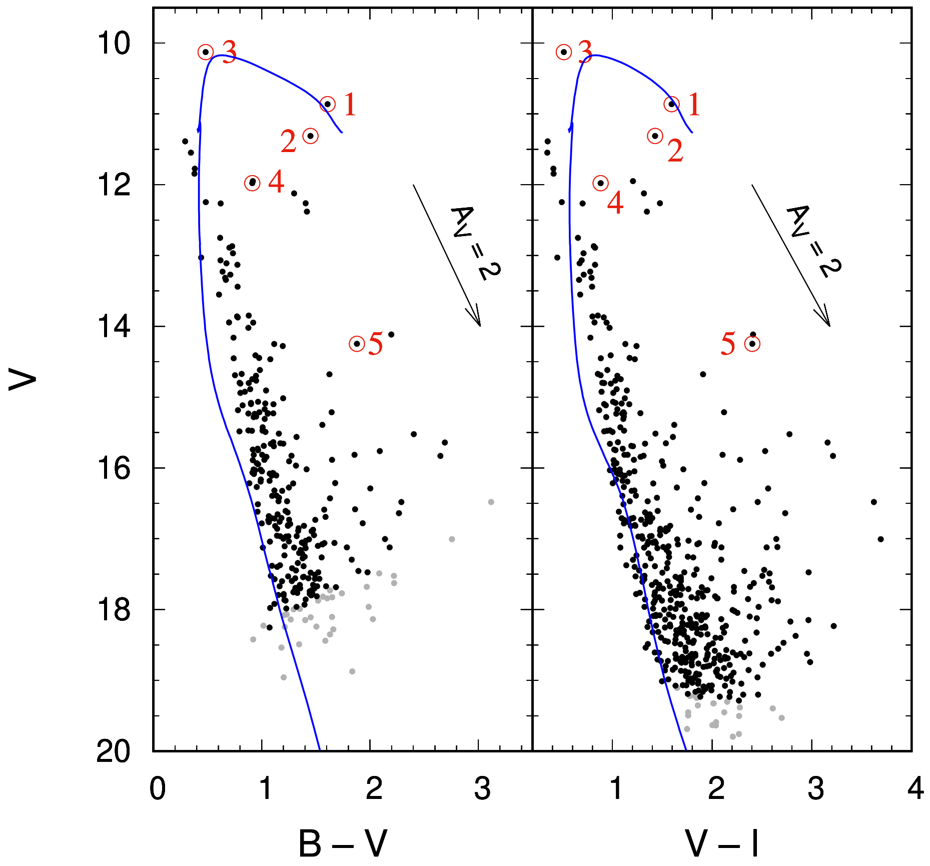

Figure 3.4: Distribution of sources from optical photometry in the color-magnitude diagrams. Spectroscopically observed sources are numbered and marked with red circles. The ZAMS from Girardi et al. (2002), corrected for the cluster distance of 2.08 kpc and reddening $E(B-V) = 0.56$ mag and $E(V-I) = 0.70$ mag (Table 3.4), is shown with blue solid lines.

Table 3.5: Photometric catalog of optically observed point sources toward the S242 region. This table is published in its entirety in the electronic edition of Panja et al. (2020). A portion is shown here to represent its form and content

Sl. No. (1)	R.A. (J2000) (deg) (2)	Decl. (J2000) (deg) (3)	V (mag) (4)	$B-V$ (mag) (5)	$V-I$ (mag) (6)	J (mag) (7)	H (mag) (8)	K (mag) (9)	[3.6] μm (mag) (10)	[4.5] μm (mag) (11)
1	87.978500	27.033672	15.661	1.084	0.976	14.139	13.770	13.681	...	...
			± 0.022	± 0.033	± 0.031	± 0.120	± 0.131	± 0.089	...	...
2	87.980881	27.032787	10.128	0.483	0.514	9.155	9.110	8.982	8.949	8.934
			± 0.025	± 0.025	± 0.025	± 0.021	± 0.025	± 0.020	± 0.034	± 0.028
3	87.983437	27.020210	16.588	1.577	1.787	13.666	12.969	12.748	12.658	12.671
			± 0.011	± 0.031	± 0.013	± 0.019	± 0.025	± 0.025	± 0.036	± 0.036
4	87.959221	27.028023	17.532	1.244	1.232	15.308	14.780	14.596	14.434	14.448
			± 0.019	± 0.068	± 0.031	± 0.036	± 0.050	± 0.073	± 0.042	± 0.065
5	87.957176	27.040668	15.740	0.918	1.019	13.929	13.515	13.420	13.271	13.291
			± 0.005	± 0.011	± 0.010	± 0.023	± 0.025	± 0.030	± 0.043	± 0.040
6	87.992310	27.041452	17.754	1.293	1.426	15.221	14.508	14.371	14.322	14.513
			± 0.023	± 0.084	± 0.037	± 0.059	± 0.063	± 0.076	± 0.093	± 0.083
7	87.977272	27.012955	16.086	0.929	1.061	14.186	13.774	13.674	13.607	13.565
			± 0.006	± 0.018	± 0.013	± 0.027	± 0.033	± 0.037	± 0.044	± 0.043
8	87.956512	27.019300	17.858	1.406	1.328	15.298	14.776	14.658	14.479	14.400
			± 0.020	± 0.091	± 0.033	± 0.040	± 0.055	± 0.073	± 0.067	± 0.078
9	87.956207	27.045404	18.069	1.231	1.567	15.354	14.788	14.590	14.296	14.245
			± 0.031	± 0.108	± 0.044	± 0.040	± 0.043	± 0.066	± 0.050	± 0.060
10	88.007477	27.036873	17.962	1.988	2.466	13.549	12.658	12.245	11.989	11.943
			± 0.033	± 0.173	± 0.035	± 0.021	± 0.028	± 0.017	± 0.043	± 0.031

Notes:
(1) Serial Number of sources.
(2-3) Equatorial coordinates of sources in degrees.
(4-6) Photometric magnitudes, colors, and their errors from DFOT (Sagar et al. 2012).
(7-9) Photometric catalog either from WIRCam (Puget et al. 2004) or 2MASS PSC (Skrutskie et al. 2006).
(10-11) Photometric catalog from *Spitzer* IRAC (Fazio et al. 2004).

3.3.3 Extinction Map Toward the S242 Region

Discriminating embedded young stars in clusters from field stars is a salient feature in the study of young stellar distributions of interest. Young cluster environments are rich with dust, reducing the density of background stellar contamination (Gutermuth et al. 2005). Often the nonuniform distribution of dust in these environments makes it far more challenging to get a proper census of detectable background stars (Gutermuth et al. 2005). In general, the distribution of dust in a cloud can be traced by measurements of the extinction of background starlight produced by the cloud (Lada et al. 1994). In order to map the extinction throughout the S242 region, we used H and K photometry from the 2MASS catalog with photometric uncertainty < 0.1 mag. Since our target area is not completely covered with WIRCam photometry, we used 2MASS catalog to generate the map. The A_K values are derived from $(H-K)$ colors, following the method outlined in more detail by Gutermuth et al. (2005). In brief, we divided the region of our interest into uniform grids of size $15'' \times 15''$. We have taken 20 nearest neighbor sources from the center of each grid to calculate the mean and standard deviation of $(H-K)$ color for each grid, excluding the sources whose $(H-K)$ values deviated 3σ from the mean value. The mean $(H-K)$ color for each grid are converted to A_K, using the reddening law $A_K = 1.82 \times [(H-K)_{obs} - (H-K)_{int}]$ from Flaherty et al. (2007). The average intrinsic color $(H-K)_{int}$ of the background population is taken into account to accurately characterize the distribution of extinction toward the region. The $(H-K)_{int}$ color is measured to be 0.2 mag using a nearby unextincted region ($\alpha_{(2000)} = 05^{\mathrm{h}}51^{\mathrm{m}}54^{\mathrm{s}}$, $\delta_{(2000)} = +28°01'54''$) of the sky from 2MASS catalog. The control field is chosen $\sim 1°$ away toward the north of S242. In an attempt to reduce the contribution from embedded young stars, only nonexcess infrared sources are used to generate the extinction map. The final extinction map has an angular resolution of $15''$ and is sensitive down to $A_V \sim 17.8$ mag. It is to be noted that the resolution and sensitivity of the map are a function of grid size and number of nearest neighbor sources used. To select the suitable grid size and number of nearest neighbor sources, we performed a series of iterations and found the grid size of $\sim 15''$ and nearest neighbor source ~ 20 are a good compromise between the sensitivity and signal-to-noise ratio of the extinction map. If the grid size is doubled ($30''$), the sensitivity dropped to $A_V \sim 1$ mag.

The variation of extinction (A_K) throughout the S242 region is shown in the Figure 3.5. The extinction shows a highly nonuniform structure throughout the region. In the map, three distinct and isolated extinction peaks are prominent. They are categorized into three subregions 'A', 'B' and 'C' and their zoomed-in distributions are shown in Figure 3.5. The subregion 'C' suffers with highest value of extinction $A_V = 17.2$ mag ($A_K = 1.5$ mag); (Cohen et al. 1981), while the subregion 'A' has a maximum extinction of $A_V = 16.1$ mag ($A_K = 1.4$ mag). The subregion 'B' shows a modest distribution of extinction, with a maximum value of $A_V = 7.4$ mag ($A_K = 0.7$ mag). Among the three extinction complexes, subregions 'A' and 'C' are the highly extincted regions. These two regions are supposed to be the dominant sites for the next generation star formation. Subregion 'B' is supposed to be relatively evolved or its association with molecular clouds is significantly less compared with 'A' and 'C'. Throughout the region

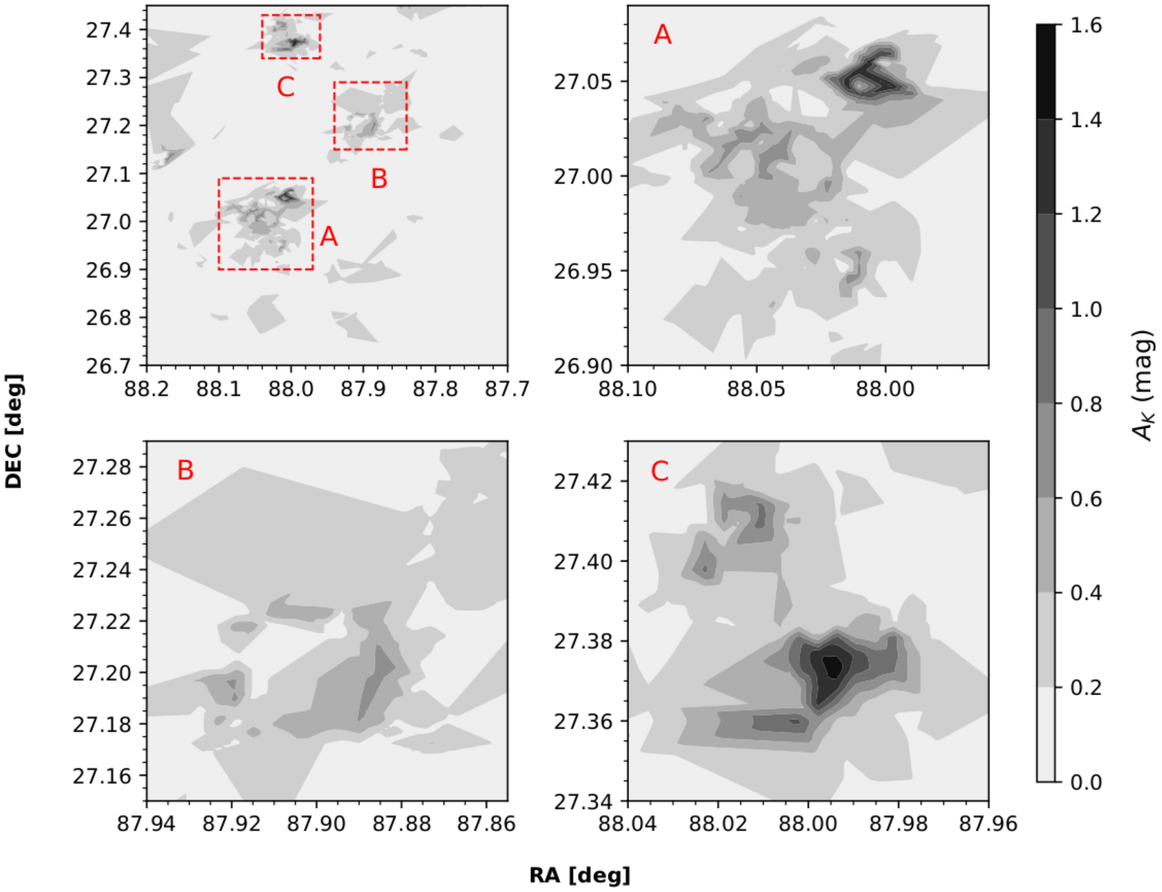

Figure 3.5: The K-band extinction map generated with $(H-K)$ colors from the 2MASS catalog. The color bar shows the variation of A_K for all the plots. The zoomed-in view of the three subregions (Section 3.3.3) is also shown.

the extinction varies from A_V = 1.3–17.2 mag (A_K = 0.1–1.5 mag), and the average value of extinction is A_V = 3.1 mag (A_K = 0.3 mag) with a standard deviation of A_V $\sim$ 0.8 mag (A_K $\sim$ 0.07 mag). Although, this analysis is limited by sensitivity of the 2MASS survey. The derived extinction can also be underestimated due to the lack of detection of a sufficient number of background stars in the heavily extincted areas.

3.3.4 Identification and Classification of the YSOs

The infrared color-color space analysis is a reasonable and standard method to identify and characterize the YSOs (Lada & Adams 1992). The YSOs show excess infrared emission due to the presence of circumstellar disks and envelopes and thus occupy certain locations in the infrared color-color diagrams. We used IRAC and JHK colors to classify the young sources toward the S242 region. We adopted the IRAC [3.6] and [4.5] μm along with the WIRCam H and K bands photometry to categorize the pre-main-sequence (PMS) populations using the methods described in Gutermuth et al. (2009). Though the infrared excess emission is an essential and powerful membership diagnostic for young and embedded sources, this method likely suffers from several potential contaminants. The dominant limitations arise from the extragalactic sources such as star-forming galaxies, narrow- and broad-line active galactic nuclei (AGNs), as well as polycyclic aromatic hydrocarbon (PAH) emission excited by young and high-mass stars (Gutermuth et al. 2008). We used JHK photometry from the WIRCam and the 2MASS catalog as an additional tool for further classification of sources that lack higher wavelength IRAC data. Since a majority of the Hα emitters toward H II regions are considered as classical T Tauri stars (CTTs; Meyer et al. 1997), due to the presence of hot and infalling gas accreting from circumstellar disks (Barentsen et al. 2011), we used the IPHAS photometry as an additional criteria to detect the young stars showing Hα emission.

Selection of YSOs from IRAC Data

Since the S242 region was observed during the *Spitzer* Warm Mission (Hora et al. 2012), this database is restricted to only the [3.6] and [4.5] μm bands. Hence, we used IRAC [3.6] and [4.5] μm along with WIRCam H and K photometry to effectively identify and classify the YSOs. The YSOs in an embedded star cluster suffer high spatially variable extinction due to the presence of natal molecular cloud clumps. We used dereddened IRAC and WIRCam colors by measuring the line-of sight extinction of each source, following the Gutermuth et al. (2009) classification scheme.

Field star contamination is removed by utilizing the extinction map generated earlier (Section 3.3.3). To compute the dereddened colors ($[[3.6]-[4.5]]_0$ and $[K-[3.6]]_0$) of each source, the extinction of the nearest grid from that source is taken into account. After removing the nonstellar contaminants, the YSOs are identified from the dereddened color-color space using the criteria given by Gutermuth et al. (2009). An additional brightness cut on the dereddened [3.6] μm photometry is applied to reduce the inclusion of dim extragalactic contaminants with Class II sources must have $[3.6]_0 < 14.5$ mag and Class I sources satisfy $[3.6]_0 < 15$ mag (Gutermuth et al. 2009). Thus a total of 27 Class I and 96 Class II sources stands out for the S242 region from the combined IRAC and WIRCam data. Figure 3.6 depicts the distribution of all those Class I (red squares) and Class II (blue triangles) sources in addition to nonexcess field stars (gray dots) in the dereddened color-color space. The reddening vector for $A_K = 2$ mag is also indicated in the diagram, adopting the color excess ratios from Flaherty et al. (2007).

Additional YSOs from WIRCam and 2MASS Photometry

We used infrared JHK photometry as an additional selection space to further distinguish the young objects enshrouded within the dust and cloud. Figure 3.7 shows the distribution of these added YSOs along with those identified in the previous section in the $(J-H)/(H-K)$ color-color diagram. This is an efficient method to distinguish the heavily reddened stars having intrinsic infrared excess from those showing normal

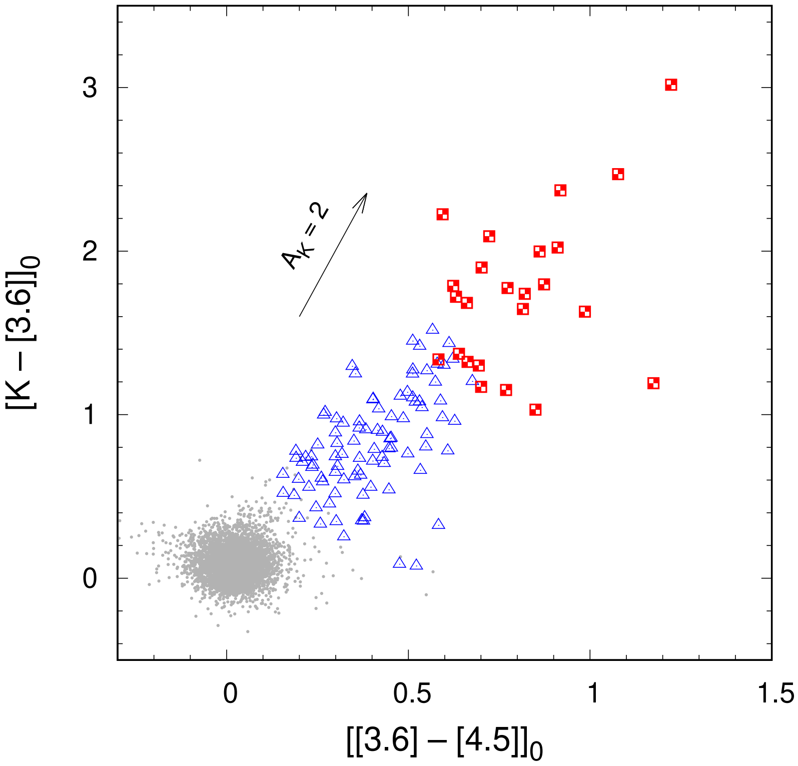

Figure 3.6: Classification of Class I and Class II sources from the dereddened color-color diagram using H, K, [3.6] μm, and [4.5] μm photometry, after removing the contaminants. Class I and Class II sources are represented by red squares and blue triangles, respectively. Reddening vector for $A_K = 2$ mag is indicated by the black arrow.

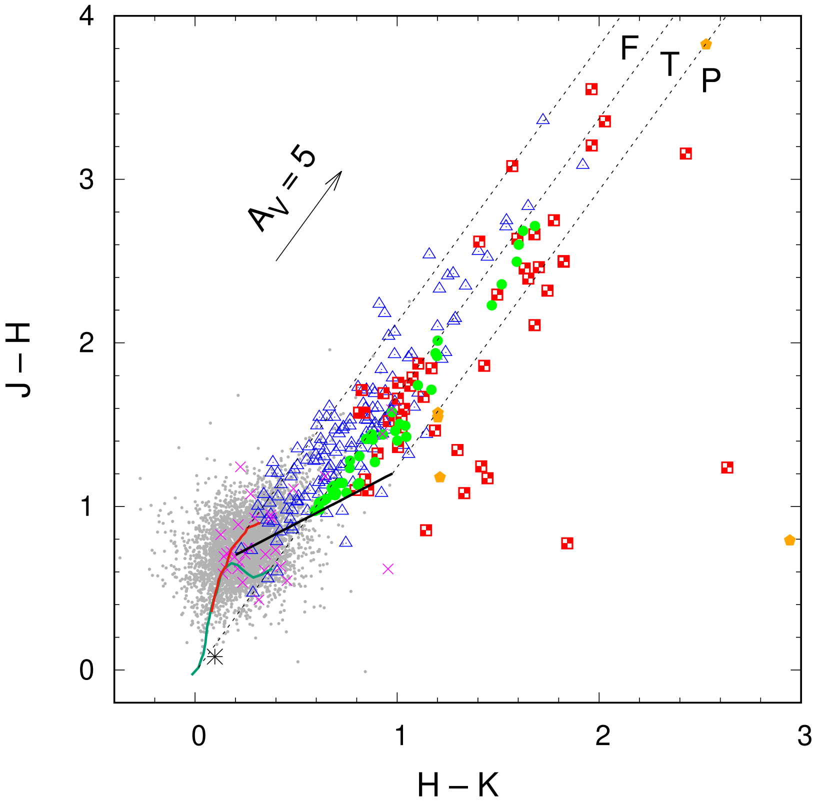

Figure 3.7: The distribution of YSOs in the near-infrared color-color diagram. The locus of points for unreddened dwarfs and giants are represented by solid green and red lines, respectively. The black solid line indicates the CTTs locus. Red and blue symbols are same as in Figure 3.6. The green circle and orange star symbols represent the additional YSOs selected from this diagram. The magenta crosses are the Hα emission line sources selected from IPHAS photometry (Section 3.3.5). The main exciting source BD+26 980 is indicated by a black star symbol and located toward the base of main-sequence locus.

unreddened photospheric colors (Lada & Adams 1992). The locus of points corresponding to unreddened main-sequence stars and giants is taken from Bessell & Brett (1988) and represented by green and red solid lines in Figure 3.7. The black solid line indicates the CTTs locus, taken from Meyer et al. (1997). All the photometric magnitudes are converted to the CIT (Elias et al. 1982) system using the relations from Carpenter (2001). The three parallel dashed lines show the reddening vectors (Lada & Adams 1992). The reddening laws ($A_J/A_V = 0.265$, $A_H/A_V = 0.155$, and $A_K/A_V = 0.090$) are taken from Cohen et al. (1981).

The near-infrared color-color space is divided into three regions, i.e. 'F', 'T' and 'P' (Lada & Adams 1992; Ojha et al. 2004). The sources located within the 'F' region are bounded by the reddening vectors drawn from the unreddened dwarf and giant branches. They have colors similar to normal stellar photospheric sources and are likely to be field stars (main-sequence stars or giants), weak-line T Tauri stars (WTTs), or Class III sources having no or less infrared excess. The ‘T’ region lies within the reddening vectors projected from main-sequence and CTTs loci. They are considered to be CTTs or Class II sources characterized by the presence of excess infrared emission. The ‘P’ region is located outward to the reddening vector drawn from the points of CTTs locus and the sources show color redder than those in ‘F’. These sources are most likely Class I objects and show large infrared excess emission due to the heated inner envelopes/atmospheres of the protostars. Although the usefulness of this method to precisely determine the nature of the YSOs is under certain potential limitations (Lada & Adams 1992).

Using the JHK photometry from WIRCam and 2MASS catalog, we have identified 9 Class I and 59 Class II sources toward S242, with given restrictions on photometric uncertainties < 0.1 mag. Among the 68 YSOs selected from $(J-H)/(H-K)$ color-color diagram, 21 sources are previously categorized from IRAC colors (Section 3.3.4). Effectively, we obtained 6 and 41 additional YSOs having colors consistent with Class I and Class II, respectively, using the JHK photometry. The S242 region is enriched with 33 Class I and 137 Class II young objects derived from the combined results of IRAC, WIRCam, and 2MASS photometry. The membership status of the YSOs is further confirmed with the inclusion of distance from the *Gaia* DR2 catalog. The distances of the young objects are derived from the available parallax measurements. The photometric and astrometric parameters of the selected YSOs are presented in the Table 3.6. While a total of 170 young sources are detected from the infrared photometry, only 28 sources (16.47%) are supplemented with distances available from the *Gaia* DR2. However we do not attempt to further distinguish the Class III objects from WTTs or field population from only this diagram, as this may lead to wrong interpretation (Andre & Montmerle 1994).

Table 3.6: Photometric catalog of the YSOs toward S242. This table is published in its entirety in the electronic edition of Panja et al. (2020)

Sl. No. (1)	R.A. (J2000) (deg) (2)	Decl. (J2000) (deg) (3)	g_{P1} (mag) (4)	y_{P1} (mag) (5)	J (mag) (6)	H (mag) (7)	K (mag) (8)	[3.6] μm (mag) (9)	[4.5] μm (mag) (10)	Distance (kpc) (11)
Class I sources										
1	88.050873	26.980659	22.056 ± 0.250	19.045 ± 0.058	17.158 ± 0.031	15.508 ± 0.024	14.647 ± 0.021	12.528 ± 0.054	11.882 ± 0.040	... ...
2	88.073463	26.780842	19.336 ± 0.003	15.986 ± 0.004	14.647 ± 0.043	17.198 ± 0.080	13.582 ± 0.044	13.373 ± 0.041	13.282 ± 0.036	2.203 ± 0.61
3	88.010284	27.060272	... ...	... ...	16.392 ± 0.026	13.475 ± 0.016	11.624 ± 0.026	9.793 ± 0.035	9.006 ± 0.038	... ...
4	88.039421	27.009676	... ...	... ...	18.336 ± 0.073	15.803 ± 0.024	14.082 ± 0.015	12.392 ± 0.060	11.394 ± 0.036	... ...
5	88.038254	26.996187	... ...	... ...	18.521 ± 0.097	15.922 ± 0.023	14.220 ± 0.014	12.907 ± 0.052	12.072 ± 0.049	... ...
6	88.049133	27.005104	... ...	... ...	... ...	... ...	12.476 ± 0.026	9.704 ± 0.066	8.823 ± 0.045	... ...
7	88.032936	26.980474	... ...	... ...	... ...	17.040 ± 0.055	14.757 ± 0.018	12.685 ± 0.056	11.795 ± 0.044	... ...
8	88.043716	26.989309	... ...	... ...	19.586 ± 0.222	16.177 ± 0.025	14.134 ± 0.016	12.317 ± 0.058	11.672 ± 0.042	... ...
9	88.054825	27.006817	... ...	... ...	... ...	17.245 ± 0.051	14.328 ± 0.025	11.924 ± 0.058	10.830 ± 0.024	... ...
10	88.047371	26.985704	... ...	... ...	17.574 ± 0.047	15.146 ± 0.021	13.583 ± 0.017	11.498 ± 0.087	10.573 ± 0.033	... ...

Notes:
(1) Serial Number of sources.
(2-3) Equatorial coordinates of sources in degrees.
(4-5) Photometric magnitudes and their errors from the Pan-STARRS 1 catalog (Chambers et al. 2016).
(6-8) Photometric catalog either from WIRCam (Puget et al. 2004) or 2MASS PSC (Skrutskie et al. 2006).
(9-10) Photometric catalog from *Spitzer* IRAC (Fazio et al. 2004).
(11) Distance of sources from the *Gaia* DR2 catalog (Gaia Collaboration et al. 2018).

Table 3.6: Continued

Sl. No. (1)	R.A. (J2000) (deg) (2)	Decl. (J2000) (deg) (3)	g_{P1} (mag) (4)	y_{P1} (mag) (5)	J (mag) (6)	H (mag) (7)	K (mag) (8)	[3.6] μm (mag) (9)	[4.5] μm (mag) (10)	Distance (kpc) (11)
Class II sources										
1	88.045395	27.021883	20.375	17.074	14.845	13.640	12.956	12.107	11.572	2.042
			± 0.012	± 0.110	± 0.015	± 0.014	± 0.016	± 0.044	± 0.038	± 0.88
2	87.967293	26.984737	20.695	16.880	15.073	13.977	13.394	12.775	12.441	1.158
			± 0.053	± 0.004	± 0.024	± 0.025	± 0.013	± 0.033	± 0.035	± 0.32
3	87.931961	27.002106	19.653	16.094	14.621	13.553	13.005	12.793	12.402	3.056
			± 0.016	± 0.004	± 0.021	± 0.025	± 0.014	± 0.035	± 0.030	± 1.35
4	87.992462	26.981787	21.939	16.875	15.129	13.876	13.461	12.808	12.487	...
			± 0.089	± 0.016	± 0.018	± 0.016	± 0.032	± 0.043	± 0.033	...
5	88.025650	27.058596	20.403	15.772	13.670	12.012	10.986	9.587	8.965	...
			± 0.026	± 0.009	± 0.017	± 0.028	± 0.020	± 0.035	± 0.030	...
6	88.002777	27.058050	...	...	19.031	16.116	14.505	13.586	13.262	...
			...	...	± 0.137	± 0.024	± 0.013	± 0.082	± 0.054	...
7	87.987411	27.070875	...	...	...	...	14.244	13.566	13.355	...
			...	...	...	...	± 0.020	± 0.063	± 0.048	...
8	88.108833	27.031178	21.635	17.130	15.486	14.388	13.939	13.365	13.016	2.306
			± 0.042	± 0.018	± 0.013	± 0.022	± 0.016	± 0.040	± 0.033	± 3.09
9	88.037003	27.015181	18.294	19.584	17.284	15.564	14.521	13.145	12.612	...
			± 0.008	± 0.127	± 0.041	± 0.023	± 0.028	± 0.062	± 0.045	...
10	88.006538	26.959366	21.216	16.795	15.346	14.053	13.284	12.506	12.256	1.685
			± 0.043	± 0.040	± 0.019	± 0.032	± 0.012	± 0.047	± 0.036	± 0.82

3.3.5 Hα Emitting Sources from Slitless Spectroscopy and IPHAS Photometry

Using the slitless spectroscopic data from the HCT, we have visually identified a total of three sources that show counterparts in Hα emission. All the three sources are depicted as blue crosses in the color-color diagram (Figure 3.8) and are also detected from IPHAS photometry. No extra sources are found from the slitless spectroscopy.

The IPHAS survey provides photometry of fainter emission line objects up to r = 20.5, and i and Hα = 19.5 mag with photometric uncertainty limited to 0.1 mag (Barentsen et al. 2014). Figure 3.8 shows the ($r - i/r-$Hα) color-color diagram for the sources detected in the IPHAS catalog toward the S242 region. The solid and dashed blue lines represent the unreddened main-sequence and the expected position of unreddened main-sequence stars with Hα emission line strengths of equivalent width (EW) = -10 Å. The nearly vertical solid black and green lines show the trend for an unreddened Rayleigh-Jeans continuum and an unreddened optically thick disk continuum (Barentsen et al. 2014), respectively. Whereas the black broken lines are predicted lines of constant net emission EW. The reliable sources are selected by applying the quality criteria of r $<$ 20 mag and photometric uncertainty $<$ 0.1 mag in all three bands in IPHAS DR2. A total of 36 Hα emission line stars is selected as lying above the dashed blue line at the level of 3σ, i.e. the distance between the selected objects and the dashed blue line is larger than three times the average uncertainty in their ($r-$Hα) color (Barentsen et al. 2014). These candidate Hα emitters are represented by magenta boxes in the color-color diagram. The majority of the Hα emitters toward a H II region are likely to be CTTs (Barentsen et al. 2011; 2014). Among the 36 Hα emitting objects, 5 sources show infrared counterparts and are classified as Class II sources either from IRAC or JHK colors. The photometric catalog of the Hα emitting sources is detailed in Table 3.7.

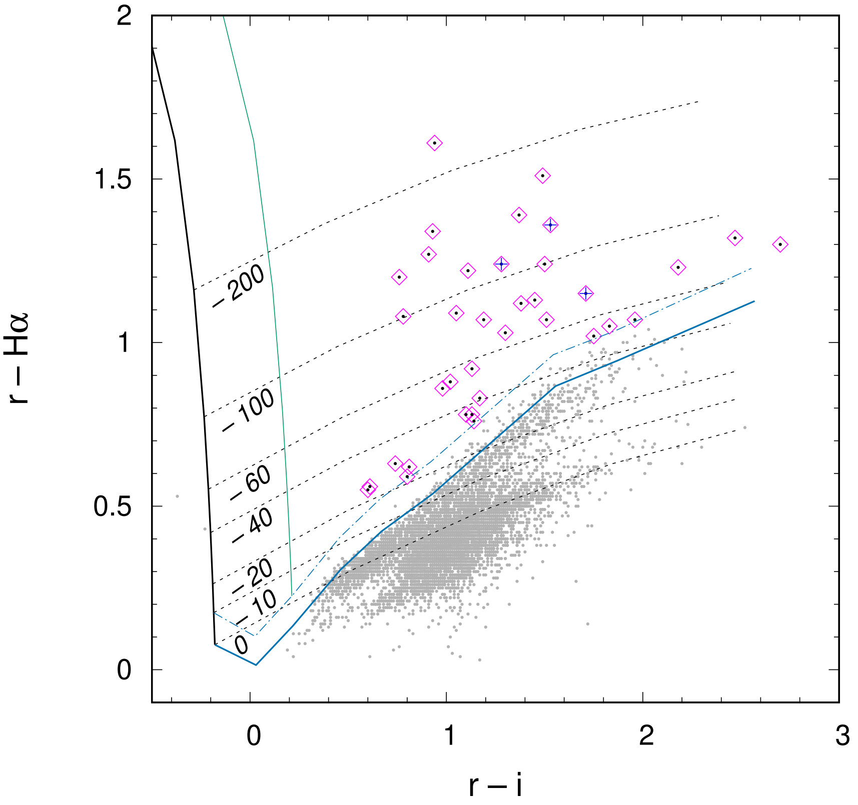

Figure 3.8: The sources detected in IPHAS photometry are shown in the color-color diagram. Blue crosses are the sources detected from slitless spectroscopy and magenta boxes are those selected from IPHAS photometry, with prominent Hα emission. Sources with no significant Hα emission lines are depicted as gray dots.

Table 3.7: Photometric catalog of Hα emitters toward S242. The entire catalog is available in the electronic version of Panja et al. (2020)

Sl. No. (1)	R.A. (J2000) (deg) (2)	Decl. (J2000) (deg) (3)	r (mag) (4)	i (mag) (5)	Hα (mag) (6)	J (mag) (7)	H (mag) (8)	K (mag) (9)	Distance (pc) (10)	Class I/ Class II (11)
1	88.006538	26.959366	18.95 ± 0.04	17.67 ± 0.02	17.71 ± 0.02	17.284 ± 0.183	16.328 ± 0.185	15.913 ± 0.224	1685 ± 821	II
2	87.985306	27.042868	19.55 ± 0.05	18.79 ± 0.05	18.35 ± 0.03	16.081 ± 0.069	15.362 ± 0.088	14.977 ± 0.101	1221 ± 1492	...
3	87.969727	27.047367	18.71 ± 0.03	17.69 ± 0.02	17.83 ± 0.02	15.342 ± 0.031	14.494 ± 0.041	14.336 ± 0.056	...	...
4	88.241554	26.771357	19.54 ± 0.06	18.37 ± 0.03	18.71 ± 0.04	16.507 ± 0.104	15.885 ± 0.122	14.876 ± 999	1655 ± 1312	...
5	87.995338	27.029369	18.36 ± 0.02	16.98 ± 0.01	17.24 ± 0.02	16.604 ± 0.100	15.755 ± 0.116	15.670 ± 0.178	735 ± 86	...
6	88.108833	27.031178	19.75 ± 0.08	18.04 ± 0.03	18.60 ± 0.04	16.464 ± 0.103	15.825 ± 0.132	15.363 ± 0.134	2306 ± 3092	II
7	87.974434	27.011446	19.50 ± 0.05	18.45 ± 0.03	18.41 ± 0.03	16.380 ± 0.080	15.835 ± 0.128	15.340 ± 0.131	...	...
8	87.983055	27.051373	19.70 ± 0.07	18.57 ± 0.04	18.92 ± 0.06	15.552 ± 0.057	14.436 ± 0.049	14.126 ± 0.048	730 ± 363	...
9	87.978638	27.010542	19.13 ± 0.04	18.15 ± 0.03	18.27 ± 0.03	15.308 ± 0.039	14.588 ± 0.051	14.306 ± 0.058	...	...
10	87.997849	27.016195	19.14 ± 0.05	17.77 ± 0.02	17.75 ± 0.02	16.124 ± 0.066	15.362 ± 0.080	15.064 ± 0.102	...	...

Notes:
(1) Serial Number of sources.
(2-3) Equatorial coordinates of sources in degrees.
(4-6) Photometric magnitudes and their errors from the IPHAS DR2 source catalog (Barentsen et al. 2014).
(7-9) Photometric catalog either from WIRCam (Puget et al. 2004) or 2MASS PSC (Skrutskie et al. 2006).
(10) Distance of sources from the *Gaia* DR2 catalog (Gaia Collaboration et al. 2018).
(11) Type of class

3.4 Discussion

3.4.1 Spectral Nature of the YSOs

The near-infrared color-magnitude ($H-K$ versus K) space serves as a practical tool to estimate the spectral nature of YSOs by incorporating their distribution in the diagram. Figure 3.9 depicts the YSOs identified from the WIRCam, 2MASS, and IRAC catalogs; Hα emitters from the IPHAS photometry, and field population distribution, respectively. The locus of ZAMS (Pecaut & Mamajek 2013), reddened by A_V = 0, 5, 10, 20, and 30 mag and corrected for the cluster distance of 2.08 kpc (taken from Table 3.4) are represented by nearly vertical lines. The slanting horizontal lines are the reddening vectors corresponding to different spectral types. All the symbols in the figure are same as in Figure 3.7. From the diagram, it is apparent that the YSOs show a large variation in spectral type from K6 to B0, with a majority concentrated within G0 to B2. The main illuminating source (BD+26 980) is located toward the reddening vector corresponding to B0 spectral type, as marked by a black star symbol. Earlier the spectral nature of this star was mentioned as B0 V, which is quite consistent with our results, and the spectroscopic analysis also reveals it as a B0.5 V (Panja et al. 2019) type star. It is prominent that a reasonable amount of YSOs suffer large reddening of about 20 to 30 mag, possibly caused due to the presence of dusty circumstellar envelopes and gaseous environments. So, S242 is a rich stellar cluster, evolving with considerable number of young members and showing wide span in their spectral variation. The gray dots, representing the sources having no or less infrared excess emission, are primarily field population. A majority of them are concentrated within $(H-K) < 0.6$ mag.

3.4.2 Average Age of the YSOs

We used Pan-STARRS 1 photometry to diagnose the age spread of the YSOs within the S242 region. Since our observed optical data are not deep enough to detect most of the young sources, we used Pan-STARRS 1 photometry. The magnitude depth of the observed optical photometry is down to $V \sim 19.4$ mag, whereas Pan-STARRS 1 provides photometry deeper down to $\mathrm{g_{P1}} \sim 22.5$ mag and $\mathrm{y_{P1}} \sim 20.2$ mag for this region. The distribution of YSOs and Hα emitting sources in the ($\mathrm{g_{P1}}-\mathrm{y_{P1}}$) versus $\mathrm{g_{P1}}$ color-magnitude diagram is shown in Figure 3.10. The ZAMS and PMS isochrones from Marigo et al. (2017), corrected for the cluster distance of 2.08 kpc, reddening $E(B-V) = 0.56$ mag (taken from Table 3.4), and $E(g_{\mathrm{P1}}-y_{\mathrm{P1}}) = 1.26$ mag (Schlafly et al. 2016) are overplotted. The evolutionary tracks for various masses are also shown to characterize the mass spectrum of the YSOs. A notable scatter in the age distribution of the YSO population is observed in Figure 3.10. The ages vary between 0.1 Myr and 10 Myr, with a majority indicating an age around 1 Myr. However, our age determination method can be subject to a few limitations: the use of different PMS evolutionary models can yield different ages (Sung et al. 2000), the presence of variable extinction, binaries, and variables may also introduce systematic errors (Herbst et al. 1994; Herbst & Shevchenko 1999). We ascertained an average age of the YSOs as 1 Myr. Most of the

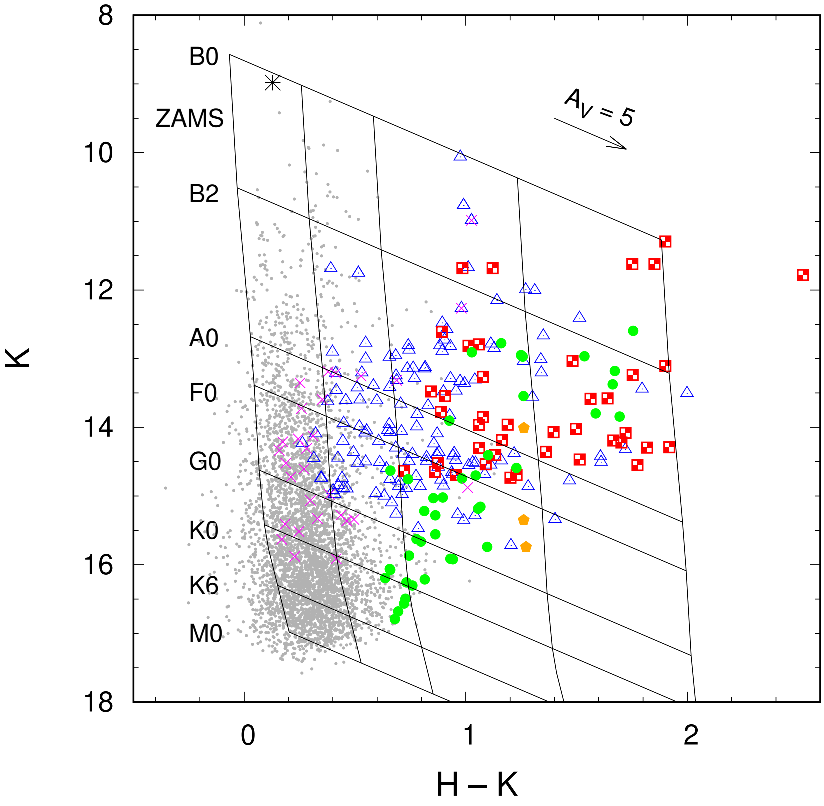

Figure 3.9: The distribution of YSOs selected from infrared catalogs, Hα emitters from IPHAS photometry, and field population toward S242. The nearly vertical lines are the loci of ZAMS (Pecaut & Mamajek 2013) with visual extinction A_V = 0, 5, 10, 20, and 30 mag and shifted for the cluster distance of 2.08 kpc. The slanting horizontal lines represent the reddening vectors corresponding to different spectral types. The symbols used in this figure are the same as in Figure 3.7.

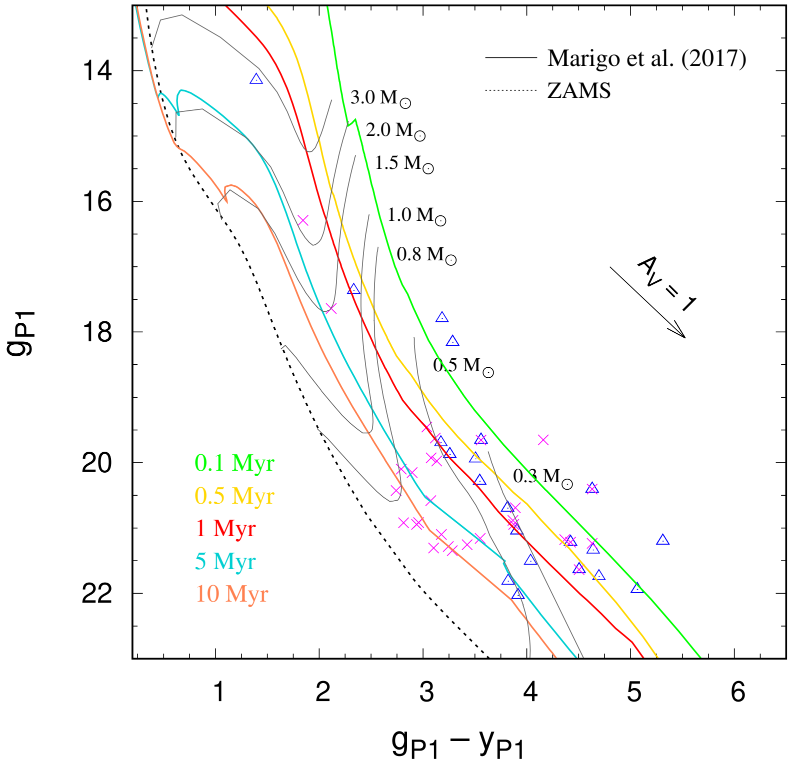

Figure 3.10: Color-magnitude diagram showing the distribution of YSOs and Hα emitting sources from the Pan-STARRS 1 catalog. The ZAMS and PMS isochrones for ages 0.1, 0.5, 1, 5, and 10 Myr are taken from Marigo et al. (2017). The evolutionary tracks for different masses are also shown. All the isochrones and tracks are corrected for a distance of 2.08 kpc and reddening $E(B-V) = 0.56$ mag. The source symbols are the same as in Figure 3.7.

Hα emitting sources are relatively evolved compared to the YSOs, as seen from their distribution in the color-magnitude diagram. As a larger fraction of the low-mass YSOs lack the reliable photometry, this diagram cannot be used as a suitable tool to estimate mass ranges of the region.

3.4.3 Mass Distribution of the YSOs

We used the near-infrared color-magnitude ($J-H$ versus J) diagram to estimate the mass ranges of candidate YSOs toward the S242 region. Since the YSOs show excess emission at longer wavelengths, we used ($J-H$) versus J diagram in an attempt to reduce the effect of excess emission (Ojha et al. 2004; 2011). The near-infrared color-magnitude diagrams allow us to manipulate two fundamental parameters of a cluster, the distance and reddening. The change in distance shifts the isochrones vertically, while the parallel slanting lines trace the reddening zones for each extincted mass vector.

Masses are estimated by comparing the distribution of young objects with theoretical PMS isochrones in the diagram. In Figure 3.11, the blue solid line presents the loci of ZAMS taken from Girardi et al. (2002) and shifted for the cluster distance of 2.08 kpc. The evolutionary models of PMS isochrones of age 0.1, 1, and 10 Myr are taken from Marigo et al. (2017) and indicated by green, black, and red solid lines. The black dashed lines are the reddening vectors corresponding to different mass tracks, respectively. We used the same symbols as in Figure 3.7 to represent the YSOs identified from infrared color-color diagrams and Hα emitters from IPHAS photometry. We used an average age of 1 Myr (Section 3.4.2) to estimate the mass ranges of YSOs. The YSOs show a wide range of variation in their masses with a majority having masses between 0.1 and 3.0 $M_\odot$, as indicated in the figure. It is also observed that the YSOs show larger variation in their color, probably an indication of the combined effect of spatially variable extinction and a weak contribution of excess emission in the J and H bands (Ojha et al. 2011). Few of the candidate YSOs are seen to be more massive (> 3.0 $M_\odot$) and also located in highly extincted ($A_V \sim$ 10-30 mag) regions. It is to be noted that estimating the stellar masses from the infrared color-magnitude diagrams relies on uncertain ages and different distances to the objects. The ambiguity is even more severe among the massive members (early B-type stars). Because the stellar mass can vary significantly when estimated from a 1 Myr PMS isochrone compared to the main-sequence isochrones of a younger age. Therefore, estimating the parameters for the massive members is difficult. Also, there can be several other causes which put constraints on this method, such as the use of separate PMS isochrones, binarity, and variable extinction (Hillenbrand et al. 2008).

3.4.4 Spatial Distribution of the PMS Population

The spatial variation of the embedded young stellar population is a footprint of how star formation has progressed throughout space and time in a given region. Figure 3.12 manifests the distribution of Class I (red circles), Class II (blue triangles), and Hα emission line (green boxes) sources, overlaid on the *WISE W1* 3.4 μm mosaic image. The location of the main ionizing star BD+26 980 is marked by a black star symbol. The FOV of DFOT optical ($18' \times 18'$), WIRCam near-infrared ($29' \times 26'$), and other archival photometric catalogs (2MASS, *Spitzer*, *Gaia* DR2, IPHAS) for a radius of $25'$ are indicated in the figure. A noticeable number of the PMS populations are preferentially concentrated around the central core region. A majority of the YSOs are seen to be spatially aligned along an elongated filamentary structure (EFS). From the distribution of young stellar candidates, the spatial extent of the elongated structure is estimated as $\sim 43'$ (26 pc). Using the ^{13}CO molecular line data, Dewangan et al. (2017) also reported the presence of an EFS of length $\sim$ 25 pc and average width $\sim$ 1.3 pc. A significant number of the Class I sources have formed two discrete groups, one at the central region and another at the northern end of the long scale structure. While Class II type sources also show a similar grouping as Class I sources along with a nice positional coincidence with the long scale feature. The three peak extinction complexes, marked by 'A', 'B' and 'C' (see Section 3.3.3 for details) are shown by red dashed boxes in the diagram.

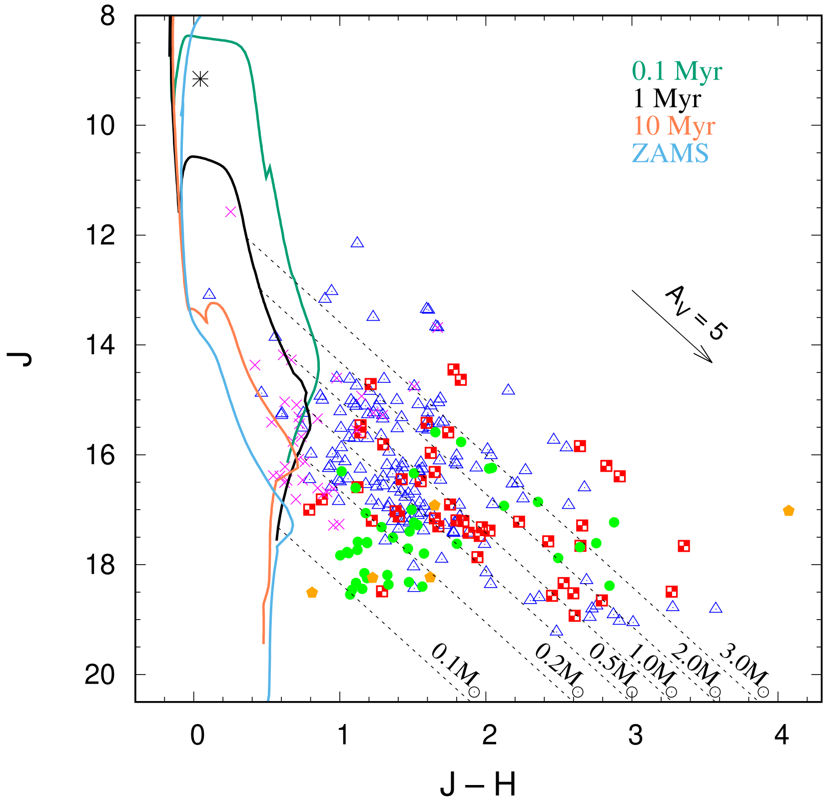

Figure 3.11: The mass spectrum of the YSOs toward S242 is shown in the color-magnitude diagram. The locus of ZAMS (Girardi et al. 2002) and PMS isochrones of ages 0.1 Myr, 1 Myr, and 10 Myr (Marigo et al. 2017) are indicated by blue, green, black, and red solid lines, respectively. The reddening vectors corresponding to different mass values are represented by black dashed lines. All other symbols are the same as in Figure 3.7.

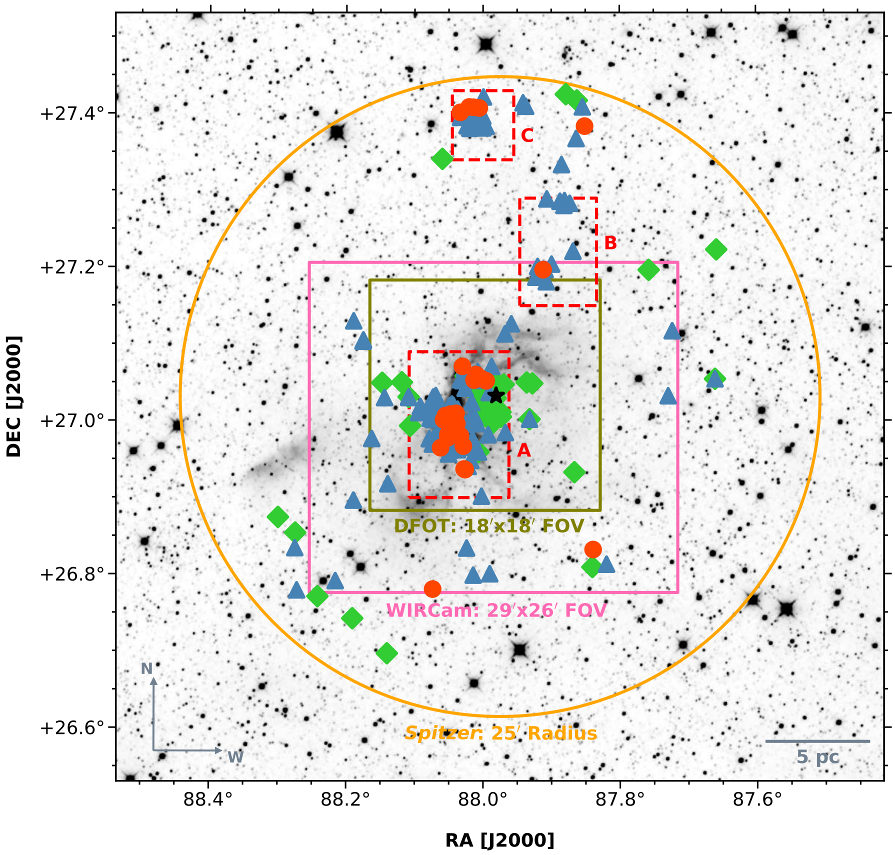

Figure 3.12: Spatial distribution of the PMS sources, overplotted on the *WISE W1* 3.4 μm mosaic image. The Class I, Class II, and Hα emitting sources are represented by red circles, blue triangles, and green boxes, respectively. The main ionizing source BD+26 980 is represented by a black star symbol. The FOV for different observed and archival catalogs (see Section 3.4.4 for details) are indicated.

The prominent clustering of the young populations nicely match the extinction complexes. The spatial distribution of YSOs along the filamentary-like extinction structure indicates that ongoing star formation is likely occurring toward the cluster.

The number of YSOs in each class is useful to estimate the relative age of the subregions in a young complex (Hatchell et al. 2007; Gutermuth et al. 2009; Saral et al. 2015). We used the ratio of number of Class I sources to the number of Class II sources to interpret the evolutionary status of the star-forming region. Since Class I objects represent the earlier phase of star formation compared to Class II sources, the Class I/II ratio serves as a proxy to estimate the relative age of the subregions (Chavarría et al. 2008). The ratio of Class I/II for the subregions ‘A’ and ‘C’ are obtained as 0.31 in both the cases. Whereas, for subregion ‘B’, the ratio is quite low: 0.08. Using a mid-infrared survey of 36 young and active star-forming clusters, Gutermuth et al. (2009) estimated the median ratio of Class I/II to be 0.27. For the overall S242 region, the ratio is obtained as $\sim$ 0.25, which is in close proximity to the value derived by Gutermuth et al. (2009). Studying a nearby star forming complex, Chavarría et al. (2008) has shown the ratio of Class I/II to vary between 0.31 and 0.78. Beerer et al. (2010) presented the Class I/II ratio to range from 0.05 to 0.78 for 13 young clusters. Jose et al. (2013) evaluated the ratio to vary between 0.13 and 0.54 for the different subregions of a large H II region. The Class I/II ratio is a function of the evolutionary stage of the complex, where the higher ratio indicates a younger cluster (Chavarría et al. 2008; Beerer et al. 2010). The ratio of Class I/II suggests that the subregions 'A' and 'C' are the locations of the youngest population for the region and the sources in these groups are evolving almost on a similar timescale. In general, it is predicted from the spatial distribution of the YSOs and the Class I/II ratio that the S242 region is in its early stage of star formation. Comparing the ratio of Class I/II with the earlier reports (Chavarría et al. 2008; Beerer et al. 2010; Jose et al. 2013; Saral et al. 2017), the average age of the young members in the S242 region is estimated around 1 Myr. Although, as the subregions 'A' and 'C' suffer the highest extinction, it may cause undercounting due to the undetectable background stars. Also limitations may occur with distance of the sources and detection sensitivity of the instruments.

3.5 Summary

In this work, we report a multiwavelength survey of the stellar content and its characterization toward the S242 region, using combined observed and archival data sets. The key results are summarized as follows:

1. The slit spectroscopic results confirm classification of the main ionizing source BD+26 980 as a massive and early-type (B0.5 V) star of the region. The spectrophotometric distance of the star is estimated as 2.08 ± 0.24 kpc, validating its membership with the region. *Gaia* DR2 also provides a similar distance (2.08 ± 0.19 kpc) for the star. The rest of the spectroscopically observed sources are late-type (either G or K) foreground or background stars.

2. The K-band extinction map is generated using a nearest neighborhood technique and the average extinction within the region is estimated as $A_V \sim 3.1$ mag. From the extinction map (diameter $\sim 50'$), three distinct extinction peaks are identified toward the region and their corresponding consequences are discussed.

3. Using the infrared color excess from the combined photometry of WIRCam, 2MASS, and *Spitzer*, a total of 33 Class I and 137 Class II objects are detected within the selected area. Thus the S242 region appears as a prominent star-forming region, where a significant number of young stellar populations are forming and evolving together.

4. The Hα emission line objects are detected from IPHAS photometry and slitless spectroscopic observations. We have identified 36 Hα emitting sources, which are bonafide young objects toward the S242 region.

5. Using parallaxes from the *Gaia* DR2 catalog, the membership status of the classified young population is revealed.

6. Using the Pan-STARRS 1 deep photometry, an average age of the YSOs is estimated as 1 Myr toward the region. From the infrared color-magnitude diagram, the masses of the young populations are found to vary between 0.1 and 3.0 $M_\odot$.

7. The cospatial distribution of the young stellar population and the filamentary-like extinction structure is an indication of recent star formation activity within the region. An EFS of length $\sim$ 25 pc is estimated from the projected distribution of the PMS sources. The relatively high fraction ($\sim$ 0.25) of Class I to Class II objects suggests that the YSO population is in a very early stage ($\sim$ 1 Myr) of evolution.

Chapter 4

Star and Cluster Formation in the Sh2-112 Filamentary Cloud Complex: Stellar Contents and Feedback Mechanisms

4.1 Introduction

Most and perhaps all stars form in clustered environments out of molecular clouds. Subsequent internal gravitational dynamics inside a giant molecular cloud prompts cloud fragmentation, with each fragment then collapsing and leading to the onset of bound prestellar core formation (André et al. 2016). Alternatively, propagation of the ionizing or explosive shocks from nearby massive stars may compress accompanying clouds, hence triggering the next epoch of star formation (Elmegreen 1998; Deharveng et al. 2005). Molecular clouds exhibit complex geometries, including smaller substructures such as sheets and filaments to elongated networks (Evans & Lada 1991; Falgarone et al. 1991; Elmegreen 1993; Myers 2009). The turbulence from expanding H II regions near a filamentary molecular cloud can generate sequential waves of star-forming cores along the long axis of the filament on either side of an H II region (Fukuda & Hanawa 2000). As the ionization front moves through the cloud, it sweeps up neutral gas, potentially increasing the star formation rate in the dense shell (Elmegreen & Lada 1977). The young protostars are preferentially tied along the filamentary axis, bearing the imprint of fragmentation of the primordial cloud.

The optically visible H II region Sh2-112 (hereafter S112, $l = 83^{\circ}\!.7589$; $b = +03^{\circ}\!.2750$, J2000), located at a distance of $\sim 2.1\,\mathrm{kpc}$ (Blitz et al. 1982) toward the rich region of the Orion arm, is physically associated with one of the most active nebulous systems of Cygnus X. Illuminated by a massive source BD+45 3216 of spectral type O8 V (Lahulla 1985), probably a double or multiple system, the region shows a circular morphology. The surrounding ionized region created by the massive star could be a possible outcome of a triggering effect and hence an efficient site for next generation star formation, given its distinct blister shaped distribution (Israel 1978). The evidence of molecular cloud association with this complex is been long established in the literature, by measurements of several cloud parameters, e.g., radial velocity ($V_{CO} = -4.0 \pm 2.0\,\mathrm{km\,s^{-1}}$; Blitz et al. 1982), ^{13}CO cloud mass (1880 $M_{\odot}$; Dobashi et al. 1994), Hα and infrared luminosities (Hunter & Massey 1990), strength of radio recombination lines (Garay & Rodriguez 1983), etc. So far, the studies have been focused considering an optical diameter of 15′, but S112 is not an isolated region. Rather, we found, the existence of accompanying dust structures spanning around 2° along the Galactic longitude, and a detectable filamentary pattern connecting all the sub-structures, keeping S112 roughly in the central location. In this context we aim to diagnose the star-forming activity via a comprehensive sample of the young stellar population plus detailed characterization of the associated molecular and ionized gas on a larger scale than previously reported in the literature.

The chapter is organized as per given order. Following the observations and data reduction techniques in Section 4.2, the dust structures across the region are studied by generating the extinction map, in Section 4.3, leading to identification and characterization of the young stellar population. Selection of the Hα emitters, as a significant fraction of them is considered to be a part of the ongoing protostellar activity, and the spatial distribution of the young objects in correspondence to the radio emission, are included in this Section. The presence of massive stars can have significant influence on their outskirts. if the nearby regions comprise molecular clouds. In Section 4.4, the properties of the massive stars from spectroscopic perspective and the ionized gas using radio continuum emission are studied. In relevance with that the possible feedback mechanisms are discussed. A large-scale ($\sim 2°$) filamentary like structure, hosting multiple dense clumps, is detected, for which we investigate the molecular cloud parameters and kinematics using the CO emission lines in Section 4.5. Thus an overall star formation census in this complex, from parental cloud distribution to protostellar formation and their evolution is interpreted. Finally, we present a concise summary of main results in Section 4.6.

4.2 Data Acquisition and Reduction

Diagnosing the stellar contents in a young complex is tricky, as in the initial phases the series of events showing diverse phenomena occur in a relatively short time-period ($\sim$ 5 Myr) and therefore require a broad wavelength coverage. The optical photometric data allow us to identify the Hα emitters and through the spectroscopic analysis the massive members are detected that can contribute significantly in the ionization activity. The protostellar candidates and the interstellar extinction are studied using the infrared photometric datasets, whereas the interlinked dust and cloud components are traced by utilizing the radio maps. A brief description of each of these data sets is given as follows.

4.2.1 Observational Data

HCT: Optical slit spectroscopic observations toward S112 are carried out using the Himalaya Faint Object Spectrograph and Camera mounted on the 2 m Himalayan Chandra Telescope (HCT). The Grism 7 (380–684 nm) with a resolution of 1330 is chosen to obtain the spectra, as the wavelength range covers the detection of important emission/absorption features from the massive stars. After being rectified by the bias subtraction and cosmic ray correction, the monodimensional spectra are extracted using the APALL task in the IRAF software. The spectra are wavelength calibrated by using the FeAr arc lamp observations and then flux calibrated from the standard star (Oke 1990) observations. The data are also corrected for the atmospheric extinction and instrument sensitivity availing the standard star observations.

PMO: The molecular line data for the three CO (^{12}CO, ^{13}CO, and C^{18}O) J=1–0 isotopologues are obtained from the Milky Way Imaging Scroll Painting (MWISP) project (Su et al. 2019). This ongoing project with an expected time span of more than ten years (2011–2022) provides large scale CO maps of the northern Galactic plane ($-10^\circ < \ell < +250^\circ$ and $|b| \lesssim 5\overset{\circ}{.}2$) with a planned sky coverage of $\sim$ 2600 deg^2. The observations are carried out by a 13.7 m diameter single-dish millimeter-wavelength telescope at the Purple Mountain Observatory (PMO) in Delingha, China. The MWISP survey provides high-quality mapping, with uniform sensitivity and moderate resolution ($\sim$ 50$''$), aimed to feature high spatially dynamic range. A multibeam sideband-separating Superconducting Spectroscopic Array Receiver system with an instantaneous bandwidth of 1 GHz is employed for simultaneous observations. The typical system temperatures are $\sim$ 250 K for ^{12}CO at the upper sideband, and $\sim$ 140 K for ^{13}CO and C^{18}O at the lower sideband, respectively. The observations are made in position-switch On-The-Fly mode with a sampling interval of 10$''$–15$''$. The rms noise levels are $\sim$ 0.5 K for ^{12}CO at the velocity resolution of 0.16 km s^{-1} and $\sim$ 0.3 K for ^{13}CO and C^{18}O at 0.17 km s^{-1}. Finally the raw data are resampled with a grid spacing of 30$''$ and mosaicked into FITS cubes using the GILDAS (Gildas Team 2013) software.

4.2.2 Archival Data

Gaia DR2: The *Gaia* Data Release 2 (*Gaia* DR2; Gaia Collaboration et al. 2018) contains homogeneous astrometry on five parameters (celestial coordinates, trigonometric parallaxes, and proper motions) for more than 1.3 billion objects, supplemented with photometry of three broad-band magnitudes in G (330–1050 nm), G_{BP} (330–680 nm), and G_{RP} (630–1050 nm) with unprecedented accuracy. We adopted the distances computed by Bailer-Jones et al. (2018), which provides empirically better estimate of distances for all the stars with parallaxes published in the *Gaia* DR2, using a probabilistic inference approach, by taking into account for the nonlinearity of the transformation and the positivity constraint of distance.

IPHAS: The Isaac Newton Telescope (INT) Photometric Hα Survey of the Northern Galactic Plane (IPHAS; Drew et al. 2005) is an imaging survey covering an 1800 deg^2 sky in broadband Sloan r (624 nm) and i (774.3 nm), and narrowband Hα (656.8 nm) filters. The camera generates a mosaic of four CCDs at a pixel scale of $0\farcs33$ pixel^{-1}. This survey offers an unique facility to detect Hα emission line objects by comprehensive CCD photometry of point sources at visible wavelengths.

2MASS: The Two Micron All Sky Survey (2MASS; Skrutskie et al. 2006) collected imaging data covering the entire celestial sphere in the near-infrared J (1.25 μm), H (1.65 μm), and K (2.16 μm) bandpasses with a pixel size of $2\farcs0$. The 2MASS Point Source Catalog has a 10σ detection level at $J \simeq 15.8$, $H \simeq 15.1$, and $K \simeq 14.3$ mag. For our work the photometric error for each of the three 2MASS bands is restricted within 0.1 mag as a quality criteria to get a signal-to-noise ratio $\gtrsim 10$.

WISE: The *Wide-field Infrared Survey Explorer* (*WISE*; Wright et al. 2010) has scanned the entire sky in four wavebands (3.4, 4.6, 12, and 22 μm) with an angular resolution of $6\farcs1$, $6\farcs4$, $6\farcs5$, and $12\farcs0$, respectively. The 3.4 μm and 12 μm filters detect prominent polycyclic aromatic hydrocarbon features, the 4.6 μm filter measures the continuum emission from very small grains, and the 22 μm filter finds both stochastic emission from small grains and the Wien tail of thermal emission from large grains (Wright et al. 2010). To ensure the good quality photometry, we considered only those sources which have magnitude uncertainties $\lesssim 0.2$ mag.

AKARI: The AKARI (Murakami et al. 2007) survey covers about 90% of the sky in four far-infrared photometric bands centred at 65, 90, 140, and 160 μm, with spatial resolutions ranging from $1'$ to $1\farcm5$. The detection limit of the four bands reaches 2.5–16 MJy sr^{-1} with relative accuracy of $< 20\%$. These data provide crucial information on the investigation and characterisation of the properties of dusty material in the interstellar medium, since a significant portion of its energy is emitted between $\sim$50 and 200 μm (Doi et al. 2015).

NVSS: The National Radio Astronomy Observatory (NRAO) Very Large Array (VLA) Sky Survey (NVSS; Condon et al. 1998) covers the northern sky (82% of the celestial sphere) at 1.4 GHz (21 cm) with $\sim 45''$ (FWHM) imaging resolution and nearly uniform sensitivity. The radio continuum maps (Stokes I) at 1.4 GHz (beam size $\sim 45''$) are extracted from the NVSS archive to trace the ionized emission.

Planck: The *Planck* space mission measures the anisotropy of the cosmic microwave background in nine frequency bands covering 30–857 GHz with angular resolution ranging from $31'$ to $5'$ (Planck Collaboration et al. 2016). With its high sensitivity and wide wavelength coverage, *Planck* provides all-sky maps of the thermal dust emission and, in particular, of the emission arising from cold dust, which is mainly associated with dense regions within molecular clouds, and is relevant for studies of the early phases of star formation.

4.3 Dust Distribution and YSOs

The YSOs in the region are identified and characterized by their infrared colors. The Hα stars are recognized by their excessive flux in the Hα filter relative to that in the short-red (as continuum) filter. Notwithstanding the possibility of red dwarfs with active chromospheric activity, an Hα sample seen against a star-forming region is dominated by PMS stars. The spatial distribution of YSO population at different evolutionary stages is then correlated with the dust distribution, estimated by the level of extinction of background stars, to infer the starbirth sequence, as discussed below.

4.3.1 The Extinction Map

The dust distribution across the region is traced by measuring the extinction of background starlight produced by the cloud. We utilized the 2MASS H- and K-band photometry, and constructed a stellar number density image by defining a spatial grid over the target area (Gutermuth et al. 2005). First, the region of our interest is subdivided into rectilinear grids, each of a size of $15'' \times 15''$. The 20 nearest-neighbor sources from the center of each grid are selected to calculate the mean and standard deviation of the $(H-K)$ color for each grid, excluding the sources for which the $(H-K)$ values deviated $\gtrsim 3\sigma$ from the mean value (Panja et al. 2021). The mean $(H-K)$ color for each grid is then converted to A_K, using the reddening law $A_K = 1.82 \times [(H-K)_{\rm obs} - (H-K)_{\rm int}]$, the difference between the observed and the intrinsic color (Flaherty et al. 2007).

The average intrinsic color $(H-K)_{\rm int}$ of the background population is measured to be ~ 0.2 mag, by using a nearby control field with nominal extinction ($A_V \simeq 1.3$ mag). To ensure a "clean" background sample, we have selected the sources with no or little infrared excess emission ($0.0 < J-H < 1.9$ mag, $0.0 < H-K < 0.7$ mag), by comparing their distribution in the $J-H$ versus $H-K$ color-color space. The resulting extinction map is displayed in Figure 4.1. The derived extinction values range from $A_V \simeq 1.33$–6.96 mag, or $A_K \simeq 0.12$–0.63 mag. Notably, the extinction is surprisingly low throughout the region, with an average of $A_V \sim 2.24$ mag, despite the young (age ~ 1 Myr) nature of the complex and its nebulous appearance. The possible reasons for such a lower reddening could be the dispersal of the parental molecular gas as the cluster has evolved over time, or, in the initial stages the cluster was composed of lower density material.

Although the extinction map shows a non-uniform distribution over the whole target area, we found a filamentary like pattern, connecting a chain of clumps and extending in the Galactic east-west direction. Across this filamentary structure the extinction varies almost consistently with an average of $A_V \sim 2.40$ mag, upto a maximum of 6.16 (Galactic east) to 6.96 mag (Galactic west). The S112 region, located roughly in the center of the filamentary structure, shows moderate extinction with a highest value of $A_V \sim 6.60$ mag.

An extinction map thus produced is somewhat limited in angular resolution by the detection of a fair number of background stars. Moreover, the color excess for any particular grid is derived in a statistical manner (Lada et al. 1994). Empirically, after a series of trials, we found a $\sim 15''$ grid size, and ~ 20 nearest neighbor stars to be optimal choices, as a compromise between sensitivity and resolution (Panja et al. 2020).

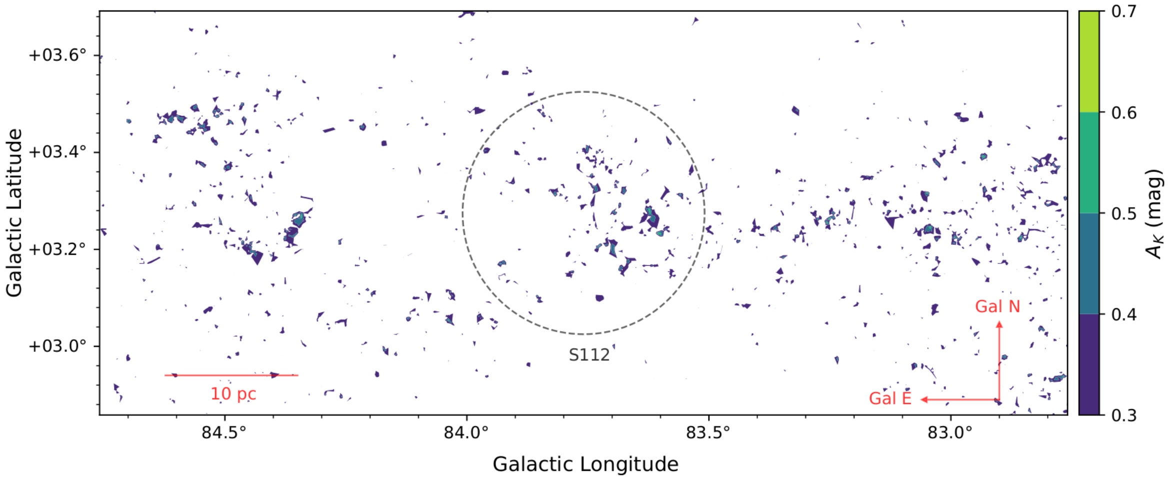

Figure 4.1: The extinction map around S112 computed by the H- and K-band photometry with a grid size of 15″ × 15″. The dashed circle marks the 15′ radius of S112. Enhanced extinction is seen generally in a filamentary zone in the Galactic east-west direction, with a multitude of dense clumps where extinction (A_V) reaches up to 6.96 mag. Altogether, the region exhibits a comparatively lower reddening with an average A_V of 2.24 mag. A 10 pc linear scale is displayed assuming a heliocentric distance of 2.1 kpc to the complex.

4.3.2 The Young Stellar Population

The infrared color excess is a primary indicator of the evolutionary phase of a YSO. As most of the low-mass stars form with circumstellar accretion disks, they show infrared excesses for as long as the dusty circumstellar material survives. Depending upon the proportion of circumstellar disk and envelope materials, these young stars occupy certain locations in the infrared color-color space. We have adopted the established three-phase source classification scheme from the Koenig et al. (2012), by using a combined photometry from *WISE* and 2MASS wavebands with given set of color and magnitude criteria, to explicitly classify the YSOs in specified category. Due to the coverage scarcity of the higher resolution (pixel scale $\sim 1\overset{''}{.}2$ pixel^{-1}) *Spitzer* Infrared Array Camera (Fazio et al. 2004) imaging, we used the complementary *WISE* catalog (angular resolution $\sim 6''$–$12''$; Wright et al. 2010).

The infrared sample is “sanitized” by removing possible contaminants. Galaxies with elevated star formation activity exhibiting increased polycyclic aromatic hydrocarbon (PAH) emission may mimic a YSO color. Unresolved broad-line active galactic nuclei (AGNs) possess mid-infrared colors very similar to those of young stars (Gutermuth et al. 2009). These PAH/star-forming galaxies, AGNs, the shock-excited extended sources are identified and removed from the sample using a combination of WISE colors.

As a next stage, in phase 1 scheme, the YSOs are extracted from the decontaminated sample by using the *WISE* 3.4, 4.6, and 12 μm photometry along with several color criteria (Koenig et al. 2012). We have classified 46 Class I and 79 Class II objects from this scheme and their color-color distribution is shown in Figure 4.2(a). A significant fraction of the unclassified objects are those visible in *WISE* 3.4 and 4.6 μm bands, but lack reliable detection in 12 or 22 μm, due to the bright background emission present at these longer wavelengths and the drop in sensitivity. To compensate for this, we used a combined photometry from *WISE* 3.4, and 4.6 μm together with 2MASS H and K bands to identify the heavily embedded protostellar candidates, referred to as phase 2 scheme. This method requires a measurement of the intrinsic colors of objects, by removing the line-of-sight extinction to each source. To account for this, we used the extinction map generated in the previous section and dereddened the colors by computing the extinction at the nearest grid of a source. Thus, additionally 4 Class I and 42 Class II objects are identified from this scheme and their distribution in addition to the previously (from phase 1) classified YSOs in the dereddened color-color space is shown in Figure 4.2(b). Finally, in phase 3 scheme, the remaining sample is further processed by utilizing the *WISE* 3.4, 4.6, and 22 μm bands, to detect the evolved transition disk (disks with photospheric colors between 3.4 and 12 μm but an excess at 22 μm) objects. Also in continuation with this phase, we rechecked the previously (from phase 1 and phase 2) classified Class I and Class II stars, that possess *WISE* 22 μm photometry. If the Class I objects do not have rising spectral energy distribution at 22 μm, then they are reclassified as reddened Class II sources and the Class II objects that possess excessively blue colors (Koenig et al. 2012) are eliminated and placed back in the unclassified pool. From all the three schemes, a total of 50 Class I, 121 Class II, and 13 transition disk objects are selected and their color-color plot is shown in Figure 4.2(c). The Table 4.1, containing photometric catalog of the YSOs, shows $\sim 33\%$ of the sources are covered with *Gaia* DR2 distance.

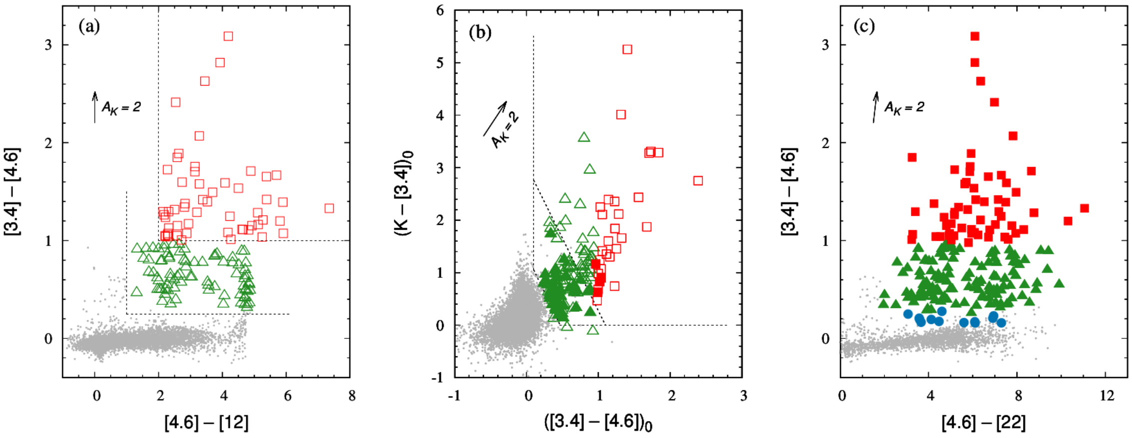

Figure 4.2: Color-color diagrams showing the distribution of Class I (red squares), Class II (green triangles), transition disk (blue circles), and non-excess (gray dots) sources, identified by adopting the three-phase source classification scheme from the Koenig et al. (2012). The dotted lines mark the several color criteria used. (a) In phase 1, Class I and Class II objects are detected by using the *WISE* 3.4, 4.6, and 12 μm photometry. (b) In phase 2, a combination of *WISE* 3.4 and 4.6 μm with 2MASS H and K bands is used to detect the heavily embedded stars. Additionally identified young stellar objects (YSOs) from this phase (solid) are overlaid with the objects identified from phase 1 (open). (c) In phase 3, transition disk objects are identified by using the *WISE* 3.4, 4.6, and 22 μm bands. This diagram depicts the YSOs identified from all the three phases.

Table 4.1: Photometric catalog of the YSOs toward S112. The complete table is made available in the electronic version of Panja et al. (2022)

Sl. No.	Glon. (deg)	Glat. (deg)	[3.4] μm (mag)	[4.6] μm (mag)	[12] μm (mag)	[22] μm (mag)	J (mag)	H (mag)	K (mag)	G (mag)	G_{BP} (mag)	G_{RP} (mag)	Distance (kpc)
						Class I							
1	83.731659	3.289791	10.285	9.037	4.801	1.755	15.402	13.717	12.728	...	...	...	...
			± 0.025	± 0.019	± 0.015	± 0.028	± 0.077	± 0.058	± 0.045	...	...	...	...
2	83.723541	3.282187	7.732	6.335	2.806	-0.189	...	...	...	...	...	...	...
			± 0.007	± 0.004	± 0.007	± 0.021	...	...	...	...	...	...	...
3	83.796066	3.306127	8.540	7.340	1.535	-2.975	15.218	12.473	11.384	...	...	...	...
			± 0.022	± 0.020	± 0.023	± 0.001	± 0.089	...	...	...	...	...	...
4	83.706696	3.281750	4.635	2.879	-0.262	-2.998	12.250	9.956	8.045	19.127	...	...	1.548
			± 0.078	± 0.073	± 0.013	± 0.001	± 0.040	± 0.038	± 0.027	± 0.012	...	...	$^{+2.08}_{-0.79}$
5	83.807014	3.309594	11.087	9.791	7.474	2.614	16.077	14.126	12.721	...	...	...	...
			± 0.033	± 0.023	± 0.107	± 0.029	...	± 0.069	± 0.039	...	...	...	...
6	83.738251	3.341169	11.176	10.064	5.423	1.760	...	...	...	...	...	...	...
			± 0.029	± 0.025	± 0.019	± 0.027	...	...	...	...	...	...	...
7	83.836639	3.293947	13.904	12.314	8.232	4.792	...	...	...	...	...	...	...
			± 0.041	± 0.036	± 0.039	± 0.087	...	...	...	...	...	...	...
8	83.808655	3.348134	14.967	13.682	8.577	4.912	...	...	...	...	...	...	...
			± 0.192	± 0.080	± 0.100	± 0.044	...	...	...	...	...	...	...
9	83.718964	3.184592	10.890	9.738	7.148	4.934	15.991	14.033	12.545	20.017	20.529	18.254	2.426
			± 0.025	± 0.021	± 0.029	± 0.080	± 0.087	± 0.049	± 0.028	± 0.006	± 0.184	± 0.055	$^{+2.09}_{-1.14}$
10	83.758064	3.374197	13.086	12.106	8.386	6.301	17.359	15.522	14.317	...	...	...	...
			± 0.111	± 0.073	...	...	...	± 0.137	± 0.070	...	...	...	...

Table 4.1: Continued

Sl. No.	Glon. (deg)	Glat. (deg)	[3.4] μm (mag)	[4.6] μm (mag)	[12] μm (mag)	[22] μm (mag)	J (mag)	H (mag)	K (mag)	G (mag)	G_{BP} (mag)	G_{RP} (mag)	Distance (kpc)
Class II													
1	83.750618	3.274682	12.019	11.528	7.955	4.577	14.468	13.795	13.297	16.494	17.025	15.628	2.857
			± 0.026	± 0.029	± 0.064	± 0.039	± 0.031	± 0.038	± 0.032	± 0.001	± 0.004	± 0.003	$^{+0.50}_{-0.38}$
2	83.771469	3.278478	12.540	11.790	7.276	3.691	15.177	14.038	13.531	18.240	18.480	16.804	3.316
			± 0.026	± 0.027	± 0.041	± 0.067	± 0.045	± 0.038	± 0.042	± 0.005	± 0.024	± 0.010	$^{+1.59}_{-0.92}$
3	83.758492	3.288390	11.500	10.721	6.684	2.884	17.311	15.255	13.927	20.475	20.016	18.227	2.547
			± 0.029	± 0.025	± 0.036	± 0.051	...	± 0.086	± 0.049	± 0.020	± 0.086	± 0.051	$^{+2.20}_{-1.31}$
4	83.757332	3.295480	12.160	11.520	6.729	3.573	15.203	13.992	13.420	19.420	19.782	17.601	4.533
			± 0.049	± 0.036	± 0.043	± 0.084	± 0.045	± 0.037	± 0.035	± 0.005	± 0.091	± 0.019	$^{+2.36}_{-1.58}$
5	83.767700	3.295630	11.685	10.848	7.103	3.138	15.059	13.838	13.146	17.966	18.536	16.550	2.109
			± 0.039	± 0.058	± 0.149	± 0.096	± 0.048	± 0.043	± 0.030	± 0.009	± 0.043	± 0.022	$^{+0.88}_{-0.50}$
6	83.737221	3.288053	10.578	10.031	7.756	6.277	13.238	12.106	11.426	16.297	17.402	15.133	2.497
			± 0.026	± 0.021	± 0.037	...	± 0.024	± 0.023	± 0.022	± 0.004	± 0.021	± 0.014	$^{+0.35}_{-0.27}$
7	83.746407	3.298622	12.123	11.659	8.433	4.734	14.172	13.015	12.565	18.052	18.967	16.363	6.684
			± 0.076	± 0.077	...	...	± 0.055	± 0.044	± 0.039	± 0.004	± 0.026	± 0.014	$^{+2.56}_{-1.85}$
8	83.759674	3.302573	13.558	12.663	8.769	3.582	16.046	14.820	14.283	...	...	...	...
			± 0.188	± 0.110	± 0.389	± 0.066	± 0.097	± 0.068	± 0.071	...	...	...	...
9	83.730827	3.302455	12.305	11.945	7.360	4.896	16.723	15.115	14.258	...	...	...	...
			± 0.036	± 0.045	± 0.083	± 0.289	± 0.173	± 0.101	± 0.064	...	...	...	...
10	83.765038	3.317215	12.096	11.377	8.091	6.506	15.290	13.550	12.798	20.086	20.745	18.370	1.442
			± 0.105	± 0.085	...	...	± 0.048	± 0.027	± 0.024	± 0.006	± 0.140	± 0.029	$^{+2.01}_{-0.69}$

Table 4.1: Continued

Sl. No.	Glon. (deg)	Glat. (deg)	[3.4] μm (mag)	[4.6] μm (mag)	[12] μm (mag)	[22] μm (mag)	J (mag)	H (mag)	K (mag)	G (mag)	G_{BP} (mag)	G_{RP} (mag)	Distance (kpc)
							Transition Disk						
1	83.735405	3.161190	12.275 ± 0.028	12.117 ± 0.028	10.436 ± 0.147	6.011 ± 0.066	15.131 ± 0.048	13.431 ± 0.030	12.667 ± 0.023	20.826 ± 0.011	21.409 ± 0.235	19.119 ± 0.060	1.996 $^{+2.09}_{-1.17}$
2	83.818115	3.134543	11.068 ± 0.023	10.861 ± 0.020	9.394 ± 0.051	7.287 ± 0.126	14.068 ± 0.025	12.351 ± 0.026	11.552 ± 0.021	19.622 ± 0.005	21.154 ± 0.215	17.906 ± 0.023	2.415 $^{+2.00}_{-1.03}$
3	83.893402	3.487516	11.880 ± 0.024	11.686 ± 0.023	10.461 ± 0.109	7.565 ± 0.104	12.745 ± 0.022	12.259 ± 0.023	12.000 ± 0.021	... ...	... ...	... ...	0.105 $^{+0.00}_{-0.00}$
4	83.968445	3.647253	11.612 ± 0.024	11.363 ± 0.022	10.491 ± 0.107	8.291 ± 0.182	12.440 ± 0.021	12.018 ± 0.026	11.703 ± 0.021	14.758 ± 0.000	15.577 ± 0.003	13.841 ± 0.002	2.751 $^{+0.23}_{-0.20}$
5	83.281326	3.251314	11.473 ± 0.023	11.299 ± 0.022	9.117 ± 0.047	6.826 ± 0.083	15.017 ± 0.054	13.159 ± 0.053	12.348 ± 0.032	20.787 ± 0.011	21.095 ± 0.240	18.839 ± 0.043	1.296 $^{+2.17}_{-0.90}$
6	83.216942	3.055202	12.743 ± 0.028	12.466 ± 0.030	10.450 ± 0.108	7.866 ± 0.193	14.936 ± 0.045	13.935 ± 0.041	13.468 ± 0.043	17.722 ± 0.006	18.719 ± 0.035	16.633 ± 0.016	2.218 $^{+0.87}_{-0.51}$
7	83.214493	3.055449	11.249 ± 0.022	11.083 ± 0.022	9.902 ± 0.072	7.421 ± 0.126	12.532 ± 0.023	11.897 ± 0.024	11.618 ± 0.022	14.844 ± 0.002	15.656 ± 0.007	13.920 ± 0.010	3.540 $^{+0.40}_{-0.33}$
8	83.113586	3.328083	11.558 ± 0.024	11.396 ± 0.023	9.703 ± 0.062	5.795 ± 0.057	12.616 ± 0.025	12.013 ± 0.024	11.790 ± 0.024	15.763 ± 0.001	17.457 ± 0.015	14.473 ± 0.002	0.070 $^{+0.00}_{-0.00}$
9	83.094971	3.295275	12.438 ± 0.030	12.208 ± 0.029	10.077 ± 0.116	5.262 ± 0.083	14.033 ± 0.032	13.371 ± 0.037	13.106 ± 0.031	16.724 ± 0.001	17.819 ± 0.019	15.650 ± 0.006	2.002 $^{+0.41}_{-0.29}$
10	83.087082	3.238889	12.171 ± 0.032	12.012 ± 0.029	9.819 ± 0.109	4.717 ± 0.032	15.637 ± 0.064	13.526 ± 0.041	12.869 ± 0.030	... ...	... ...	... ...	... ...

4.3.3 The Hα Emitters

Most young low-mass stars show Hα emission, from either chromospheric activity or accretion. With the launch of IPHAS survey, the detection of Hα emission line stars is boosted effectively with sensitivity reaching down to $r \simeq 20$ mag (10σ). In Figure 4.3, the distribution of sources detected in IPHAS imaging is shown, by considering a reliability criteria of $r < 20$ mag and photometric uncertainty < 0.1 mag in all three bands. The benefit of forming $(r - i)$ as abscissa and $(r-\mathrm{H}\alpha)$ as ordinate in generating a color-color plot is that objects with Hα-band excesses appear higher within the diagram, while intrinsically redder or more highly reddened objects are over to the right (Drew et al. 2005). Because, the $(r-\mathrm{H}\alpha)$ color tends to act as a coarse proxy for the spectral type and is less sensitive to the reddening than $(r - i)$. The stars located above the track of unreddened main-sequence stars with Hα emission line strengths of -10 Å (equivalent width) are considered as candidate emission-line objects (Barentsen et al. 2014). We have applied an additional 3σ cut, i.e. the difference of $(r-\mathrm{H}\alpha)$ color between the object and the main locus of non-emission-line objects is larger than three times the average uncertainty in their $(r-\mathrm{H}\alpha)$ color, to filter the more subtle candidate emission-line stars.

Thus, we found a total of 357 Hα emitters toward the S112 regime, satisfying the above mentioned criteria. From the color-color plane (Figure 4.3), a large ensemble of sources are observed to have excessive $(r-\mathrm{H}\alpha)$ color, reflecting strong Hα line strength, while a few of the sources are located toward the higher reddening zone. In contrast, the field star distribution shows two well-defined loci, revealing two distinct stellar populations, one for the unreddened main-sequence and other for the giant branch. An estimation of the reddening from such a color-color diagram would be inappropriate, as the reddening tracks are curved in a way that depends on the spectral energy distribution and the amount of reddening. Among the 357 Hα emitters, 18 sources are found to have infrared counterparts and are previously (Section 4.3.2) classified as either Class I, Class II, or transition disk objects. The photometric parameters of the Hα emitting sources are detailed in Table 4.2, which shows more than 98% of the total objects have *Gaia* DR2 distance measurements.

4.3.4 Average Age of the YSOs

The average age of the stellar sources, which are the most profoundly traceable entity of a cluster, can hint on the timescale and dynamics of the cluster evolution. We have estimated the age of the YSOs by comparing their (Class I, Class II, and transition disk) distribution with theoretical isochrones in the ($G_{\mathrm{BP}} - G_{\mathrm{RP}}$ vs G) color-magnitude diagram (Figure 4.4) from the *Gaia* DR2. The *Gaia* mission (Lindegren et al. 2018), supported by astrometry and photometry over the whole sky with higher precision and homogeneity, allows to reach a much deeper ($G \sim 20$ mag) level into the sky. This higher sensitivity when combined with relatively lower reddening ($A_V \sim 2.24$ mag; Section 4.3.1) across the region, the *Gaia* DR2 photometry tends to offer reliable detection for a handful of YSO samples. Conversely, the Hα emitters are excluded in the age determination to avoid any overestimation of age. Because, not all the Hα emitters fall into

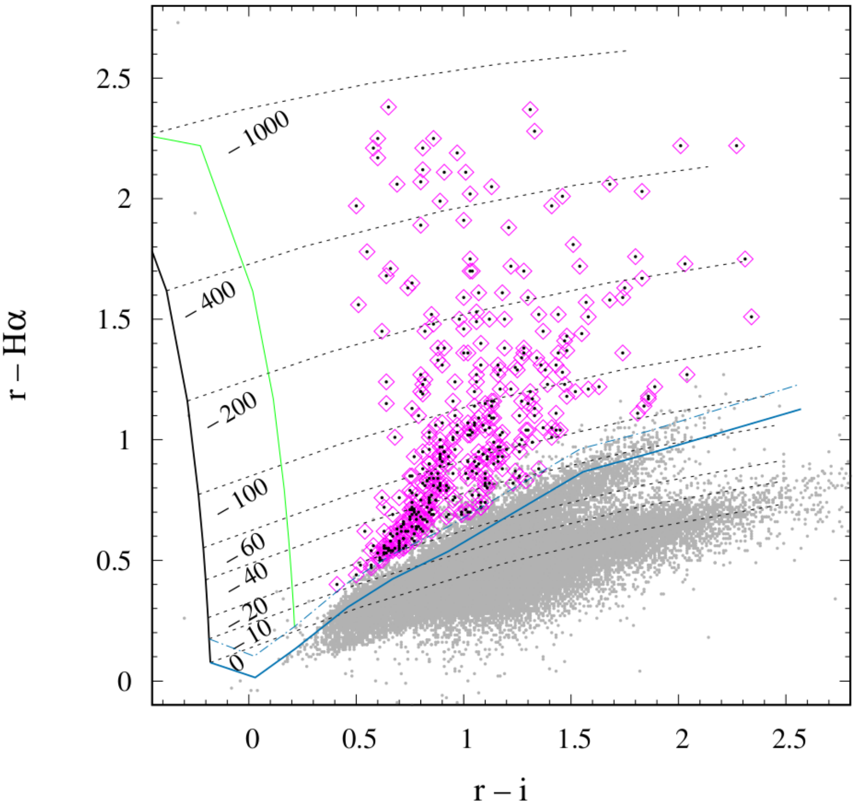

Figure 4.3: Color-color distribution of the sources detected in IPHAS photometry. The candidate Hα emitters are represented by magenta diamonds, whereas the field interlopers with no significant Hα emission are depicted as gray dots. The solid and dashed blue lines represent the unreddened main-sequence, which normally serves as the upper bound to the main stellar locus, and the expected position of unreddened main-sequence stars with Hα emission line strengths of equivalent width = -10 Å. The nearly vertical solid black and green lines show the trend for an unreddened Rayleigh-Jeans continuum and an unreddened F0 continuum, respectively. The black broken lines are the predicted lines of constant net emission.

Table 4.2: Photometric catalog of the Hα emitters toward S112. The entire catalog is made available in the electronic version of Panja et al. (2022)

Sl. No.	Glon. (deg)	Glat. (deg)	r (mag)	i (mag)	Hα (mag)	Distance (kpc)	YSO Class
1	83.771469	3.278478	18.34 ± 0.01	17.31 ± 0.02	16.59 ± 0.01	$3.316^{+1.59}_{-0.92}$	II
2	83.767700	3.295630	18.04 ± 0.01	16.97 ± 0.01	16.43 ± 0.01	$2.109^{+0.88}_{-0.50}$	II
3	83.746407	3.298622	18.92 ± 0.02	17.95 ± 0.03	17.89 ± 0.02	$6.684^{+2.56}_{-1.85}$	II
4	83.799644	3.291358	13.66 ± 0.00	13.02 ± 0.00	12.51 ± 0.00	$2.258^{+0.08}_{-0.07}$	II
5	83.759445	3.319530	19.92 ± 0.04	18.38 ± 0.04	18.20 ± 0.03	$1.409^{+1.62}_{-0.56}$	II
6	83.706696	3.281750	18.64 ± 0.02	16.80 ± 0.01	17.50 ± 0.03	$1.548^{+2.08}_{-0.79}$	I
7	83.815514	3.274818	18.41 ± 0.02	17.51 ± 0.02	17.10 ± 0.02	$2.640^{+1.55}_{-0.81}$	II
8	83.737213	3.343827	19.66 ± 0.03	18.85 ± 0.05	18.43 ± 0.03	$2.508^{+0.16}_{-0.14}$	II
9	83.680313	3.232444	19.82 ± 0.04	18.52 ± 0.04	18.78 ± 0.04	$3.005^{+2.16}_{-1.31}$	II
10	83.731277	3.182579	18.27 ± 0.01	17.44 ± 0.02	17.55 ± 0.02	$1.446^{+1.48}_{-0.55}$	II
11	83.621269	3.324824	13.39 ± 0.00	12.55 ± 0.00	12.65 ± 0.00	$2.361^{+0.24}_{-0.20}$	II
12	83.612801	3.186152	19.51 ± 0.03	17.88 ± 0.03	18.29 ± 0.03	$2.375^{+1.54}_{-0.77}$	I
13	83.968445	3.647253	14.72 ± 0.00	13.86 ± 0.00	14.03 ± 0.00	$2.751^{+0.23}_{-0.20}$	TD
14	83.325523	3.131974	17.44 ± 0.01	16.33 ± 0.01	16.64 ± 0.01	$2.601^{+0.89}_{-0.55}$	II
15	83.399910	3.150243	15.99 ± 0.01	15.45 ± 0.01	15.37 ± 0.01	$1.455^{+1.32}_{-0.52}$	...
16	83.311424	3.215623	19.21 ± 0.05	17.32 ± 0.02	17.99 ± 0.02	...	...
17	83.593498	3.269075	12.96 ± 0.00	12.23 ± 0.00	12.40 ± 0.00	$0.223^{+0.00}_{-0.00}$	...
18	83.282005	3.374590	18.69 ± 0.03	17.93 ± 0.02	17.56 ± 0.02	$2.055^{+0.52}_{-0.35}$	...
19	83.284859	3.402773	12.78 ± 0.00	11.30 ± 0.00	11.35 ± 0.00	$0.912^{+0.04}_{-0.04}$	...
20	83.290916	3.432787	13.41 ± 0.00	12.14 ± 0.00	12.41 ± 0.00	$1.534^{+0.08}_{-0.08}$	...
21	83.320366	3.417897	13.56 ± 0.00	12.46 ± 0.00	12.70 ± 0.00	$2.219^{+0.10}_{-0.09}$	...
22	83.343117	3.425873	19.77 ± 0.06	16.92 ± 0.01	17.17 ± 0.01	$2.929^{+2.24}_{-1.38}$	...
23	83.306496	3.452927	13.63 ± 0.00	12.86 ± 0.00	12.93 ± 0.00	$0.743^{+0.01}_{-0.01}$	...
24	83.343170	3.447589	13.63 ± 0.00	12.39 ± 0.00	12.76 ± 0.00	$2.958^{+0.27}_{-0.23}$	...
25	83.340164	3.451650	13.43 ± 0.00	12.63 ± 0.00	12.75 ± 0.00	$1.825^{+0.08}_{-0.07}$	...
26	83.382019	3.453895	13.76 ± 0.00	13.13 ± 0.00	13.23 ± 0.00	$0.820^{+0.01}_{-0.01}$	...
27	83.370216	3.460896	12.79 ± 0.00	11.11 ± 0.00	11.21 ± 0.00	$2.667^{+0.20}_{-0.18}$	...
28	83.362137	3.491259	13.46 ± 0.00	12.67 ± 0.00	12.76 ± 0.00	$2.767^{+0.12}_{-0.11}$	...
29	83.354385	3.495025	13.28 ± 0.00	12.46 ± 0.00	12.47 ± 0.00	$1.144^{+0.03}_{-0.03}$	...
30	83.441032	3.448251	12.72 ± 0.00	11.61 ± 0.00	11.79 ± 0.00	$1.256^{+0.04}_{-0.04}$	...
31	83.447723	3.447110	12.76 ± 0.00	11.31 ± 0.00	11.72 ± 0.00	$1.851^{+0.09}_{-0.08}$	...
32	83.403450	3.470877	12.98 ± 0.00	11.86 ± 0.00	11.93 ± 0.00	$1.580^{+0.06}_{-0.05}$	...
33	83.423195	3.471457	13.35 ± 0.00	12.27 ± 0.00	12.61 ± 0.00	$2.135^{+0.07}_{-0.07}$	...
34	83.433670	3.498786	12.83 ± 0.00	11.36 ± 0.00	11.60 ± 0.00	$2.016^{+0.13}_{-0.11}$	...
35	83.422340	3.491502	13.39 ± 0.00	12.61 ± 0.00	12.76 ± 0.00	...	...
36	83.410774	3.489886	12.82 ± 0.00	11.69 ± 0.00	11.68 ± 0.00	$0.838^{+0.03}_{-0.03}$	...
37	83.461601	3.508683	13.10 ± 0.00	11.84 ± 0.00	12.00 ± 0.00	$2.158^{+0.13}_{-0.12}$	...
38	83.520432	3.452245	12.84 ± 0.00	11.68 ± 0.00	11.93 ± 0.00	$0.775^{+0.01}_{-0.01}$	...
39	83.519020	3.488169	13.40 ± 0.00	12.32 ± 0.00	12.68 ± 0.00	$1.970^{+0.06}_{-0.06}$	...
40	83.559433	3.505183	13.06 ± 0.00	11.71 ± 0.00	12.18 ± 0.00	$2.545^{+0.17}_{-0.15}$	...

the pre-main-sequence group, but a significant fraction among the post-main-sequence stars, interacting binaries, supergiants, luminous blue variables, and post-asymptotic giant branch stars also exhibit Hα line emission (Drew et al. 2005). Also, the inclusion of foreground or background sources from the distance and their uncertainty analysis could be a risk factor for the Hα emitters.

The stellar evolutionary tracks are computed by using the PAdova and TRieste Stellar Evolution Code (`PARSEC`; Bressan et al. 2012) facility with version release 1.2S. For the *Gaia* sources, the photometric sensitivity curves are collected from Evans et al. (2018), as they give empirically the best fit to our data. In Figure 4.4, while there is a spread in the inferred YSO age, the majority of the YSOs are scattered between 0.1–10 Myr, yielding a compromising age of ~ 1 Myr. For a few sources the ages are older than 10 Myr and nearing the zero-age main sequence. The relatively lower extinction throughout the region, diagnosed earlier (Section 4.3.1), could be a possible outcome of the sweeping out of the dust over this reasonable time, as the cluster has gradually evolved from its initial birthline. Toward the fainter ($G \gtrsim 20.5$ mag) limit, reliable detection of low-mass ($\mathrm{M} \lesssim 0.4\ M_\odot$) members becomes poor. Although, estimating age from the color-magnitude diagram is quite a standard procedure, nevertheless, the estimated age can be subject to a few limitations: the use of different evolutionary models can yield different ages, and the presence of variable extinction may also introduce systematic errors.

4.3.5 Spatial Distribution of the PMS Population

The spatial distribution of young population could reveal ample of essential information regarding the length- and time-scale of the star formation activity in association with a cloud complex. Figure 4.5 manifests the distribution of Class I, Class II, and transition disk objects, overplotted on the *Planck* 353 GHz map. A clear existence of a filamentary like pattern, aligned from the Galactic east to west, is evident from the *Planck* intensity map. The location of three high intensity subregions (Clump A, S112, and Clump B) is revealed, with all of them are interconnected via the filamentary structure. Not only the positional distribution of the YSOs are traced along the higher intensity clouds, but also the clusterings of the YSOs nicely coincide with those of the subregions. Moreover, a good degree of similarity is observed between this spatial map with that of the extinction map (Figure 4.1), generated earlier from the infrared star counts (Section 4.3.1). Altogether, a combination of spatial distribution of young objects, intensity morphology, and extinction map favours of an ongoing star formation activity in a broader and continuous scale ($\sim 2^\circ$) spanned across the Galactic longitude.

A profound look to the intensity map unveils of the fluctuation in cloud density over the region, with a peak and intense distribution toward the S112 subregion, where an elevated concentration of YSOs is also found. In accordance with the spatial map, the relative number of Class I sources notably decreases as one shifts direction from the Galactic east to west. Since the Class I sources normally represent an earlier phase compared to the Class II sources, the ratio of Class I/Class II sources could be used to interpret the evolutionary stage of the subregions, while a higher ratio indicates a

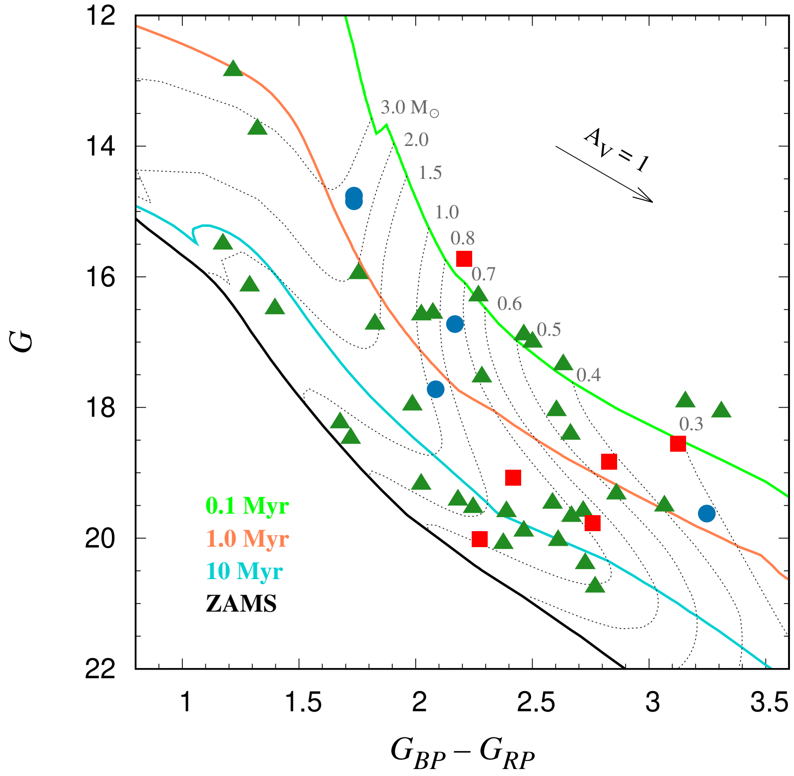

Figure 4.4: *Gaia* DR2 color-magnitude diagram of the YSOs (Class I: red squares; Class II: green triangles; transition disk: blue circles). Overplotted in solid lines are the theoretical isochrones for the pre-main-sequence population of ages 0.1, 1.0, and 10 Myr and the zero-age-main-sequence (ZAMS) stars generated from the PAdova and TRieste Stellar Evolution Code (Bressan et al. 2012). The evolutionary tracks for different masses (dotted lines) according to the ZAMS isochrone are overlaid. All the isochrones are adjusted for a cluster distance of 2.1 kpc (Blitz et al. 1982) and reddening $A_V \sim 2.24$ mag (Section 4.3.1).

younger cluster. The source ratio for the subregions Clump A, S112, and Clump B is estimated to be 0.45, 0.41, and 0.23, respectively, varying considerably from east to west. Literature studies of several young and nearby star forming regions have shown this ratio to vary in a wide range, between $\sim$ 0.1–0.8, with a median of 0.27 (Gutermuth et al. 2009). This suggests that the sources associated with Clump A and S112 subregions are evolving almost in a similar timescale and are the younger population, while the sources to the western periphery are comparatively older in nature. There is a slight possibility of undercounting of embedded stellar sources toward the western side as the reddening marginally increases. In S112, majority of the YSOs are found to be distributed toward the northern vicinity of BD+45 3216, while the Class I sources are preferentially located at the outskirts of the dense cloud, with almost none of them are located near the central core. Being precursors to the Class II sources, the Class I sources have less evolved circumstellar environments, this indicates that the star formation is still continuing at the outer parts. Most probably, these Class I sources are the next-generation stars of the region whose formation is induced by the expansion of the H II region powered by the massive star.

4.4 Feedback Mechanisms and Ionized Gas

In response of a quest, if the massive ionizing sources played any significant role in their surrounding environs to initiate and restrain the stellar evolutionary processes, we have presented spectroscopic observations supplemented with infrared imaging. Further, radio continuum measurements are included to curb the dynamical evolution of the ionized gas associated with the subregions.

4.4.1 Spectral Synthesis of the Observed Stars

Optical spectroscopy for a few of the bright ($J < 13$ mag) stars toward S112 are conducted owing to the time limited observations facility. The spectroscopic results will provide a precise knowledge of the spectral type, therefore help to find any influence of the ionizing radiation emitted by the massive star on the surrounding star formation activity via any feedback mechanism. The flux-calibrated normalized spectra of the observed stars are presented in Figure 4.6.

Spectral classifications are done in comparison with the standard spectral libraries of Jacoby et al. (1984), Walborn & Fitzpatrick (1990), and Torres-Dodgen & Weaver (1993). The classification scheme relied on the marking of strong and conspicuous emission/absorption features and measurement of their equivalent widths, following the procedure outlined in Panja et al. (2020). Furthermore, the spectral indices are compared with the spectral atlas of Danks & Dennefeld (1994), Kobulnicky et al. (2012), and Hernández et al. (2004) for a better estimate. Primarily, for the early-type stars upto A, we have adopted the line strengths of hydrogen Balmer series (Hδ 4102 Å, Hγ 4340 Å, Hβ 4861 Å, Hα 6563 Å), He I (5876, 6678, 7065 Å), and He II (4200, 4541, 4686, 5411, 5720 Å). For the cooler stars (F type or later), we have relied on various metallic line

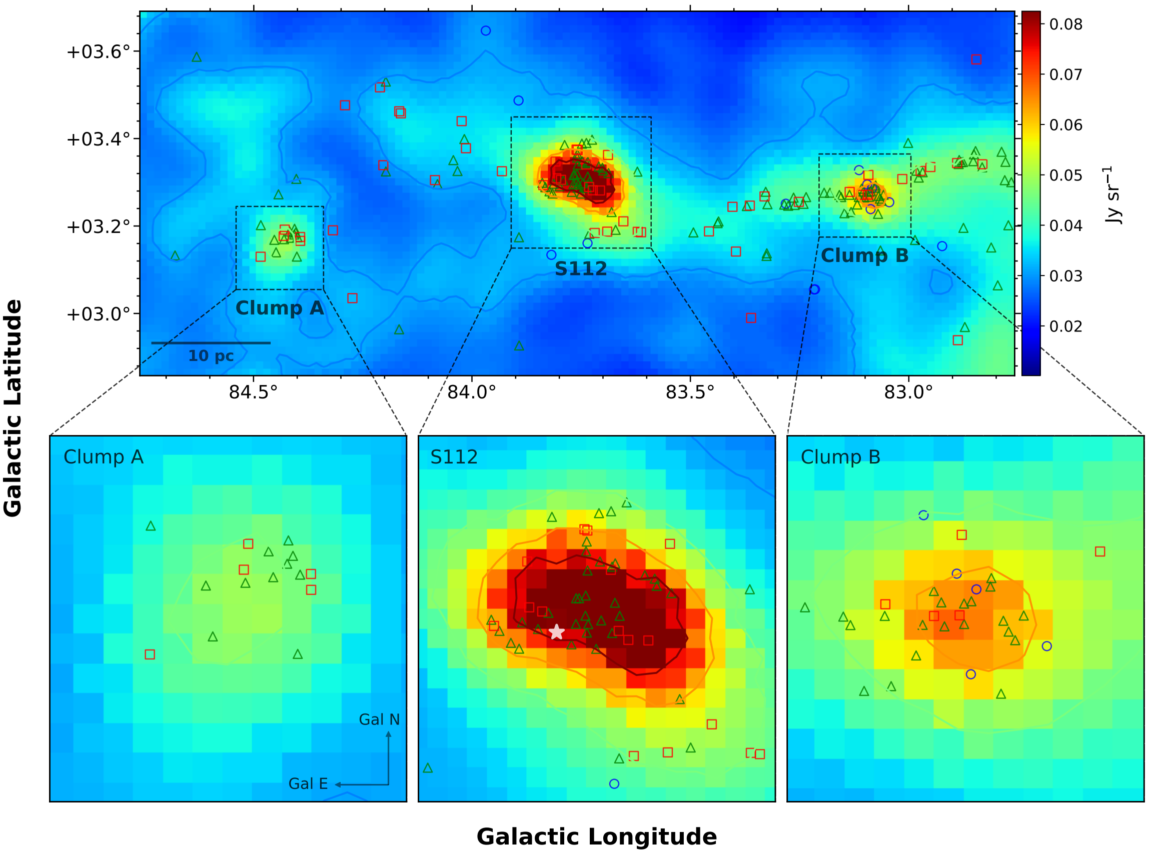

Figure 4.5: Top: Spatial distribution of the YSOs (Class I: red square; Class II: green triangle; transition disk: blue circle) overlaid on the *Planck* 353 GHz map. The stellar density peaks at three subregions (Clump A, S112, and Clump B), also coincide well with the high intensity structures. The contour levels are at 0.031, 0.046, and 0.061 Jy sr^{-1}, respectively. Bottom: Zoomed-in map of the three subregions. The main ionizing source BD+45 3216 is represented by a white star symbol.

features, such as, Na I (5890, 5896 Å), Mg I triplet (5167, 5172, 5183 Å), Mg II (4481, 6347 Å), Ca I (6122, 6162 Å), Ca II triplet (8498, 8542, 8662 Å), and Fe I (6495, 7749, 7834 Å). A brief description of the spectral features for each observed star is given as follows.

S1: The star S1 shows prominent He I (4144, 4387, 4471, 5876, 6678, 7065 Å), He II (4541, 4686, 5411 Å), and hydrogen (4101, 4340, 4861, 6563 Å) lines, with an evidence of strong absorption features at He I (5876, 6678, 7065 Å), He II (4541, 5411 Å), and Hα (6563 Å) lines, which restricts the spectral type to O as a dwarf star. In case of supergiants, the Hα line strength is extremely weak from O5 to B8. The presence of Si II (4128 Å), O III (4415 Å), and moderate nitrogen enhancement is an indicator of later O-type spectra. The line ratio of He I (4471 Å)/He II (4541 Å) is found to be marginally greater than 1, suggesting a spectral type of later than O7. Finally, by comparing the equivalent widths of He I (5876 Å), He II (5411 Å), and Hα (6563 Å) and a visual comparison of the spectrum with the spectral libraries, we assigned the spectral type of the star as O8 V.

S2: The star S2 shows a peculiar feature of very strong Hα (6563 Å) emission, along with strong absorption at Na I (5890, 5896 Å) and Ca II triplet (8498, 8542, 8662 Å). The presence of Ca I (6162 Å), Fe I + Ti I + Cr I (6362 Å), Fe I (6495 Å), and C II (6580 Å) suggests a spectral range between early-mid G type. Further, the absorption at Mg I triplet (5167, 5172, 5183 Å) is an indication of G type spectrum. Comparing the line ratios of Hα, Na I doublet, and Ca II triplet, we choose the spectral type to be G3 V–III, whereas for the same spectral type Ca II triplet line strength is much stronger for the supergiants.

S3: The declining strengths of Na I (5890, 5896 Å), Hα (6563 Å), and Ca II triplet (8498, 8542, 8662 Å) in the spectrum of S3 signal the spectral type of a late-F star. From the additional features of Ca II (K) (3933 Å), CH (G band) (4300 Å), and Fe I (4271, 5329, 7749 Å), we picked a spectral type of F7 V–III.

S4: The spectrum of S4 exhibits weak presence of He I (5876 Å) and very strong Hα (6563 Å) absorption, indicating a relatively hot star (late-B type). The line ratio of Hα (6563 Å)/He I (5876 Å) suggests a spectral type of B8 or later. Moreover, from the presence of C III + O II (4070 Å), Si III (4552 Å), CN + Fe I (4175 Å), Fe I (4383 Å), and Na I (5890, 5896 Å) features, we set the spectral type of this star as B9 V.

S5: The star S5 shows spectral features of CN + Fe I (4175 Å), Fe I (4532, 6495, 7749 Å), Ca I (6162 Å), and Fe II (6242 Å) blend, which are a signature of late-F type star. From the additional features of Na I (5890, 5896 Å), Hα (6563 Å), and Ca II triplet (8498, 8542, 8662 Å), we estimated the spectral type to be F9 V–III.

S6: The spectrum of S6 shows a quite similar diagnostic as in S4, with presence of weaker He I (5876 Å) and strong Hα (6563 Å) absorption, including C III + O II (4070 Å), CN + Fe I (4175 Å), Si II (4128 Å), Si IV (4089 Å), Mn I + Fe I (4458 Å), and N III (4511 Å) features. Considering the line strength of Hα (6563 Å)/He I (5876 Å), we classified the star as a B9.5–A0 V type.

To be noted that, based on the low-resolution spectroscopy, an uncertainty of ±1 spectral subtype for early-type stars up to A- and ±3 subtype for F-type and later

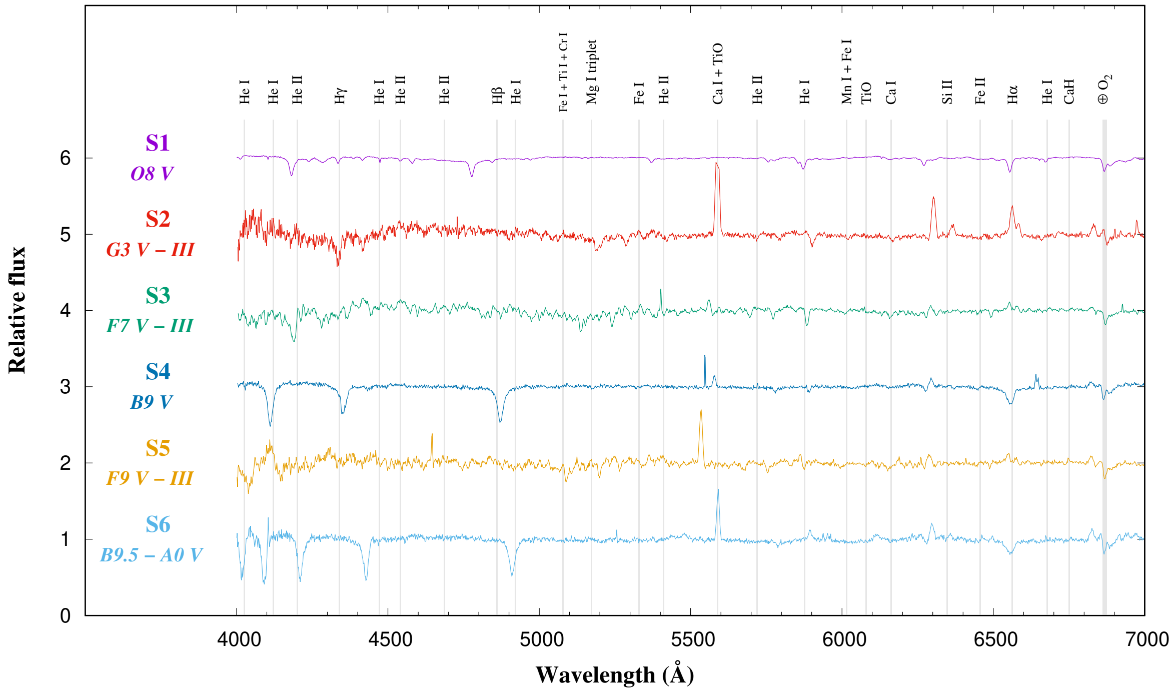

Figure 4.6: The flux-calibrated normalized spectra of the spectroscopically observed stars toward S112, obtained with the 2 m HCT using Grism 7. The important emission and absorption line features are marked.

stars is expected. The distribution of variable reddening and any contribution from circumstellar dust emission can have considerable effects on the nature of spectral class, as will be discussed in the next section.

4.4.2 Reddening and Membership of the Observed Stars

Spectrophotometric parameters of the observed stars are derived from the estimated spectral types and the infrared photometry. In order to calculate the spectroscopic A_V of each source, we utilized the JHK-band color excess relations (Panja et al. 2020), with reddening laws taken from Cohen et al. (1981) and the intrinsic colors collected from Pecaut & Mamajek (2013). We also cross-checked the line-of-sight reddening of each source from the extinction map (Section 4.3.1), by considering the nearest grid value. Moreover, distribution of the sources in the infrared color-color diagram (Figure 4.7) provides a census of their reddening properties. The Table 4.3, containing relevant parameters of the observed stars, points out excessive spectroscopic A_V particularly for S3 and S5 (3.2–3.8 mag), and moderate for S2 (2.5 mag), clearly inconsistent with the line-of-sight extinction ($\sim$ 2.0 mag). The surplus reddening for these three objects is accounted by the noticeable infrared excess as exhibited in Figure 4.7, a consequence of intrinsic emission phenomenon. Although, their excess emission is not sufficient enough to place them into the YSO pool. In addition, they spatially fit both the dwarfs and

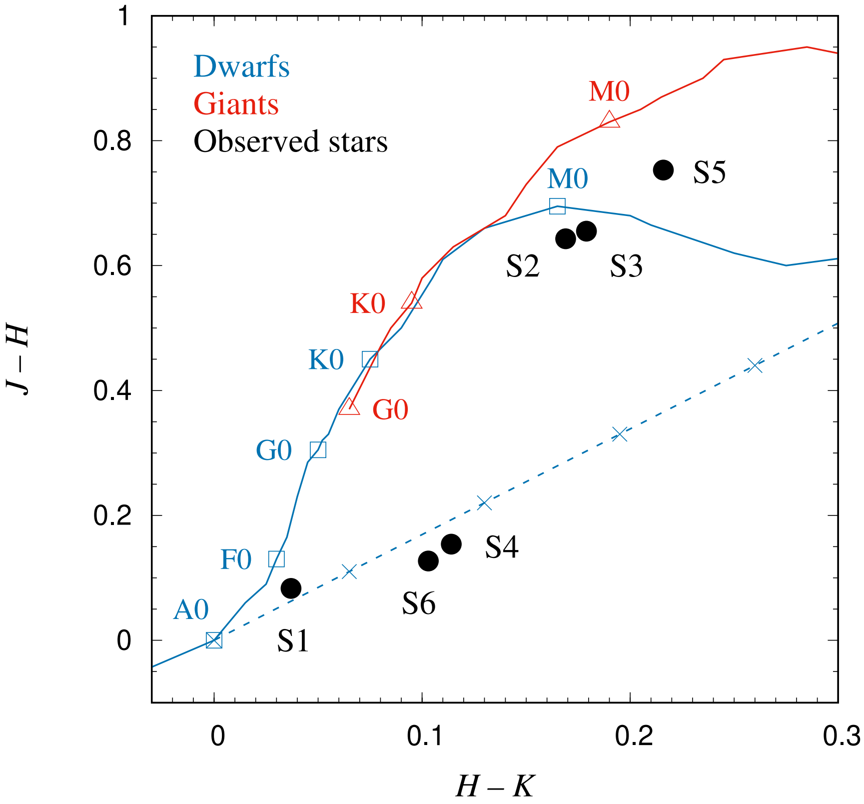

Figure 4.7: Shows distribution of the spectroscopically observed stars (black filled circles) on the infrared plane portraying the nature of reddening. The locus of points for unreddened main-sequence (blue solid line) and giant (red solid line) stars are adopted from the Bessell & Brett (1988). A reddening vector drawn from the A0 loci is represented by blue dashed line, along which the consecutive cross marks indicate a shift in reddening for $A_V = 1$ mag.

giants locus, yielding to infer that these three objects have the possibility of being any of reddened main-sequence or giant stars. On the contrary, objects S1, S4, and S6 are located in a lesser reddened zone ($A_V \lesssim 2.0$ mag) with trivial excess emission and are most likely dwarfs.

To calculate the spectroscopic distance of each source, we first derived the distance modulus from spectroscopic A_V, observed (JHK) and absolute magnitudes (Pecaut & Mamajek 2013). We also verified the distances from the *Gaia* DR2 database, computed with the Bailer-Jones et al. (2018) approach. From Table 4.3, the *Gaia* DR2 distance for all of the observed stars is consistent with the cluster, therefore considered as members.

Table 4.3: Parameters of the spectroscopically observed stars

Star ID	Glon. (deg)	Glat. (deg)	J (mag)	H (mag)	K (mag)	Exposure Time (s)	Spectral Type	Spectroscopic A_V (mag)	A_V (mag) from Extinction map	Distance (kpc)	*Gaia* DR2 Distance (kpc)
S1	083.783904	+03.288649	8.182 ± 0.019	8.099 ± 0.020	8.062 ± 0.020	300	O8 V	2.027 ± 0.068	1.379 ± 0.046	1.758 ± 0.137	$1.822^{+1.704}_{-0.705}$
S2	083.694004	+03.300749	12.870 ± 0.021	12.227 ± 0.021	12.058 ± 0.019	1500	G3 V – III	2.509 ± 0.128	2.134 ± 0.035	...	$1.971^{+0.092}_{-0.084}$
S3	083.883029	+03.229439	10.836 ± 0.020	10.181 ± 0.021	10.002 ± 0.018	1200	F7 V – III	3.206 ± 0.191	1.779 ± 0.034	...	$1.990^{+0.064}_{-0.060}$
S4	083.834016	+03.389542	12.920 ± 0.024	12.766 ± 0.029	12.652 ± 0.030	1200	B9 V	1.693 ± 0.081	1.496 ± 0.048	2.158 ± 0.238	$2.044^{+0.076}_{-0.071}$
S5	083.655728	+03.347573	11.079 ± 0.020	10.326 ± 0.019	10.110 ± 0.016	1200	F9 V – III	3.823 ± 0.204	1.670 ± 0.032	...	$2.049^{+0.073}_{-0.068}$
S6	083.951724	+03.276741	12.942 ± 0.020	12.815 ± 0.024	12.712 ± 0.024	1200	B9.5 V – A0 V	1.426 ± 0.056	3.236 ± 0.039	2.214 ± 0.199	$1.985^{+0.072}_{-0.067}$

4.4.3 Feedback Mechanisms of the Massive Stars

Our spectroscopic observations yielded only a single massive (O8 V) star, that is capable of producing sufficient ultraviolet radiation, responsible for creating and sustaining an ionized region. A color composite image of the S112 region is presented in Figure 4.8, generated with a combination of near-to-mid infrared wavebands, highlighting the locations of the spectroscopically observed stars. The intensity of infrared emission strengthens along the Galactic north and extends across a much wider range compared to the other side, above the main illuminating source BD+45 3216 (ID S1) of the region. The brightest objects in the *WISE* 3.4 μm band are stars, but this band also has counterparts from a weak, diffuse PAH feature at 3.3 μm possibly from scattered starlight. The 12 μm emission, sensitive to warm dust, shows dominant contribution permeating the region. A vivid rim-like structure, forming almost a semi-circular shape exists, surrounding which the trails of dust content are found to be prominent. The northern top of this rim-like structure shows an enhance and definite morphology, where the main exciting star BD+45 3216 resides. Toward the northern vicinity, multiple sub-filaments are seen to be interconnected via diffuse emission nebulosity. A significant amount of dust is contained across these diffuse clouds, as traced by the strength of 12 μm emission. Inside the rim formation, the 22 μm detection with a decreasing gradient away from the exciting star is seen to be eminent, a primary signature of ionized emission. As, part of the 22 μm detection comes from the continuum emission of small grains, located in the extended ionized gas (Pomarès et al. 2009). Small grains can survive in strong ultraviolet fields, while large molecules cannot (Peeters et al. 2002).

The *WISE* 12 μm band is efficient in detecting both PAH emission (11.3 μm) and amorphous silicate absorption (10 μm) in nearby star-forming galaxies. PAHs are destroyed inside the ionized gas due to strong contributions from thermal emission by O star, but are excited in the hot photodissociation zone by the radiation leaking from the H II region (Leger & Puget 1984). In this context, encircling the ionized region, a brighter layer is observed adjacent to the ionization front, where it encounters with the ultraviolet illuminated surfaces of molecular clouds, giving rise to the arc-like formation. The curvature of the arc-like structure appears to be facing toward the ionizing source at the center. So, the rim/arc-like structure serves as an interface between ionized zone and molecular cloud distribution. The higher dust intensity, when exposed to a large flux of ultraviolet radiation that excites PAHs but is not energetic enough to destroy them, resulted in a formation of the brightest arc feature near BD+45 3216. The molecular cloud density is much higher toward the Galactic north and the massive exciting star is located almost at the edge of cloud distribution. The propagation of the ionization/shock front compressed the nearby molecular cloud, triggering subsequent star formation. The molecular cloud morphology in the infrared matches well with that of the *Planck* 353 GHz radio map (Figure 4.5). The spatial distribution of the YSOs further suggests a star formation activity is actively taking place toward the northern cloud, with a scattered population distributed along the south-west sub-filament. The positional correlation of the massive star, ionizing radiation, and molecular cloud distribution led to designate this region as a blister-type H II region (Israel 1978; Panwar

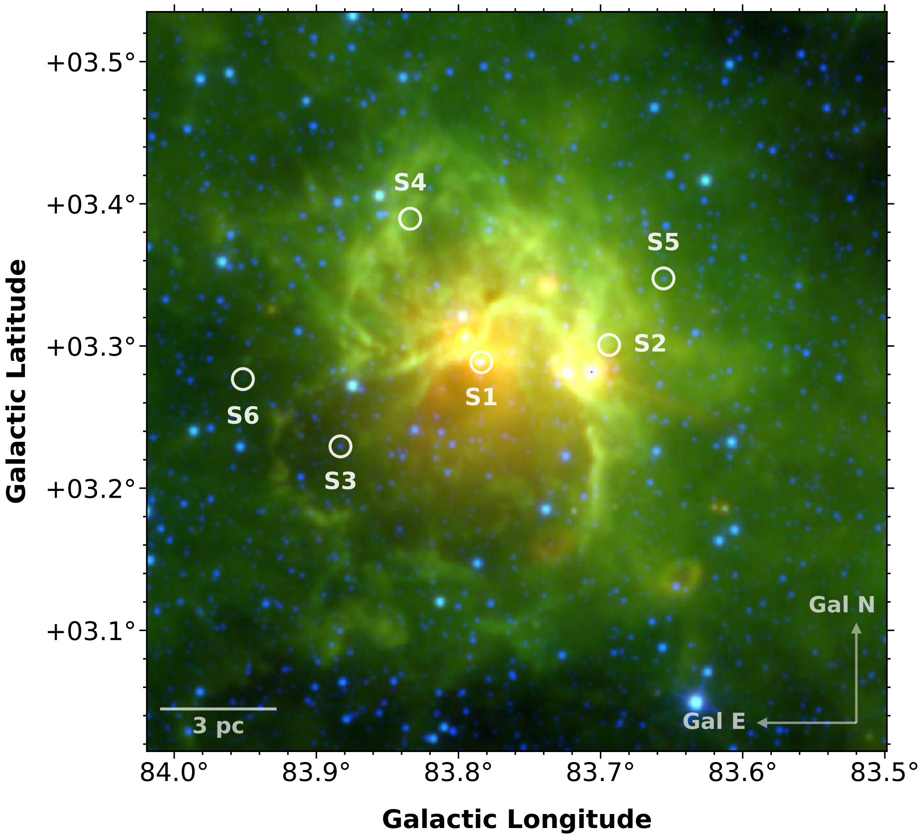

Figure 4.8: Color composite image of S112 created with *WISE* $W4$ 22 μm (red), $W3$ 12 μm (green), and $W1$ 3.4 μm (blue) bands. Spatial locations of the spectroscopically observed sources are marked (white circles).

et al. 2020). At the moment, more evidence such as cloud dynamics is needed to justify our postulate of triggering star formation in the vicinity.

4.4.4 Properties of the Ionized Gas

Compact H II regions are largely composed of ionized hydrogen, influenced either by massive exciting star/stars or evolving protostars, emitting thermal radiation strongly detectable in the radio range, resulted from the free-free radiation (also called the Bremsstrahlung). We have utilized the NVSS 1.4 GHz radio continuum observations to estimate the physical parameters of the ionized gas associated with the three subregions. The radio continuum distribution, overlaid on a far-infrared map (160 μm), for the three subregions is shown in Figure 4.9 and the derived parameters are given in Table 4.4. The expression of Lyman continuum photons (N_{uv}), considering an optically thin, homogeneous and spherical H II region, is given by (Matsakis et al. 1976)

$$N_{uv}(s^{-1}) = 7.5\,\times\,10^{46}\left(\frac{S_\nu}{Jy}\right)\left(\frac{D}{kpc}\right)^2\left(\frac{T_e}{10^4K}\right)^{-0.45}\times\left(\frac{\nu}{GHz}\right)^{0.1} \tag{4.1}$$

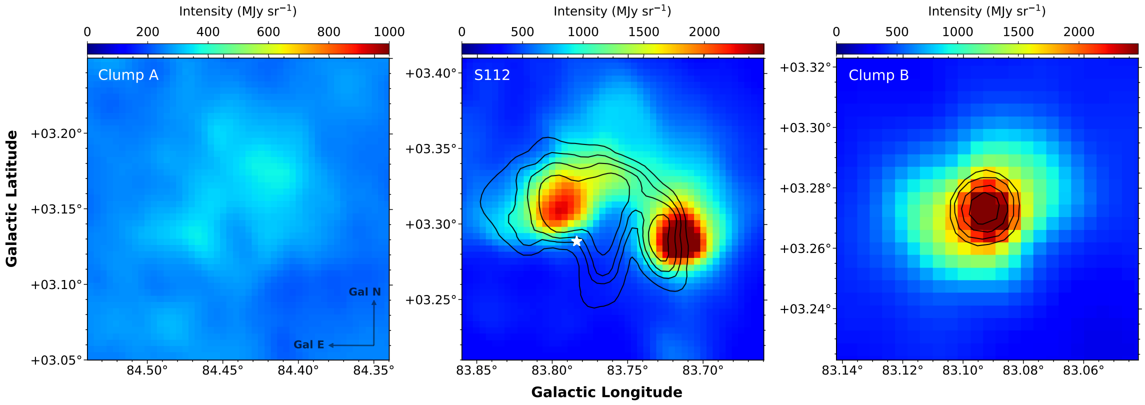

Figure 4.9: The AKARI 160 μm intensity map, superimposed with NVSS 1.4 GHz radio continuum (contours) for the three subregions (Clump A, S112, and Clump B). For Clump A, no significant 1.4 GHz emission is detected. The contour levels for S112 subregion are at 0.003, 0.010, 0.020, and 0.040 Jy/beam. The main illuminating source BD+45 3216 is indicated by a white asterisk symbol. The contour levels for Clump B are at 0.003, 0.006, 0.012, and 0.020 Jy/beam.

where S_ν is the integrated flux density in Jy, D is the distance in kpc, T_e is the electron temperature, and ν is the frequency in GHz. Substituted values are the measured radio flux (Table 4.4), an average distance of 2.1 kpc (Table 4.3), and an electron temperature of 10^4 K (Matsakis et al. 1976). For Clump A, no definite radio peak is observed, also the total ionized flux density is nominal. While for S112, two radio emission peaks are distinctly identifiable, but the main exciting star (BD+45 3216) does not coincide with any of the peaks. Clump B shows a single and definite peak with moderate ionization level. The Lyman continuum flux corresponds to the spectral class of a single ionizing star (Panagia 1973). In case of S112, the spectral class resulted to be O9.5–B0 V, which shows close agreement with our optical spectroscopic determinations (O8 V). The spatial correlation of the ionized gas with the dusty material as traced by the 160 μm detection, directs that the estimated N_{uv} is a lower limit of the actual stellar ionizing flux. As a significant fraction of the stellar ultraviolet radiation will be absorbed for heating the dust rather than ionizing the gas, consequently reducing the free-free flux. Evidently, from Figure 4.9, the coincidence of dust emission with radio continuum differs: in S112, both emissions near BD+45 3216 are comparatively devoid, indicating the H II region to be exclusively powered by BD+45 3216. In contrary, in Clump B a higher intensity plus the compact morphology points to the possibility of ionization caused by clusters of stars (early-B type) that are still embedded in the cloud, rather than a single ionizing star alone (Martín-Hernández et al. 2003). This conforms to the notion that, often OB stars are formed in small groupings or binaries, where the H II regions from various stars overlap, and the regions appear as one large H II region.

The size of the ionized gas, that depends on the stellar ultraviolet flux and density of the gas, is expressed in terms of radius of the Strömgren sphere (R_s), given by

$$R_s = (3N_{uv}/4\pi n_0^2 \alpha_B)^{1/3} \tag{4.2}$$

where the radiative recombination coefficient $\alpha_B = 2.6 \times 10^{-13}$ $(10^4\ \mathrm{K}/T_e)^{0.7}$ cm^3 s^{-1} (Kwan 1997), and n$_0$ is the initial particle number density of the ambient neutral gas with a typical value of 10^3 cm^{-3}. Thereafter, the dynamical age (t_{dyn}) of the H II regions associated with the three subregions is computed using the relation (Dyson & Williams 1980)

$$t_{dyn} = \left(\frac{4\,R_s}{7\,c_s}\right) \left[\left(\frac{R_{HII}}{R_s}\right)^{7/4} - 1\right] \tag{4.3}$$

where c_s is the isothermal sound velocity in the ionized gas (c_s = 11 km s^{-1}; Bisbas et al. 2009) and R_{HII} is the radius of the H II region. From Table 4.4, the dynamical age of the H II regions is found to vary between 0.16–1.0 Myr, which is consistent with our earlier estimates (Section 4.3.4). So, the S112 region seems to be relatively evolved compared to the other two subregions, subject to the fact that variation in the dust density may induce substantial change in the dynamical age distribution.

Table 4.4: Physical parameters of the ionized gas associated with the subregions

Sub-region	Glon. (deg)	Glat. (deg)	R_{HII} (pc)	S_ν (mJy)	N_{uv} (s^{-1})	$\log(N_{uv})$	Spectral type	R_s (pc)	t_{dyn} (Myr)
Clump A	084.432560	+03.159770	0.388	1.203	4.115×10^{44}	44.614	B2–B3 V	0.0234	0.164
S112	083.758934	+03.275037	3.038	1414	4.836×10^{47}	47.684	O9.5–B0 V	0.2473	1.023
Clump B	083.088982	+03.269279	0.668	32.39	1.108×10^{46}	46.044	B0.5–B1 V	0.0702	0.184

4.5 Molecular Cloud Morphology

We now present a quantitative measurement of the molecular cloud parameters derived from the CO data analysis. The distribution of the total molecular gas traced by ^{12}CO reveals structures of the diffuse gas (density $\sim 10^2$ cm^{-3}), whereas optically thinner ^{13}CO and C^{18}O lines trace denser (density $\sim 10^3$–10^4 cm^{-3}) components of the molecular gas. A combination of ^{12}CO, ^{13}CO, and C^{18}O isotopologues thus provides complementary information of the molecular cloud morphology, from diffuse gas in cloud envelopes to denser gas in giant molecular clouds, from cloud fragmentation to pre-stellar core formation. The methodology used to derive the cloud parameters are explicitly mentioned in Sun et al. (2020).

4.5.1 Intensity Distribution

The intensity distributions for the three CO isotopologues in the velocity interval -33 to 15 km s^{-1} are presented in Figure 4.10. The large scale extended diffuse cloud structures are prominent in the ^{12}CO emission. In the ^{13}CO map, multiple subfilaments with enhanced emission are seen to be connected mainly with the subregions Clump A and S112. Earlier in the spatial map of the YSOs (Figure 4.5), a higher fraction of the Class I objects were detected across these clouds. Whereas these two subregions are the active site of ongoing star formation activity, the associated subfilaments serve as efficient sites for next generation star formation. The C^{18}O emission is detected mostly at the location of the three subregions, where only the compact and dense cloud structures exist. The S112 subregion is observed to have fragmented into two separate dense cores. The complete filamentary cloud, which is traced by the ^{13}CO intensity contours (Figure 4.11), is extended over $\sim$ 80 pc, aligned mostly along the Galactic longitude. Along the filamentary axis, cloud fragmentation and creation of several cloud cores in addition to the three subregions are observed.

4.5.2 Velocity Distribution

The overall velocity distribution (longitude-velocity map) of molecular gas within the mapped region is displayed in Figure 4.12. The velocity range ([-33, 15] km s^{-1}) for the complete molecular structure is relatively wide. Therefore, the cloud structures are studied in three velocity channels in [-33, -10] km s^{-1}, [-10, 6.5] km s^{-1}, and [6.5, 15] km s^{-1}, where prominent emission is detected. The velocity channel maps for ^{12}CO and ^{13}CO are shown in Figure 4.13 and Figure 4.14, respectively. For the C^{18}O map, significant emission is detected only in the [-10, 6.5] km s^{-1} channel. Clearly the velocity channels [-33, -10] km s^{-1} and [6.5, 15] km s^{-1} are not consistent with the cloud distribution, and hence any further analysis are conducted considering the velocity interval [-10, 6.5] km s^{-1}.

The moment maps integrated over the velocity range [-10, 6.5] km s^{-1} are displayed in Figure 4.15, Figure 4.16, and Figure 4.17 for ^{12}CO, ^{13}CO, and C^{18}O, respectively. The moment 1 (velocity) map in ^{12}CO shows considerable velocity gradient from Galactic

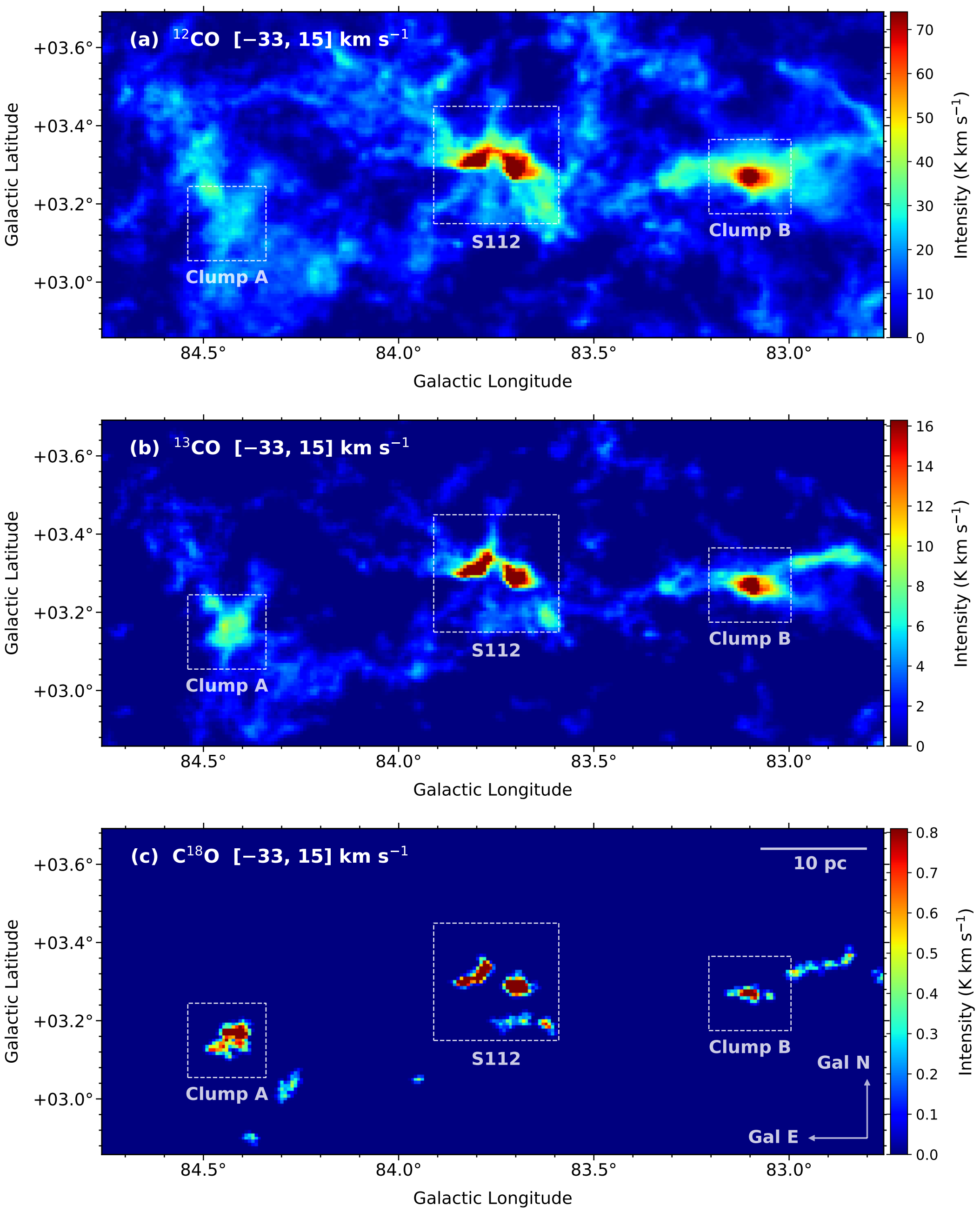

Figure 4.10: Intensity maps (moment 0) for ^{12}CO, ^{13}CO, and C^{18}O integrated over the complete velocity range [−33, 15] km s^{-1}. The location of the three subregions is marked by the dashed rectangles.

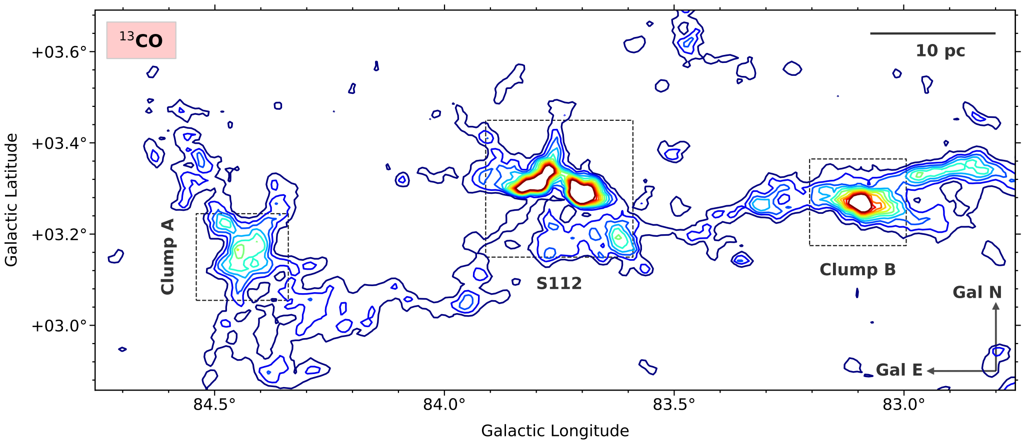

Figure 4.11: Contour map for the ^{13}CO intensity distribution. The contour levels start at 1.234 K km s^{-1} and are increased at the same level at each step upto 13.576 K km s^{-1}. The three subregions are interconnected via an elongated filamentary structure of length $\sim$ 80 pc, stretching in the Galactic east-west direction.

east to west. Toward the Galactic east, velocity varies almost uniformly between -2.5 to -5.0 km s^{-1} with an average of -3.8 km s^{-1}. Whereas toward the Galactic west, the overall velocity distribution shows much fluctuation, but along the filamentary axis velocity varies consistently with an average of -2.7 km s^{-1}. The velocity dispersion (moment 2) is also relatively lower (average $\sim$ 2.7 km s^{-1}) toward the Galactic east and slightly increases (average $\sim$ 3.4 km s^{-1}) toward the west. The ^{13}CO moment 1 map properly depicts the molecular cloud distribution. The velocity varies almost consistently along the complete filamentary structure from -4.2 km s^{-1} (east) to -3.1 km s^{-1} (west). The velocity dispersion is also much lower (average $\sim$ 1.4 km s^{-1}) compared to the ^{12}CO. Similar results are obtained from the C^{18}O map, where the gradual velocity increase is observed from the Galactic east to west.

4.5.3 Column Density Distribution

The excitation temperature map, derived from ^{12}CO considering optically thick, is presented in Figure 4.18(a). Along the filamentary cloud, the excitation temperature varies steadily with an average value of $\sim$ 10 K, which is similar to the typical kinetic temperature of molecular clouds. Evidently the temperature peaks are observed at the location of the three subregions. The Clump B manifests highest temperature (32.4 K), followed by S112 (28.6 K) and Clump A (13.7 K). The derived optical depths for ^{13}CO and C^{18}O are presented in Figure 4.18(b) and Figure 4.18(c), respectively. The optical depths are then used to make saturation corrections to the column densities. The H$_2$ column density is derived by adopting a CO-to-H$_2$ conversion factor, $X_{\rm CO} \equiv 2 \times 10^{20}$ cm^{-2} (K km s^{-1})$^{-1}$ for ^{12}CO and by assuming local thermodynamic equilibrium and abundance ratios of H$_2$ to CO for ^{13}CO and C^{18}O, respectively. The H$_2$ column density map for the CO

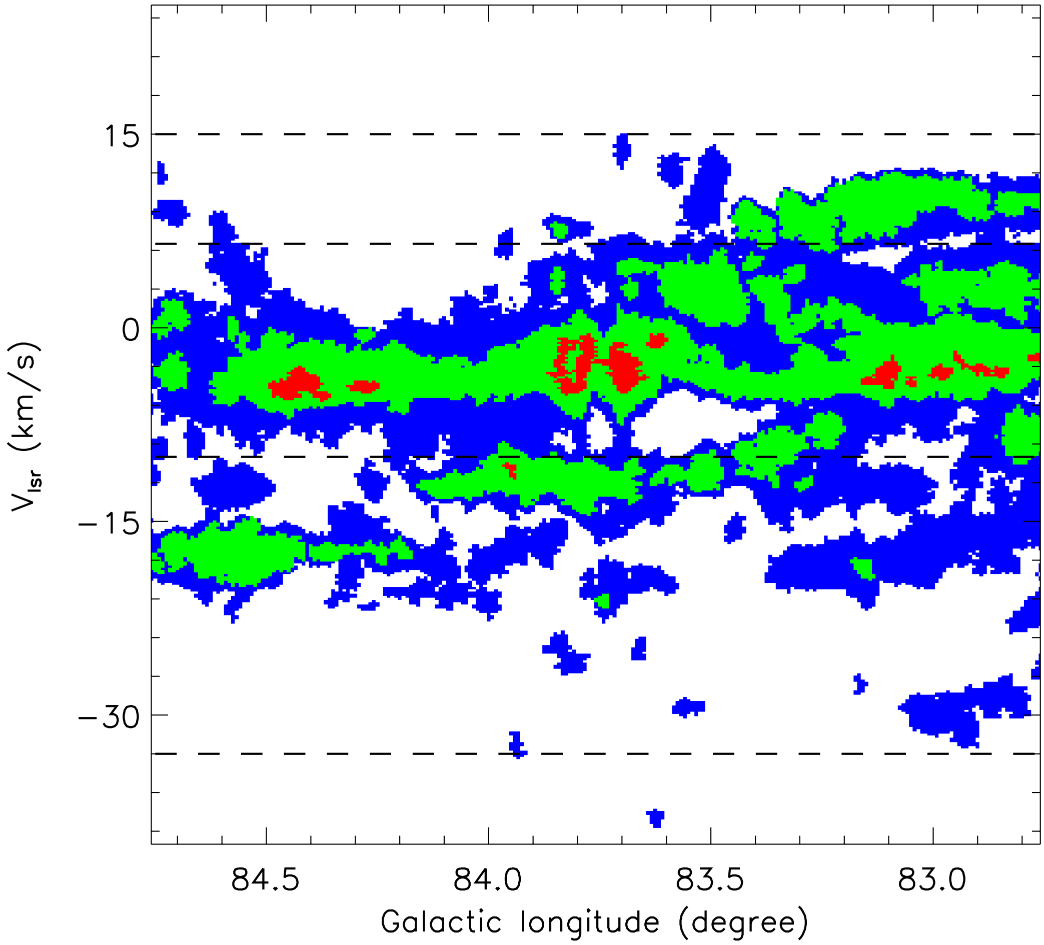

Figure 4.12: Longitude-velocity (l–v) map of the entire field toward S112, integrated over the Galactic latitude range of $b = [2\overset{\circ}{.}8583, 3\overset{\circ}{.}6917]$. The blue, green, and red colors indicate the regions exhibiting ^{12}CO, ^{13}CO, and C^{18}O emission, respectively. The four horizontal dashed lines mark the V$_{lsr}$ = −33, −10, 6.5, and 15 km s^{-1}.

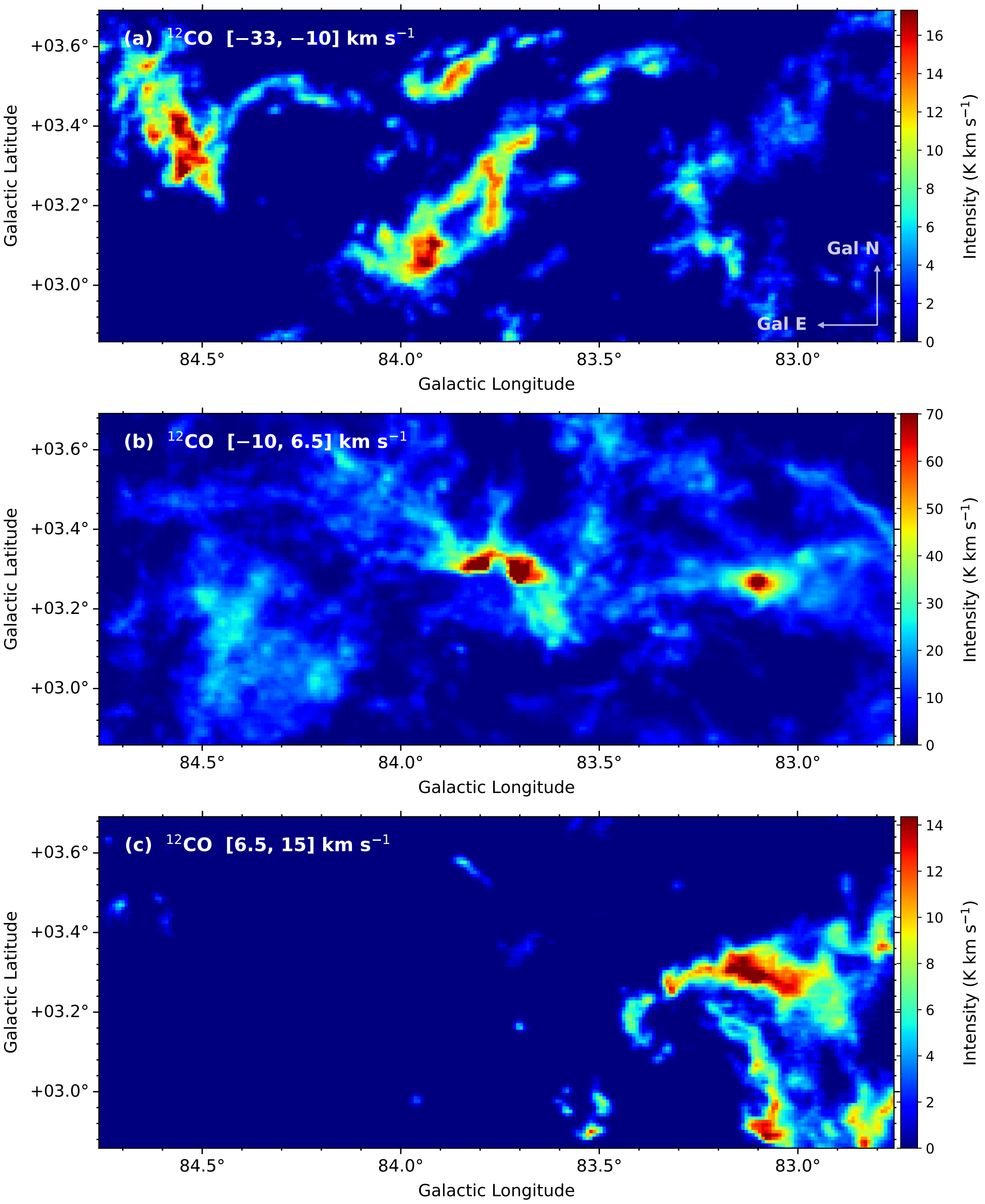

Figure 4.13: The channel maps for ^{12}CO, where the velocity ranges are depicted in the figures.

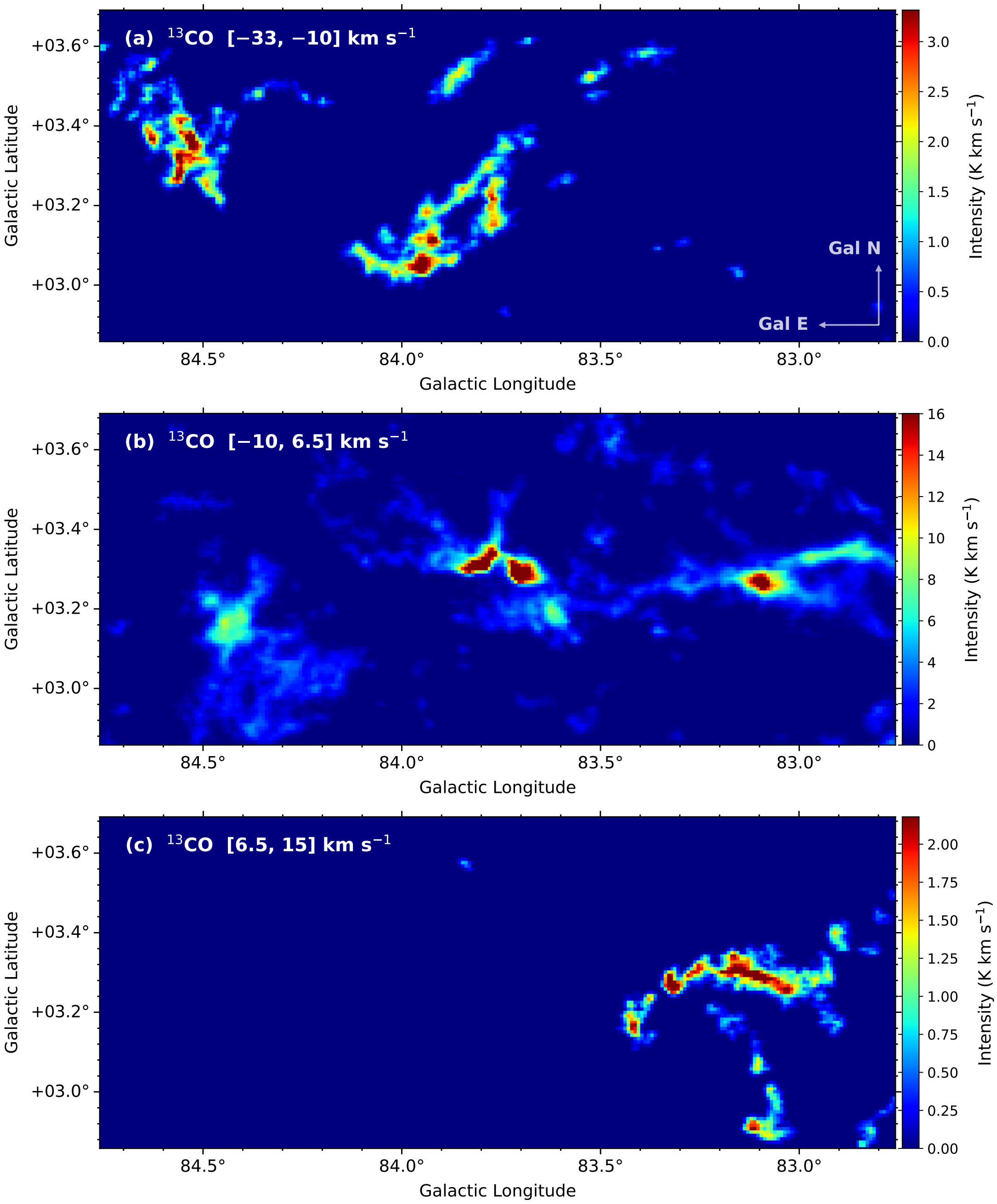

Figure 4.14: The channel maps for ^{13}CO.

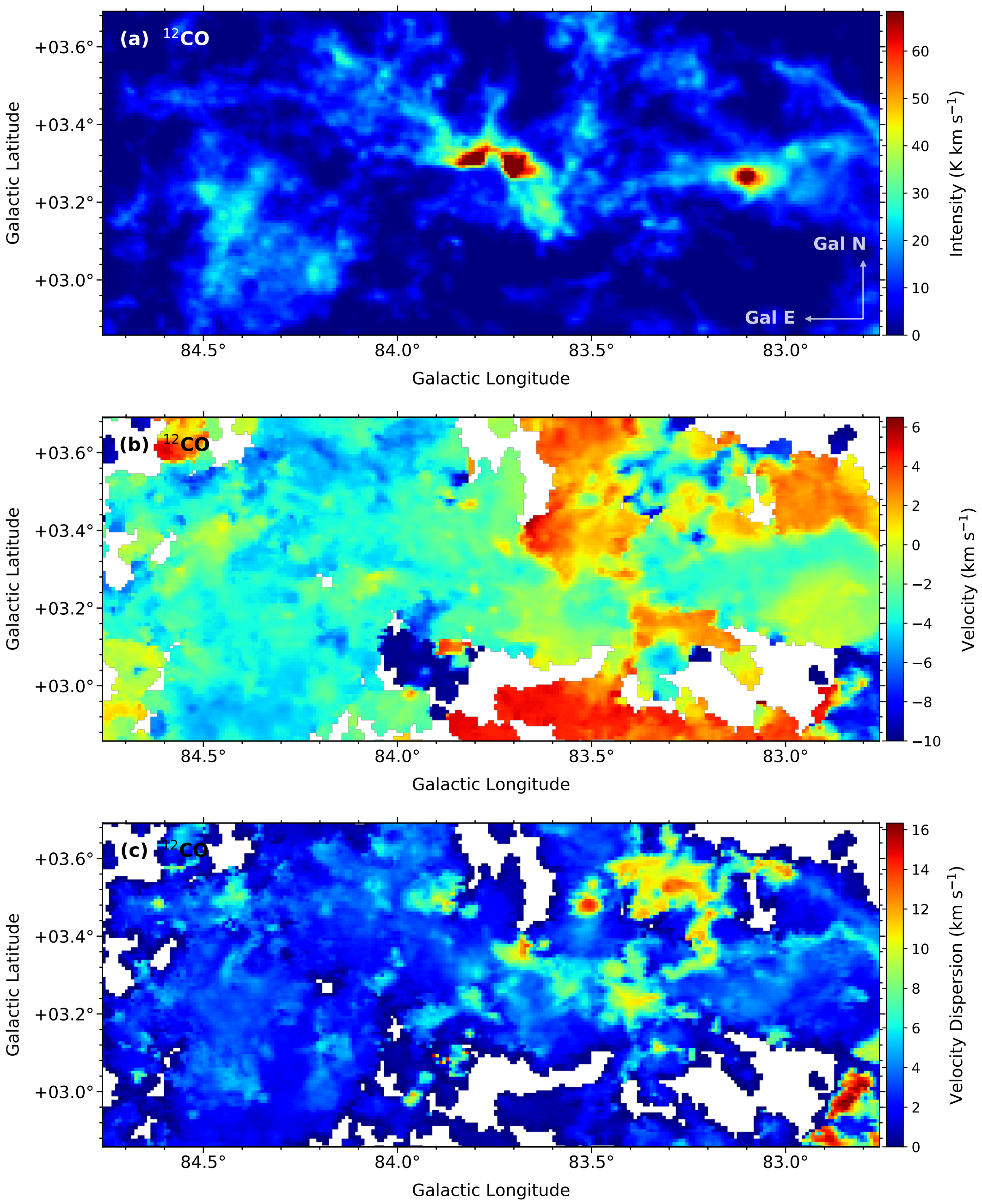

Figure 4.15: Moment maps for ^{12}CO for the velocity range [-10, 6.5] km s^{-1}.

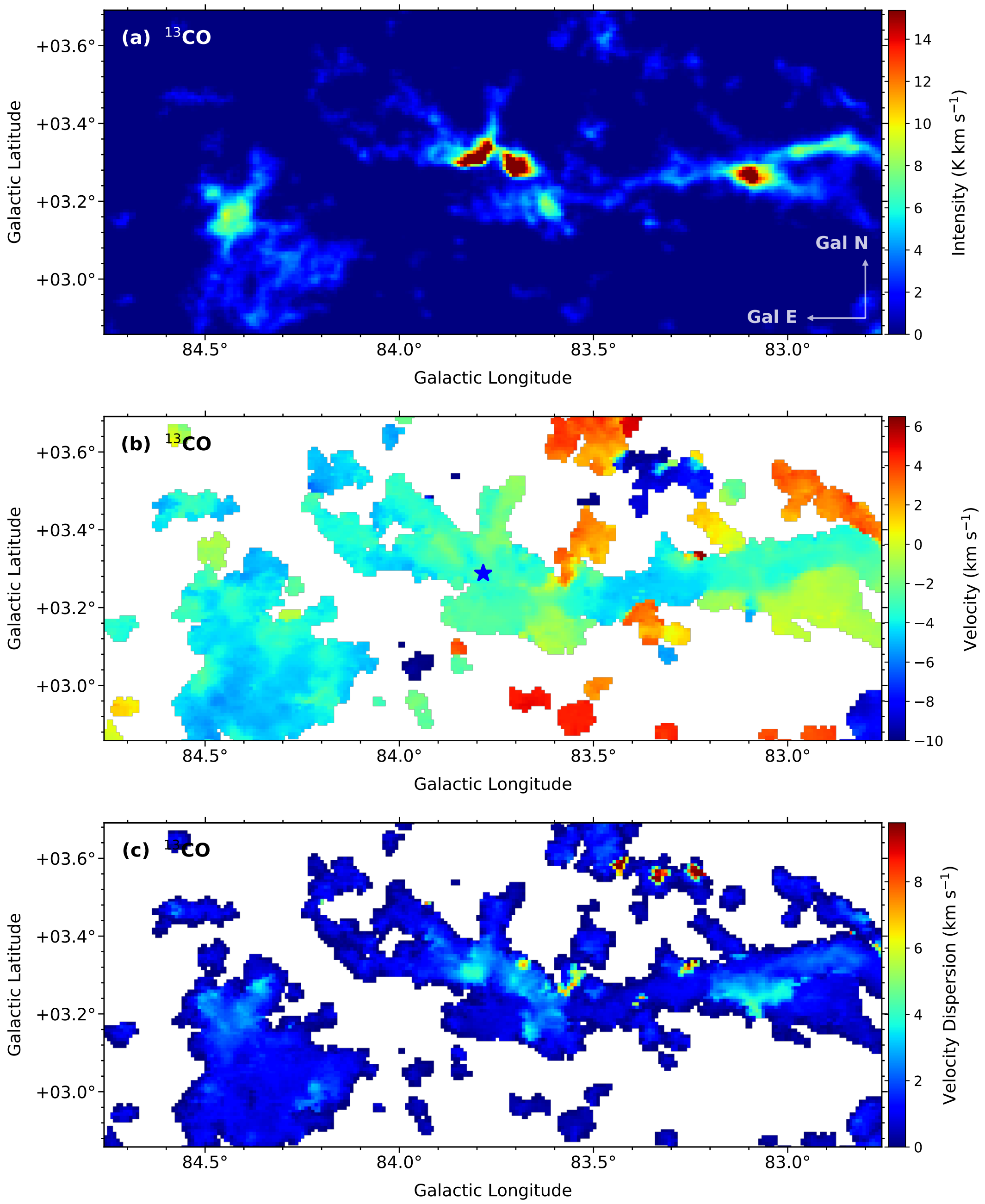

Figure 4.16: Moment maps for ^{13}CO for the velocity range [−10, 6.5] km s^{-1}. A blue star symbol in the middle panel represents the main ionizing source BD+45 3216.

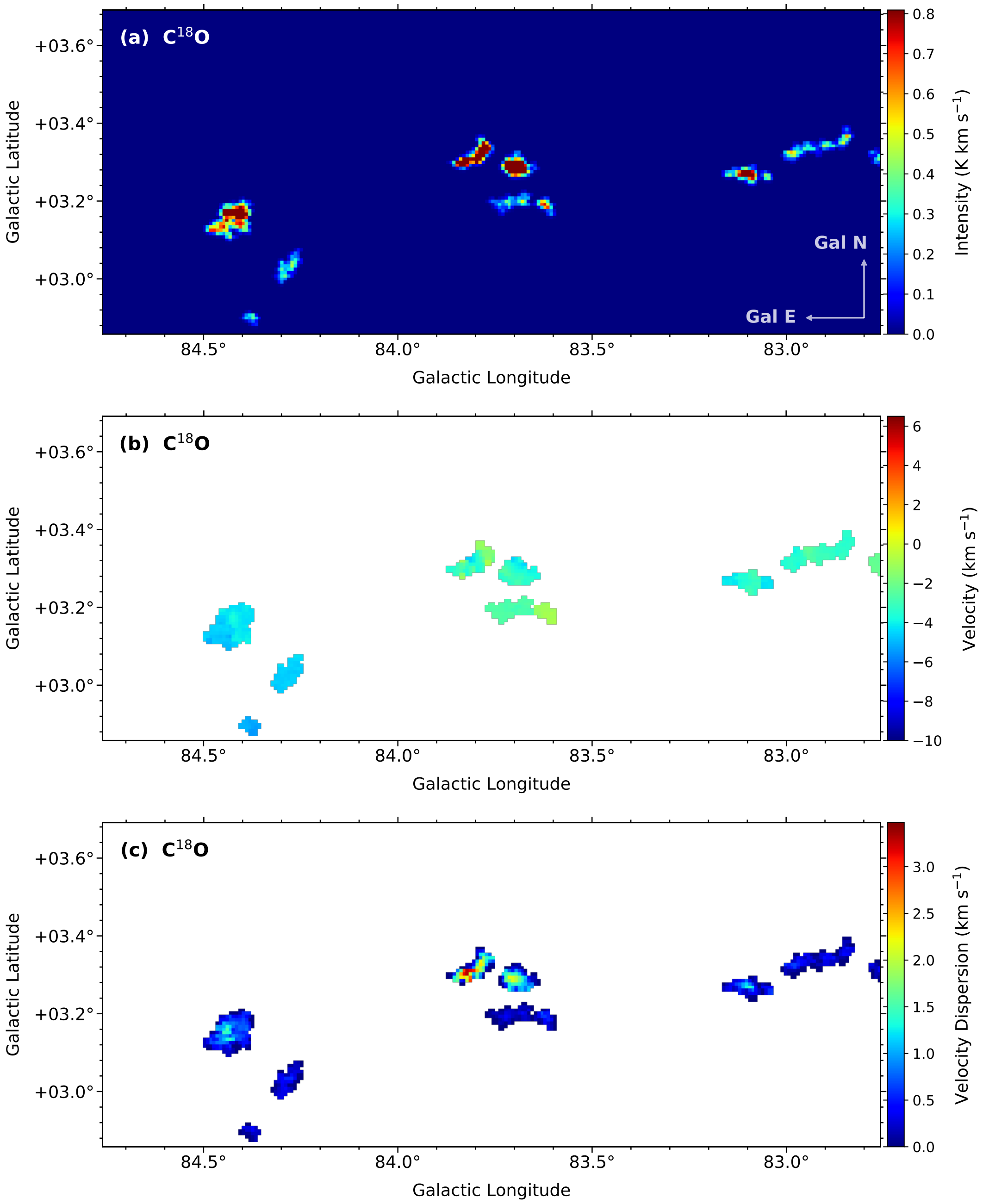

Figure 4.17: Moment maps for $C^{18}O$ for the velocity range [−10, 6.5] km s^{-1}.

triplet is shown in Figure 4.19. Within S112 and Clump B, the average column density varies at the order of 5–6 $\times$ 10^{21} cm^{-2}, with highest values ranging between 4–5 $\times$ 10^{22} cm^{-2}. Whereas the corresponding values are relatively lower in Clump A (average $\sim$ 3–4 $\times$ 10^{21} cm^{-2}, peak $\sim$ 7.5 $\times$ 10^{21} cm^{-2}). For the results presented here, the C^{18}O emission is relatively discrete due to less velocity crowding and line blending (Su et al. 2019), in comparison with the extended ^{12}CO and ^{13}CO emission. Therefore, the C^{18}O emission is useful in detecting the denser components, which are mainly associated with the cloud cores.

4.5.4 Star Formation Activity in the Filamentary Complex

The star formation activity exhibited toward this cluster is occurring in a bulk-scale, that in fact is supported by a number of observed facts. The YSO clusterings are exclusively found at the higher column density zones, where accumulation of molecular material has maximized. The clusters of YSOs are further interconnected via the filamentary cloud. Alongside to that majority of the young populations spatially coincide with the filamentary axis along which the cloud condensation is higher. The extinction pattern resembles well with that of the molecular cloud morphology. The velocity measurements constrain the cloud structure and its kinematics. Considering a median cloud velocity of ~ -3.65 km s^{-1} from the ^{13}CO map, the axisymmetric Galactic rotation model (Reid et al. 2019) produces a kinematic distance of $\sim 1.52 \pm 0.12$ kpc (local arm), marginally shallower than the distance ($\sim 1.76 \pm 0.14$ kpc) of the main exciting star. In the velocity channel maps (Figure 4.13 and Figure 4.14), considerable amount of cloud structures were detected for the channels $[-33, -10]$ km s^{-1} and $[6.5, 15]$ km s^{-1}. The Galactic rotation model points out that these are actually either background (distance $\gtrsim 3.0$ kpc) or foreground (distance $\lesssim 1.3$ kpc) clouds located along the same line-of-sight. Although considering the distances, the possibility of any interaction or association with these clouds can not be ruled out. The plausible explanation of the velocity gradient that exists across the filamentary cloud is that the cloud distance varies from our point-of-view, i.e. the eastern side cloud is located farther away compared to the western side.

The higher fraction of Class I objects toward the Galactic east compared to the west indicates that the western side cloud is relatively evolved. It is therefore proposed that the star formation has initially begun toward the western side, then propagated toward the east through the filamentary axis. The gravitational collapse along such extended filamentary structures initiated cloud fragmentation that in turn subsequently led to the core formation, which are the progenitor to protostars. Several dense cloud cores along the filament axis are detected in Figure 4.11, that clarify the filament fragmentation and core formation activity. However, the formation of the main ionizing source (BD+45 3216) is far from any conclusion, but one possibility is from the disruption of the gas filament. Notably, in Figure 4.16(b), in the nearness of BD+45 3216 the gas velocity is mostly coherent and is relatively higher. Whereas further away from BD+45 3216, the gas velocity decreased gradually. Clearly the expanding H II region has played a dominant role in excavating the nearby molecular clouds. Toward the eastern side cloud

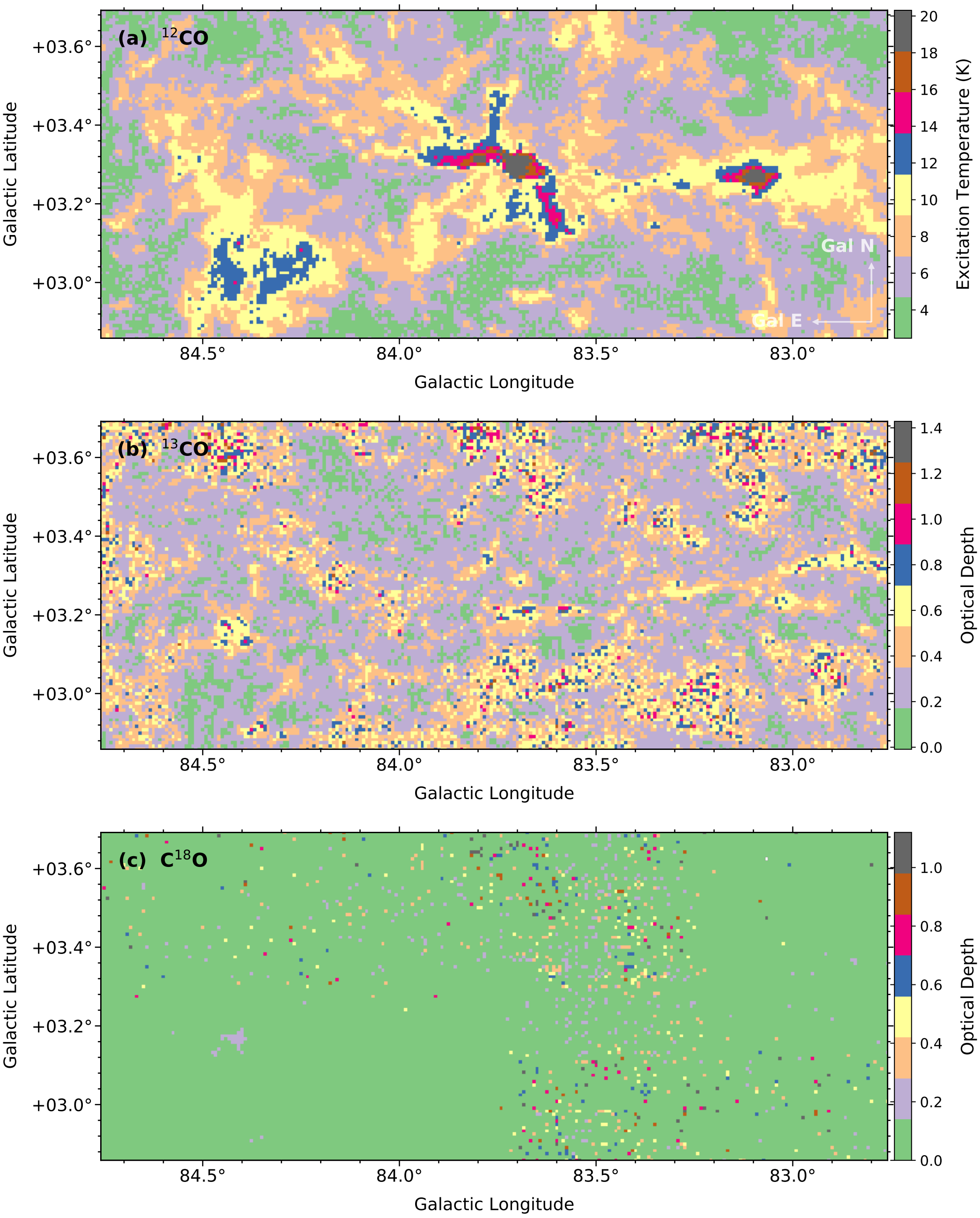

Figure 4.18: (a) Excitation temperature map for ^{12}CO and (b, c) optical depths for ^{13}CO and C^{18}O respectively.

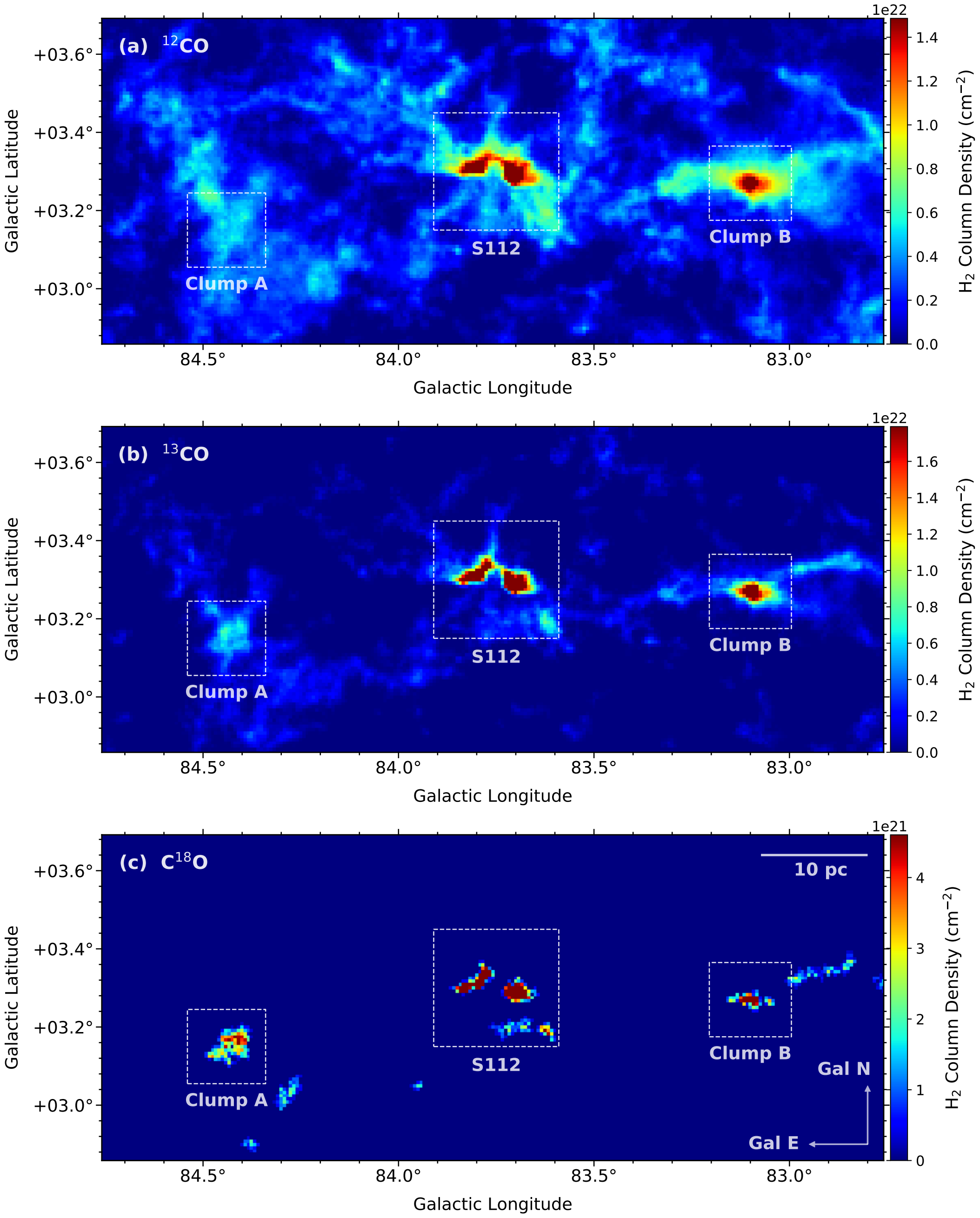

Figure 4.19: The H_2 column density distribution for ^{12}CO, ^{13}CO, and C^{18}O respectively.

(Clump A), the gas acceleration is most likely caused by its own gravity. In Clump A, at the zones where velocity is < -4 km s^{-1}, higher excitation temperature ($\sim$ 12–13 K) is detected. Thus the S112 region is encapsulated as a complex site, hosting young stellar sources at various evolutionary stages, entangled subfilament and subregion systems, and showing evidence of parental cloud disruption in a broad range.

4.6 Summary

We have diagnosed the stellar contents associated with the S112 complex using multiwavelength observational approach. A link between YSO evolution, dust and cloud morphology, and ionized gas is established to understand the overall star formation activity around this site. The key objectives are summarized as follows:

1. The K-band extinction map uncovers the extent of dust content for an extended region ($\sim 2^\circ$) along the Galactic longitude with a filamentary-like distribution. The overall extinction is moderate, averaging $A_V \sim 2.24$ mag, except a few clumps reaching maxima of $A_V \sim 7$ mag.

2. The complex harbours a considerable number of young populations (more than 180), identified using the infrared excess criteria. Using the theoretical isochrone fitting, the best-fit age of these young objects is estimated to be $\sim$ 1 Myr. Additionally, from the Hα emission line profiles, a numerous number (> 350) of Hα emitting sources is detected, signifying that the region is substantially dominated by strong ionization activity.

3. The spatial distribution of the YSOs shows a preferential alignment along the filamentary-like structure, also abundantly coincides with the radio morphology, inferring to a star formation activity in a bulk scale. The highest concentrations of YSOs are observed to be confined at three locations, referred to as Clump A, S112, and Clump B subregions, all inter-connected via the filamentary cloud.

4. Spectroscopy of luminous stars suggests the O8 V star BD+45 3216 to be the only viable ionizing source in the region. Its location relative to the young population, ionized gas, and molecular cloud suggests a triggering star formation sequence in the blister-shaped S112 H II region.

5. Analysis of the ionized gas associated with the three subregions using radio continuum observations implied their dynamical age to be $\sim$ 0.16–1.0 Myr, consistent with the age estimation from the isochrone fitting of the YSOs.

6. The molecular cloud traced by the CO maps has a median velocity of ~ -3.65 km s^{-1}, with a gradual increase from the Galactic east (~ -4 km s^{-1}) to west (~ -3 km s^{-1}). The filament, extending over $\sim$ 80 pc, shows evidence of cloud fragmentation and formation of multiple compact and dense cloud cores, correlated with the YSO groupings. Overall, the filament temperature remains coherent ($\sim$ 10 K), except at dense cores (column density $> 10^{22}$ cm^{-2}) where it reaches up to $\sim$ 32 K.

Chapter 5

Sustaining Star Formation in the Galactic Star Cluster M 36?

5.1 Introduction

A giant molecular cloud fragments to form aggregates of stellar associations or clusters. As the giant molecular cloud itself disperses, individual aggregates may or may not remain gravitationally bound (Lada & Lada 2003; Krumholz et al. 2019). "Timescale" is key to the hierarchical structuring. Giant molecular clouds have a life expectancy of $\sim 10^8$ years in orbiting the Galactic plane through spiral arms. More massive ones ($\gtrsim 10^5$ $\mathrm{M}_\odot$), capable of producing thousands of stars, thereby likely hosting luminous OB stars, are more vulnerable to photoevaporation, and would be destructed on timescales $\lesssim$ 30–40 Myr (Williams & McKee 1997). Within a cloud that ends up producing a cluster, starbirth may not proceed simultaneously in the dense cores hosting individual protostars. With a coeval onset of formation, massive stars will be gone by a couple of million years, whereas low-mass members in the same star cluster would take tens of million years to evolve to the main sequence stage.

Stellar formation and evolution is hardly in isolation, however. The spatial structure of an open cluster starts out as the relic of the conditions in the parental cloud; that is, massive stars may preferentially be formed in the denser, central parts of a cloud, and via their strong radiation and stellar winds, disrupt the surrounding gas and dust, hindering any subsequent star formation activity. Alternatively, given proper conditions, the ionizing or explosive shocks may compress neighboring clouds, hence triggering the next epoch of star formation. In this scenario, an evolved stellar population and an episodically younger group of stars would coexist in the same region.

M 36 (NGC 1960, R.A. = $05^{\mathrm{h}}36^{\mathrm{m}}18^{\mathrm{s}}$, Decl. = $+34^\circ08'24''$, J2000) is a rich star cluster near the center of the Aur OB1 association. Dominated by about 15 bright ($V \lesssim 11$ mag) stars, the cluster spans an angular extent of $\sim 10'$ (Lynga & Palous 1987). Barkhatova et al. (1985) estimated a reddening $E(B-V) = 0.24$ mag, a distance of 1.20 kpc to the cluster, and an age of 30 Myr from the main-sequence turn-off. With proper motion data (to a limit of $V \sim 14$ mag), BV photometry ($V \lesssim 19$ mag), and using isochrone fitting, Sanner et al. (2000) derived $E(B-V) = 0.25 \pm 0.02$ mag, a distance of 1.32 ± 0.12 kpc, an age of 16^{+10}_{-5} Myr, and metallicity of $Z = 0.02$. Haisch et al. (2001) reported a circumstellar disk fraction of $3\% \pm 3\%$ on the basis of $JHKL$ photometry, suggestive a cluster age of 30 Myr. Sharma et al. (2006) estimated a core radius to be $3\farcm2$ (1.2 pc), extending up to $14'$ (5.4 pc) using the projected radial density profile of the main-sequence stars down to $V \lesssim 18$ mag, and concluded that the core of this relatively young cluster is spherical, whereas the outer region is experiencing external disturbances. Furthermore, from the optical and infrared color-color and color-magnitude diagram analysis, they calculated log(age) = 7.4 (25 Myr) and a distance of ~ 1.33 kpc, with a reddening $E(B-V) = 0.22$ mag. Using Johnson & Morgan (1953) photometry, Mayne & Naylor (2008) reported $E(B-V) = 0.20 \pm 0.02$ mag, a distance of $1.17^{+0.06}_{-0.04}$ kpc, and an age of ~ 20 Myr. Bell et al. (2013), on the other hand, derived an age of 20 Myr, a distance modulus of $10.33^{+0.02}_{-0.05}$ mag (hence a distance of $1.16^{+0.01}_{-0.03}$ kpc), and $E(B-V) = 0.20$ mag. Applying the lithium depletion boundary technique on a sample of very low-mass cluster members, Jeffries et al. (2013) determined an age of 22 ± 4 Myr.

So far, literature results have indicated consistently an age of 20–30 Myr for M 36. In this chapter, we present membership identification using the *Gaia* DR2 data to re-affirm the age and other parameters of the cluster. Moreover, we recognize a nearby ($\sim 2\farcm8$ to the south-west) stellar population in association with molecular clouds that harbor protostellar activity, i.e., with an age less than a couple of Myr, and is physically related to M 36, thereby providing a compelling case of prolonged star formation spanning up to 30 Myr in the cloud complex. We describe in Section 5.2 the data sets used in the study, their quality and limitations, and analysis processes. The results are presented in Section 5.3 on how cluster members are selected, from which the cluster parameters are derived. Despite its Messier entry, somewhat surprisingly, the cloud contents in M 36 have not been well characterized before. Section 5.4 presents the distribution of extinction, in relevance to the young stellar population in the region. This leads to the discussion in Section 5.5, presents molecular cloud structures using CO line emissions and implication of sustaining starbirth processes. We then summarize the main results of our study in Section 5.6.

5.2 Data Sources

This study has made use of a variety of data. Stellar membership is diagnosed on the basis of space position, proper motion, and parallax. A combination of near- to far-infrared photometric data allows us to estimate the extinction distribution and identification of young stellar objects (YSOs). Molecular line emissions have been measured for CO isotopes to trace the spatial extents and kinematics of dense gas, as well as the possible star formation link of YSOs and molecular gas associated with the cluster, with which some of the member stars with radial velocity measurements are compared. A brief description of each of these data sets is given as follows.

5.2.1 Astrometry and Photometry from the *Gaia* DR2

The *Gaia* Data Release 2 (*Gaia* DR2; Gaia Collaboration et al. 2018) furnishes precise astrometry on five parameters, i.e., celestial coordinates, trigonometric parallaxes, and proper motions for more than 1.3 billion objects from the observations and analysis of the European Space Agency *Gaia* satellite (Gaia Collaboration et al. 2016a). In addition to the homogeneous astrometry over the whole sky, *Gaia* DR2 is further enriched with photometry of three broad-band magnitudes in G (330–1050 nm), G_{BP} (330–680 nm), and G_{RP} (630–1050 nm) with unprecedented accuracy. The G band photometry ranges between 3 mag and 21 mag, although stars with $G \lesssim 6$ mag generally have inferior astrometry due to calibration issues. The median uncertainty in parallax is about 0.04 mas for bright ($G \lesssim 14$ mag) sources, 0.1 mas at $G = 17$ mag, and 0.7 mas at $G = 20$ mag (Luri et al. 2018). The corresponding uncertainties in proper motion components are 0.05, 0.2, and 1.2 mas yr^{-1}, respectively (Lindegren et al. 2018). The *Gaia* DR2 also provides radial velocity measurements for sources with $G \lesssim 13$ mag, and a photometric catalogue of about 0.5 million variable stars (Gaia Collaboration et al. 2018).

5.2.2 Infrared Photometry from the UKIDSS, 2MASS, and *Spitzer*

The near-infrared J-, H-, and K-band photometric data were obtained from the UKIDSS DR10PLUS Galactic Plane Survey (GPS; Lawrence et al. 2007) and the 2MASS Point Source Catalog (PSC; Skrutskie et al. 2006). UKIDSS has a finer angular resolution ($0\farcs8$ FWHM, $0\farcs2$ pixels at K) compared to 2MASS ($1''$ FWHM, $2''$ pixels), as well as fainter limits. The UKIDSS GPS has median 5σ detection limits at $J = 19.77$ mag, $H = 19.00$ mag, and $K = 18.05$ mag (Lucas et al. 2008), whereas 2MASS is limited to $J = 15.8$, $H = 15.1$, and $K_S = 14.3$ mag (S/N = 10; Skrutskie et al. 2006). Selection of reliable sources from the UKIDSS catalog was carried out by utilizing the Structured Query Language (SQL[1]) query and adopted the criteria published by Lucas et al. (2008), which eliminates saturated, non-stellar, and unreliable sources near the sensitivity limits. The UKIDSS GPS shows saturation limits at $J = 13.25$ mag, $H = 12.75$ mag, and $K = 12.00$ mag (Lucas et al. 2008). To supplement the UKIDSS saturated sources with 2MASS photometry, we set 0.5 mag fainter than quoted values (Alexander et al. 2013). For the near-infrared bands, photometric uncertainty $\lesssim 0.1$ mag was considered as quality criteria, which give S/N $\gtrsim 10$.

The mid-infrared photometric data for point sources toward the M 36 cluster was obtained from the *Spitzer* Warm Mission (Hora et al. 2012) survey. Magnitudes for Infrared Array Camera (IRAC; Fazio et al. 2004) [3.6] μm and [4.5] μm bands were downloaded from the Glimpse360[2] catalog (Program Name/Id: WHITNEY_GLIMPSE360_2/61070) with a pixel scale of $1\farcs2$ pixel^{-1}. We restricted the sources with uncertainty < 0.2 mag for all the IRAC bands to achieve good quality photometric catalog.

---

[1] `http://wsa.roe.ac.uk/sqlcookbook.html`

[2] `http://www.astro.wisc.edu/sirtf/glimpse360/`

5.2.3 Stellar Parameters from the LAMOST DR5

The Large Sky Area Multi-Object Fiber Spectroscopic Telescope (LAMOST, also called the Guoshoujing Telescope) is a reflecting Schmidt telescope (Wang et al. 1996) with an effective aperture of 3.6–4.9 m, a focal length of 20 m, and a field of view of 5° (Cui et al. 2012; Zhao et al. 2012). After a five-year regular survey[3] conducted between 2012 to 2017, more than eight million spectra were obtained, with a spectral resolution of R $\sim$ 1800 over the wavelength range of 370–900 nm. The raw 2D spectra are processed uniformly with the LAMOST 2D reduction pipeline (Luo et al. 2015) to generate the 1D spectra, from which stellar parameters, including radial velocity (RV), effective temperature (T_{eff}), surface gravity ($\log g$), and metallicity ([Fe/H]), are then derived. Both the 1D spectra and the stellar parameters are publicly available via the LAMOST data releases[4] (Luo et al. 2012; 2015). The stellar parameters are collected from LAMOST DR5[5] for this work.

5.2.4 CO Data and Reduction

The CO observations toward M 36 were conducted on 2 March 2014 using the 13.7 m millimeter-wavelength telescope of the Purple Mountain Observatory (PMO) in Delingha, China, as a part of the Milky Way Imaging Scroll Painting (MWISP) project dedicated to map the molecular gas along the northern Galactic plane (Su et al. 2019). The nine-beam Superconducting Spectroscopic Array Receiver system was used as the front end, and each Fast Fourier transform spectrometer with a bandwidth of 1 GHz provided 16,384 channels and a spectral resolution of 61 kHz (see the details in Shan et al. 2012). The molecular lines of ^{12}CO (J=1–0) in the upper sideband, and ^{13}CO (J=1–0) together with C^{18}O (J=1–0) in the lower sideband were observed simultaneously. Typical system temperature is 150–200 K in the lower sideband and 250–300 K in the upper sideband. The on-the-fly mode was applied with typical sample steps $10''$–$15''$ and scanned along both the Galactic longitude and latitude, in order to reduce the fluctuation of noise. The on-the-fly raw data were then resampled into $30'' \times 30''$ grids and mosaicked to a FITS cube using the GILDAS software package[6].

For the data reported here, the typical sensitivity was about 0.3 K ($T_{\rm mb}$) in ^{13}CO and C^{18}O at the resolution of 0.17 km s^{-1}, and 0.5 K ($T_{\rm mb}$) in ^{12}CO at the resolution of 0.16 km s^{-1}. The beam widths were about $55''$ and $52''$ at 110 GHz and 115 GHz, respectively. The pointing of the telescope has an rms accuracy of about $5''$. It should be noted that any results presented in the figures and tables are on the brightness temperature scale ($T_{\rm R}^*$), corrected with the beam efficiencies (from the status report of the telescope[7]) using $T_{\rm mb} = T_{\rm A}^*/\eta_{\rm mb}$, with a calibration accuracy within 10%.

---

[3] http://www.lamost.org/public/node/311?locale=en

[4] http://www.lamost.org/

[5] http://dr5.lamost.org/

[6] http://www.iram.fr/IRAMFR/GILDAS

[7] http://www.radioast.nsdc.cn/mwisp.php

5.3 Cluster Diagnostics

The proper motion, distance, and radial velocity are key parameters to study the fundamental properties of open clusters, as well as the Galactic dynamics (Dias & Lépine 2005; Wu et al. 2009). A consistent membership probability can also be estimated from the photometric study of the sources (Wu et al. 2007). Open star clusters are embedded in the Galactic disk population and identification of membership is generally affected by the field star contamination. The primary source of field stars are foreground or background stars in the direction of the cluster, that have different origins and evolutionary phases. Hence, the membership analysis of stars in a cluster region has become an intense subject of interest to understand the cluster properties and its evolution.

Identification of members within the cluster region relies on grouping of stars in spatial distribution, proper motion distribution, and measurements of parallax. We used a combination of UKIDSS, 2MASS, and *Gaia* DR2 catalogs to estimate those parameters.

5.3.1 Radial Density Profile

M 36 has been known to have an elongated shape, with the aspect ratio of 0.2–0.3, tilted some 20° away from the plane (Chen et al. 2004; Kharchenko et al. 2009). Using King profiles, Piskunov et al. (2007) estimated an empirical angular radius $16\farcm2$, and a total mass ~ 200 M$_\odot$ within the tidal radius of 9 pc.

In order to determine the cluster extension, we utilized the UKIDSS K-band data. The central coordinates ($\alpha_{2000} = 05^{\rm h}36^{\rm m}18^{\rm s}$, $\delta_{2000} = +34^{\rm d}08^{\rm m}24^{\rm s}$) as informed in the SIMBAD database[8] are adopted to construct the radial density profile with respect to the background. The radial profile is generated by counting the number of stars inside, and divided by the area of, each concentric annulus of 1.5 arcmin width, up to a radius of 35 arcmin. The projected radial stellar density distribution toward M 36 is shown in Figure 5.1. The peak radial density is estimated to be $\sim 26.4 \pm 2.5$ stars arcmin^{-2}, in contrast to the mean background stellar density of $\sim 14.8 \pm 0.3$ stars arcmin^{-2}. The density profile starts to blend with that of the field population at radius $\sim 13\farcm5 \pm 0\farcm4$, which we adopt as the cluster boundary. Our estimation of the cluster radius is consistent with the earlier work of Sharma et al. (2006), determined as $14'$ using optical photometry. The fluctuation around radius $6'$ arises from the possible boundary of the associated molecular cloud (Section 5.5.1 and 5.5.2).

5.3.2 Astrometric Membership Criteria

The velocity dispersion of the cluster members is typically much lower than that of the field stars, so the members can be generally distinguished by their uniform kinematics (Kraus & Hillenbrand 2007). The kinematic membership is tested on the basis of the *Gaia* DR2 proper motion and parallax data. The proper motion distribution of all the

---

[8] `http://simbad.u-strasbg.fr/simbad/sim-fid`

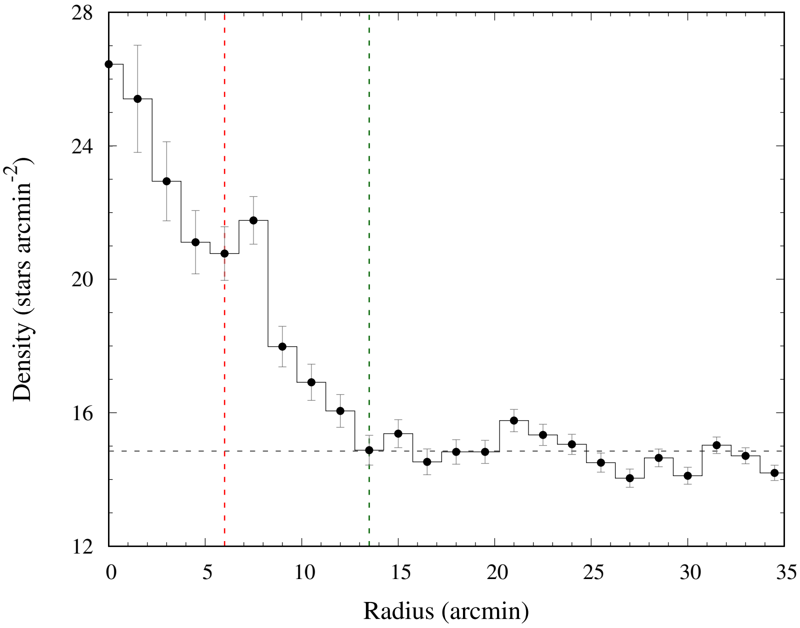

Figure 5.1: Radial density profile of the stars toward M 36, taken from the UKIDSS K-band data. The cluster radius is taken as 13.′5, depicted by the green vertical dashed line, where the cluster density merges with that of the background field, marked by the horizontal line. The red vertical line near 6′ signifies the fluctuation due to the boundary of the molecular cloud structure (Section 5.5.1 and 5.5.2).

sources within a radius of 30$'$ from the center ($\alpha_{2000} = 05^{\rm h}36^{\rm m}18^{\rm s}$, $\delta_{2000} = +34^{\rm d}08^{\rm m}24^{\rm s}$) of M 36 is shown in Figure 5.2(a). There are two distinct enhancements, one for the cluster members ($\mu_\alpha \cos\delta \approx -0.2$ mas yr^{-1}, $\mu_\delta \approx -3.4$ mas yr^{-1}), and the other for field stars ($\mu_\alpha \cos\delta \approx 0.48$ mas yr^{-1}, $\mu_\delta \approx -1.76$ mas yr^{-1}). Conceivably, around the peak for the cluster, the distribution is dominated by members, whereas away from peak the contamination by field stars becomes prominent. A clear separation between the cluster and field motion enables us to select member stars of M 36 relatively reliably.

The proper motion distribution around the cluster peak is analysed for a square region of width 1.5 mas yr^{-1}. The zoomed-in distributions for all the sources within this box region for a radius of 30$'$ and of 13$'\!.5$ from the cluster center are shown in Figure 5.2(b). We estimated the relative contribution of members versus field stars by projecting the distribution along $\mu_\alpha\ cos\delta$ and μ_δ. Each background subtracted rescaled histogram was then fitted with a Gaussian function to quantify the proper motion centroid. The expectation values (μ) of the Gaussian fits, assuming a radius of 30$'$, give $\mu_\alpha \cos\delta = -0.17 \pm 0.01$ mas yr^{-1} and $\mu_\delta = -3.34 \pm 0.02$ mas yr^{-1} with standard deviations (σ) of 0.12 ± 0.01 and 0.14 ± 0.02 mas yr^{-1}, respectively. Likewise, should a radius of 13.5$'$ be adopted, we derived $\mu_\alpha\ \cos\delta = -0.13 \pm 0.01$ mas yr^{-1} and $\mu_\delta = -3.36 \pm 0.02$ mas yr^{-1} with standard deviations of 0.16 ± 0.02 and 0.16 ± 0.02 mas yr^{-1}, respectively. We adopted the proper motion center of the cluster as the mean of the above two values, i.e., $\mu_\alpha \cos\delta = -0.15 \pm 0.01$ mas yr^{-1} and $\mu_\delta = -3.35 \pm 0.02$ mas yr^{-1}. The optimal range of proper motions is selected within a radius of 0.5 mas yr^{-1} ($\simeq 3\sigma$) from this center. In Figure 5.2(e) and 5.2(f), the normalization of the histograms permits us to estimate the integrated number of members along $\mu_\alpha\ cos\delta$ as 208, and along μ_δ as 257, enabling an estimate of the number of missing members (incompleteness) after the parallax constraint is introduced.

We further constrained the membership by including *Gaia* DR2 parallax measurements. Figure 5.3 compares the parallaxes for stars in the cluster region (radius $\simeq 13'\!.5$), with those in a nearby control field, centered around R.A. $= 05^{\rm h}36^{\rm m}14^{\rm s}$, Decl. $= +33°21'22''$ (J2000) ($\ell = 175\overset{\circ}{.}1877$; $b = 0\overset{\circ}{.}6383$), roughly 47$'$ south, with the same sky area as the cluster region. Overplotted are the stars that are located within the cluster region, and satisfying the proper motion criteria (average proper motion < 0.5 mas yr^{-1} from the proper motion center). It is assuring to see a sharp rise in the parallax range between 0.70 ± 0.11 mas and 0.90 ± 0.08 mas. The parallax range 0.7–0.9 mas is thus adopted to further refine the membership selection. The number of stars satisfying the positional (inside the cluster region), kinematic (inside the proper motion range), and parallax criteria are 207, which follows to a variation in the incompleteness factor of ∼1–19%.

5.3.3 Cluster Members

We have identified a total of 200 member candidates by imposing the astrometric and kinematic criteria within the cluster region, that is, within a radius of $\simeq 13'\!.5$, with proper motion less than 0.5 mas yr^{-1} from the cluster proper motion center ($\mu_\alpha\ cos\delta = -0.15$ mas yr^{-1}, $\mu_\delta = -3.35$ mas yr^{-1}), and parallax between 0.7 mas to 0.9 mas. The

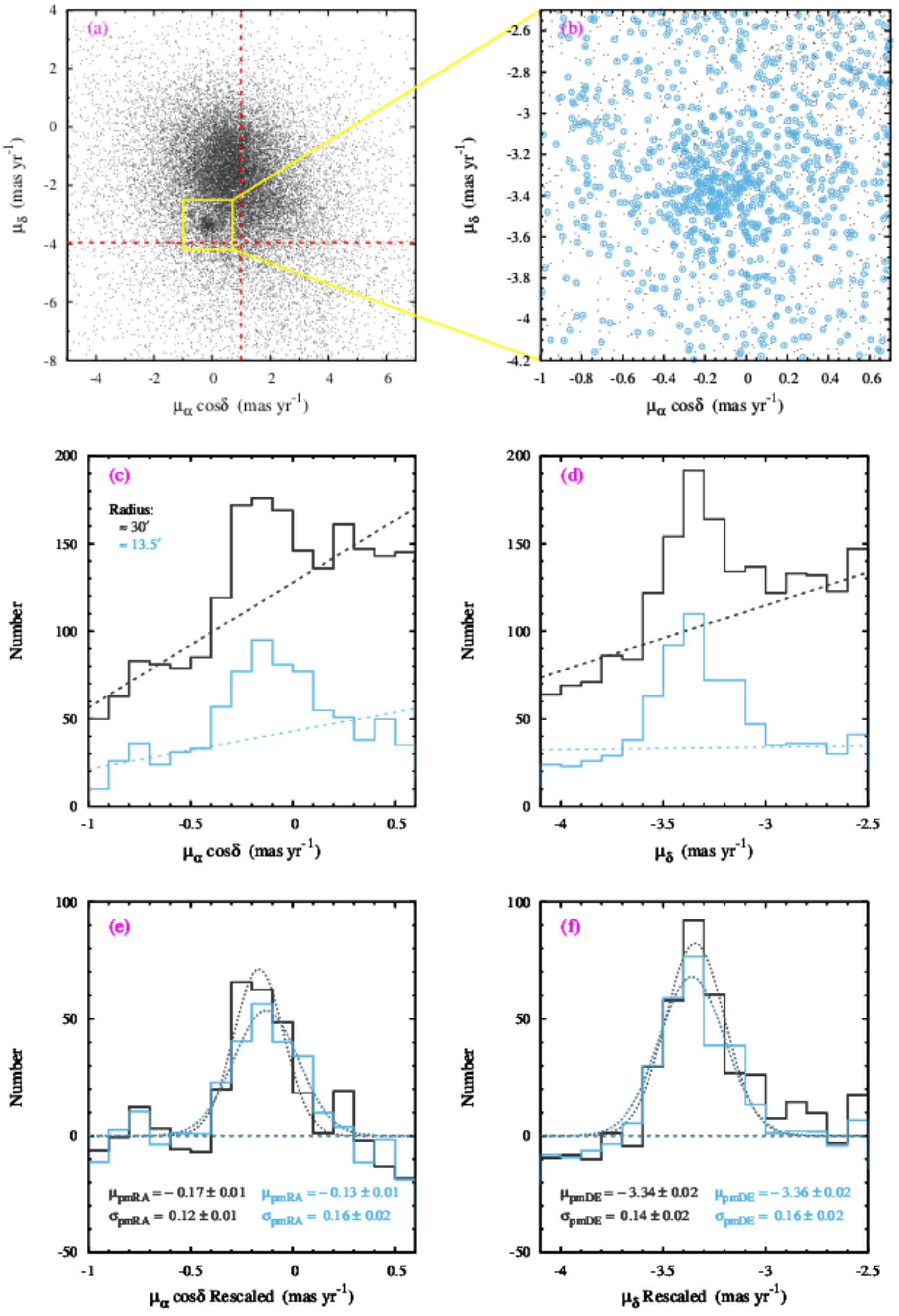

Figure 5.2: (a): The proper motion vector plot for all the sources toward M 36 within a radius of 30′. Proper motion of M 36 as listed in SIMBAD (Loktin & Beshenov 2003) is presented by red dashed lines, which deviates from our analysis based on *Gaia* DR2 results. (b): Enlargement to show the yellow square in (a), that is, a width of 1.5 mas yr^{-1} centered around the most concentrated range. (c): Histograms of $\mu_\alpha \cos\delta$ in (b) contrasting the enhancement in the cluster region and in the field. (d): The same as in (c) but for μ_δ. (e): The background subtracted rescaled distributions, together with a Gaussian fit, of (c). The black and blue colors represent the sources within 30′ and 13′.5, respectively. (f): The same as in (e) but for the distributions in (d). See text (Section 5.3.2) for details.

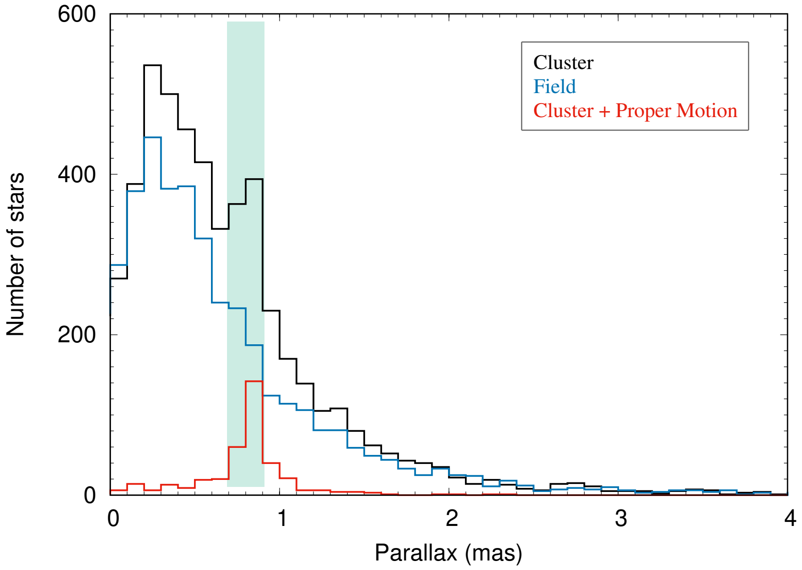

Figure 5.3: Parallax for all the sources, marked by the histogram in black, within the cluster region (radius of 13′.5), and for those within the control field with the same sky area as the cluster region, marked in blue. The sources within the cluster region and also satisfy the proper motion criteria are plotted in red. The shade depicts the parallax range adopted for the cluster.

median of the parallax for the members is obtained as 0.82 ± 0.07 mas, corresponding to a distance of 1.20 ± 0.13 kpc. The photometric and astrometric parameters of all the member candidates are listed in Table 5.1. The spatial distributions of the members are shown in Figure 5.4. Among a total of 7948 sources within the cluster region, 757 are found to satisfy the parallax criteria alone and 402 sources satisfy the proper motion criteria alone, with 200 sources satisfying all the above criteria. It is to be noted that, among the members list, 94% sources have parallax errors less than 20%. Moreover, for those sources that satisfy the membership criteria, but have higher parallax errors (20% or above), we compared their distribution with the theoretical isochrones in both color-magnitude diagrams (Figure 5.5(b) and 5.5(e)), to be presented in the next Section. Additionally 12 sources are thus included as members. In total, among the 200 members, 182 sources have reliable photometry and 18 sources have higher photometric uncertainty in any of the J, H, K, [3.6], or [4.5] bands.

Our selection does not completely reject field stars; some fraction of the candidates may well be field stars. To estimate the level of contamination, we choose the same control field as in the previous section, with the same sky area, and exercised the same set of selection criteria as in the cluster region. We obtained 16 sources in the control field that share similar kinematics. This gives a false positive rate of 8% in the candidate sample, indicating statistically 184 of the 200 sources to be true members of the cluster.

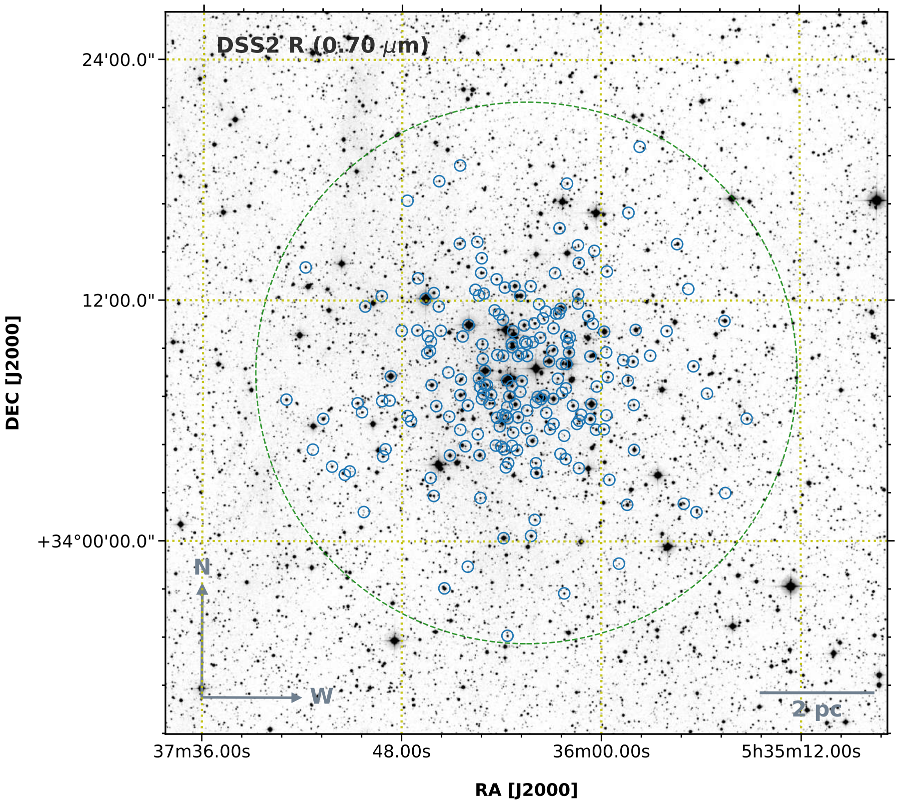

Figure 5.4: Spatial distribution of the member candidates of M 36 (marked with blue circles), overlaid on the DSS2 R 0.70 μm image. The green dashed circle represents the cluster extent of a radius of 13.′5.

Table 5.1: Photometry and astrometry of members toward M 36.
The table is published in its entirety in the electronic edition of Panja et al. (2021)

ID No.	R.A. (J2000) (deg)	Decl. (J2000) (deg)	J (mag)	H (mag)	K (mag)	[3.6] (mag)	[4.5] (mag)	G (mag)	G_{BP} (mag)	G_{RP} (mag)	$\mu_\alpha \cos\delta$ (mas yr^{-1})	μ_δ (mas yr^{-1})	Parallax (mas)	Distance (kpc)
1	84.039139	34.123608	13.622	13.238	13.117	13.050	12.993	15.048	15.522	14.399	-0.113	-3.539	0.8658	1.120
			± 0.026	± 0.028	± 0.030	± 0.038	± 0.036	± 0.002	± 0.007	± 0.005	± 0.072	± 0.052	± 0.0369	$^{+0.05}_{-0.04}$
2	84.141708	34.312340	14.709	14.195	14.042	13.786	13.798	16.460	17.091	15.688	0.033	-3.630	0.8516	1.146
			± 0.003	± 0.003	± 0.005	± 0.049	± 0.059	± 0.004	± 0.025	± 0.007	± 0.158	± 0.111	± 0.0811	$^{+0.12}_{-0.10}$
3	84.270081	34.062000	13.341	13.043	12.932	12.824	12.823	14.546	14.917	14.003	-0.086	-3.008	0.7292	1.322
			± 0.021	± 0.022	± 0.026	± 0.035	± 0.037	± 0.000	± 0.002	± 0.001	± 0.061	± 0.045	± 0.0357	$^{+0.07}_{-0.06}$
4	84.220413	34.203709	13.458	13.065	12.957	12.858	12.822	14.829	15.260	14.229	-0.045	-3.414	0.8494	1.141
			± 0.023	± 0.022	± 0.024	± 0.043	± 0.047	± 0.001	± 0.003	± 0.002	± 0.063	± 0.048	± 0.0362	$^{+0.05}_{-0.05}$
5	84.065506	34.064941	13.849	13.517	13.415	13.292	13.303	15.273	15.735	14.645	-0.124	-3.478	0.8375	1.158
			± 0.001	± 0.001	± 0.003	± 0.043	± 0.041	± 0.001	± 0.005	± 0.004	± 0.078	± 0.055	± 0.0505	$^{+0.07}_{-0.07}$
6	84.093369	34.065090	13.426	13.166	13.041	12.982	12.952	14.611	14.990	14.065	-0.010	-3.149	0.8782	1.104
			± 0.023	± 0.026	± 0.026	± 0.036	± 0.029	± 0.000	± 0.002	± 0.002	± 0.056	± 0.040	± 0.0313	$^{+0.04}_{-0.04}$
7	84.094398	34.133839	9.035	9.081	9.088	9.135	9.064	9.078	9.096	9.044	-0.151	-3.451	0.7819	1.241
			± 0.022	± 0.019	± 0.018	± 0.039	± 0.034	± 0.001	± 0.002	± 0.002	± 0.131	± 0.097	± 0.0646	$^{+0.11}_{-0.09}$
8	84.114609	34.129707	13.381	13.129	13.073	13.017	12.899	14.607	14.976	14.053	-0.371	-3.372	0.8466	1.144
			± 0.029	± 0.030	± 0.029	± 0.040	± 0.040	± 0.000	± 0.002	± 0.002	± 0.053	± 0.039	± 0.0300	$^{+0.04}_{-0.04}$
9	84.121284	34.128357	12.934	12.707	12.614	12.646	12.505	13.989	14.300	13.512	-0.002	-3.314	0.8558	1.133
			± 0.022	± 0.022	± 0.023	± 0.039	± 0.033	± 0.000	± 0.002	± 0.001	± 0.057	± 0.041	± 0.0383	$^{+0.05}_{-0.05}$
10	84.211266	34.137028	...	11.372	9.986	9.923	9.877	10.188	10.251	10.071	-0.588	-3.433	0.8461	1.147
			...	± 0.000	± 0.000	± 0.038	± 0.023	± 0.001	± 0.002	± 0.003	± 0.096	± 0.073	± 0.0485	$^{+0.07}_{-0.06}$

5.3.4 Color-Magnitude Diagram Analysis

Figure 5.5 compares the color-magnitude diagram for stars seen toward the cluster region with that toward the control field region, with photometric data collected from *Gaia* DR2 and UKIDSS, and converted to absolute magnitudes by adopting the distance values computed by Bailer-Jones et al. (2018) from the *Gaia* parallax, which provides empirically better estimate of distances for all the stars with parallaxes published in the *Gaia* DR2, using a probabilistic inference approach, which takes into account for the nonlinearity of the transformation and the positivity constraint of distance.

The average age of the members is estimated by comparing with theoretical PARSEC isochrones (Bressan et al. 2012; Marigo et al. 2017; Pastorelli et al. 2019). The photometric sensitivity curves from Maíz Apellániz & Weiler (2018) are assumed for the *Gaia* sources, as they give empirically the best fit to our data. The majority of the members are consistent with an age between 5 to 30 Myr, with a best fit age of 15 Myr as seen in Figures 5.5(b) and 5.5(e). The estimated age is slightly younger than the values reported in literature (Section 5.1), where the age consistently varied from 20 Myr to 30 Myr. The candidate sample in this analysis is limited down to $G \sim 20.3$ mag, $G_{BP} \sim 21.1$ mag, $G_{RP} \sim 19.0$ mag, $J \sim 17.6$ mag, and $K \sim 16.7$ mag, equivalent to member masses $\gtrsim 0.6$ $M_\odot$.

5.3.5 Luminosity Function and Mass Function

The luminosity function of the cluster is derived by statistically subtracting the number of stars in the control field from that toward the cluster region, for each magnitude bin. Field stars are chosen on the basis of satisfying the same proper motion and parallax criteria as for the member candidates. The decontaminated distribution of the luminosity function, generated with both the G and J bands is depicted in Figure 5.6(a). The luminosity function peaks around 14–15 mag for G band and 13–14 mag for J band, after which it declines swiftly owing to the data incompleteness.

The mass function of the cluster is derived on the basis of luminosity function and is presented in Figure 5.6(b). Member masses are estimated according to the PARSEC isochrones of an age of 15 Myr (Section 5.3.4), corrected for a distance of 1.22 kpc (Section 5.3.3) and reddening $E(B-V) = 0.25$ mag (Sanner et al. 2000), with a polynomial interpolation of discrete data points. The slope of a power-law least-squares fit to the mass function, expressed as $\Gamma = d \log N(\log m)/d \log m$, where $N(\log m)$ is the number of stars per unit logarithmic mass, up to the photometric sensitivity, gives a slope of $\Gamma = -1.37 \pm 0.18$ for the G band, and a slightly steeper $\Gamma = -1.55 \pm 0.14$ for the J band. The mass range used to derive the mass function is $1.38 \lesssim M/M_\odot \lesssim 7.11$ for the G band and $1.28 \lesssim M/M_\odot \lesssim 7.54$ for the J band.

In comparison to literature works, Sanner et al. (2000) derived the cluster mass function with a slope of $\Gamma = -1.23 \pm 0.17$ for the mass interval $0.72 \lesssim M/M_\odot \lesssim 9.40$, on the basis of proper motion membership and statistical field star subtraction. Using the V band photometry and a statistical field star subtraction approach, Sharma et al. (2008) reported a slope of $\Gamma = -1.80 \pm 0.14$ for the mass range $1.01 \lesssim M/M_\odot \lesssim 6.82$. Recently,

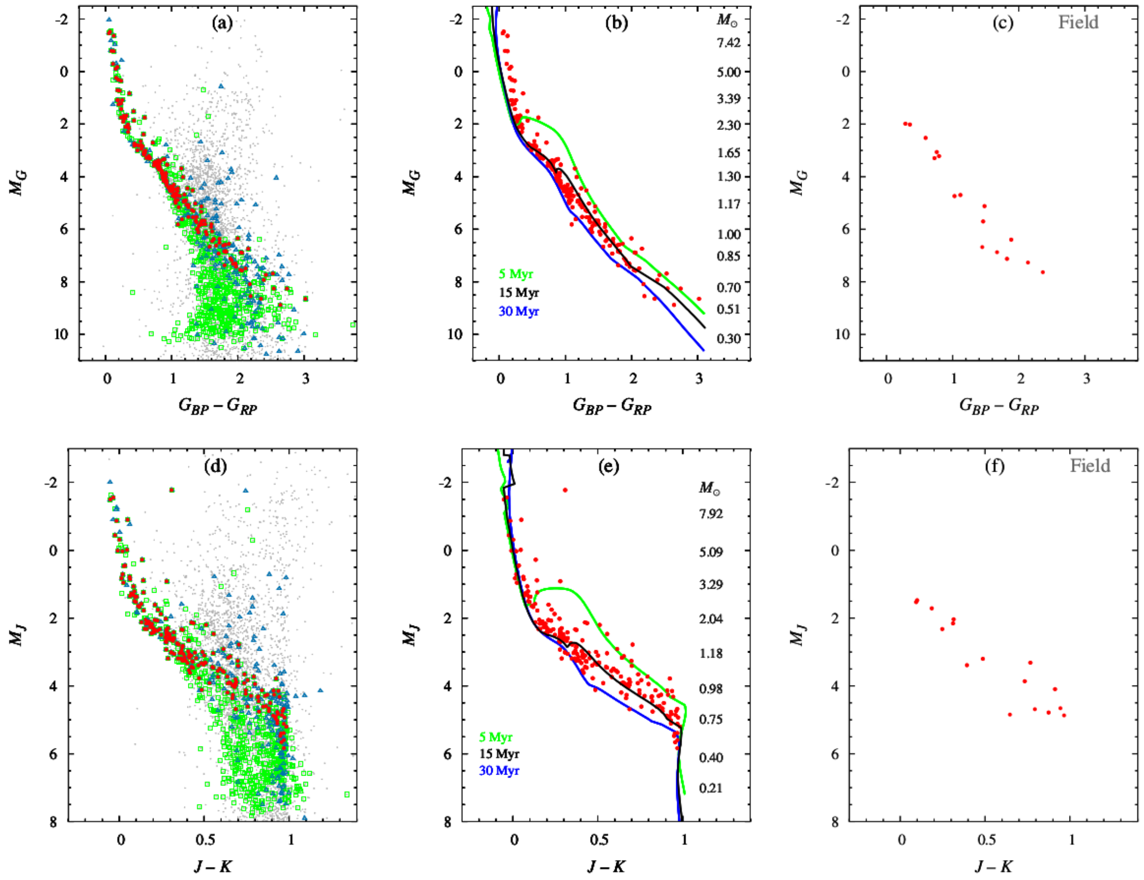

Figure 5.5: Color-magnitude diagrams for (top panels) the *Gaia* DR2 data, and (bottom panels) the UKIDSS data. The gray dots represent all in the cluster region, whereas the blue symbols mark the stars passing the proper motion selection only, the green ones are stars passing the parallax selection only, and the red symbols are stars satisfy both criteria, so are member candidates. The central panels compares the member candidates with the PARSEC isochrones of ages 5, 15, and 30 Myr, assuming a reddening correction $E(B-V) = 0.25$ mag (Sanner et al. 2000) and metallicity [Fe/H]$= -0.15$. The stellar masses according to the 15 Myr isochrone are indicated.

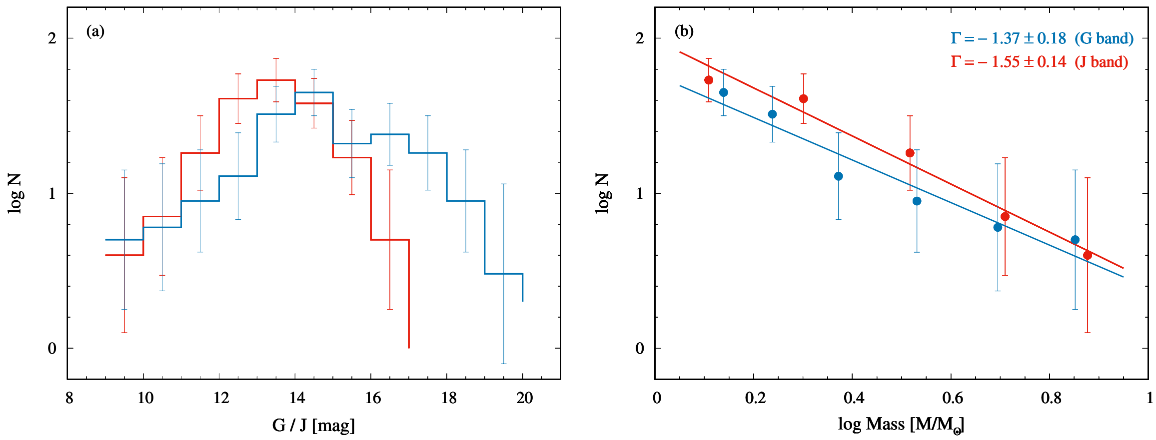

Figure 5.6: (a) The luminosity function of the cluster generated with G (blue) or J (red) band, after removing field star contamination. The error bars represent Poisson errors. (b) The mass function of the cluster derived from the luminosity function using the PARSEC isochrones of an age of 15 Myr, adjusted according to the cluster distance and reddening.

Joshi et al. (2020) estimated $\Gamma = -1.26 \pm 0.19$ for the mass range $0.72 \lesssim M/M_{\odot} \lesssim 7.32$, by considering members only. Our results, based on reliable membership above ~ 1 solar mass selected with *Gaia* parallax and proper motions plus contamination subtraction, fall within the values published in the literature, and are consistent with the canonical value of $\Gamma = -1.35$ in the solar neighborhood (Salpeter 1955).

5.4 The Young Stellar Population

The overall distribution of dust in a cloud can be traced by measuring the extinction of background starlight (Lada et al. 1994). However, because the dust clouds are often clumpy, it is challenging to get a complete census of detectable background stars, particularly toward embedded sources (Gutermuth et al. 2005). The situation is mitigated in near-infrared wavelengths where the dust opacity is modest and the reddening law appears universal (Jones & Hyland 1980; Martin & Whittet 1990; Whittet et al. 1993; Flaherty et al. 2007). We have used measurements of infrared color excess, together with certain aspects of stellar number counts of background stars, to map the extinction distribution throughout the cloud.

5.4.1 Extinction Map

Given that optical extinction decreases with increasing wavelength, observations made at longer wavelengths can detect more background stars through a cloud, and probe deeper cloud depths (Straw & Hyland 1989; Dickman & Herbst 1990). We utilized the H and K band photometry from the UKIDSS catalog, and constructed a number density image by defining a grid over the target area, following the method outlined in Gutermuth et al. (2005). Briefly, the region was divided into uniform grids of size $5'' \times 5''$. The 20 nearest-neighbor sources from the center of each grid were selected to calculate the mean and standard deviation of the $(H - K)$ color for each grid, excluding the sources for which the $(H - K)$ values deviated $\gtrsim 3\sigma$ from the mean value. The mean $(H - K)$ color for each grid then was converted to A_K, using the reddening law $A_K = 1.82 \times [(H - K)_{\rm obs} - (H - K)_{\rm int}]$, the difference between the observed and the intrinsic color (Flaherty et al. 2007).

From a nearby comparison field with little extinction, the average intrinsic color $(H - K)_{\rm int}$ was estimated to be ~ 0.2 mag. To restrict our analysis as far as possible to background objects, we have selected only sources with little extinction ($J - H <$ 1.0 mag, $H - K < 0.6$ mag) for analysis (Panja et al. 2020). The resulting extinction map is displayed in Figure 5.7. The derived extinction values range from $A_V \simeq 1.33$–22.82 mag, or $A_K \simeq 0.12$–2.05 mag. Inspection of the extinction map reveals a compact region ($\sim 1\rlap{.}'9 \times 1\rlap{.}'2$, centering around $\alpha_{2000} = 84\rlap{.}^{\circ}023$, $\delta_{2000} = +34\rlap{.}^{\circ}103$) with excessive extinction ($A_V \sim 22.8$ mag). The rest of the cluster has otherwise relatively low extinction, with $A_V \lesssim 4.56$ mag.

An extinction map thus produced is limited in angular resolution by the availability of detectable background stars. Moreover, the extinction value along a particular line of sight is estimated in a statistical manner (Lada et al. 1994). Empirically, we found a $\sim 5''$ grid size, and ~ 20 nearest neighbor stars to be optimal choices, as a compromise between sensitivity and resolution. Our extinction map with an angular resolution of $5''$ and sensitivity down to $A_V \sim 27$ mag serves to guide the identification of heavily embedded sources such as protostellar objects, as will be discussed in the next section.

5.4.2 YSOs from the Infrared Photometry

A certain combination of infrared colors can be used to distinguish YSOs at different evolutionary stages, as the amount of excessive infrared emission arising from the young circumstellar disks and infalling envelopes diminishes with age. We use such a color-color diagram to diagnose the possible nature of our targets. Lacking longer wavelength IRAC [5.8] and [8.0] μm detection, we utilized IRAC [3.6] and [4.5] μm along with UKIDSS H and K band photometry to characterize the YSOs (Panja et al. 2020) toward M 36.

It has been shown that $[3.6]-[4.5]$ is a useful YSO class discriminant color (Allen et al. 2004; Megeath et al. 2004), provided that the colors are dereddened. The dereddened ($[[3.6]-[4.5]]_0$ versus $[K-[3.6]]_0$) color-color diagram is displayed in Figure 5.8. To deredden a source, we estimated its line-of-sight extinction from the extinction map (Section 5.4.1) and exercised the reddening laws from Flaherty et al. (2007) to compute the dereddened colors. We used the set of equations developed by Gutermuth et al. (2009) to identify the YSOs based on different color criteria. To minimise contamination from extragalactic sources, an additional brightness cut was applied on the dereddened [3.6] μm magnitude by requiring a Class II object to have $[3.6]_0 < 14.5$ mag and a Class I object to satisfy $[3.6]_0 < 15$ mag (Gutermuth et al. 2009). While the majority of the field stars and main-sequence stars have dereddened colors about 0.0 mag to 0.2 mag,

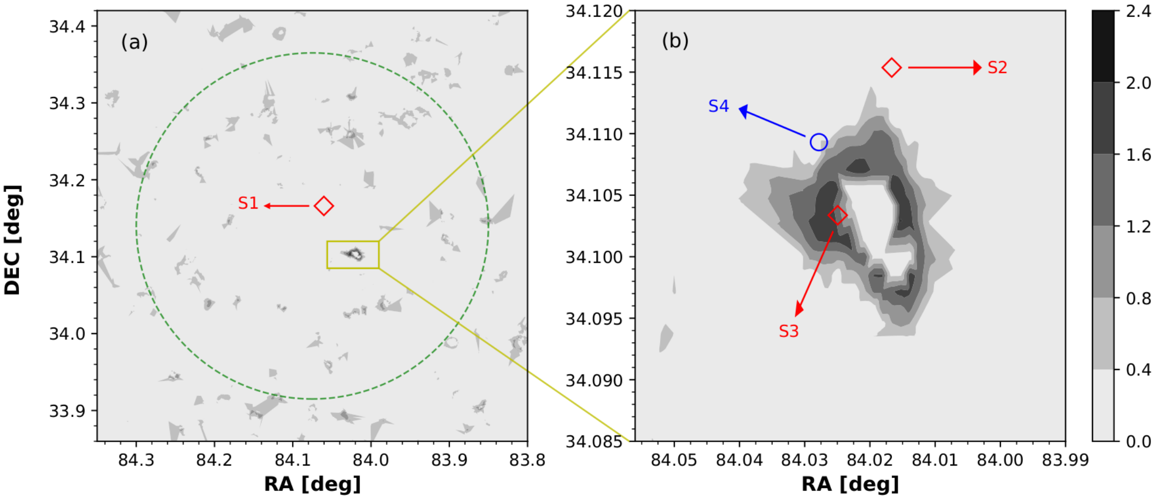

Figure 5.7: (a) The K-band extinction map generated using the UKIDSS photometry. The green dashed circle depicts the 13$'\!.$5 cluster radius. The yellow box marks the region of very high extinction, with A_V up to $\sim$ 22.8 mag. (b) The extinction distribution of the yellow box in (a), in which the S1, S2, and S3 (all Class I objects) and S4 (a Class II object) YSOs are identified (Section 5.4.2). The A_K values are represented by the gray-scale contours.

three Class I and one Class II candidates stand out, with three of them in close physical association with, signifying ongoing star formation in, the dusty clump depicted in Figure 5.7. The photometric parameters of these YSOs are listed in Table 5.2.

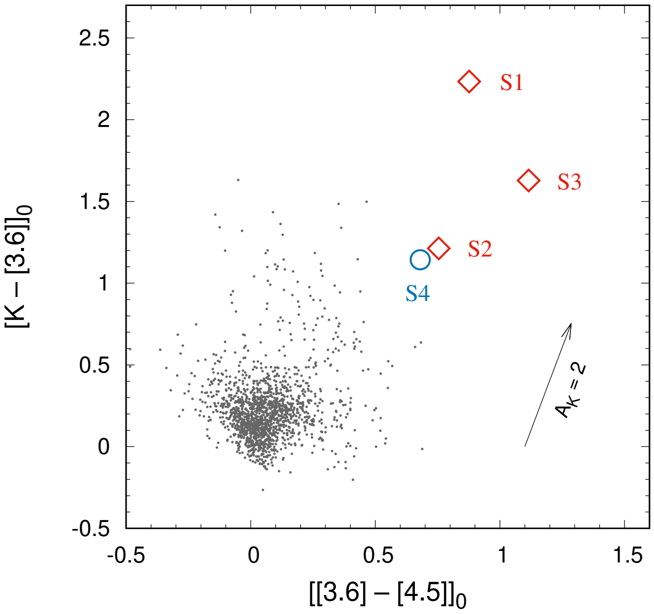

Figure 5.8: Dereddened color-color diagram from the *Spitzer* and UKIDSS photometry, showing the distribution of field stars and main-sequence sources (gray dots), Class II (blue circle), and Class I objects (red diamonds). The black arrow marks the reddening vector for $A_K = 2$ mag.

Table 5.2: Photometry and astrometry of YSOs

Star ID	R.A. (J2000) (deg)	Decl. (J2000) (deg)	J (mag)	H (mag)	K (mag)	[3.6] (mag)	[4.5] (mag)	Distance (kpc)	Type
S1	84.060254	+34.166009	18.922 ± 0.062	17.953 ± 0.059	16.718 ± 0.040	14.435 ± 0.048	13.546 ± 0.037	...	Class I
S2	84.016659	+34.115367	13.73 ± 0.026	12.555 ± 0.023	11.717 ± 0.020	10.441 ± 0.039	9.671 ± 0.031	$1.395^{+0.40}_{-0.26}$	Class I
S3	84.024939	+34.103370	13.397 ± 0.033	11.975 ± 0.028	10.487 ± 0.022	8.81 ± 0.041	7.683 ± 0.032	...	Class I
S4	84.027821	+34.109306	16.577 ± 0.008	15.357 ± 0.006	14.397 ± 0.005	13.205 ± 0.045	12.513 ± 0.04	...	Class II

Table 5.3: Flux parameters of the YSOs used to fit the SEDs

Band	Flux (mJy) values S1	S2	S3	S4	Catalog
V	...	0.642 ± 0.096	0.136 ± 0.020	...	NOMAD
J	0.043 ± 0.003	5.134 ± 0.133	6.977 ± 0.230	0.373 ± 0.003	2MASS
H	0.067 ± 0.004	9.734 ± 0.224	16.607 ± 0.465	0.737 ± 0.004	2MASS
K	0.137 ± 0.005	13.713 ± 0.274	42.573 ± 0.936	1.162 ± 0.006	2MASS
3.6 μm	0.467 ± 0.022	18.487 ± 0.721	83.035 ± 3.404	1.450 ± 0.065	IRAC
4.5 μm	0.685 ± 0.025	24.303 ± 0.753	151.65 ± 4.853	1.774 ± 0.071	IRAC
8.28 μm	...	...	563 ± 56	...	*MSX*
14.65 μm	...	...	1287 ± 193	...	*MSX*
21.34 μm	...	...	2067 ± 413	...	*MSX*
12 μm	...	...	871 ± 130	...	*IRAS*
25 μm	...	...	2610 ± 391	...	*IRAS*
60 μm	...	...	10700 ± 1605	...	*IRAS*
100 μm	...	...	15900 ± 2385	...	*IRAS*

5.4.3 Spectral Energy Distribution of the YSOs

To reveal the underlying stellar and circumstellar properties of the young objects, we fitted their spectral energy distributions (SEDs) using theoretical models (Zhang et al. 2015). We used the radiative transfer models of Robitaille et al. (2006; 2007) to derive the physical parameters of the YSOs. The grids of models cover a wide range of parameters, consisting of pre-main-sequence stars plus a combination of axisymmetric circumstellar disks, infalling flattened envelopes, and outflow cavities. These models also span a large range of possible evolutionary stages (from deeply embedded protostars to stars surrounded only by optically thin disks) and stellar masses (from 0.1 to 50 $M_\odot$). The radiative transfer solution is subject to parameter degeneracy, but fluxes covering a sufficiently wide range of wavelengths can reduce this degeneracy.

The photometric fluxes of the YSOs are collected from NOMAD (V; Zacharias et al. 2004), UKIDSS (J, H, and K; Lawrence et al. 2007), IRAC ([3.6] and [4.5] μm; Fazio et al. 2004), *MSX* (8.28, 14.65, and 21.34 μm; Sjouwerman et al. 2009), and *IRAS* (12, 25, 60, and 100 μm; Neugebauer et al. 1984), wherever available, detailed in Table 5.3. We required at least a minimum of five data points for each source to construct the SEDs, which then are fitted with the distance and visual extinction as input parameters to constrain the SEDs. We varied the distance as 1.20 ± 0.13 kpc (Section 5.3.2) and extinction $A_V \sim 1.3$ mag to 23 mag (Section 5.4.1). For each source, the "best-fit" model is defined by constraining $\chi^2 - \chi^2_{\text{best}} < 3$ (per data point), where χ^2_{best} quantifies the goodness-of-fit parameter. The SEDs and their best-fit models of the four YSOs are shown in Figure 5.9. Expecting that the fitted SEDs are moderately degenerate, we adopted the weighted mean and standard deviations of each physical parameter, and they are given in Table 5.4. The degeneracies obtained for sources S1, S2, S3, and S4 are 36, 6, 2, and 9, respectively.

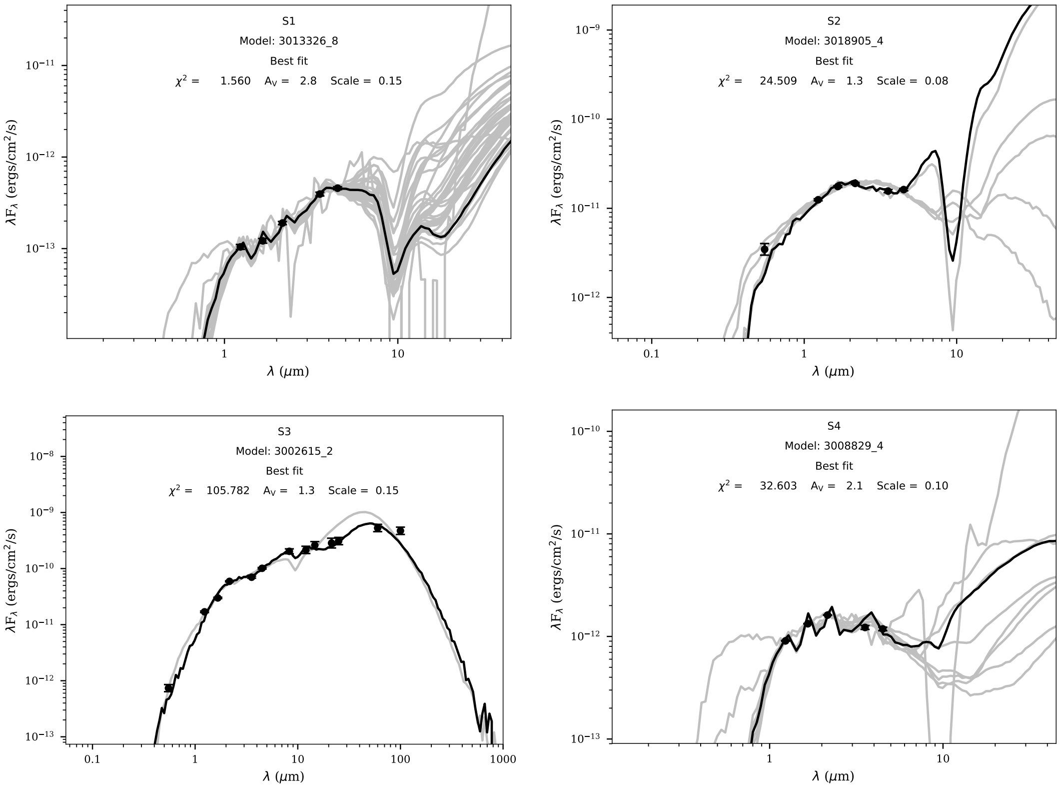

Figure 5.9: Spectral energy distributions of the YSOs, fitted with the grid models of Robitaille et al. (2007). In each case, the black filled circles are the observed fluxes listed in Table 5.3. The solid black and grey lines indicate, respectively, the best-fit model and consecutive good fits for, per data point, $\chi^2 - \chi^2_{\mathrm{best}} < 3$.

Table 5.4: Physical parameters of embedded sources

Parameter	S1	S2	S3	S4
Age (t) [10^4 yr]	7.41 ± 1.78	3.60 ± 1.20	19.3 ± 6.3	1.30 ± 0.54
Stellar mass (M_*) [$M_\odot$]	0.118 ± 0.017	5.774 ± 1.727	6.492 ± 1.469	0.162 ± 0.013
Stellar radius (R_*) [$R_\odot$]	2.50 ± 0.48	24.65 ± 6.66	17.35 ± 0.46	4.21 ± 1.70
Stellar temperature (T_*) [K]	2833 ± 246	4466 ± 875	6255 ± 939	2931 ± 288
Envelope accretion rate ($\dot{M}_{env}$) [$10^{-5} M_\odot$ yr^{-1}]	3.002 ± 1.219	10.89 ± 2.73	7.026 ± 0.292	0.1077 ± 0.0369
Envelope radius (R_{env}^{max}) [10^3 AU]	1.292 ± 0.461	3.917 ± 0.656	71.44 ± 3.01	1.732 ± 0.738
Envelope cavity angle ($\theta_{\rm cavity}$) [deg]	31.19 ± 5.52	20.60 ± 1.98	45.19 ± 1.07	20.62 ± 3.84
Disk mass (M_{disk}) [$M_\odot$]	$(2.350 \pm 0.335)\times10^{-3}$	$(3.055 \pm 0.152)\ \times10^{-1}$	$(1.564 \pm 0.015)\times10^{-2}$	$(2.038 \pm 0.736)\times10^{-4}$
Disk outer radius ($R_{disk}^{\rm max}$) [AU]	46.96 ± 17.67	113.4 ± 27.92	690 ± 12	16.96 ± 2.36
Disk inner radius ($R_{disk}^{\rm min}$) [AU]	0.039 ± 0.006	1.033 ± 0.153	24.5 ± 0.150	3.21 ± 0.425
Disk accretion rate ($\dot{M}_{disk}$) [$M_\odot$ yr^{-1}]	$(2.429 \pm 0.568)\times10^{-8}$	$(3.593 \pm 0.185)\times10^{-6}$	$(1.426 \pm 0.311)\times10^{-7}$	$(2.427 \pm 0.369)\times10^{-9}$
Total luminosity (L_{tot}) [$L_\odot$]	0.39 ± 0.13	240 ± 69	415 ± 7	1.18 ± 0.43

The SEDs of the YSOs suggest stellar infancy, with ages less than 0.2 Myr. The stellar masses range from $\sim 0.1 M_\odot$ to $6.5 M_\odot$, radii from $\sim 2.5 R_\odot$ to $24.6 R_\odot$, and temperatures from ~ 2830 K to 6260 K. The envelope and disk parameters serve to probe the evolutionary phase. Class I objects typify earlier stages of star formation compared to Class II objects. At the initial phases, the envelope and disk accretion rates are usually high, and then decrease with time. It is expected that envelopes with accretion rates $\lesssim 10^{-6} M_\odot$ yr^{-1} do not contribute significantly to the SED (Robitaille et al. 2007). Among the four objects, S4 has the lowest envelope accretion rate ($\sim 10^{-6} M_\odot$ yr^{-1}), the lowest disk mass ($\sim 10^{-4} M_\odot$), and the lowest disk accretion rate ($\sim 10^{-9} M_\odot$ yr^{-1}), all consistent with our earlier results of S4 being a Class II object. The contribution to the SED from the disk related to that from the envelope is difficult to disentangle, because the envelope may not be largely dispersed yet. The YSO S3 is associated with IRAS 05327+3404 (nickname "Holoea"[9]), first detected by Magnier et al. (1996) and classified as being transitional between Class I and Class II, and in the process of becoming optically exposed (Magnier et al. 1999a; 1999b). This object, with strong far-infrared fluxes, has a very prominent circumstellar disk, extending from an inner radius of ~ 25 AU to an outer radius of ~ 690 AU.

5.5 Cluster Cloud Interaction

5.5.1 Molecular Cloud Morphology and Physical Parameters

Despite being the most abundant molecular species in cold interstellar media, H_2 molecules are difficult to detect due to a lack of a permanent electric dipole moment. CO lines are therefore often used to trace molecular clouds. Using J=1–0 ^{12}CO and ^{13}CO data, we map the molecular cloud structures and estimate their kinematic and physical properties. A compact and massive core is detected around the position $\alpha_{2000} = 84^\circ\!.0308$, $\delta_{2000} = +34^\circ\!.1094$ for which we investigated the intensity, excitation temperature, H_2 column density, and velocity distribution. The complete procedures and expressions used to derive these parameters are detailed in Sun et al. (2020).

Intensity and Excitation Temperature

The total integrated intensity ($I_{\rm CO}$) maps for ^{12}CO (J=1–0) and ^{13}CO (J=1–0), along with the excitation temperature are exhibited in Figures 5.10. The mean intensity of the cloud is calculated to be 8.8 K km s^{-1} using ^{12}CO and 2.6 K km s^{-1} using ^{13}CO. A peak in the intensity is observed at ($\alpha_{2000} = 84^\circ\!.0308$, $\delta_{2000} = +34^\circ\!.1094$) for both isotopologues.

Assuming ^{12}CO is optically thick, we determined the excitation temperature ($T_{\rm ex}$) for each pixel from the peak intensity of ^{12}CO (Sun et al. 2020). The excitation temperature within the cloud core ranges from 4 K to 14 K with a mean of 7 ± 0.6 K.

---

[9] In Hawaiian for "flowing gas"

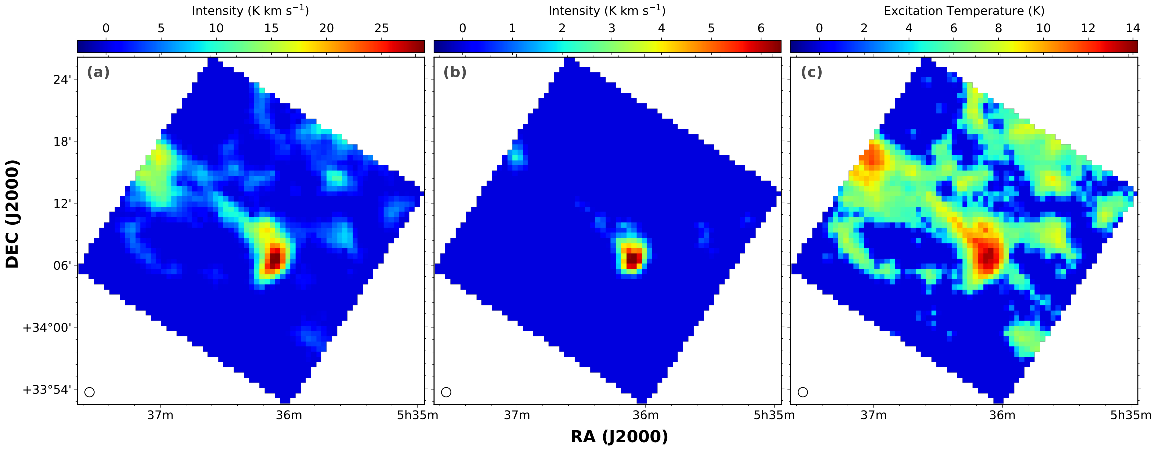

Figure 5.10: (a)-(b) Intensity maps of the molecular gas traced by ^{12}CO and ^{13}CO emission. (c) Excitation temperature map derived from ^{12}CO by assuming optically thick. A small circle at the bottom left represents the beam size.

Radial Velocity

The velocity distribution of the cloud in ^{12}CO and ^{13}CO emission is shown in Figures 5.11. Around the cloud core, the velocity structure shows a uniform distribution and varies between -20 and -22 km s^{-1}. The cloud is found to be confined within a radius of $6'$ from the cluster center $\alpha_{2000} = 84^{\circ}.0750$, $\delta_{2000} = +34^{\circ}.1400$ ($\ell = 174^{\circ}.5345$; $b = 1^{\circ}.0721$). Figure 5.12 presents the CO spectra integrated over the whole region, indicating an average velocity of -20.2 ± 1.7 km s^{-1} for ^{12}CO and -21.5 ± 0.7 km s^{-1} from ^{13}CO.

Molecular Column Density

The H$_2$ column density ($N_{\mathrm{H_2}}$) is estimated by two methods. For ^{12}CO, we adopted a CO-to-H$_2$ conversion factor, $X_{\mathrm{CO}} \equiv N_{\mathrm{H_2}}/I_{\mathrm{CO}} \equiv 2 \times 10^{20}$ cm^{-2} (K km s^{-1})$^{-1}$ (Bolatto et al. 2013), i.e., with the X-factor method; for the area traced by ^{13}CO, the local thermodynamic equilibrium (LTE) method is applied (Sun et al. 2020). The H$_2$ column density in the cloud core varies, for ^{12}CO from 2×10^{20} to 7×10^{21} cm^{-2}, with an average value of 1.5×10^{21} cm^{-2}, and for ^{13}CO from 3×10^{20} to 9×10^{21} cm^{-2}, with an average value of 3.7×10^{21} cm^{-2}. The column density maps for ^{12}CO and ^{13}CO isotopologues are displayed in Figures 5.11(c) for ^{12}CO, and 5.11(d) for ^{13}CO.

H$_2$ Mass

The molecular mass is estimated by integrating the column density over the area of each region. To calculate the H$_2$ mass, again we used the X-factor method for ^{12}CO, and the LTE method for ^{13}CO, and the mass distributions are presented in Figure 5.11(e) and Figure 5.11(f). A compact cloud structure is detected within a radius of $6'$ from the

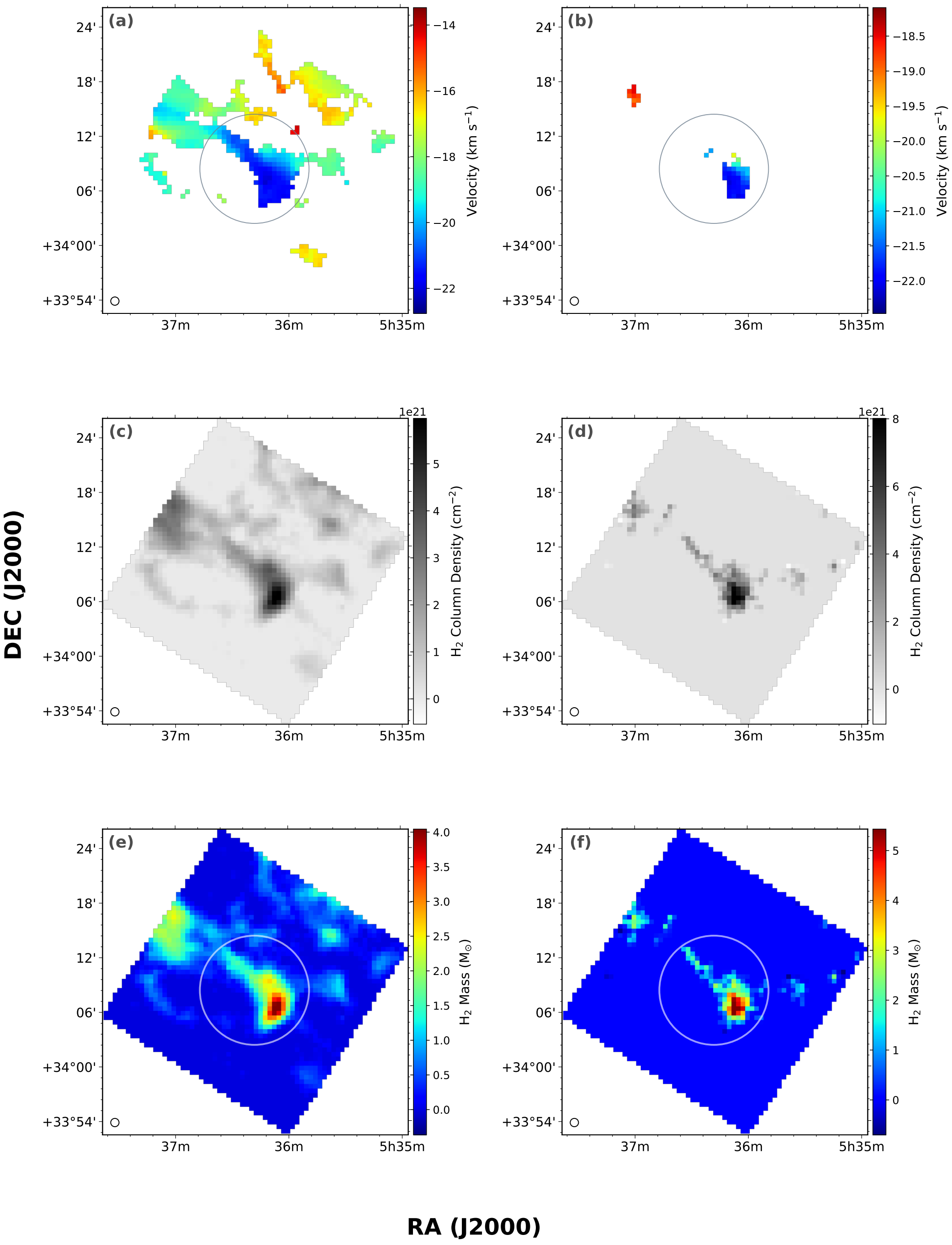

Figure 5.11: The velocity distributions of the emission peaks of (a) ^{12}CO and (b) ^{13}CO. The H_2 column density distributions derived (c) from ^{12}CO by adopting an X-factor of 2×10^{20}, and (d) from ^{13}CO by assuming LTE. The H_2 mass distributions derived from (e) ^{12}CO by the X-factor method, and (f) from ^{13}CO by assuming LTE, by integrating the column density over the velocity channels of the clouds. The circle has a radius of $6'$ from the cluster center ($\alpha_{2000} = 84^{\circ}.0750$, $\delta_{2000} = +34^{\circ}.1400$). A small circle at the bottom left in each panel represents the beam size.

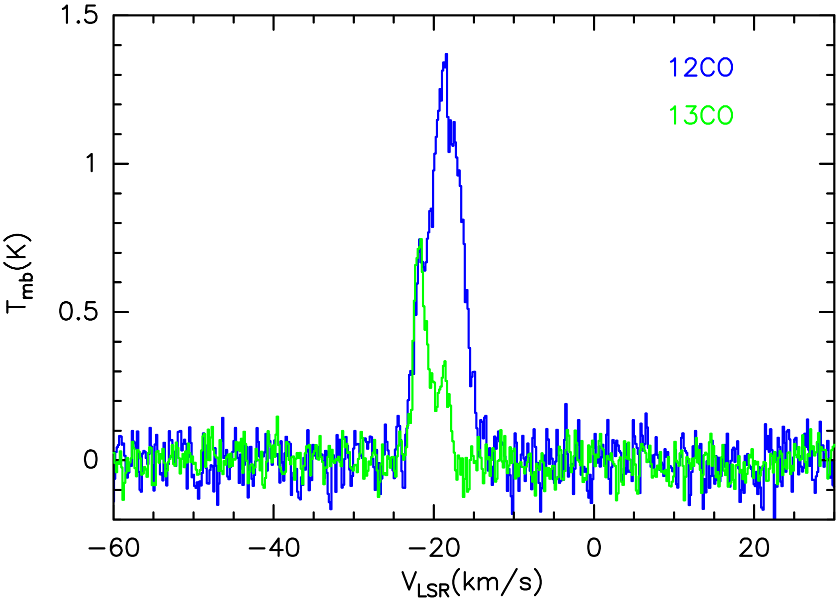

Figure 5.12: Averaged spectra integrated over the whole region. Only pixels with at least three contiguous channels above 3σ are averaged.

cluster center traced by both ^{12}CO and ^{13}CO emission. The total mass of this cloud complex is estimated to be 313 ± 0.9 $M_\odot$ for ^{12}CO and 210 ± 1.2 $M_\odot$ for ^{13}CO. Generally ^{12}CO emission traces the total gas content distributed in the molecular cloud, including lower density ($\sim 10^2$ cm^{-3}) diffuse gas, while the optically thinner ^{13}CO emission traces typically denser ($\sim 10^3$–10^4 cm^{-3}) components, a reason of higher H_2 mass derived from ^{12}CO compared with ^{13}CO.

5.5.2 Physical Association Between the YSOs and Molecular Gas

Of the 200 member candidates of M 36, 16 (8%) were observed as LAMOST DR5 targets. RV measurements were not included in our membership selection, because of the limited amounts of data available, and because of possible variations due to binary orbital motion. The RV and metallicity measurements are presented in Figure 5.13. The RVs of the majority of members range between -5 km s^{-1} and -20 km s^{-1}. This is consistent with that reported by Frinchaboy & Majewski (2008, RV$= -17.83 \pm 0.99$ km s^{-1}), and matches approximately with the RV (≈ -21 km s^{-1}) of the molecular cloud.

The distance to the cloud is uncertain. Adopting RV$= -21$ km s^{-1}, the nominal Milky Way rotation (Reid et al. 2019) suggests a kinematic distance of 1.68 ± 0.05 kpc, placing the cloud somewhat in the background but physical association of the cloud with the cluster (~ 1.2 kpc) cannot be ruled out, in evidence notably of the *Gaia* distance of $1.395^{+0.40}_{-0.26}$ kpc (Table 5.2) for the young object S2 in the cloud. While not unambiguously established at this time, the proximate angular separation, radial velocity, and distance provides tantalizing evidence of a physical connection between the cloud and the cluster.

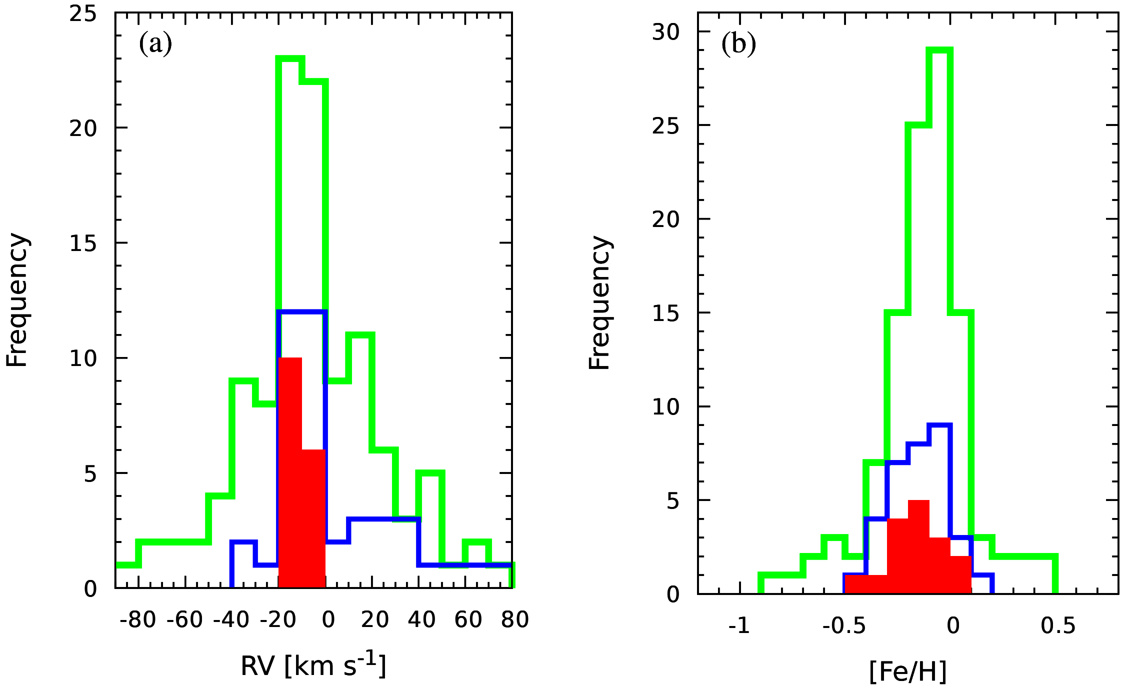

Figure 5.13: (a) Radial velocity (RV) and (b) metallicity ([Fe/H]) distributions of the sources from the LAMOST DR5 data. The color scheme for the histograms is the same as in Figure 5.5, i.e., sources satisfying the parallax criteria only are marked in green, those satisfying the proper motion criteria are in blue, and those satisfying both (member candidates) are in red.

The metallicity distribution of member candidates peaks around -0.1 to -0.2, with an average of -0.15 ± 0.10. Though the dispersion is relatively large, our result, based on a relatively reliable list of members, suggests a subsolar metallicity for M 36.

Star formation activity at the earliest stages (1–2 Myr) is difficult to trace due to heavy dust obscuration. Star formation is believed to be regulated by dense gas in molecular clouds (Gao & Solomon 2004; Wu et al. 2005), and the star formation rate is known to be correlated with the molecular mass (Wong & Blitz 2002; Lada et al. 2010; 2012). Surveys of star-forming regions have demonstrated that approximately 75% of the stars are formed in groups or clusters (Carpenter 2000; Allen et al. 2007; Gutermuth et al. 2009), whereas about 80% of all young stars are located in embedded clusters (Lada & Lada 2003; Porras et al. 2003). Several factors are involved in the formation and early evolution of a cluster, such as the structure of the parental molecular cloud (Samal et al. 2015), fragmentation in the parental cloud due to turbulent motions and/or gravity, dynamical motions of the young stars, and the feedback from young stars (Gutermuth et al. 2009). While infrared surveys are an eminent tool to parameterize young embedded clusters, data at much longer millimeter wavelengths are also powerful to trace the gaseous contents and the distribution of dust throughout a molecular cloud.

A color composite image of the M 36 cluster, made from optical (B band), near-

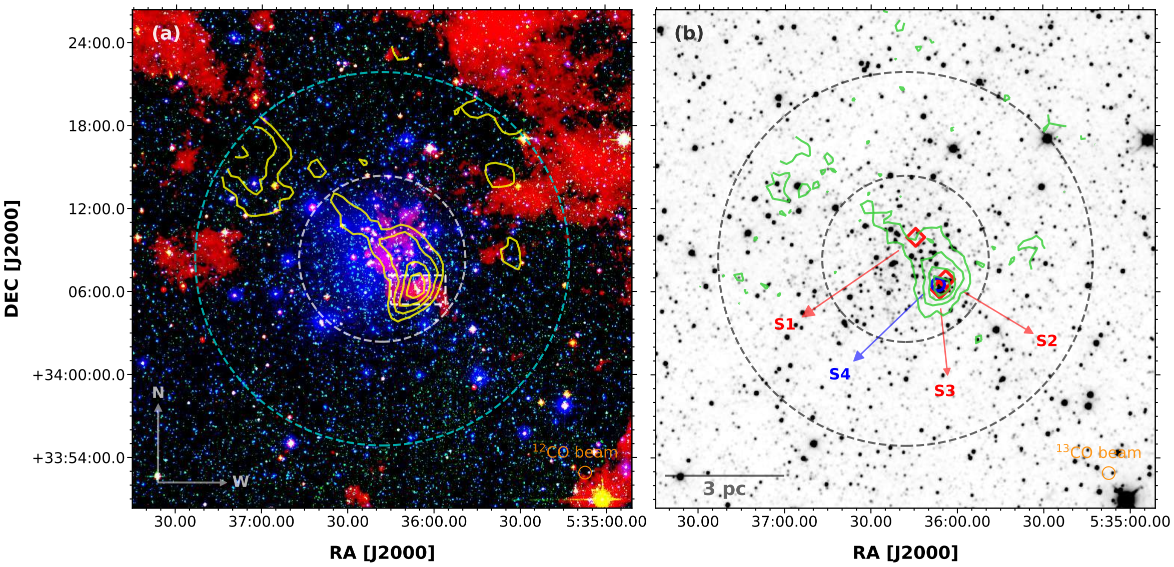

Figure 5.14: (a) Color composite image of M 36 using optical and infrared data, taken from DSS2 *B* 0.44 μm (blue), 2MASS *K* 2.2 μm (green), and *WISE W*3 12 μm (red) for a region of $30' \times 30'$. The ^{12}CO (J=1–0) distribution is traced by the yellow contours, at contour levels of (6.27, 12.55, 18.82, 25.09, and 31.37) K km s^{-1}. The high extinction complex (Section 5.4.1) is depicted by the white rectangle. (b) The corresponding *WISE W*2 4.6 μm image, with the green contours representing the ^{13}CO (J=1–0) integrated intensity, at the contour levels at (1.62, 3.24, 4.86, 6.48, and 8.10) K km s^{-1}. The four YSOs (Section 5.4.2) are indicated. The circles of radii of $6'$ and $13'.5$ mark the possible boundaries of the molecular cloud and of the cluster extension, respectively.

infrared (*K* band), and far-infrared (*WISE/W3* 12 μm) data, is presented as Figure 5.14(a). The *WISE* 12 μm emission, sensitive to warm dust (Dunham et al. 2008), coincides well with the extinction complex and CO gas. The ^{12}CO and ^{13}CO distributions reveal a compact cloud with a linear extent of $\sim 10'.4$ (3.6 pc), extending from north-east to south-west plus a core located at the south-west corner where the three YSOs discussed earlier reside near the densest part, within $\sim 1'$, of the cloud core. This is where active star formation is taking place.

5.5.3 Sustaining Star Formation

The timescale of star formation plays a significant role in the evolution of a star cluster. It depends not only on the initial cloud conditions, such as the density and temperature profiles, but also on how the new-born stars interplay with the remnant clouds, so as to induce the birth of next-generation stars, e.g., by the dynamical compression of an H 2 front, and change in self-gravity (Fukuda & Hanawa 2000). Alternative to clustering, star formation may proceed in an isolated or distributed mode (Koenig et al. 2008; Evans et al. 2009), leading to multiple stellar populations within a cloud (Gratton et al. 2012; Bouy et al. 2015; Bekki & Tsujimoto 2017).

The four YSOs identified by this work are in the proximity of the cloud core, with angular separations of 3.′69 (for S1), 0.′79 (for S2), 0.′46 (for S3), and 0.′15 (for S4). The source S2 has a measured *Gaia* DR2 distance of $1.395^{+0.40}_{-0.26}$ kpc (Table 5.2), matching well with the cluster distance. In particular, S3 coincides spatially with an IRAS source (IRAS 05327+3404), which drives a powerful ionizing outflow with a velocity of ~ 650 km s^{-1}, that aligns with a CO outflow (Magnier et al. 1996). Its SED indicates stellar infancy with ample circumstellar material. S3 is clearly a part of the continuing stellar formation episode in the dense core, and its outflows may have a profound effect on the surrounding environments to prompt future formation of stars.

Star formation processes in an open cluster may span about 5 Myr to 20 Myr (Lim et al. 2016), with the low-mass members spending up to some $\sim 10^8$ years in the pre-main sequence phase (Herbig 1962). Star clusters older than ~ 5 Myr are typified with little parental molecular gas (Leisawitz et al. 1989). M 36, with an age of ~ 15 Myr (Section 5.3.4), is therefore unusual in connection with a nearby voluminous molecular cloud harboring a protostellar population with ages < 0.2 Myr. More evidence is clearly needed to confirm or to discredit the physical connection between the star-forming cloud and the cluster. If the cloud and the cluster share the same formation scenario, this presents a rare case of sustaining star formation in a cloud complex. Even if the cloud happens to be in the intermediate background of the cluster, our discovery of a cloud active in star formation offers added information of the star formation history in this part of the Galactic disk.

5.6 Summary

We report the stellar contents of the nearby young open cluster M 36 using multiwavelength data sets. Cluster membership is diagnosed using five dimensional astrometric parameters. The nature of the young objects and associated molecular cloud is analysed using molecular emission (^{12}CO and ^{13}CO lines), supplemented with infrared photometry. The key outcomes of this work are summarized as follows:

1. A list of 200 member candidates are presented based on proper motions and parallax measurements from the *Gaia* DR2 catalog. Applying the same set of selection criteria on a nearby control field, a false positive rate of 8% is expected.

2. The cluster exhibits a distinct proper motion from the field, with member candidates concentrated within 0.5 mas yr^{-1} around the peak of $\mu_\alpha\ cos\delta = -0.15 \pm 0.01$ mas yr^{-1}, and $\mu_\delta = -3.35 \pm 0.02$ mas yr^{-1}. The parallax measurements of the member candidates suggest a parallax range of 0.7–0.9 mas with a median of 0.82 ± 0.07 mas (distance $\sim 1.20 \pm 0.13$ kpc). The cluster has an angular diameter of $27' \pm 0.'4$, equivalent to a linear extent of 9.42 ± 0.14 pc. The member candidates have an age of ~ 15 Myr, consistent with the literature values.

3. The K-band extinction map leads to identification of a high extinction ($A_V \sim$ 23 mag), small complex ($\sim 1\rlap{.}'9 \times 1\rlap{.}'2$). This high-extinction region coincides with a molecular cloud core, both in ^{12}CO and ^{13}CO. The cloud shows a uniform velocity (-20 to -22 km s^{-1}) structure with a total mass of (2–3)$\times10^2$ M$_\odot$. In addition to spatial association, the cloud's radial velocity agrees with that of the cluster members, indicative of physical association. Four protostars with ages < 0.2 Myr are found, with three of them being located in close proximity to the high extinction complex.

4. The discovery of a molecular cloud harboring stars in their infancy provides new clues on the star formation history in the vicinity of M 36. If the cloud is physically associated with the cluster, this presents a tantalizing case of sustaining starbirth in a cloud complex, with a cluster formed $\sim$ 15 Myr ago, to a dense molecular cloud core currently active in star formation.

Chapter 6

Conclusions

A comprehensive study on the formation and early evolution of stars, in the Galactic scale, from the observational point of view, is presented in this thesis. Dense molecular clouds are an integral part of young star forming regions, where the early phases of stellar evolution begin. At the earliest stages, the young objects encompass a diverse range of activity, out of which the most prominent are collapse, accretion, and outflow. The interactions among such evolving young objects tend to regulate the physical environment of associated molecular clouds. In addition to that, the effects from any external perturbation can trigger the molecular cloud to undergo a structural transformation and initiate the star formation process. The length scale of star formation depends on the distribution and properties of dense gas within the prenatal molecular cloud.

The types of objects that are targeted for this dissertation radiate energy in an arbitrary wavelength coverage, therefore the overall analysis is performed in a multi-wavelength perspective. Within the nm to GHz wavelength range, a large set of observational facilities (astrometric, photometric, and spectroscopic) are available throughout and they are frequently employed in this study. Data that are publicly accessible as well as via direct observations through successful proposal submission system are utilized. The infrared photometric datasets are used to diagnose the YSOs and the dust properties. The infrared imaging maps trace the molecular clouds and filaments. The radio emission surveys detect cloud cores, sub-filaments, and outflows to ionized gas. For the relatively evolved population or at where the opacity has reduced, using the optical data is appropriate to study the kinematic motion and Hα emission of the stellar sources.

In this context, the major consequences of the results are followed up, and in continuation of which the likelihood of the future avenues based on these research works is discussed.

6.1 Summary of Results

The key outcomes of Chapter 3, Chapter 4, and Chapter 5 are summarized in this section.

S242

Stars form preferably in a clustered environment, a fact supported by numerous observational evidences for decades. Some prevalent signposts of star formation are the presence of giant molecular clouds, embedded infrared sources, young stellar clusters, and dense cloud cores. The young region S242 is among one of such sites that depicts star formation activity in a broader scale (length $\sim$ 25 pc). The distance measurements ($\sim$ 2.1 kpc) of the region place it in the Taurus constellation in the Perseus arm. The extinction distribution reveals existence of a filamentary-like structure, along which three peak extinction complexes are identified. The excessive reddening ($A_V \sim$ 16–17 mag) in two of them is suggestive of a heavy amount of dust content across those locations. These two subregions are presumed to be the productive sites for next generation star formation. The S242 region turns to be an efficient stellar birth site by hosting a significant number ($\sim$ 180) of young populations. Moreover, the cospatial distribution of the YSOs and the filamentary-like extinction structure is a convincing evidence of ongoing star formation activity. The clusters of YSOs preferentially coincide with the high extinction complexes, where the dust density is highest. From the theoretical isochrone fitting, the average age of the low-mass (0.1–3.0 $M_\odot$) YSOs is estimated to be $\sim$ 1 Myr, consistent with the age derived from the ratio of Class I to Class II sources. The Hα emission is a pertinent property of young star forming regions, where hydrogen in the medium is continuously ionized by newly formed stars. Thus the detection of Hα emission line stars is a signature of the strength of ionization activity in the region. Thereafter, we have detected a total of 36 Hα emitting sources, among them five sources have infrared excess counterparts. Besides, the S242 site contains an early-type star BD+26 980 of spectral nature B0.5 V, confirmed by spectroscopic observations, that is capable of producing adequate ionizing radiation and restraining the ionization activity. By inspecting the positional distribution of the YSOs, the massive star BD+26 980 is proposed to have played a dominant role in creating a suitable birth place for development of stars by modulating the surrounding environment through high energy stellar wind. Thus, in overall, the S242 site manifests as a combination of multiple young stellar activities, that involves dust, cloud, YSO, and ionization, all happening in a similar timescale.

S112

The optically visible emission nebula S112 is located at a distance of $\sim$ 2.1 kpc in the Cygnus constellation of the Orion arm. A larger dimension ($2\overset{\circ}{.}0 \times 0\overset{\circ}{.}83$) of molecular cloud structure with a spatially elongated appearance is found to be associated with this region. In order to trace the dust distributions along the line of sight that might have influences on the background stellar radiation, an extinction map is generated. The $15''$ resolution map depicts the existence of manifold dust clumps that are appearing to be chained in a filamentary pattern. However, throughout the region the reddening is comparatively low (average $A_V \sim$ 2.24 mag) and varies consistently with a peak of $A_V \sim$ 7 mag. About a total of 180 YSOs are identified using a combination of mid-infrared (3.4–22 μm) colors and for those deeply embedded YSOs that lack reliable higher wavelength (> 4.6 μm) photometry, a combination of dereddened near- to mid-infrared (2.16–4.6 μm) colors is used. While majority of them have an average age $\sim$ 1 Myr, a scattered population with age variation in the range 0.1–10 Myr is also noticeable. Additionally, the detection of a huge number (> 350) of Hα emitters infers that the region is dominated by strong ionization activity. In the spatial map, the YSO concentrations are highest at three locations, referred as subregions (Clump A, S112, and Clump B), at where the molecular cloud density is also maximum. Besides, the positional sequence between the YSOs and the high density molecular cloud axis distributed in an elongated filamentary pattern is a signpost of continuing star formation activity in a broad scale. Among the three subregions, the densest cloud is traced at S112 and is distributed in a relatively extended zone that accumulates highest number of YSOs. The fraction of younger population increases toward the Galactic east and in the central location compared with the Galactic west. The S112 subregion hosts a very early-type (O8 V) star BD+45 3216, which is responsible for creating an almost circular (radius $\sim$ 3 pc) shaped luminous H II region at its surroundings. The pressure of the expanding H II region has forced the nearby molecular clouds to compress and form a dense shell-like structure. Because of the fact that, BD+45 3216 is located almost at the edge of the cloud distribution, the bright arc-like structure has taken roughly a semi-circular shape, a manifestation of the blister-type H II region. The presence of a large number of YSOs at the peripherals of the arc-like structure is a possible outcome of the triggered star formation induced by BD+45 3216. Along the filamentary complex (linear extension $\sim$ 80 pc) several dense cloud cores are detected in the CO maps, a signature of cloud collapse and fragmentation. Even the S112 subregion has fragmented into two dense separable cores. Along the filament, the cloud velocity is dynamic and increases toward the Galactic west compared to the east at the order of $\sim$ 1 km s^{-1}. Nevertheless, the kinematic maps produce a median cloud velocity of ~ -3.65 km s^{-1}. Together, this site offers to study the physical mechanisms related with early stages of stellar formation and evolution from large scale molecular cloud distributions.

M 36

The formation of protostars from molecular clouds takes place within a timescale of few tens of million years, after which the remanent diffuse clouds are left to dissipate. The stars, that are formed in a group, are still exposed to subsequent internal stellar dynamics, surviving which they evolve as a star cluster in proximity to one another. In relevance to that, an extensive survey of the Galactic open cluster M 36 is conducted to diagnose the stellar members, alongside to that, YSOs, dust and cloud properties are analysed to infer the evolutionary nature of this cluster. M 36 is among very few of those open clusters that exhibits a distinct proper motion from the field, revealed by the deeper coverage *Gaia* DR2 astrometry. Furthermore, the parallax distribution shows a clearly distinguishable peak for the cluster members in comparison with the field population. The radial density profile provides the cluster extension (angular diameter $\sim 9.42 \pm 0.14$ pc), at where the density drops and roughly merges with the background field. Based on the position and space motion, about 200 member candidates with a contamination rate of 8% are identified, having a median distance of $\sim 1.20 \pm 0.13$ kpc. The members are moderately evolved and relatively younger (average age $\sim$ 15 Myr) in nature. In analogous to this evolved stellar population toward M 36, a compact and dense cloud core along the same line of sight is discovered. The cloud core mapped by CO lines coexists with a heavily obscured ($A_V \sim 23$ mag), small dust complex ($\sim 1\rlap{.}'9 \times 1\rlap{.}'2$) traced by the high resolution ($5''$) extinction map. Interestingly, three out of the four detected YSOs, which are in a very early stage (age $<$ 0.2 Myr) of their evolution, reside within this complex. Notably, one YSO is associated with an *IRAS* source, that drives a high velocity ($\sim$ 650 km s^{-1}) ionized outflow roughly co-aligned with the CO outflow. Another one has a *Gaia* DR2 parallax measurement, that corresponds to a distance of $1.395^{+0.40}_{-0.26}$ kpc, matching well with the cluster distance. Clearly, the YSOs are a part of the ongoing stellar formation activities within the compact cloud core. The cloud kinematics is consistent throughout the structure with a uniform velocity continuity of -20 to -22 km s^{-1}. The molecular cloud mass ((2–3)$\times 10^2$ M$_\odot$) is relatively higher in comparison with its compact scale (linear extension $\sim$ 3.6 pc). Besides, radial velocity of the cloud agrees well with that of the cluster members, indicative of physical association. However, the kinematic distance ($\sim 1.68 \pm 0.05$ kpc) of the cloud places it somewhat in the background. All together, M 36 presents a sustaining starbirth scenario where multiple stellar formation episodes are continuing in a time interval of $\sim$ 15 Myr. Considering the spatial correspondence, radial velocity, and distance between the cloud and the cluster, a tantalizing case of physical association between them is ambiguously established.

In concise notes, an extensive survey primarily on the YSO identification and characterization is carried out. Their association and interaction with the molecular clouds, in addition to cloud parameters are exploited. A quantitative dust mapping and hence measurement of the extinction is conducted. The ionized gas properties in relevance with the massive stars are analysed. The space motion and kinematics of the stellar sources are studied

6.2 Future Prospects

The ever expanding observational technology, with improved sensitivity and resolution, is continuously creating new dimensions of scientific opportunities at the forefront of modern astrophysics. The 3.6 m Devasthal Optical Telescope (DOT; Sagar et al. 2020) reaches photometric depths of $B = 24.5 \pm 0.2$ mag (optical) and $K = 18.2 \pm 0.1$ mag (near-infrared), that are well suited for the search of YSOs still within the protostellar envelopes and very low-mass stellar populations (M dwarfs, brown dwarfs). The Atacama Large Millimeter/submillimeter Array (ALMA), operating at wavelengths 0.32–3.6 mm, is a state-of-the-art high-precision telescope, that is able to capture light from some of the coldest objects in the Universe. The James Webb Space Telescope (*Webb*; Kalirai

2018) with a 6.5 m primary mirror, supporting imaging, spectroscopy, and coronagraphy covering the wavelength range 0.6–28.8 μm, is capable to address the fundamental questions about the origins of planets, stars, and galaxies in the Universe. These are a subset among the revolutionary instruments of similar kind designed for breakthrough research in many astronomical disciplines. Like so, in the verge of existing and upcoming facilities, the following relevant topics can be enlightened.

Filaments to Core Formation

A proposed fact that the prestellar core mass is determined by the fragmentation of gravitationally unstable filaments (André et al. 2010). However, this theory is somewhat inappropriate to explain the high-mass (> 8 $M_\odot$) star formation situations, where a *clump-fed* (Wang et al. 2010a) scenario is more favourable. It is an accretion related model, in which the cores gain mass through simultaneous collapse of the surrounding parsec-scale mass reservoir. More often, the dense and massive cores are observed at the locations where filaments converge, because of the higher gradient of gravitational acceleration. Therefore a correlation is supposed to exist between the clump morphology and the core mass. As a clump/core evolutionary tracer, high-angular resolution (sub)millimeter dust continuum observations of cold and compact sources are necessary.

Protostellar Jets and Outflows

The earliest phases of the formation of a star encompass the dramatic events of collapse and condensation of prestellar core, formation of disk, accumulation of central mass through accretion, development of jets and outflow activities, and variation in the outflow velocity with time. Protostellar outflows are the dynamically evolving systems that provide fossil records of the accretion histories of the source stars. For the youngest (Class 0) objects, jets can be detected in (sub)millimeter (CO, SiO, and SO molecules) and infrared (H_2 molecule) wavelengths. Conversely, for the relatively evolved (Class I and Class II) population, jets can be traced in atomic and ionized (O I, Hα, and S II) gas (Bally 2016). High spatial and velocity resolution (sub)millimeter and infrared observations are suitable for a systematic search of jet and outflow components driven by the protostellar objects. Thus to construct a standard theory on the significance of protostellar jets and outflows based on the observational findings, a large number of extremely young objects at different evolutionary phases are needed to be studied.

Protoplanetary Disk Evolution

Protoplanetary disks have dual significance both on the star and the planet formation. Disks serve as a bridge for the prestellar core mass accretion as well as progenitor for the planetary systems constraining the mass for planet formation. The disk mass and size are observable properties that are dependent on two key cluster environments, external photoevaporation and dynamical truncation (Parker et al. 2021). The molecular line emissions from the dust- and gas-rich disks around young stars encode information on disk ionization levels, temperature structures, kinematics, metallicity, and gas surface densities. The high spatial resolution observations of a large number of molecular lines are essential to expand our understanding on the mechanism of planet formation within the protoplanetary disks.

Young Open Cluster Kinematics

The interplay among evolving young stars in combination with tidal forces or differential rotation decide the fate of a star cluster. Open clusters are recognized as efficient tracer of the Galactic disk population and structure. In order to improve our understanding on how the young stars regulate the dynamics of a star cluster, the stellar parameters such as extinction, radial, and projected rotational velocities, and chemical abundances of a large number of young open clusters are needed to be characterized. In addition, a light of information on the early phases of substellar (very low-mass objects and brown dwarfs) formation and evolution can be shed.

Besides, some more interesting topics have gained current importance. Such as, massive star formation and their feedback, interstellar bubbles and dark clouds, mapping of magnetic field geometry in clouds through polarization, variability in YSOs, SED fitting of YSOs, flares in young brown dwarfs, and so on.

Bibliography

Adams, F. C. 2010, ARA&A, 48, 47, doi: 10.1146/annurev-astro-081309-130830

Adams, F. C., Lada, C. J., & Shu, F. H. 1987, ApJ, 312, 788, doi: 10.1086/164924

Adams, F. C., Proszkow, E. M., Fatuzzo, M., & Myers, P. C. 2006, ApJ, 641, 504, doi: 10.1086/500393

Alexander, M. J., Kobulnicky, H. A., Kerton, C. R., & Arvidsson, K. 2013, ApJ, 770, 1, doi: 10.1088/0004-637X/770/1/1

Allen, L., Megeath, S. T., Gutermuth, R., et al. 2007, in Protostars and Planets V, ed. B. Reipurth, D. Jewitt, & K. Keil, 361. https://arxiv.org/abs/astro-ph/0603096

Allen, L. E., & Strom, K. M. 1995, AJ, 109, 1379, doi: 10.1086/117370

Allen, L. E., Calvet, N., D'Alessio, P., et al. 2004, ApJS, 154, 363, doi: 10.1086/422715

Anderson, L. D., Bania, T. M., Balser, D. S., et al. 2014, ApJS, 212, 1, doi: 10.1088/0067-0049/212/1/1

André, P. 1994, in The Cold Universe, ed. T. Montmerle, C. J. Lada, I. F. Mirabel, & J. Tran Thanh Van, 179

André, P., Di Francesco, J., Ward-Thompson, D., et al. 2014, in Protostars and Planets VI, ed. H. Beuther, R. S. Klessen, C. P. Dullemond, & T. Henning, 27, doi: 10.2458/azu_uapress_9780816531240-ch002

Andre, P., & Montmerle, T. 1994, ApJ, 420, 837, doi: 10.1086/173608

Andre, P., Ward-Thompson, D., & Barsony, M. 1993, ApJ, 406, 122, doi: 10.1086/172425

André, P., Men'shchikov, A., Bontemps, S., et al. 2010, A&A, 518, L102, doi: 10.1051/0004-6361/201014666

André, P., Revéret, V., Könyves, V., et al. 2016, A&A, 592, A54, doi: 10.1051/0004-6361/201628378

Andrews, S. M., & Williams, J. P. 2005, ApJ, 631, 1134, doi: 10.1086/432712

—. 2007, ApJ, 659, 705, doi: `10.1086/511741`

Astropy Collaboration, Robitaille, T. P., Tollerud, E. J., et al. 2013, A&A, 558, A33, doi: `10.1051/0004-6361/201322068`

Astropy Collaboration, Price-Whelan, A. M., Sipőcz, B. M., et al. 2018, AJ, 156, 123, doi: `10.3847/1538-3881/aabc4f`

Bachiller, R. 1996, ARA&A, 34, 111, doi: `10.1146/annurev.astro.34.1.111`

Bailer-Jones, C. A. L., Rybizki, J., Fouesneau, M., Mantelet, G., & Andrae, R. 2018, AJ, 156, 58, doi: `10.3847/1538-3881/aacb21`

Bally, J. 2007, Ap&SS, 311, 15, doi: `10.1007/s10509-007-9531-7`

—. 2016, ARA&A, 54, 491, doi: `10.1146/annurev-astro-081915-023341`

Barentsen, G., Vink, J. S., Drew, J. E., et al. 2011, MNRAS, 415, 103, doi: `10.1111/j.1365-2966.2011.18674.x`

Barentsen, G., Farnhill, H. J., Drew, J. E., et al. 2014, MNRAS, 444, 3230, doi: `10.1093/mnras/stu1651`

Barkhatova, K. A., Zakharova, P. E., Shashkina, L. P., & Orekhova, L. K. 1985, Azh, 62, 854

Bastian, N., & Lardo, C. 2018, ARA&A, 56, 83, doi: `10.1146/annurev-astro-081817-051839`

Baumgardt, H., & Makino, J. 2003, MNRAS, 340, 227, doi: `10.1046/j.1365-8711.2003.06286.x`

Beerer, I. M., Koenig, X. P., Hora, J. L., et al. 2010, ApJ, 720, 679, doi: `10.1088/0004-637X/720/1/679`

Bekki, K., Jeřábková, T., & Kroupa, P. 2017, MNRAS, 471, 2242, doi: `10.1093/mnras/stx1609`

Bekki, K., & Tsujimoto, T. 2017, ApJ, 844, 34, doi: `10.3847/1538-4357/aa77ae`

Bell, C. P. M., Naylor, T., Mayne, N. J., Jeffries, R. D., & Littlefair, S. P. 2013, MNRAS, 434, 806, doi: `10.1093/mnras/stt1075`

Berriman, G. B., & Good, J. C. 2017, PASP, 129, 058006, doi: `10.1088/1538-3873/aa5456`

Bertin, E., & Arnouts, S. 1996, A&AS, 117, 393, doi: `10.1051/aas:1996164`

Bertoldi, F. 1989, ApJ, 346, 735, doi: `10.1086/168055`

Bessell, M. S., & Brett, J. M. 1988, PASP, 100, 1134, doi: 10.1086/132281

Bisbas, T. G., Wünsch, R., Whitworth, A. P., & Hubber, D. A. 2009, A&A, 497, 649, doi: 10.1051/0004-6361/200811522

Blitz, L., Fich, M., & Stark, A. A. 1982, ApJS, 49, 183, doi: 10.1086/190795

Blitz, L., & Shu, F. H. 1980, ApJ, 238, 148, doi: 10.1086/157968

Bohlin, R. C., Savage, B. D., & Drake, J. F. 1978, ApJ, 224, 132, doi: 10.1086/156357

Bolatto, A. D., Wolfire, M., & Leroy, A. K. 2013, ARA&A, 51, 207, doi: 10.1146/annurev-astro-082812-140944

Bonnarel, F., Fernique, P., Bienaymé, O., et al. 2000, A&AS, 143, 33, doi: 10.1051/aas:2000331

Bouy, H., Bertin, E., Barrado, D., et al. 2015, A&A, 575, A120, doi: 10.1051/0004-6361/201425505

Bressan, A., Marigo, P., Girardi, L., et al. 2012, MNRAS, 427, 127, doi: 10.1111/j.1365-2966.2012.21948.x

Calvet, N., Muzerolle, J., Briceño, C., et al. 2004, AJ, 128, 1294, doi: 10.1086/422733

Calzetti, D. 2001, PASP, 113, 1449, doi: 10.1086/324269

Carpenter, J. M. 2000, AJ, 120, 3139, doi: 10.1086/316845

—. 2001, AJ, 121, 2851, doi: 10.1086/320383

Chambers, K. C., Magnier, E. A., Metcalfe, N., et al. 2016, arXiv e-prints, arXiv:1612.05560. https://arxiv.org/abs/1612.05560

Chavarría, L. A., Allen, L. E., Hora, J. L., Brunt, C. M., & Fazio, G. G. 2008, ApJ, 682, 445, doi: 10.1086/588810

Chen, W. P., Chen, C. W., & Shu, C. G. 2004, AJ, 128, 2306, doi: 10.1086/424855

Churchwell, E. 2004, in Astronomical Society of the Pacific Conference Series, Vol. 322, The Formation and Evolution of Massive Young Star Clusters, ed. H. J. G. L. M. Lamers, L. J. Smith, & A. Nota, 329–338

Clark, J. S., Negueruela, I., Crowther, P. A., & Goodwin, S. P. 2005, A&A, 434, 949, doi: 10.1051/0004-6361:20042413

Cohen, J. G., Frogel, J. A., Persson, S. E., & Elias, J. H. 1981, ApJ, 249, 481, doi: 10.1086/159308

Collins, K. A., Kielkopf, J. F., Stassun, K. G., & Hessman, F. V. 2017, AJ, 153, 77, doi: 10.3847/1538-3881/153/2/77

Condon, J. J., Cotton, W. D., Greisen, E. W., et al. 1998, AJ, 115, 1693, doi: 10.1086/300337

Crampton, D., & Fisher, W. A. 1974, Publications of the Dominion Astrophysical Observatory Victoria, 14, 283

Cui, X.-Q., Zhao, Y.-H., Chu, Y.-Q., et al. 2012, Research in Astronomy and Astrophysics, 12, 1197, doi: 10.1088/1674-4527/12/9/003

Danks, A. C., & Dennefeld, M. 1994, PASP, 106, 382, doi: 10.1086/133390

de Graauw, T., Helmich, F. P., Phillips, T. G., et al. 2010, A&A, 518, L6, doi: 10.1051/0004-6361/201014698

de Grijs, R., Gilmore, G. F., Johnson, R. A., & Mackey, A. D. 2002, MNRAS, 331, 245, doi: 10.1046/j.1365-8711.2002.05218.x

Deharveng, L., Zavagno, A., & Caplan, J. 2005, A&A, 433, 565, doi: 10.1051/0004-6361:20041946

D'Ercole, A., Vesperini, E., D'Antona, F., McMillan, S. L. W., & Recchi, S. 2008, MNRAS, 391, 825, doi: 10.1111/j.1365-2966.2008.13915.x

Dewangan, L. K., Baug, T., Ojha, D. K., et al. 2017, ApJ, 845, 34, doi: 10.3847/1538-4357/aa7da2

Dias, W. S., & Lépine, J. R. D. 2005, ApJ, 629, 825, doi: 10.1086/431456

Dickman, R. L., & Herbst, W. 1990, ApJ, 357, 531, doi: 10.1086/168940

Dickman, R. L., Horvath, M. A., & Margulis, M. 1990, ApJ, 365, 586, doi: 10.1086/169512

Dinnbier, F., & Walch, S. 2020, MNRAS, 499, 748, doi: 10.1093/mnras/staa2560

Dobashi, K., Bernard, J.-P., Yonekura, Y., & Fukui, Y. 1994, ApJS, 95, 419, doi: 10.1086/192106

Dobashi, K., Uehara, H., Kandori, R., et al. 2005, PASJ, 57, S1, doi: 10.1093/pasj/57.sp1.S1

Doi, Y., Takita, S., Ootsubo, T., et al. 2015, PASJ, 67, 50, doi: 10.1093/pasj/psv022

Draine, B. T. 2003, ARA&A, 41, 241, doi: 10.1146/annurev.astro.41.011802.094840

Drew, J. E., Greimel, R., Irwin, M. J., et al. 2005, MNRAS, 362, 753, doi: 10.1111/j.1365-2966.2005.09330.x

Dunham, M. M., Crapsi, A., Evans, Neal J., I., et al. 2008, ApJS, 179, 249, doi: 10.1086/591085

Dutta, S., Mondal, S., Samal, M. R., & Jose, J. 2018, ApJ, 864, 154, doi: 10.3847/1538-4357/aadb3e

Dyson, J. E., & Williams, D. A. 1980, Physics of the interstellar medium

Elias, J. H., Frogel, J. A., Matthews, K., & Neugebauer, G. 1982, AJ, 87, 1029, doi: 10.1086/113185

Elmegreen, B. G. 1993, in Protostars and Planets III, ed. E. H. Levy & J. I. Lunine, 97

Elmegreen, B. G. 1998, in Astronomical Society of the Pacific Conference Series, Vol. 148, Origins, ed. C. E. Woodward, J. M. Shull, & J. Thronson, Harley A., 150. https://arxiv.org/abs/astro-ph/9712352

Elmegreen, B. G. 2007, ApJ, 668, 1064, doi: 10.1086/521327

Elmegreen, B. G., & Lada, C. J. 1977, ApJ, 214, 725, doi: 10.1086/155302

Evans, D. W., Riello, M., De Angeli, F., et al. 2018, A&A, 616, A4, doi: 10.1051/0004-6361/201832756

Evans, N. J., I., & Lada, E. A. 1991, in Fragmentation of Molecular Clouds and Star Formation, ed. E. Falgarone, F. Boulanger, & G. Duvert, Vol. 147, 293

Evans, Neal J., I., Dunham, M. M., Jørgensen, J. K., et al. 2009, ApJS, 181, 321, doi: 10.1088/0067-0049/181/2/321

Falgarone, E., Phillips, T. G., & Walker, C. K. 1991, ApJ, 378, 186, doi: 10.1086/170419

Farias, J. P., Fellhauer, M., Smith, R., Domínguez, R., & Dabringhausen, J. 2018, MNRAS, 476, 5341, doi: 10.1093/mnras/sty597

Fazio, G. G., Hora, J. L., Allen, L. E., et al. 2004, ApJS, 154, 10, doi: 10.1086/422843

Fischer, P., Pryor, C., Murray, S., Mateo, M., & Richtler, T. 1998, AJ, 115, 592, doi: 10.1086/300212

Flaherty, K. M., Pipher, J. L., Megeath, S. T., et al. 2007, ApJ, 663, 1069, doi: 10.1086/518411

Frinchaboy, P. M., & Majewski, S. R. 2008, AJ, 136, 118, doi: 10.1088/0004-6256/136/1/118

Fukuda, N., & Hanawa, T. 2000, ApJ, 533, 911, doi: 10.1086/308701

Gaia Collaboration, Prusti, T., de Bruijne, J. H. J., et al. 2016a, A&A, 595, A1, doi: 10.1051/0004-6361/201629272

Gaia Collaboration, Brown, A. G. A., Vallenari, A., et al. 2016b, A&A, 595, A2, doi: 10.1051/0004-6361/201629512

—. 2018, A&A, 616, A1, doi: 10.1051/0004-6361/201833051

—. 2021, A&A, 649, A1, doi: 10.1051/0004-6361/202039657

Gao, Y., & Solomon, P. M. 2004, ApJ, 606, 271, doi: 10.1086/382999

Garay, G., & Rodriguez, L. F. 1983, ApJ, 266, 263, doi: 10.1086/160775

Gildas Team. 2013, GILDAS: Grenoble Image and Line Data Analysis Software. http://ascl.net/1305.010

Ginsburg, A., Glenn, J., Rosolowsky, E., et al. 2013, ApJS, 208, 14, doi: 10.1088/0067-0049/208/2/14

Girardi, L., Bertelli, G., Bressan, A., et al. 2002, A&A, 391, 195, doi: 10.1051/0004-6361:20020612

Goodwin, S. P., & Bastian, N. 2006, MNRAS, 373, 752, doi: 10.1111/j.1365-2966.2006.11078.x

Górski, K. M., Hivon, E., Banday, A. J., et al. 2005, ApJ, 622, 759, doi: 10.1086/427976

Gratton, R. G., Carretta, E., & Bragaglia, A. 2012, A&ARv, 20, 50, doi: 10.1007/s00159-012-0050-3

Griffin, M. J., Abergel, A., Abreu, A., et al. 2010, A&A, 518, L3, doi: 10.1051/0004-6361/201014519

Gutermuth, R. A., Megeath, S. T., Myers, P. C., et al. 2009, ApJS, 184, 18, doi: 10.1088/0067-0049/184/1/18

Gutermuth, R. A., Megeath, S. T., Pipher, J. L., et al. 2005, ApJ, 632, 397, doi: 10.1086/432460

Gutermuth, R. A., Myers, P. C., Megeath, S. T., et al. 2008, ApJ, 674, 336, doi: 10.1086/524722

Haisch, Karl E., J., Lada, E. A., & Lada, C. J. 2001, ApJ, 553, L153, doi: 10.1086/320685

Hatchell, J., Fuller, G. A., Richer, J. S., Harries, T. J., & Ladd, E. F. 2007, A&A, 468, 1009, doi: 10.1051/0004-6361:20066466

Hauser, M. G., & Dwek, E. 2001, ARA&A, 39, 249, doi: 10.1146/annurev.astro.39.1.249

Herbig, G. H. 1962, ApJ, 135, 736, doi: 10.1086/147316

Herbst, W., Herbst, D. K., Grossman, E. J., & Weinstein, D. 1994, AJ, 108, 1906, doi: 10.1086/117204

Herbst, W., & Shevchenko, V. S. 1999, AJ, 118, 1043, doi: 10.1086/300966

Hernández, J., Calvet, N., Briceño, C., Hartmann, L., & Berlind, P. 2004, AJ, 127, 1682, doi: 10.1086/381908

Hernández, J., Hartmann, L., Megeath, T., et al. 2007, ApJ, 662, 1067, doi: 10.1086/513735

Hillenbrand, L. A., Bauermeister, A., & White, R. J. 2008, in Astronomical Society of the Pacific Conference Series, Vol. 384, 14th Cambridge Workshop on Cool Stars, Stellar Systems, and the Sun, ed. G. van Belle, 200. https://arxiv.org/abs/astro-ph/0703642

Hora, J. L., Marengo, M., Park, R., et al. 2012, in Society of Photo-Optical Instrumentation Engineers (SPIE) Conference Series, Vol. 8442, Space Telescopes and Instrumentation 2012: Optical, Infrared, and Millimeter Wave, ed. M. C. Clampin, G. G. Fazio, H. A. MacEwen, & J. Oschmann, Jacobus M., 844239, doi: 10.1117/12.926894

Houck, J. R., Roellig, T. L., van Cleve, J., et al. 2004, ApJS, 154, 18, doi: 10.1086/423134

Hunter, D. A., & Massey, P. 1990, AJ, 99, 846, doi: 10.1086/115378

Israel, F. P. 1978, A&A, 70, 769

Jacoby, G. H., Hunter, D. A., & Christian, C. A. 1984, ApJS, 56, 257, doi: 10.1086/190983

Jeffries, R. D., Naylor, T., Mayne, N. J., Bell, C. P. M., & Littlefair, S. P. 2013, MNRAS, 434, 2438, doi: 10.1093/mnras/stt1180

Johnson, H. L., & Morgan, W. W. 1953, ApJ, 117, 313, doi: 10.1086/145697

Jones, T. J., & Hyland, A. R. 1980, MNRAS, 192, 359, doi: 10.1093/mnras/192.3.359

Jose, J., Pandey, A. K., Samal, M. R., et al. 2013, MNRAS, 432, 3445, doi: 10.1093/mnras/stt700

Joshi, Y. C., Maurya, J., John, A. A., et al. 2020, MNRAS, 492, 3602, doi: 10.1093/mnras/staa029

Joye, W. A., & Mandel, E. 2003, in Astronomical Society of the Pacific Conference Series, Vol. 295, Astronomical Data Analysis Software and Systems XII, ed. H. E. Payne, R. I. Jedrzejewski, & R. N. Hook, 489

Kahn, F. D. 1954, Bull. Astron. Inst. Netherlands, 12, 187

—. 1974, A&A, 37, 149

Kalirai, J. 2018, Contemporary Physics, 59, 251, doi: 10.1080/00107514.2018.1467648

Kawada, M., Baba, H., Barthel, P. D., et al. 2007, PASJ, 59, S389, doi: 10.1093/pasj/59.sp2.S389

Kennicutt, Robert C., J. 1989, ApJ, 344, 685, doi: 10.1086/167834

Kenyon, S. J., Gómez, M., & Whitney, B. A. 2008, in Handbook of Star Forming Regions, Volume I, ed. B. Reipurth, Vol. 4, 405

Kharchenko, N. V., Berczik, P., Petrov, M. I., et al. 2009, A&A, 495, 807, doi: 10.1051/0004-6361/200810407

Kharchenko, N. V., Piskunov, A. E., Röser, S., Schilbach, E., & Scholz, R. D. 2005, A&A, 440, 403, doi: 10.1051/0004-6361:20052740

Kharchenko, N. V., Piskunov, A. E., Schilbach, E., Röser, S., & Scholz, R. D. 2013, A&A, 558, A53, doi: 10.1051/0004-6361/201322302

Kobulnicky, H. A., Lundquist, M. J., Bhattacharjee, A., & Kerton, C. R. 2012, AJ, 143, 71, doi: 10.1088/0004-6256/143/3/71

Koenig, X. P., Allen, L. E., Gutermuth, R. A., et al. 2008, ApJ, 688, 1142, doi: 10.1086/592322

Koenig, X. P., Leisawitz, D. T., Benford, D. J., et al. 2012, ApJ, 744, 130, doi: 10.1088/0004-637X/744/2/130

Koornneef, J., & Code, A. D. 1981, ApJ, 247, 860, doi: 10.1086/159096

Kraus, A. L., & Hillenbrand, L. A. 2007, AJ, 134, 2340, doi: 10.1086/522831

Kroupa, P., Tout, C. A., & Gilmore, G. 1993, MNRAS, 262, 545, doi: 10.1093/mnras/262.3.545

Krumholz, M. R., McKee, C. F., & Bland-Hawthorn, J. 2019, ARA&A, 57, 227, doi: 10.1146/annurev-astro-091918-104430

Kwan, J. 1997, ApJ, 489, 284, doi: 10.1086/304773

Lada, C. J. 1987, in Star Forming Regions, ed. M. Peimbert & J. Jugaku, Vol. 115, 1

Lada, C. J. 2006, ApJ, 640, L63, doi: 10.1086/503158

Lada, C. J., & Adams, F. C. 1992, ApJ, 393, 278, doi: 10.1086/171505

Lada, C. J., Forbrich, J., Lombardi, M., & Alves, J. F. 2012, ApJ, 745, 190, doi: 10.1088/0004-637X/745/2/190

Lada, C. J., & Lada, E. A. 2003, ARA&A, 41, 57, doi: 10.1146/annurev.astro.41.011802.094844

Lada, C. J., Lada, E. A., Clemens, D. P., & Bally, J. 1994, ApJ, 429, 694, doi: 10.1086/174354

Lada, C. J., Lombardi, M., & Alves, J. F. 2010, ApJ, 724, 687, doi: 10.1088/0004-637X/724/1/687

Lada, E. A., Depoy, D. L., Evans, Neal J., I., & Gatley, I. 1991, ApJ, 371, 171, doi: 10.1086/169881

Lahulla, J. F. 1985, A&AS, 61, 537

—. 1987, AJ, 94, 1062, doi: 10.1086/114541

Landolt, A. U. 1992, AJ, 104, 340, doi: 10.1086/116242

Larson, R. B. 1972, MNRAS, 156, 437, doi: 10.1093/mnras/156.4.437

—. 1981, MNRAS, 194, 809, doi: 10.1093/mnras/194.4.809

—. 1985, MNRAS, 214, 379, doi: 10.1093/mnras/214.3.379

—. 2003, Reports on Progress in Physics, 66, 1651, doi: 10.1088/0034-4885/66/10/R03

Lasker, B. M., Sturch, C. R., McLean, B. J., et al. 1990, AJ, 99, 2019, doi: 10.1086/115483

Lawrence, A., Warren, S. J., Almaini, O., et al. 2007, MNRAS, 379, 1599, doi: 10.1111/j.1365-2966.2007.12040.x

Lefloch, B., & Lazareff, B. 1994, A&A, 289, 559

Leger, A., & Puget, J. L. 1984, A&A, 500, 279

Leisawitz, D., Bash, F. N., & Thaddeus, P. 1989, ApJS, 70, 731, doi: 10.1086/191357

Lim, B., Sung, H., Kim, J. S., et al. 2016, ApJ, 831, 116, doi: 10.3847/0004-637X/831/2/116

Lindegren, L., Hernández, J., Bombrun, A., et al. 2018, A&A, 616, A2, doi: 10.1051/0004-6361/201832727

Loktin, A. V., & Beshenov, G. V. 2003, Astronomy Reports, 47, 6, doi: 10.1134/1.1538491

Lucas, P. W., Hoare, M. G., Longmore, A., et al. 2008, MNRAS, 391, 136, doi: 10.1111/j.1365-2966.2008.13924.x

Lundquist, M. J., Kobulnicky, H. A., Alexander, M. J., Kerton, C. R., & Arvidsson, K. 2014, ApJ, 784, 111, doi: `10.1088/0004-637X/784/2/111`

Luo, A. L., Zhang, H.-T., Zhao, Y.-H., et al. 2012, Research in Astronomy and Astrophysics, 12, 1243, doi: `10.1088/1674-4527/12/9/004`

Luo, A. L., Zhao, Y.-H., Zhao, G., et al. 2015, Research in Astronomy and Astrophysics, 15, 1095, doi: `10.1088/1674-4527/15/8/002`

Luri, X., Brown, A. G. A., Sarro, L. M., et al. 2018, A&A, 616, A9, doi: `10.1051/0004-6361/201832964`

Lynga, G. 1982, A&A, 109, 213

Lynga, G., & Palous, J. 1987, A&A, 188, 35

Magnier, E. A., Volp, A. W., Laan, K., van den Ancker, M. E., & Waters, L. B. F. M. 1999a, A&A, 352, 228

Magnier, E. A., Waters, L. B. F. M., Groot, P. J., et al. 1999b, A&A, 346, 441

Magnier, E. A., Waters, L. B. F. M., Kuan, Y. J., et al. 1996, A&A, 305, 936

Magnier, E. A., Chambers, K. C., Flewelling, H. A., et al. 2020a, ApJS, 251, 3, doi: `10.3847/1538-4365/abb829`

Magnier, E. A., Schlafly, E. F., Finkbeiner, D. P., et al. 2020b, ApJS, 251, 6, doi: `10.3847/1538-4365/abb82a`

Mahoney, W. A., Garcia, L. J., Hunt, Joseph, J., et al. 2010, in Society of Photo-Optical Instrumentation Engineers (SPIE) Conference Series, Vol. 7737, Observatory Operations: Strategies, Processes, and Systems III, ed. D. R. Silva, A. B. Peck, & B. T. Soifer, 77371W, doi: `10.1117/12.857814`

Maíz Apellániz, J., & Weiler, M. 2018, A&A, 619, A180, doi: `10.1051/0004-6361/201834051`

Marigo, P., Girardi, L., Bressan, A., et al. 2017, ApJ, 835, 77, doi: `10.3847/1538-4357/835/1/77`

Martin, P. G., & Whittet, D. C. B. 1990, ApJ, 357, 113, doi: `10.1086/168896`

Martín-Hernández, N. L., van der Hulst, J. M., & Tielens, A. G. G. M. 2003, A&A, 407, 957, doi: `10.1051/0004-6361:20030982`

Mathis, J. S. 1990, ARA&A, 28, 37, doi: `10.1146/annurev.aa.28.090190.000345`

Mathis, J. S., Rumpl, W., & Nordsieck, K. H. 1977, ApJ, 217, 425, doi: `10.1086/155591`

Matsakis, D. N., Evans, N. J., I., Sato, T., & Zuckerman, B. 1976, AJ, 81, 172, doi: 10.1086/111871

Mayer, P., & Macák, P. 1973, Bulletin of the Astronomical Institutes of Czechoslovakia, 24, 50

Mayne, N. J., & Naylor, T. 2008, MNRAS, 386, 261, doi: 10.1111/j.1365-2966.2008.13025.x

McKee, C. F., & Ostriker, E. C. 2007, ARA&A, 45, 565, doi: 10.1146/annurev.astro.45.051806.110602

McLean, B. J., Greene, G. R., Lattanzi, M. G., & Pirenne, B. 2000, in Astronomical Society of the Pacific Conference Series, Vol. 216, Astronomical Data Analysis Software and Systems IX, ed. N. Manset, C. Veillet, & D. Crabtree, 145

McMillan, S. L. W., Vesperini, E., & Portegies Zwart, S. F. 2007, ApJ, 655, L45, doi: 10.1086/511763

Megeath, S. T., Allen, L. E., Gutermuth, R. A., et al. 2004, ApJS, 154, 367, doi: 10.1086/422823

Merrill, K. M., Russell, R. W., & Soifer, B. T. 1976, ApJ, 207, 763, doi: 10.1086/154545

Meyer, M. R., Calvet, N., & Hillenbrand, L. A. 1997, AJ, 114, 288, doi: 10.1086/118474

Mink, D. J. 1997, in Astronomical Society of the Pacific Conference Series, Vol. 125, Astronomical Data Analysis Software and Systems VI, ed. G. Hunt & H. Payne, 249

Miyama, S. M., Narita, S., & Hayashi, C. 1987a, Progress of Theoretical Physics, 78, 1051, doi: 10.1143/PTP.78.1051

—. 1987b, Progress of Theoretical Physics, 78, 1273, doi: 10.1143/PTP.78.1273

Monet, D. G., Levine, S. E., Canzian, B., et al. 2003, AJ, 125, 984, doi: 10.1086/345888

Montillaud, J., Juvela, M., Vastel, C., et al. 2019, A&A, 631, L1, doi: 10.1051/0004-6361/201936377

Motte, F., Bontemps, S., & Louvet, F. 2018, ARA&A, 56, 41, doi: 10.1146/annurev-astro-091916-055235

Murakami, H., Baba, H., Barthel, P., et al. 2007, PASJ, 59, S369, doi: 10.1093/pasj/59.sp2.S369

Muzerolle, J., Hillenbrand, L., Calvet, N., Briceño, C., & Hartmann, L. 2003, ApJ, 592, 266, doi: 10.1086/375704

Myers, P. C. 2009, ApJ, 700, 1609, doi: 10.1088/0004-637X/700/2/1609

Myers, P. C., Fuller, G. A., Goodman, A. A., & Benson, P. J. 1991, ApJ, 376, 561, doi: `10.1086/170305`

Myers, P. C., Fuller, G. A., Mathieu, R. D., et al. 1987, ApJ, 319, 340, doi: `10.1086/165458`

Myers, P. C., & Ladd, E. F. 1993, ApJ, 413, L47, doi: `10.1086/186956`

Neugebauer, G., Habing, H. J., van Duinen, R., et al. 1984, ApJ, 278, L1, doi: `10.1086/184209`

Ochsenbein, F., Bauer, P., & Marcout, J. 2000, A&AS, 143, 23, doi: `10.1051/aas:2000169`

Ojha, D. K., Tamura, M., Nakajima, Y., et al. 2004, ApJ, 608, 797, doi: `10.1086/420876`

Ojha, D. K., Samal, M. R., Pandey, A. K., et al. 2011, ApJ, 738, 156, doi: `10.1088/0004-637X/738/2/156`

Oke, J. B. 1990, AJ, 99, 1621, doi: `10.1086/115444`

Onaka, T., Matsuhara, H., Wada, T., et al. 2007, PASJ, 59, S401, doi: `10.1093/pasj/59.sp2.S401`

Palla, F., & Stahler, S. W. 2002, ApJ, 581, 1194, doi: `10.1086/344293`

Panagia, N. 1973, AJ, 78, 929, doi: `10.1086/111498`

Pang, X., Li, Y., Tang, S.-Y., Pasquato, M., & Kouwenhoven, M. B. N. 2020, ApJ, 900, L4, doi: `10.3847/2041-8213/abad28`

Panja, A., Chen, W. P., Dutta, S., et al. 2021, ApJ, 910, 80, doi: `10.3847/1538-4357/abded4`

Panja, A., Mondal, S., Dutta, S., et al. 2020, AJ, 159, 153, doi: `10.3847/1538-3881/ab737a`

—. 2019, Bulletin de la Societe Royale des Sciences de Liege, 88, 270

Panja, A., Sun, Y., Chen, W. P., & Mondal, S. 2022, ApJ, 939, 46, doi: `10.3847/1538-4357/ac940f`

Panwar, N., Sharma, S., Ojha, D. K., et al. 2020, ApJ, 905, 61, doi: `10.3847/1538-4357/abc42e`

Parker, R. J., Alcock, H. L., Nicholson, R. B., Panić, O., & Goodwin, S. P. 2021, ApJ, 913, 95, doi: `10.3847/1538-4357/abf4cc`

Pastorelli, G., Marigo, P., Girardi, L., et al. 2019, MNRAS, 485, 5666, doi: `10.1093/mnras/stz725`

Pecaut, M. J., & Mamajek, E. E. 2013, ApJS, 208, 9, doi: 10.1088/0067-0049/208/1/9

Peeters, E., Martín-Hernández, N. L., Damour, F., et al. 2002, A&A, 381, 571, doi: 10.1051/0004-6361:20011516

Pilbratt, G. L., Riedinger, J. R., Passvogel, T., et al. 2010, A&A, 518, L1, doi: 10.1051/0004-6361/201014759

Piskunov, A. E., Kharchenko, N. V., Röser, S., Schilbach, E., & Scholz, R. D. 2006, A&A, 445, 545, doi: 10.1051/0004-6361:20053764

Piskunov, A. E., Schilbach, E., Kharchenko, N. V., Röser, S., & Scholz, R. D. 2007, A&A, 468, 151, doi: 10.1051/0004-6361:20077073

Planck Collaboration, Ade, P. A. R., Aghanim, N., et al. 2016, A&A, 594, A28, doi: 10.1051/0004-6361/201525819

Poglitsch, A., Waelkens, C., Geis, N., et al. 2010, A&A, 518, L2, doi: 10.1051/0004-6361/201014535

Pomarès, M., Zavagno, A., Deharveng, L., et al. 2009, A&A, 494, 987, doi: 10.1051/0004-6361:200811050

Porras, A., Christopher, M., Allen, L., et al. 2003, AJ, 126, 1916, doi: 10.1086/377623

Portegies Zwart, S. F., McMillan, S. L. W., & Gieles, M. 2010, ARA&A, 48, 431, doi: 10.1146/annurev-astro-081309-130834

Prabhu, T. P. 2014, Proceedings of the Indian National Science Academy Part A, 80, 887, doi: 10.16943/ptinsa/2014/v80i4/55174

Price, D. J., & Bate, M. R. 2009, MNRAS, 398, 33, doi: 10.1111/j.1365-2966.2009.14969.x

Price, S. D., Egan, M. P., Carey, S. J., Mizuno, D. R., & Kuchar, T. A. 2001, AJ, 121, 2819, doi: 10.1086/320404

Puget, P., Stadler, E., Doyon, R., et al. 2004, in Society of Photo-Optical Instrumentation Engineers (SPIE) Conference Series, Vol. 5492, Ground-based Instrumentation for Astronomy, ed. A. F. M. Moorwood & M. Iye, 978–987, doi: 10.1117/12.551097

Reid, M. J., Dame, T. M., Menten, K. M., & Brunthaler, A. 2016, ApJ, 823, 77, doi: 10.3847/0004-637X/823/2/77

Reid, M. J., Menten, K. M., Brunthaler, A., et al. 2019, ApJ, 885, 131, doi: 10.3847/1538-4357/ab4a11

Reipurth, B., & Bally, J. 2001, ARA&A, 39, 403, doi: 10.1146/annurev.astro.39.1.403

Rieke, G. H., Young, E. T., Engelbracht, C. W., et al. 2004, ApJS, 154, 25, doi: 10.1086/422717

Robitaille, T. 2019, APLpy v2.0: The Astronomical Plotting Library in Python, 2.0, Zenodo, doi: 10.5281/zenodo.2567476

Robitaille, T. P., Whitney, B. A., Indebetouw, R., & Wood, K. 2007, ApJS, 169, 328, doi: 10.1086/512039

Robitaille, T. P., Whitney, B. A., Indebetouw, R., Wood, K., & Denzmore, P. 2006, ApJS, 167, 256, doi: 10.1086/508424

Roeser, S., Demleitner, M., & Schilbach, E. 2010, AJ, 139, 2440, doi: 10.1088/0004-6256/139/6/2440

Sagar, R., Kumar, B., Omar, A., & Pandey, A. K. 2012, in Society of Photo-Optical Instrumentation Engineers (SPIE) Conference Series, Vol. 8444, Ground-based and Airborne Telescopes IV, ed. L. M. Stepp, R. Gilmozzi, & H. J. Hall, 84441T, doi: 10.1117/12.925634

Sagar, R., Kumar, B., & Sharma, S. 2020, Journal of Astrophysics and Astronomy, 41, 33, doi: 10.1007/s12036-020-09652-9

Salpeter, E. E. 1955, ApJ, 121, 161, doi: 10.1086/145971

Samal, M. R., Ojha, D. K., Jose, J., et al. 2015, A&A, 581, A5, doi: 10.1051/0004-6361/201322787

Sanders, D. B., Scoville, N. Z., & Solomon, P. M. 1985, ApJ, 289, 373, doi: 10.1086/162897

Sandford, M. T., I., Whitaker, R. W., & Klein, R. I. 1982, ApJ, 260, 183, doi: 10.1086/160245

Sanner, J., Altmann, M., Brunzendorf, J., & Geffert, M. 2000, A&A, 357, 471. https://arxiv.org/abs/astro-ph/0003327

Santos-Silva, T., & Gregorio-Hetem, J. 2012, A&A, 547, A107, doi: 10.1051/0004-6361/201219695

Saral, G., Hora, J. L., Willis, S. E., et al. 2015, ApJ, 813, 25, doi: 10.1088/0004-637X/813/1/25

Saral, G., Hora, J. L., Audard, M., et al. 2017, ApJ, 839, 108, doi: 10.3847/1538-4357/aa6575

Savage, B. D., & Mathis, J. S. 1979, ARA&A, 17, 73, doi: 10.1146/annurev.aa.17.090179.000445

Schlafly, E. F., Finkbeiner, D. P., Jurić, M., et al. 2012, ApJ, 756, 158, doi: 10.1088/0004-637X/756/2/158

Schlafly, E. F., Meisner, A. M., Stutz, A. M., et al. 2016, ApJ, 821, 78, doi: 10.3847/0004-637X/821/2/78

Schneider, S., & Elmegreen, B. G. 1979, ApJS, 41, 87, doi: 10.1086/190609

Shan, W., Yang, J., Shi, S., et al. 2012, IEEE Transactions on Terahertz Science and Technology, 2, 593, doi: 10.1109/TTHZ.2012.2213818

Sharma, S., Pandey, A. K., Ogura, K., et al. 2008, AJ, 135, 1934, doi: 10.1088/0004-6256/135/5/1934

—. 2006, AJ, 132, 1669, doi: 10.1086/507094

Sjouwerman, L. O., Capen, S. M., & Claussen, M. J. 2009, ApJ, 705, 1554, doi: 10.1088/0004-637X/705/2/1554

Skrutskie, M. F., Cutri, R. M., Stiening, R., et al. 2006, AJ, 131, 1163, doi: 10.1086/498708

Smithsonian Astrophysical Observatory. 2000, SAOImage DS9: A utility for displaying astronomical images in the X11 window environment. http://ascl.net/0003.002

Spitzer, Lyman, J. 1958, ApJ, 127, 17, doi: 10.1086/146435

Spitzer, L. 1978, Physical processes in the interstellar medium, doi: 10.1002/9783527617722

—. 1987, Dynamical evolution of globular clusters

Stark, A. A., & Blitz, L. 1978, ApJ, 225, L15, doi: 10.1086/182783

Stetson, P. B. 1987, PASP, 99, 191, doi: 10.1086/131977

—. 1990, PASP, 102, 932, doi: 10.1086/132719

Stetson, P. B. 1992, in Astronomical Society of the Pacific Conference Series, Vol. 25, Astronomical Data Analysis Software and Systems I, ed. D. M. Worrall, C. Biemesderfer, & J. Barnes, 297

Straw, S. M., & Hyland, A. R. 1989, ApJ, 340, 318, doi: 10.1086/167395

Strömgren, B. 1939, ApJ, 89, 526, doi: 10.1086/144074

Stubbs, C. W., Doherty, P., Cramer, C., et al. 2010, ApJS, 191, 376, doi: 10.1088/0067-0049/191/2/376

Su, Y., Yang, J., Zhang, S., et al. 2019, ApJS, 240, 9, doi: 10.3847/1538-4365/aaf1c8

Sun, Y., Yang, J., Xu, Y., et al. 2020, ApJS, 246, 7, doi: 10.3847/1538-4365/ab5b97

Sung, H., Chun, M.-Y., & Bessell, M. S. 2000, AJ, 120, 333, doi: 10.1086/301450

Terebey, S., Shu, F. H., & Cassen, P. 1984, ApJ, 286, 529, doi: 10.1086/162628

Tody, D. 1986, in Society of Photo-Optical Instrumentation Engineers (SPIE) Conference Series, Vol. 627, Instrumentation in astronomy VI, ed. D. L. Crawford, 733, doi: 10.1117/12.968154

Tody, D. 1993, in Astronomical Society of the Pacific Conference Series, Vol. 52, Astronomical Data Analysis Software and Systems II, ed. R. J. Hanisch, R. J. V. Brissenden, & J. Barnes, 173

Tonry, J. L., Stubbs, C. W., Lykke, K. R., et al. 2012, ApJ, 750, 99, doi: 10.1088/0004-637X/750/2/99

Torres-Dodgen, A. V., & Weaver, W. B. 1993, PASP, 105, 693, doi: 10.1086/133222

Tremblin, P., Anderson, L. D., Didelon, P., et al. 2014, A&A, 568, A4, doi: 10.1051/0004-6361/201423959

Trumpler, R. J. 1930a, PASP, 42, 214, doi: 10.1086/124039

—. 1930b, Lick Observatory Bulletin, 420, 154, doi: 10.5479/ADS/bib/1930LicOB.14.154T

Umemoto, T., Minamidani, T., Kuno, N., et al. 2017, PASJ, 69, 78, doi: 10.1093/pasj/psx061

van Dishoeck, E. F., & Black, J. H. 1988, ApJ, 334, 771, doi: 10.1086/166877

Verschueren, W., & David, M. 1989, A&A, 219, 105

Vesperini, E., McMillan, S. L. W., & Portegies Zwart, S. 2009, ApJ, 698, 615, doi: 10.1088/0004-637X/698/1/615

Walborn, N. R., & Fitzpatrick, E. L. 1990, PASP, 102, 379, doi: 10.1086/132646

Wang, P., Li, Z.-Y., Abel, T., & Nakamura, F. 2010a, ApJ, 709, 27, doi: 10.1088/0004-637X/709/1/27

Wang, S.-G., Su, D.-Q., Chu, Y.-Q., Cui, X., & Wang, Y.-N. 1996, Appl. Opt., 35, 5155, doi: 10.1364/AO.35.005155

Wang, W.-H., Cowie, L. L., Barger, A. J., Keenan, R. C., & Ting, H.-C. 2010b, ApJS, 187, 251, doi: 10.1088/0067-0049/187/1/251

Wells, D. C., Greisen, E. W., & Harten, R. H. 1981, A&AS, 44, 363

Wenger, M., Ochsenbein, F., Egret, D., et al. 2000, A&AS, 143, 9, doi: 10.1051/aas:2000332

Werner, M. W., Roellig, T. L., Low, F. J., et al. 2004, ApJS, 154, 1, doi: 10.1086/422992

Whittet, D. C. B., Martin, P. G., Fitzpatrick, E. L., & Massa, D. 1993, ApJ, 408, 573, doi: 10.1086/172615

Whitworth, A. 1979, MNRAS, 186, 59, doi: 10.1093/mnras/186.1.59

Whitworth, A. P., Bhattal, A. S., Chapman, S. J., Disney, M. J., & Turner, J. A. 1994, A&A, 290, 421

Wilking, B. A., Lada, C. J., & Young, E. T. 1989, ApJ, 340, 823, doi: 10.1086/167439

Williams, J. P., de Geus, E. J., & Blitz, L. 1994, ApJ, 428, 693, doi: 10.1086/174279

Williams, J. P., & McKee, C. F. 1997, ApJ, 476, 166, doi: 10.1086/303588

Wong, T., & Blitz, L. 2002, ApJ, 569, 157, doi: 10.1086/339287

Wright, E. L., Eisenhardt, P. R. M., Mainzer, A. K., et al. 2010, AJ, 140, 1868, doi: 10.1088/0004-6256/140/6/1868

Wu, J., Evans, Neal J., I., Gao, Y., et al. 2005, ApJ, 635, L173, doi: 10.1086/499623

Wu, Z.-Y., Zhou, X., Ma, J., & Du, C.-H. 2009, MNRAS, 399, 2146, doi: 10.1111/j.1365-2966.2009.15416.x

Wu, Z.-Y., Zhou, X., Ma, J., et al. 2007, AJ, 133, 2061, doi: 10.1086/512189

York, D. G., Adelman, J., Anderson, John E., J., et al. 2000, AJ, 120, 1579, doi: 10.1086/301513

Zacharias, N., Monet, D. G., Levine, S. E., et al. 2004, in American Astronomical Society Meeting Abstracts, Vol. 205, American Astronomical Society Meeting Abstracts, 48.15

Zacharias, N., Finch, C., Subasavage, J., et al. 2015, AJ, 150, 101, doi: 10.1088/0004-6256/150/4/101

Zhang, H.-X., Gao, Y., Fang, M., et al. 2015, Research in Astronomy and Astrophysics, 15, 1294, doi: 10.1088/1674-4527/15/8/014

Zhao, G., Zhao, Y.-H., Chu, Y.-Q., Jing, Y.-P., & Deng, L.-C. 2012, Research in Astronomy and Astrophysics, 12, 723, doi: 10.1088/1674-4527/12/7/002